2018-01-01

Additive Manufacturing Of Multi-Functional Nanocomposites For Sensor And Energy Storage Devices

Hoejin Kim
University of Texas at El Paso, kimhoejin@gmail.com

ADDITIVE MANUFACTURING OF MULTI-FUNCTIONAL NANOCOMPOSITES FOR SENSOR AND ENERGY STORAGE DEVICES

HOEJIN KIM

Doctoral Program in Mechanical Engineering

APPROVED:

Tzu-Liang B. Tseng, Ph.D., Chair

Yirong Lin, Ph.D., Co-Chair

Barry A. Benedict, Ph.D.

Juan C. Noveron, Ph.D.

Norman D. Love, Ph.D.

Charles Ambler, Ph.D.
Dean of the Graduate School

Dedication

To my wife Jihu and my parents

and

Almighty God Father, Jesus, and Holy Spirit

ADDITIVE MANUFACTURING OF MULTI-FUNCTIONAL NANOCOMPOSITES FOR SENSOR AND ENERGY STORAGE DEVICES

by

HOEJIN KIM, M.S.

DISSERTATION

Presented to the Faculty of the Graduate School of

The University of Texas at El Paso

in Partial Fulfillment

of the Requirements

for the Degree of

DOCTOR OF PHILOSOPHY

Mechanical Engineering Doctoral Program

THE UNIVERSITY OF TEXAS AT EL PASO

May 2018

Acknowledgements

Firstly, I would like to give my wife, Jihu Kang, my deepest gratitude. All of her supports, encouragements, and love when the times got rough is much appreciated. Moreover I would like to express a great appreciation to my parents and parents in law for their all supports and prayers.

Secondly, I would like to express the deepest appreciation to my committee chairs, Drs. Tzu-Liang Bill Tseng and Yirong Lin, who have the attitude and the substance of a genius: they continually and convincingly conveyed a spirit of adventure in regard to research. Without their guidance and persistence help this dissertation would not have been possible. Moreover, I would like to thank my committee members, Drs. Juan C. Noveron, Barry A. Benedict, and Norman D. Love, who supported my dissertation and encouraged me continuously on research projects.

I would like to express the appreciation to all of my coworkers, Dr. Aditya Akundi, Carlos Garcia, Luis Chavez, Tariqul Islam, Didarul Islam, Fernando Torres, Mingyue Li, Jeffrey Johnson, and Bethany R. Wilburn. And I thank my colleagues: Yuxin Wen, Honglun Xu, MD Fashiar.

Lastly, I thank God who is my great intercessor and source of peace, encouragement, wisdom, knowledge, and love.

Abstract

The goal of this research is to develop novel 3D printing process and design nanocomposites for piezoelectric and dielectric devices using fused deposition modeling (FDM) and stereolithography (SL) 3D printing techniques for use in sensor and energy storage applications. Techniques for electric and corona assisted in-situ poling during 3D printing were developed to improve the piezoelectric property and ease of manufacture. Poly(vinylidene fluoride) (PVDF) and barium titanate ($BaTiO_3$, BT) are well-known for their high piezo- and dielectric constants among polymers and ceramics, while multi-walled carbon nanotubes (CNTs) were introduced to improve efficiency of stress reinforcement and conductivity for charge carriers between the two. It was investigated that filament extrusion and FDM 3D printing processes provide homogeneous dispersion of nanoparticles, removal of internal defects, and alleviation of nanoparticles' agglomeration in polymer matrix which enhance piezoelectric and mechanical properties than traditional solvent-casting. Increasing both BT and CNTs nanoparticles improves both piezoelectric and dielectric properties as well as mechanical toughness, while CNTs have a threshold at each property where increasing content switched from improving their properties to being conductive. The best combination for the maximum output current/voltage (±1 nA/340 mV) and piezoelectric coefficient (0.65 pC/N) while subjecting the materials to cyclic loads at 40 N were obtained at 0.4wt.%-CNT/18wt.%-BT/PVDF. Moreover, the best mixture of relative dielectric constant and loss properties (118 and 0.119) was obtained for the nanocomposites containing 1.7wt.%-CNT/45wt.%-BT/PVDF. In mechanical testing results, BT and CNTs nanoparticles played a significant role of improving toughness of 3D printed nanocomposites, highest tensile strength (24.2 MPa) and strain (579%) were obtained at 1wt.%-CNT/12wt.%-BT/PVDF. An effective and scalable 3D printing techniques for the manufacture of piezoelectric and dielectric nanocomposites was demonstrated.

Table of Contents

List of Tables

List of Figures

Chapter 1: Introduction

1.1 MOTIVATIONS

The motivation of this research lies in development of a novel 3D/4D printing process and design of multi-functional (structural/functional) nanocomposites for sensor and energy storage industry. During past few decades, smart materials have been paid attentions to researchers to incorporate in multi-functional nanocomposites for the purposes of sensing, energy harvesting and storage, self-healing, shape recovery, etc. while maintaining or enhancing their mechanical properties of the structure. While there exists many types of useful smart materials, piezoelectric ceramics and polymers remain the most widely used smart material for a number of reasons. Firstly, piezoelectric ceramics retain high piezoelectric coefficient (e.g. PMN-PT d_{33}: ~ 2500 pC/N). Usually, piezoelectric ceramics possessing high piezoelectric coefficient provide relatively high dielectric constant (e.g. PMN-PT ε_r: ~ 20000). Secondly, piezoelectric polymers, as opposed to ceramics, retain relatively lower piezoelectric coefficient (e.g. PVDF d_{33}: ~ 33 pC/N) and dielectric constant. However, it retains high mechanical durable, tough, and flexible and extremely high chemical and thermal stability and resistivity. Because of these unique properties, it has been widely used in fields of robotic, aircraft and bridge vibration monitoring, electronic devices, automobile, bio-medical, energy harvesting, and energy storage. However, there are several limitations to implementing this delicate active material during manufacturing process. Firstly, piezoelectric ceramics are brittle nature resulting in design limitation for large scale and complex geometry and requires time-consuming and high cost of fabrication processing due to applying high temperature and pressure. Secondly, in order to transform regular to electro-active piezoelectric materials, traditional poling process is required to polarize randomly oriented dipoles. This process requires high electric field (300 MV/m), 1 – 15hr processing time, and complicated process setup and results in quality issues such as heterogeneous distribution of dipole polarization and dimensional accuracy.

In this research work, to resolve the above-mentioned issues in material nature, piezoelectric performance, manufacturing process, and quality, firstly traditional poling process was integrated with Additive Manufacturing (AM) process to reduce time, complexity, and cost of fabrication process. The AM is an emerging technology that can provide three-dimensional structure with freedom of design though simple way. Secondly, piezoelectric ceramic powder is dispersed in piezoelectric polymer matrix to share each advantage of relative piezo/dielectric properties and flexibility and overcome brittle natures. However, this composition results in low mechanical coupling coefficient between ceramic powder and polymer matrix. Therefore, graphitic nanomaterials were dispersed within composites as stress reinforcing and conductive agents in order to improve piezoelectric and mechanical performances. It is believed that achieved results from this research work will benefit to sensor and energy related industries.

1.2 BACKGROUND

Multi-functional composite material provides the load-carrying function and other functional requirement such as electrical, magnetic, optical properties. Functional composites bring together various material properties and often combine the advantages of different classes of materials. Figure 1.1 shows a basic example of multi-functional composites application that Aircraft is flying by electricity powered by solar panel. This solar panel not only converts solar radiant light to electrical energy but also increase mechanical strength of wing structure.

Figure 1.1: Example of multi-functional composites, aircraft powered by solar panel.

In order to empower functional properties into the structure, smart materials are mostly used as a shape of nanomaterial inclusion within a matrix. As seen in Figure 1.2, various smart materials are introduced such as piezoelectric, pyroelectric, dielectric, self-healing, thermoelectric, shape-memory, triboelectric materials, and others. A typical example of composites with dominating importance of the electrical properties is piezoelectric and dielectric materials, which can generate or store energy in response to external stress or external electrical input.

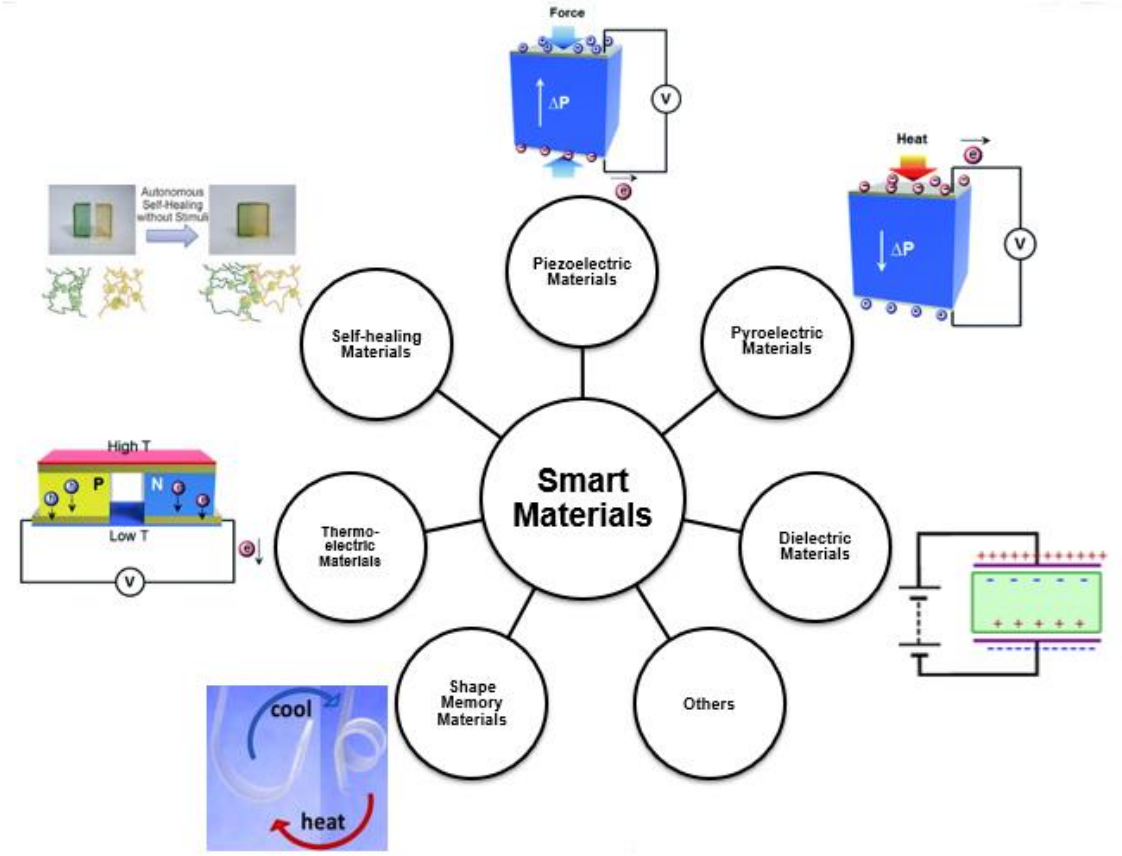

Figure 1.2: Category and illustration of various smart materials.

1.2.1 Piezoelectric Materials

Applications of piezoelectric material is seen in Figure 1.3. Commercial piezoelectric material is widely used as sensors, actuators, capacitors, energy harvesting, health monitoring in electronic devices, biomedical, aerospace, and transportation (i.e. human embedded sensor and

energy harvesting, robotic sensor, vibration monitoring in aircraft and bridge, sonar in warship, oil, pressure, torque, airbag sensors, etc.).

Figure 1.3: Commercial piezoelectric devices and its applications.

Piezoelectric Ceramics

Among the piezoelectric ceramics, PMN-PT (lead magnesium niobite-lead titanate) is the highest piezoelectric performance about > 2200 pC/N, PZT (lead zirconate titanate) is the second highest about > 600, and $BaTiO_3$ (barium titanate) is the third about > 190 [1]. Since PMN-PT and PZT contain Pb (lead) element which is harmful for human health and detrimental for environment, $BaTiO_3$ was used for this research. A lattice structure of $BaTiO_3$ (BT) is composed of eight Ba atoms at the comer, six O atoms in each plane, and Ti atom in center. BT has four different phases under the different temperatures as shown in Figure 1.4. At room temperature, it is existed as tetragonal phase.

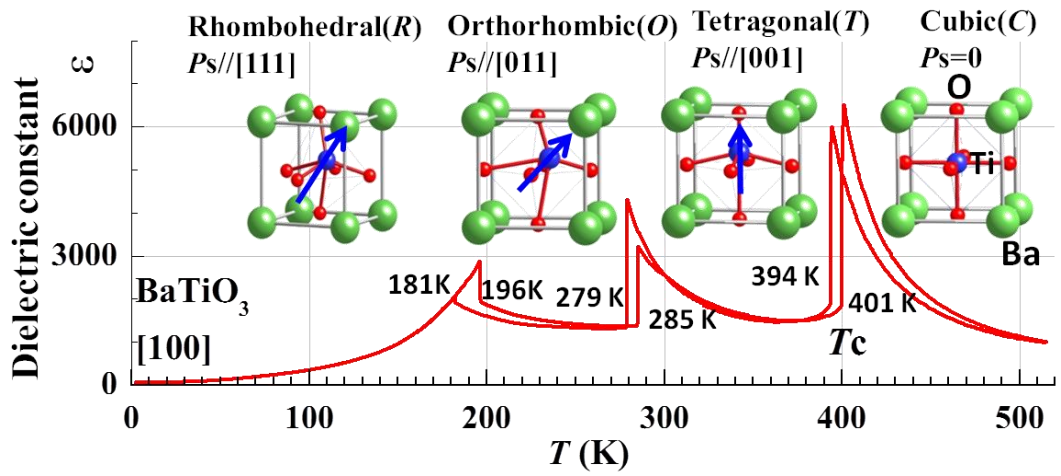

Figure 1.4: Four different phases of $BaTiO_3$ under various temperature ranges [2].

In atomic scale, Ti atom has enough space to freely move around in the middle of lattice structure. When high electric field is applied through the piezoelectric material which is also called poling process, Ti atom is dragged to the direction of electric field as shown in Figure 1.5. In this moment, BT lattice shapes asymmetric atom configuration and dipole moments occur when there is a separation of charge. By shifting Ti atom up or down depending on the field direction, one side of BT lattice becomes positively net charged so that it attracts negative charges. In contrast, the other side of BT lattice relatively becomes negatively net charged to attract positive changes from the air (see an example of working principle of piezoelectric quartz in Figure 1.5). This dipole moments arise from intensity of electric field. This dipole remains still when releasing external electric field due to remanent polarization effect. However, dipole moment is lost above Curie temperature (120 °C). When external stress is applied to the direction of dipole moment in piezoelectric material, this stress would break the asymmetric atom configuration so that accumulated charges on each side would be released which becomes a source of electricity.

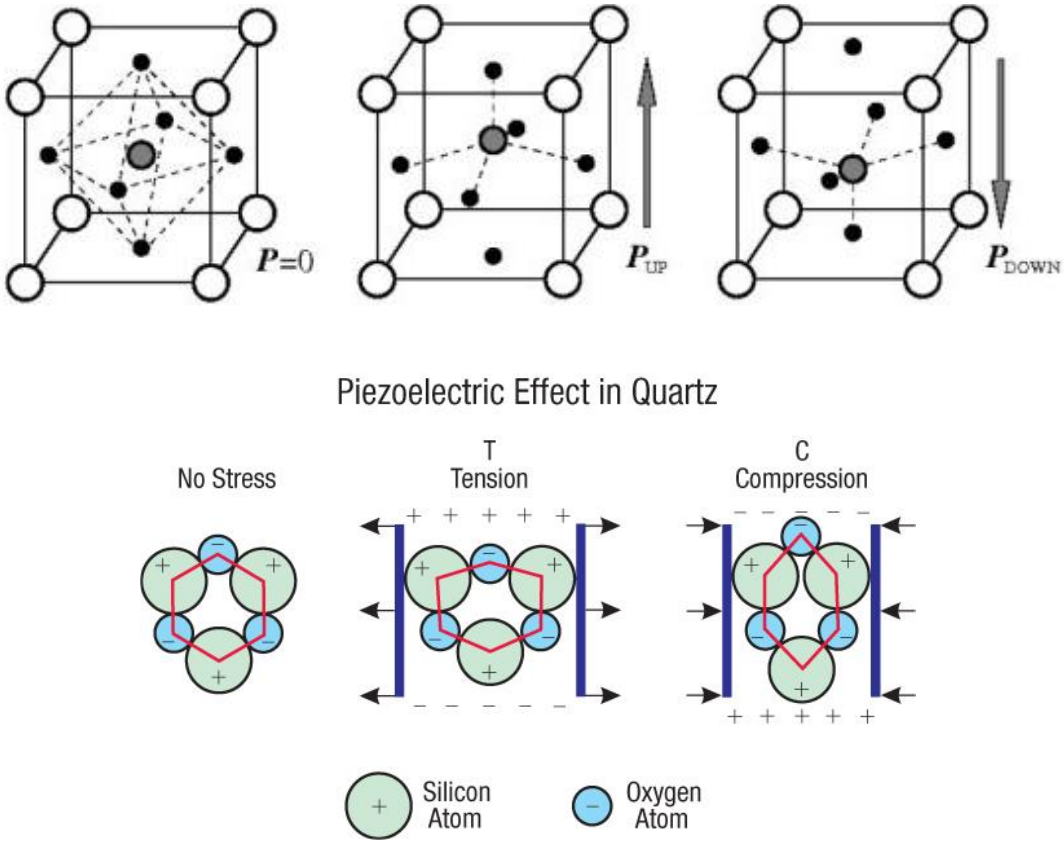

Figure 1.5: Schematic of a lattice structure of $BaTiO_3$ and charge separation (attraction and release) of piezoelectric quartz as an example.

In micro scale, dipoles are randomly oriented in each domain boundary when no electric field is applied. However, when applying appropriate electric field dipoles are being aligned and domain boundary is expanding. Strong electric field allows entire dipoles oriented in the direction of field as well as removing domain boundary as shown in Figure 1.6.

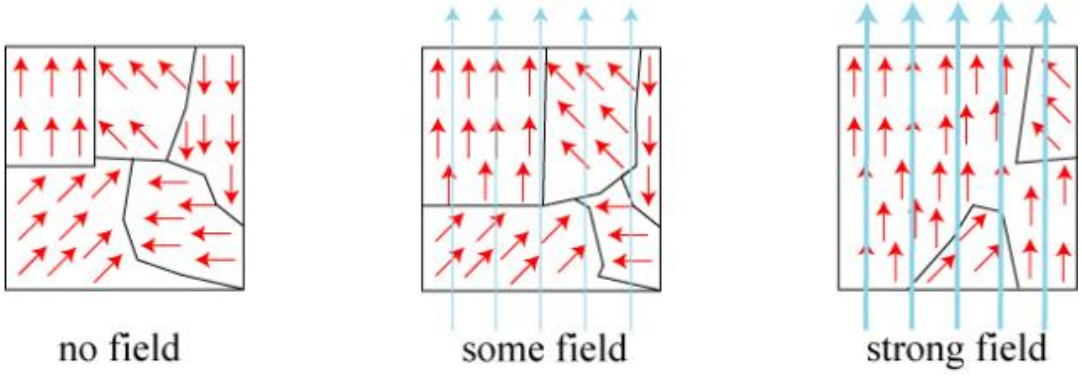

Figure 1.6: Schematic of dipoles' orientation when applying external electric field through the piezoelectric material.

The basic working principle of piezoelectricity is understood as the electricity which is the byproduct of electromechanical interactions, primarily electrical and mechanical oscillations. Figure 1.7 shows two piezoelectric working modes: generator and actuator modes. Generator mode is to generate electricity in response to external stress which can be quantify producing electricity through the equation $D = dT$, denote D is electric displacement (C/m^2), d is piezoelectric coefficient (C/N), and T is stress. In actuator mode, volume change of piezoelectric material occurs when applying AC electric current through the equation $S = dE$, denote that S is strain and E is applied electric field strength (V/m).

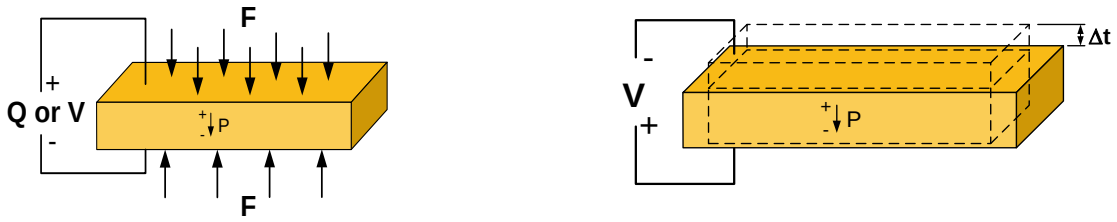

Generator Mode

$$D = dT$$

Actuator Mode

$$S = d^t E$$

Figure 1.7: Schematic of piezoelectric two working principle: generator and actuator modes [3].

Piezoelectric Polymers

Among the piezoelectric polymer such as polyvinylidene fluoride (PVDF), PTrFE, EAP, P(VDF-TrFE), PVDF is the highest piezoelectric performance about 33 pC/N which is relatively lower than BT. It retains relatively higher Curie temperature (150 °C), mechanically durable, tough, and flexible. Additionally, it is thermally and chemically extremely stable and resistant. PVDF is composed of H, F, and C atoms and has typically three phases: α, β, and γ as shown in Figure 1.8. The α-phase is randomly oriented asymmetric configuration which has no piezoelectric effect. However, after poling process each H and F atom is aligned in opposite sides and become

symmetric configuration. This configuration attracts opposite charges on each side which provides electricity.

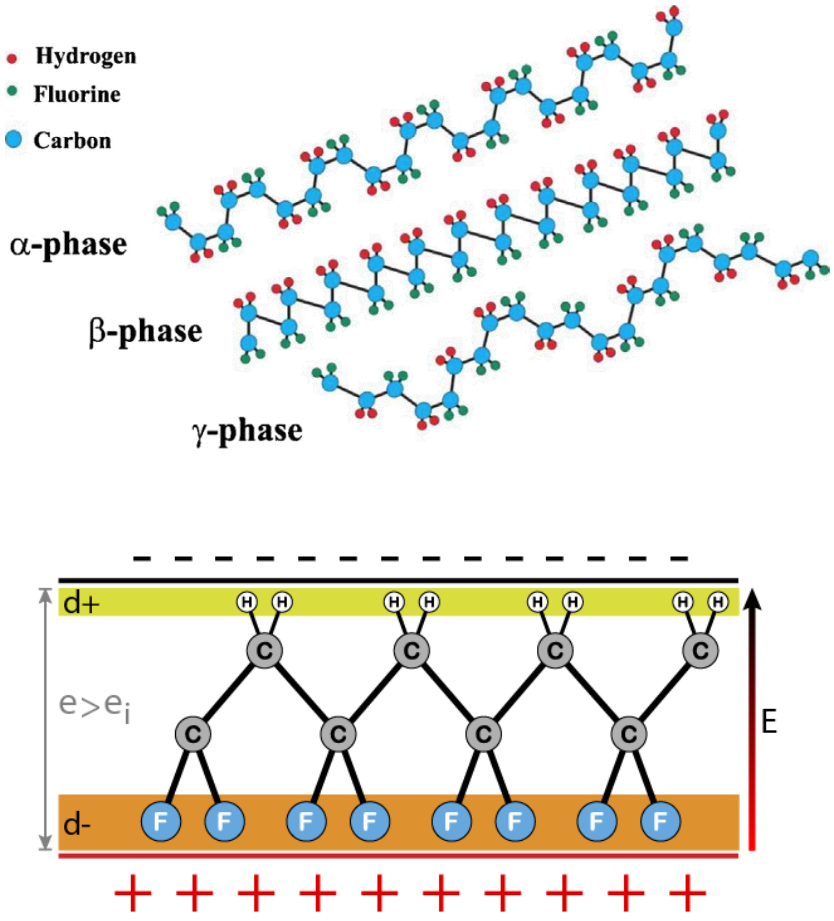

Figure 1.8: Schematic of three different phases of PVDF and dipole arrangement upon electric field.

1.2.2 Dielectric Materials

Dielectric materials are widely used for capacitor and energy storage devices. Above-mentioned piezoelectric materials are used as electrical insulator that can be polarized by an applied electric field between two electrodes. Because of polarization, as shown in Figure 1.9, positive charges are displaced in the direction of the field and negative charges shift in the opposite direction. This creates a small internal electric field that is opposite to main field and reduces the

overall field within the dielectric itself. If the dielectric material has strong polarization dipole, stronger internal electrical field occurs so that it resists electrical flow (electrical breakdown) through the medium. Once electric field is removed, accumulated charges still remain in opposite side. Ability to store the electrical charges are varied according to dielectric constant (ε_r).

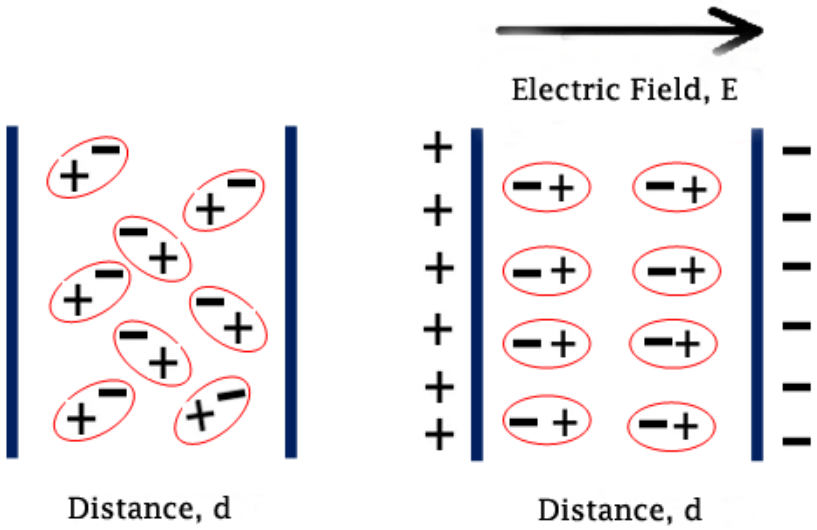

Figure 1.9: Schematic of dielectric materials' polarization between two electrodes under applied electric field.

Dielectric constant, also known as relative permittivity, is calculated from the following equation:

$$\varepsilon_r = Ct/\varepsilon_0 A \quad (1)$$

where *C* is capacitance which is the ability of a body to store an electric charge, *t* is the distance between the two electrodes, ε_0 is the permittivity of free space (8.85×10^{-12} F/m), and *A* is the area of the electrodes. Permittivity is the measure of resistance that is encountered when forming an electric field in a particular medium. More specifically, permittivity describes the amount of charge needed to generate one unit of electric flux in a particular medium. Accordingly, a charge will yield more electric flux in a medium with low permittivity than in a medium with high permittivity. Thus, permittivity is the measure of a material's ability to resist an electric field. The relative permittivity (relative dielectric constant) is absolute permittivity expressed as a ratio

relative to the permittivity of vacuum. Likewise, relative permittivity is the ratio of the capacitance of a capacitor using that material as a dielectric, compared with a similar capacitor that has vacuum as its dielectric. Relative permittivity is also commonly known as dielectric constant, a term deprecated in physics and engineering as well as in chemistry.

1.2.3 Manufacturing Processes

Traditional Manufacturing Processes

Solvent casting, hot embossing, and spin coating are commonly used fabrication methods for piezoelectric polymer device. Mostly used fabrication methods for piezoelectric ceramics are hot pressing and sintering. There are four traditional poling manufacturing processes in order to transform regular piezoelectric to electro-active material. Figure 1.10 shows Stretch poling is to physically orient piezoelectric polymer molecules to the direction of uniaxial tension. This method causes dimensional inaccuracy. Electro-spinning is to deposit piezoelectric liquid solution to the rotating substrate under high electric field between metallic needle and metal substrate. This method can only produce piezoelectric fibers and has a difficulty in controlling sample dimension.

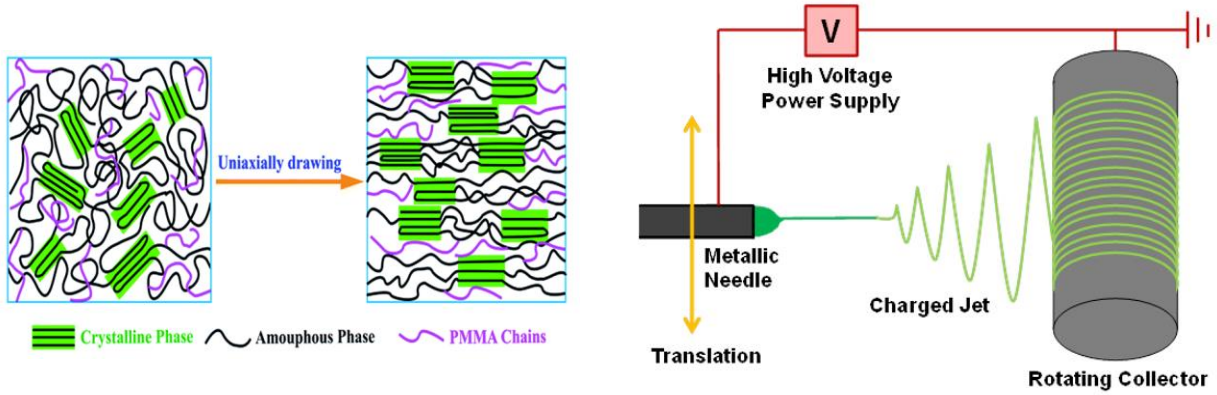

Figure 1.10: Traditonal poling procsses: stretch poling (left) and electro-spinning (right).

Figure 1.11 shows another two traditional poling methods. Electrical poling is to apply high electric field between two metal electrodes contacted to the surface of piezoelectric material. Another method is corona poling that uses a metallic needle above on top of sample and metallic

substrate on the bottom of sample. While high electric field is applying between the metallic needle and substrate, the metallic needle ionizes the air and turns to positively charged ions evenly distributing on the top surface of piezoelectric sample. The positive charges and negative charges create high electric field to polarize dipoles of piezoelectric molecules.

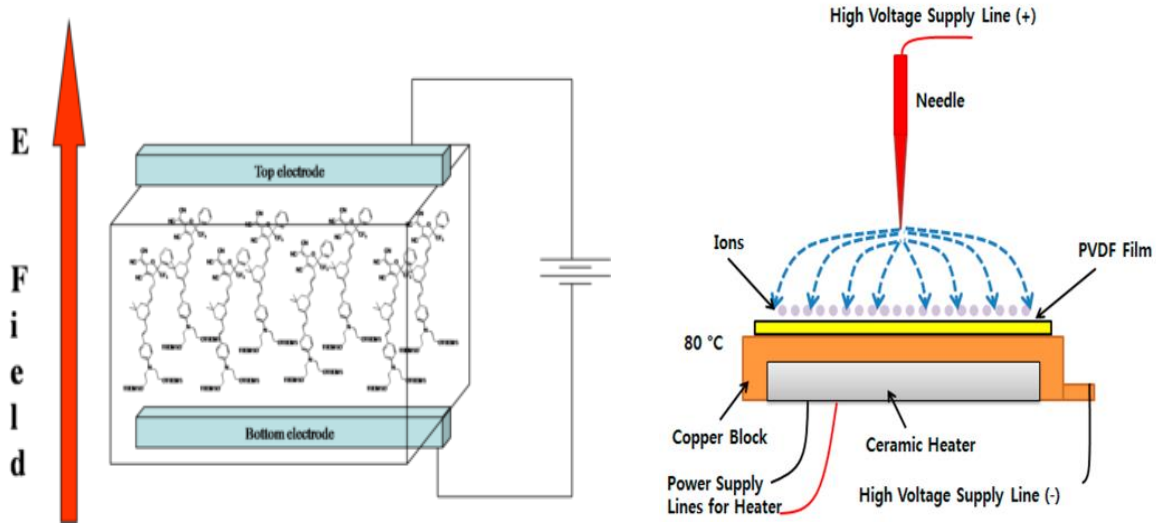

Figure 1.11: Traditonal poling procsses: electrical poling (right) and corona poling (left).

Additive Manufacturing Processes

Additive manufacturing (AM) technology, also known as 3D printing, is a process which materials is solidified under computer control to create 3D structure. Recently, a researcher at MIT developed 4D printing technology which use the same techniques of 3D printing through computer programmed deposition of material to create 3D structure. However, 4D printing adds the dimension of transformation or functionalities to 3D structure. Therefore, 3D printed structure reacts with parameters within the environment (i.e. temperature, humidity, stress, etc.) and change its form or produce its functionalities accordingly.

Among the typical seven different techniques in AM technology as shown in Figure 1.12, extrusion-based processes (EBP) deposit material in form of a continuous flow layer by layer to build a 3D structure. These processes have diverse technique concepts but are classified into two main groups; melting based extrusion and non-melting based extrusion [4]. 3D-bioplotting is the

most representative of non-melting-based extrusion techniques and fused deposition modeling in melting based extrusion techniques.

Photopolymer vat processes (PVP) are based on the selective solidification of a liquid photopolymer using light sources (e.g. ultraviolet) [4]. Stereolithography (SL or SLA) is the main technique that is widely used especially in biomedical engineering field such as implant and tissue engineering [5, 6]. Melchels (2010) reviewed two different techniques of SL techniques: scanning SL and projection SL. The scanning SL builds a structure from bottom with scanning laser while the projection SL builds from top to bottom with digital light projection [7]. The latter technique not only provides better surface finish and dimensional accuracy but also saves materials and fabrication time [4].

These two FDM and SL techniques are relatively cost-effective and user friendly to operate hardware and software as well as easily purchased by online, compared with other rest of techniques. Therefore, here FDM and SL are selected for this research project.

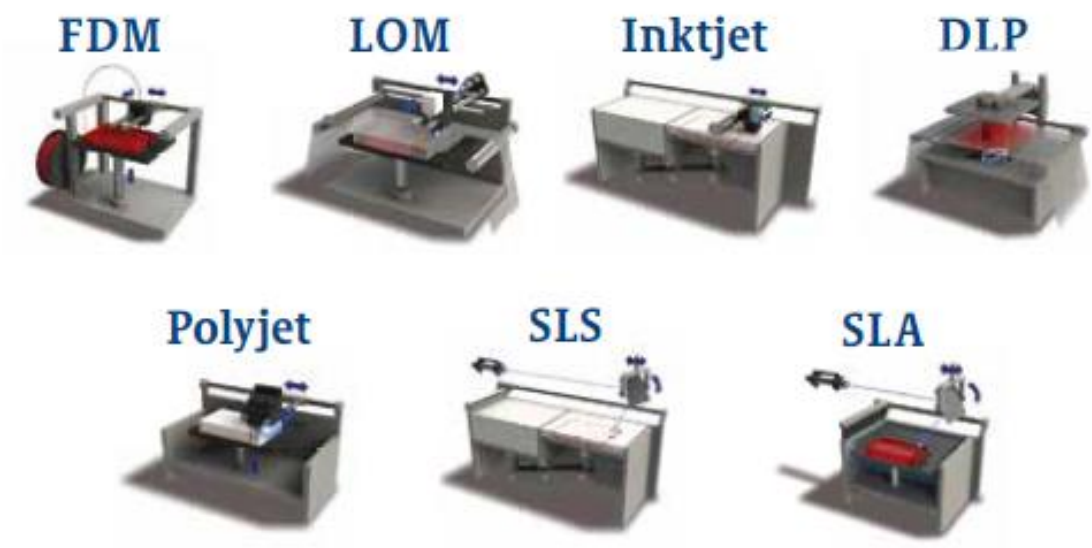

Figure 1.12: Typical seven techniques of additive manufacturing.

1.3 CHALLENGES

As mentioned above, disadvantages of mechanical, electrical properties, and fabrication process of piezoelectric ceramics and polymers were discussed. To resolve the disadvantages, Figure AM technology, which is emerging method to make production much agile and freedom of design, can be utilized to fabricate 3D structure of piezoelectric materials. The FDM technique requires thermoplastic base material to repeat the melting and solidifying during production. The piezoelectric PVDF is the thermoplastic material fitted for FMD and BT nanoparticles which can be combined with PVDF to enhance piezoelectric and mechanical properties. In addition, traditional poling process can be integrated with 3D printing process to develop in-situ poling fabrication process.

Therefore, multifunctional composites can be fabricated with 1) simple methods and freedom of design, 2) reduced time, complexity, and cost of fabrication, and 3) improved mechanical and electrical performances. It would end up benefitting to sensor and energy industries.

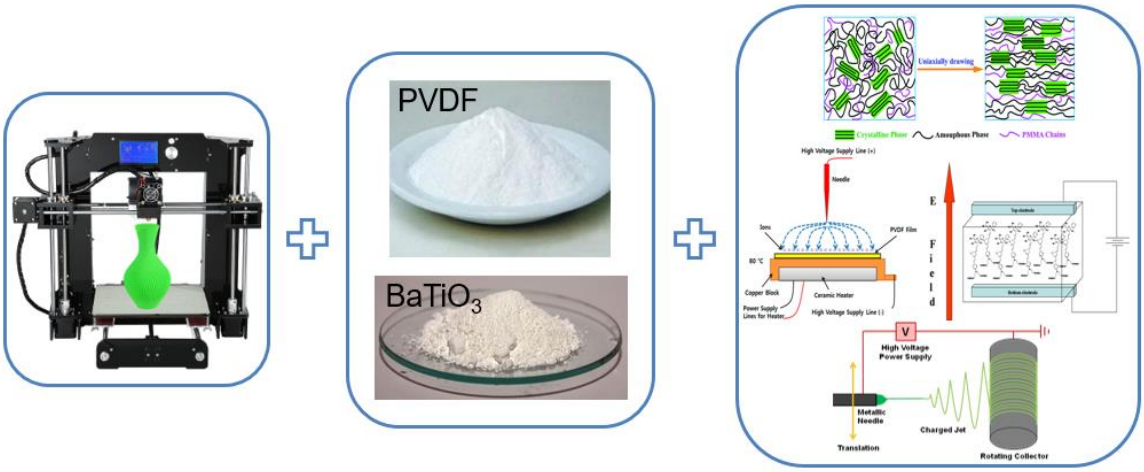

Figure 1.13: Integration of AM, piezoelectric ceramics and polymer, and traditional poling process.

1.4 Dissertation Overview

The following five sections will present the contribution of this research to AM of multi-functional devices for sensor and energy harvesting and provide a detailed description of each research performed in each chapter.

Chapter 2 starts by conducting comparison between traditional and 3D printing process to investigate the effect of 3D printing process on piezoelectric performance and morphology through the filament extrusion and 3D printing processes. As following, Chapter 3 discusses about integrating 3D printing with poling processes such as corona and electric poling process. Next Chapter 4 covers composites design by adding multiwall carbon nanotubes to PVDF/BT nanocomposites as stress reinforcing agent and other reasons for multi-functional property testing such as dielectric and temperature/strain. Lastly, Chapter 4 provides stereolithography 3D printing of photopolymer resin based PVDF piezoelectric composites for pressure sensing application as shown in Figure 1.14.

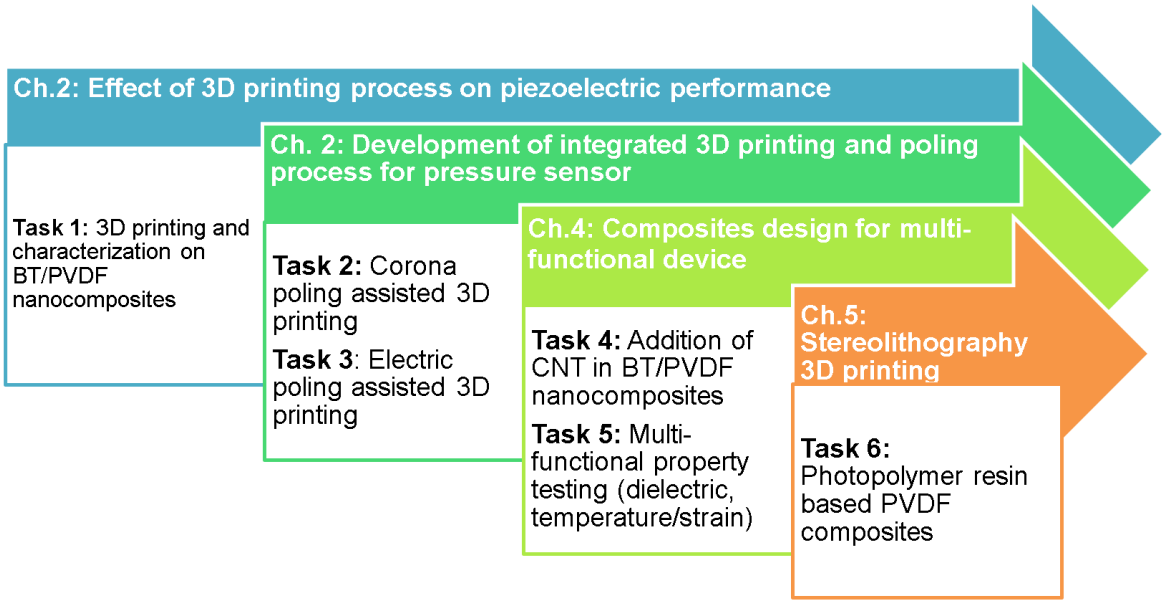

Figure 1.14: Schematic diagram of research projects' overview from Chapter 2 to 5.

Chapter 2: Effect of Fused Deposition Modeling 3D Printing Process on Piezoelectric Performance

This chapter presents a fabrication process to enhance homogeneous dispersion of BaTiO3 (BT) nanoparticles in polyvinylidene fluoride (PVDF) matrix nanocomposites using fused deposition modeling (FDM) 3D printing technique. The nanocomposites integrate the functional property (piezoelectric, pyroelectric, and dielectric) of BT with the flexibility and lightweight of PVDF. Traditionally, the simple yet effective way to fabricate the nanocomposites includes solvent-casting, spin-coating, and hot-embossing. However, these methods have disadvantages such as heterogeneous dispersion of BT nanoparticles in PVDF matrix due to the higher density of BT compared with PVDF and agglomeration during fabrication process. This heterogeneous dispersion could weaken functional and mechanical properties. Herein, fused deposition modeling 3D printing technique was utilized for homogeneous dispersion to alleviate the agglomeration of BT in PVDF through two processes: filament extrusion and 3D printing. In addition, thermal poling was applied to further enhance piezoelectric response of the BT/PVDF nanocomposites. It is found that 3D printed BT/PVDF nanocomposites exhibit three times higher piezoelectric response than solvent-casted nanocomposites.

2.1 INTRODUCTION

Ceramic-polymer based composites, where the properties of two or more materials are combined, are used widely in various industry applications that range from sensors and actuators to embedded electronics [8]. For these purposes, composites of 0-3 connectivity, which means that a three-dimensionally connected polymer phase is loaded with isolated ceramic particles, has gained interest specifically to enable freedom of design in flexible form as well as inexpensive fabrication process [9]. Nanocomposites integrating piezoelectric ceramic fillers within a polymer matrix have attracted great interest due to a unique combination of piezoelectric properties and polymer matrix flexibility. Poly(vinylidene fluoride) (PVDF) is used as polymeric matrix which also exhibits a well-known polymorphism based on crystal orientation of four different phases; α,

β, γ, δ. Due to its unique chain conformation in crystal unit cell and its high highest remnant polarization, β-phase has attracted the most attention among the PVDF phases for its enhanced piezoelectric and pyroelectric applications among polymers [10]. On the other side, piezoelectric ceramics have been utilized as excellent dielectric materials in the electronics industry. $BaTiO_3$ (BT) is preferred as inorganic filler due to its environmentally friendly nature and ease in handling as lead-free material [11]. However, BT has poor flexibility which limits applications for large scale fabrication. To solve this issue, ceramic-polymer based composites have been considered as candidate dielectric materials for new-type capacitors. Recently, BT/PVDF nanocomposites are attractive to energy harvesting and sensor applications due to their simple and convenient fabrication process, low cost, and excellent properties [12].

There are several traditional methods for preparing BT/PVDF nanocomposites such as solvent-casting, spin-coating, and hot-embossing. A simple effective way to fabricate the nanocomposites is the solvent-casting method [11]. However, this method has a disadvantage in heterogeneous dispersion and agglomeration of BT nanoparticles within the PVDF matrix. This is because particles with high surface energy are easy to agglomerate and hydrophilic nanoparticles and hydrophobic polymer are not compatible in nature, which result in poor interfacial interaction [13]. Although many formulation and process factors are influencing the particle dispersion, coupling agents (including dispersant and surfactant) have been found to improve the dispersion [14]. However, these coupling agents can scarcely bring about remarkable improvement on chemical interaction and agglomeration. In addition, micro fabrication using solvent-casting results in a PVDF matrix with a higher degree of porosity, opaque, and fragility [15]. For these reasons, heterogeneous dispersion, agglomerates, and porosity can weaken piezoelectric and dielectric properties and mechanical strength of nanocomposites [16].

In this chapter, fused deposition modeling (FDM) 3D printing technique was utilized to promote homogeneous dispersion and alleviating agglomeration of BT nanoparticles in PVDF through filament extrusion and 3D printing. In addition, thermal poling was processed to further enhance piezoelectric response of the BT/PVDF nanocomposites. X-ray diffraction (XRD),

Fourier transform infrared spectroscopy (FTIR), and scanning electron microscopy (SEM) were used for material characterization. A dynamic load frame was used for characterization of piezoelectric response.

2.2 EXPERIMENTAL

2.2.1 Materials

PVDF powder (M_W~534,000; Sigma-Aldrich) and BT powder (100nm; Inframat®) were used as the main components for the Nanocomposites solvent-casting. N-Dimethylformamide (DMF, OmniSolv®) was used as the solvent material to dissolve PVDF and BT.

2.2.2 Synthesis and Fabrication

Preparation of Solvent-Cast Film

Paragraph titles with the style Heading 4, h4 applied can be extracted to appear in the table of contents as level 2 subsections. 9wt.%-BT/PVDF sheets were fabricated via solvent-casting. Solution was prepared by dissolving a 10wt.% PVDF powder in DMF solvent. Solution was then placed in a water bath at 80°C and was stirred using a magnetic stir bar at 100rpm for approximately 30 minutes. After PVDF powder fully dissolved, BT powder was introduced to the solution. This attained nanocomposites solution was then heated and stirred using the same parameters for approximately 15 minutes. BT built up at the bottom of solution was addressed by ultra-sonication (Branson Sonifier 450) for 20 minutes. DMF solvent is then evaporated by dispersing nanocomposites solution onto a glass substrate and heated to a temperature of 120°C for 12 hrs. The procedure yields a thin BT/PVDF nanocomposites film of 0.15mm in thickness, the sheet sample was then cut with required dimensions for further testing and sample preparation.

Preparation of 3D Printed Film

To further enable a homogeneous dispersion of material, the casted sheet was prepared for extrusion. The sheet was cleaved into several $5cm^2$ squares. The cleaved samples were then fed to a filament extruder (Filabot) at a temperature of 200°C. Filament of 2.7mm in diameter was

extruded and spooled, special measures were taken to avoid contamination during extrusion. Fabricated BT/PVDF Nanocomposites filament was then inserted to FDM 3D printer, also known as extrusion-based process, which deposits materials in form of a continuous flowing layer by layer to build a 3D structure [4]. Here an FDM 3D printing machine (Lulzbot Taz 5) was used to fabricate thin films of 0.33mm in thickness with dimensions of 11.5×37mm at a nozzle temperature of 250˚C, the printing speed was set at 5mm/s, and the heating bed temperature at 80˚C. It is important to note that BT may burn and clog the nozzle when printing at such high temperature. This issue is addressed by limiting the amount of time the filament remains within the heated nozzle.

Thermal Poling Process

After fabricating the two films by solvent-casting and 3D printing processes, the samples were then prepared for a thermal poling process, where extensive research has indicated the transformation of PVDF β-phase [12]. Copper paint electrodes were attached on samples, connected to a high voltage source, and exposed to a high electric field of 35MV/m, which was found to be maximum electric field before experiencing electric breakdown, a schematic of the set-up is shown in Figure 2.2(b). It is important to note that PVDF requires at least 50MV/m to be polarized due to high coercive electric field however BT requires only about 35KV/m [17, 18]. Electric breakdown was avoided by dipping samples into silicon oil at 90˚C which also helps accelerating polarization during the process. Thermal poling was performed for 2 hours on both 3D printed and solvent-casted films. The entire procedure of the solution casting and 3D printing sample preparation is shown in Figure 2.1.

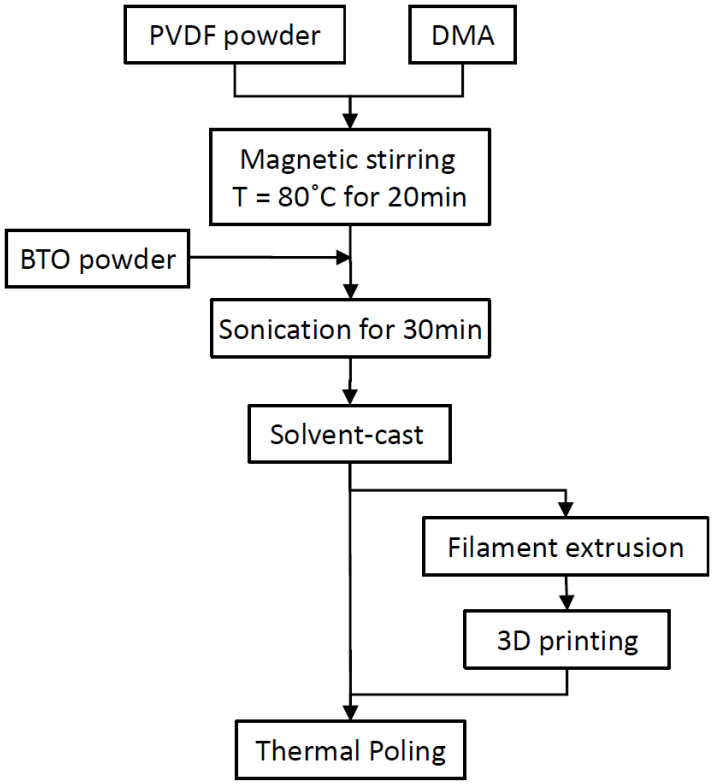

Figure 2.1: Flow-chart of the sample preparation method.

2.2.3 Structural, Morphological, and Functional Characterizations

X-ray diffraction was performed on solvent-casted and 3D printed films in order to characterize crystallinity and phase transformation using CuKα radiation on a D8 Discover diffractometer (Bruker, USA). In addition, FTIR (Agilent Technologies Cary 630 ATR-IR) analysis was performed in the 600-1600 cm^{-1} wavenumber range at room temperature to characterize the infrared spectrum of absorption of 3D printed and solvent-cast BT/PVDF nanocomposites. The morphology of the nanocomposites was observed in a scanning electron microscopy (SEM, TM-1000, Hitachi). Piezoelectric output current was measured by fatigue load frame (Bose ElectroForce) and picoammeter (Keithley 6485) as shown in Figure 2.2(a).

2.2.4 Experimental Setup

To quantify the piezoelectric property of BT/PVDF nanocomposites, both 3D printed and solvent-casted films were prepared with 8×33mm Cu paint electrodes in top and bottom surfaces,

the electrodes were then extended with Cu tape to allow a proper connection with the picoammeter as shown in Figure 2.2(a) and (b). Dynamic force was applied on BT/PVDF film to measure periodic output current. Fatigue load frame generated 50 cyclic loads on the sample under a range from 5 to 45N at 1Hz while the picoammeter is measuring current output. To prevent noise from fatigue machine during measurement, the two grips handing the sample were covered with insulating tape.

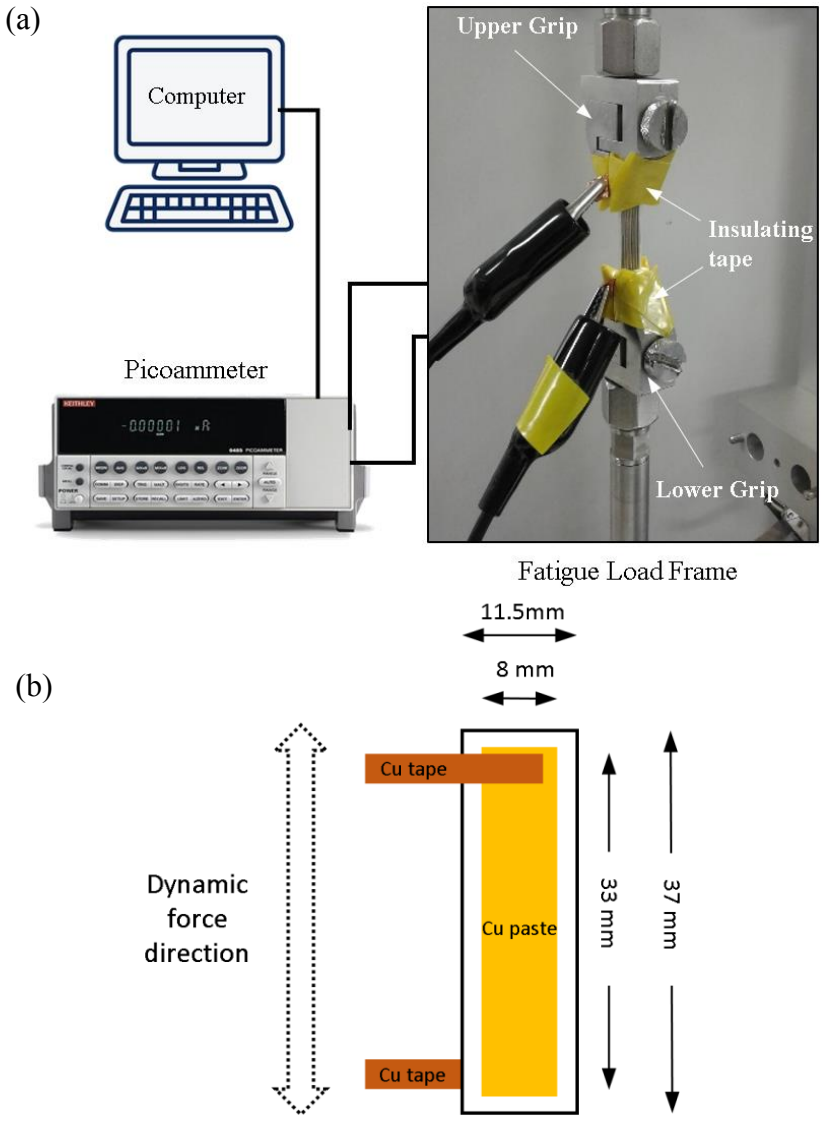

Figure 2.2: Schematic diagram of (a) the experimental setup for piezoelectric output current measurement and (b) sample and electrode design.

2.3 RESULTS AND DISCUSSION

2.3.1 Scanning Electron Microscopy (SEM) Analysis

SEM was performed to analyze surface topography of BT/PVDF nanocomposites films. Top and bottom surfaces and cross-sections of 3D printed and solvent-casted films were characterized and compared. Obtained SEM images are shown in Figures 2.3 and 2.4. In the solvent cast film, shown in Figures 2.3(a) and (b), it can be observed that there is a clear difference of nanoparticles dispersion between the top and bottom surface. In the top surface, BT particles are sparsely observed within the PVDF matrix. In addition, the PVDF agglomerated, and porosities and micro-surface cracks were observed. These are defects that occur upon the drying of the DMF solvent. In the bottom surface, there was higher presence of large BT nanoparticles, this is due to the higher density of BT compared with PVDF. However, in the 3D printed materials, as shown in Figure 2.3(c) and (d), both the top and bottom surface had no clear indication of a BT-dominated surface which points to a more heterogeneous dispersion of BT in PVDF. In addition, there is visible reduction of agglomerations and disappearance of porosities and micro-surface cracks.

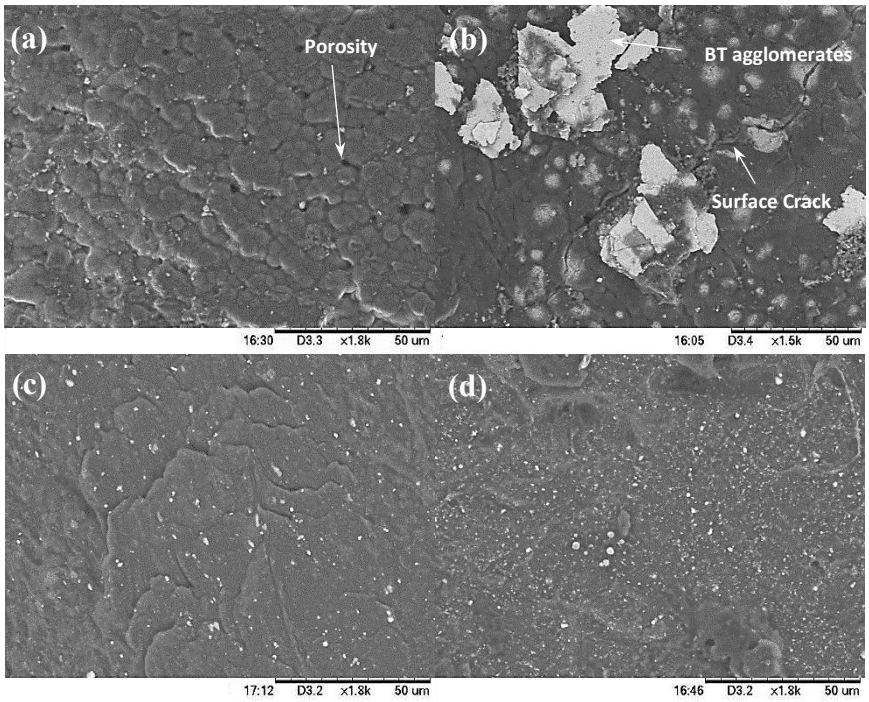

Figure 2.3: SEM images of (a) top and (b) bottom surfaces respectively of solvent-casted 9wt.%-BT/PVDF films, (c) top and (d) bottom surfaces respectively of 3D printed 9wt.%-BT/PVDF films.

Figure 4 shows cross-sections of each 3D printed and solvent-casted film and displays how BT nanoparticles are dispersed in PVDF matrix. Nanoparticles in solvent-casted film were significantly agglomerated in the bottom surface and relatively were observed at the top surface. However, it was shown that nanoparticles in 3D printed film are well-uniformly dispersed throughout the entire cross-section area.

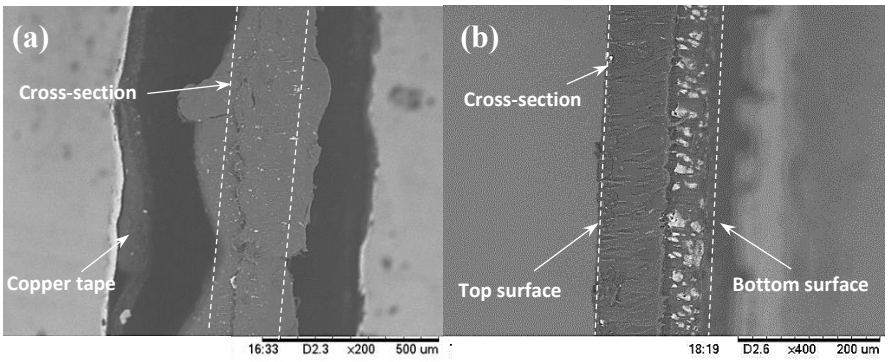

Figure 2.4: SEM images of cross-section of (a) 3D printed and (b) solvent-casted 9wt.%-BT/PVDF films.

2.3.2 X-Ray Diffraction (XRD)

XRD analysis was performed to characterize crystal structure of BT/PVDF nanocomposites films. The results of the XRD analysis, shown in Figure 2.5 and 2.6, demonstrate the polymorphism of BT/PVDF nanocomposites. Figure 2.5 (a) and (b) shows reflected spectra of the top and bottom sides of 3D printed BT/PVDF respectively before and after thermal poling. The reflections at 18.4˚(020), 20.0˚(110), 26.6˚(021) correspond to α phase of PVDF, reflections at 20.8˚(110), 35.9˚(200) correspond to β-phase of PVDF, and reflections at 19.2˚(002), 20.1˚(110), 20.3˚(101), 26.8˚(022) correspond to γ-phase of PVDF. And reflections at 22.2˚(100), 31.6˚(110), 38.9˚(111), and 45.3˚(200) corresponds to BT [19-22]. These reflections were measured in the top and bottom sides, indicating that the top and bottom sides contain uniformly dispersed BT nanoparticles which proves the coexistence of the materials within the sample. The peak at

20.8˚(110) corresponding to β-phase of PVDF was absent before thermal poling, however it appeared and broadened after thermal poling in both the top and bottom sides. In addition, a peak at 26.6˚(021) corresponding to α-phase of PVDF slightly decreased in both the top and bottom sides due to thermal poling which indicates some degree of α to β-phase transformation with a heterogeneous distribution of BT.

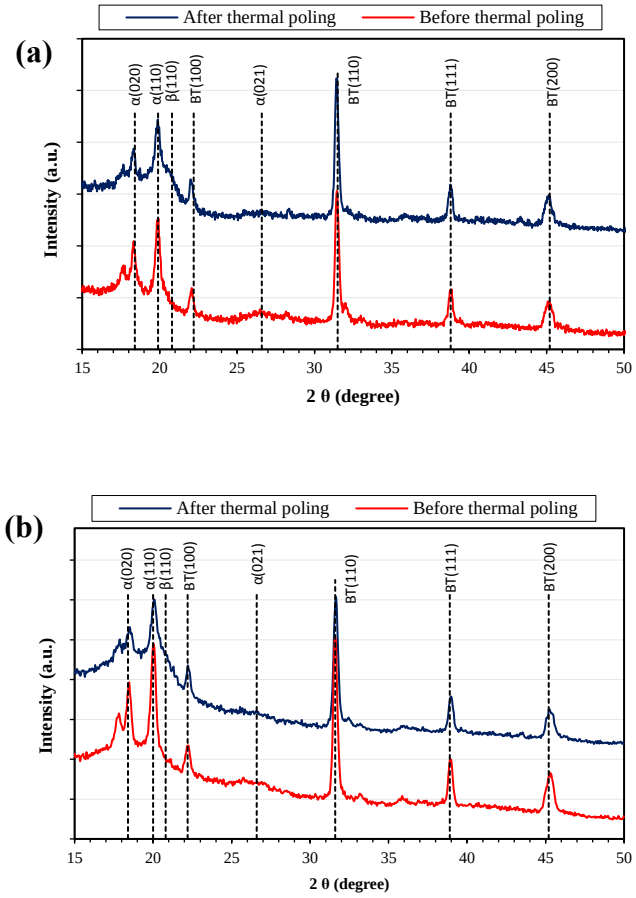

Figure 2.5: XRD comparison of (a) the top and (b) bottom sides of 3D printed 9wt.%-BT/PVDF films respectively.

Figure 2.6(a) and (b) represent the reflected spectra on the top and bottom sides of solvent-casted BT/PVDF before and after thermal poling. Reflected spectra of the top side of solvent casted BT/PVDF, as shown in Figure 2.6(a), indicate all relevant peaks at 20.8˚(110) and 35.9˚(200) corresponding to β-phase of PVDF, at 19.2˚(002), 20.3˚(101) corresponding to γ-phase of PVDF,

and at 22.2˚(100), 31.6˚(110), and 38.9˚(111) corresponding to BT. The intensity of peaks relevant to BT in the top surface were significantly diminished and some disappeared because the top side is dominated by PVDF. Peaks at 19.2˚ and 20.3˚ corresponding to γ-phase were observed before thermal poling because γ-phase was formulated during solvent-casting process at 120˚C [23]. It can be explained that CH_2-CF_2 dipoles were formulated when BT particles are added to PVDF/DMF solution and these dipoles were locally oriented around surface of BT nanoparticles acting as nucleation agent [15, 24-26]. These oriented CH_2-CF_2 dipoles were packed in TTT configuration characteristic of β-phase or γ-phase [27-29]. However, after thermal poling a peak at 20.8˚ corresponding to β-phase was appeared and a peak at 36.6˚ correspond to β-phase was slightly increased. In addition, the peak at 20.8˚ slightly shifted to higher degree and broadens. Figure 2.6(b), which shows the bottom sides of solvent-casted BT/PVDF, display all of the major reflections that are relevant to BT which also has a higher intensity compared with Figure 2.6(a). Therefore, this supports that compounds of BT/PVDF in solvent-casted film is not uniformly dispersed.

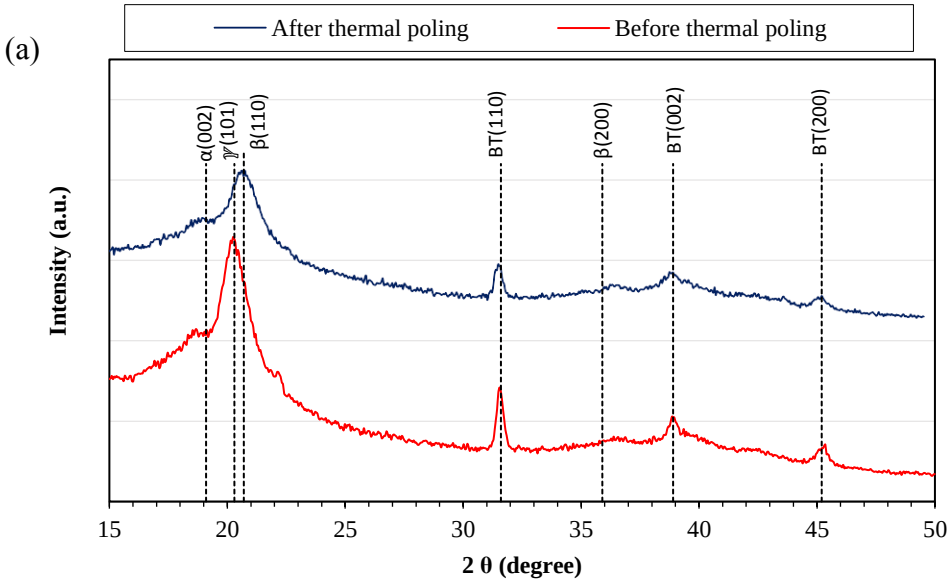

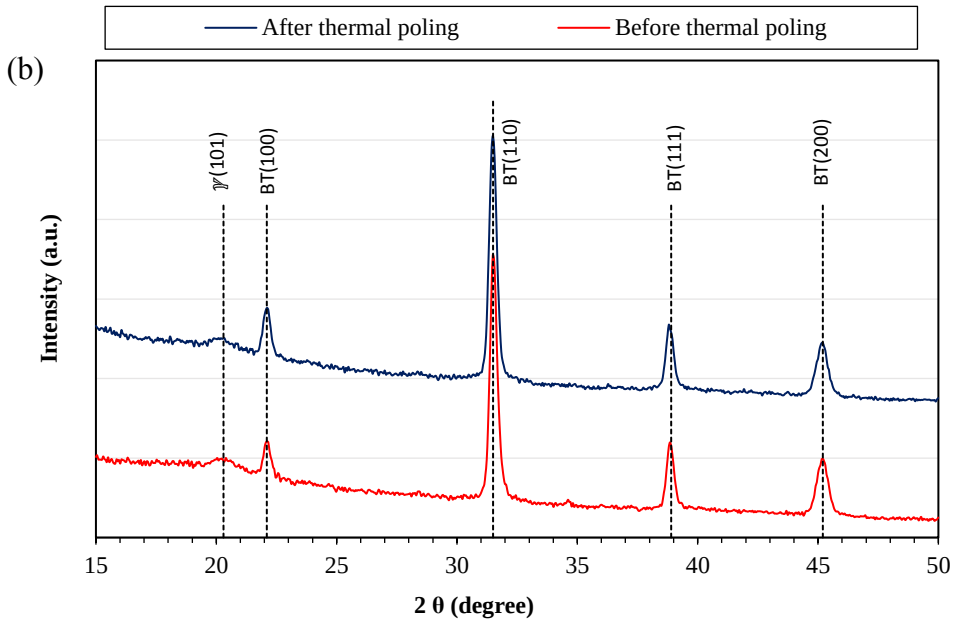

Figure 2.6: XRD comparison of (a) the top and (a) bottom sides of solvent-cast 9wt.%-BT/PVDF films respectively.

2.3.3 FTIR Analysis

FTIR analysis was performed on 3D printed and solvent-cast BT/PVDF nanocomposites films to determine the degree of crystallinity of α- and β-phases with IR absorption bands at 766 and 840 cm^{-1} which are characteristics of the α- and β-phases, respectively. The β- and γ-phases resemble each other structurally and spectroscopically at 510 and 840 cm^{-1} so that it made the differentiation more difficult, however these two phases can be clarified by checking the bands around at 1275 and 1234 cm^{-1} to identify the existence of the β- and γ-phases [22, 26, 30, 31]. The procedure was similar to references of Salimi et al and Gregorio et al [32, 33]. Figure 2.7 shows the FTIR spectra of 3D printed and solvent-cast films before and after thermal poling as well as raw PVDF. It was observed that electroactive β/γ-phases (840 cm^{-1}) increase relatively due to the effect of thermal poling process as shown in Figure 7 (c) and (e). These coexisting two phases can be clarified by Figure 2.7 (d-e). The γ-phase at 1234 cm^{-1} decreased after thermal poling, whereas β-phase at 1275 cm^{-1} increased. This means that γ-phase transferred to β-phase which is a good agreement with XRD spectra of β- and γ-phases as shown in Figure 2.6 (a). Particularly, solvent-

cast film (d-e) shows relatively lower α-phase peaks (614, 766, 795, 854, 976 cm^{-1}) were observed than that of 3D printed film (b-c).

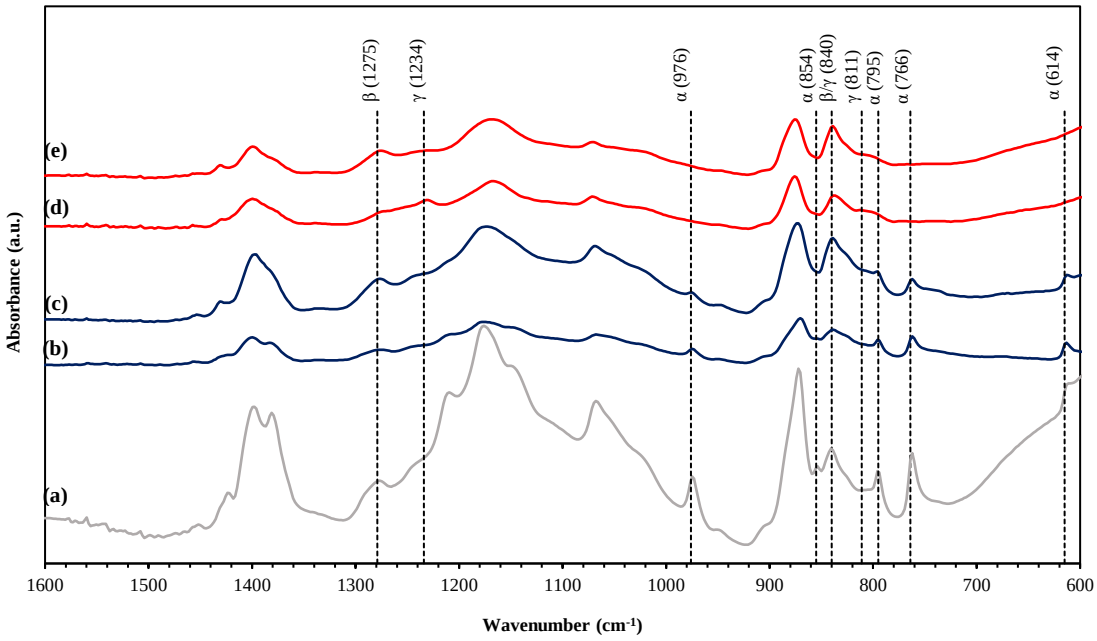

Figure 2.7: FTIR spectra for (a) raw PVDF, (b) 3D printed 9wt.%-BT/PVDF films before thermal poling, (c) 3D printed 9wt.%-BT/PVDF films after thermal poling, (d) solvent-cast 9wt.%-BT/PVDF films before thermal poling, (e) solvent-cast 9wt.%-BT/PVDF films after thermal poling.

Table 2.1 shows the calculated β-phase contents at each sample followed by the Lambert-Beer law. Solvent-cast film shows higher β-phase percentage than 3D printed film regardless of poling. As described in XRD analysis, β-phase of solvent-cast film before thermal poling was nucleated due to dipole polarization on BT surface. This result is good agreement with XRD spectra. However, through the heating process such as filament extrusion and 3D printing, the β-phase content was diminished because crystalline was repolarized by thermal effect. After thermal poling, both 3D printed and solvent-cast films had increased β-phase contents. It is noted that γ and δ-phases have been ignored in this content calculation due to small amount in the sample.

Table 2.1: β-phase contents for 3D printed and solvent-cast 9wt.%-BT/PVDF nanocomposites films before and after thermal poling.

	β-phase content (%) Before thermal poling	β-phase content (%) After thermal poling
3D printed film	56.8	61.2
Solvent-cast film	65.4	68.1

2.3.4 Measurement of Piezoelectric Property

The piezoelectric property of BT/PVDF films can be characterized by measuring current output as a function of applied cyclic mechanical stresses. In piezoelectric material and device, piezoelectric effect can be evaluated using d_{33} meter. However, for piezoelectric nanocomposites, charge amplified circuit is typically needed to amplify output current since piezoelectric coefficient is too small to be measured by d_{33} meter. Therefore, a fatigue load frame was implemented to apply 50 cyclic loads under 40N at 1Hz as shown in Figure 2.8 and piezoelectric d_{31} response was measured accordingly [34-36].

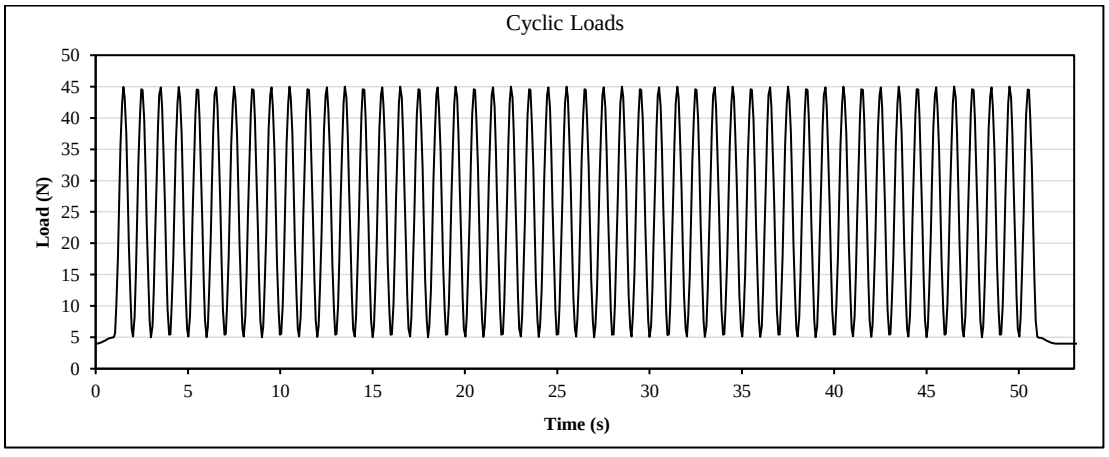

Figure 2.8: Cyclic loadings at 1Hz applied on samples by fatigue machine.

It was measured that the solvent-casted film before the thermal poling process generated ±0.05nA current output while the 3D printed film generated relatively lower current of ±0.03nA than solvent-casted one, as shown in Figure 2.9. This may be due to the higher presence of PVDF β-phase found right after solvent-casting. However, after the thermal poling process, 3D printed nanocomposites generated ±0.15nA current output increased than ±0.09nA of solvent-cast one, shown in Figure 10. In total, current output of the solvent-casted film after thermal poling has increased to 180%, however the 3D printed film has increased to 500%.

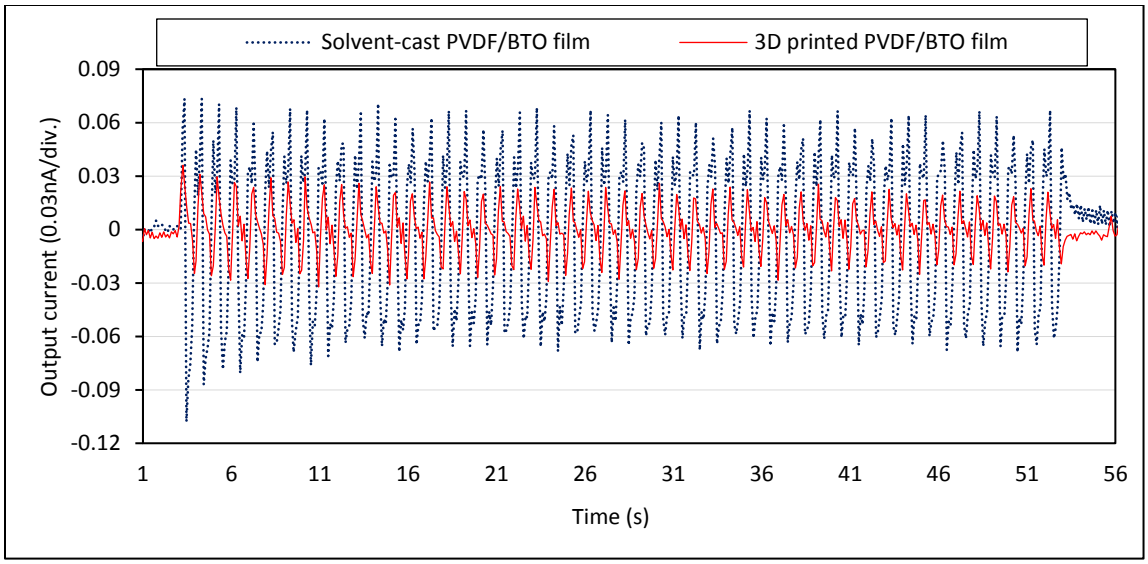

Figure 2.9: Current output of solvent-cast and 3D printed 9wt.%-BT/PVDF film before thermal poling process.

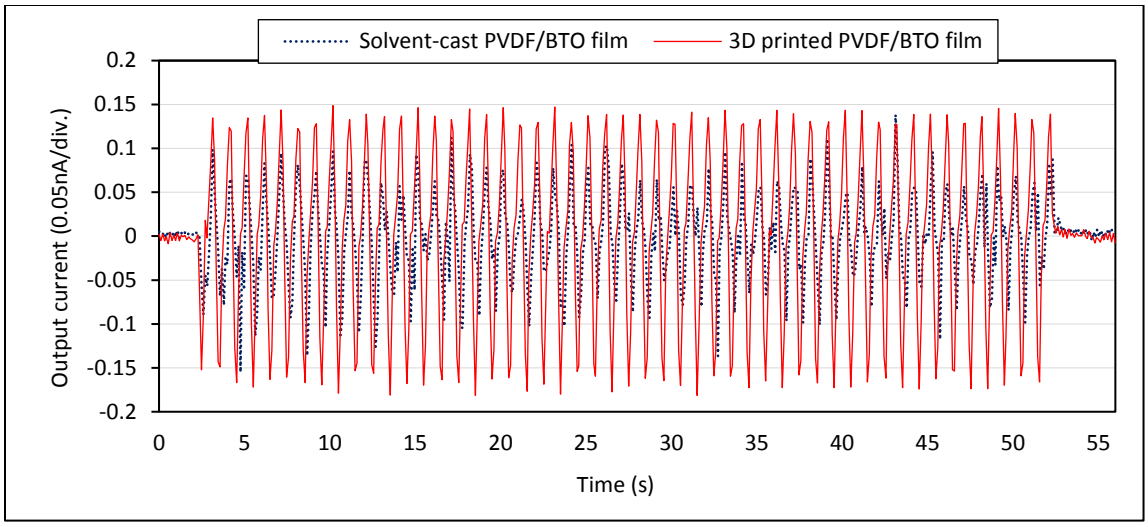

Figure 2.10: Current output of solvent-cast and 3D printed 9wt.%-BT/PVDF film after thermal poling process.

To calculate piezoelectric coefficient d_{31},

$$D_i = d_{ij}\sigma_j \tag{1}$$

where D_i is the electrical displacement, σ_j is the applied stress, and d_{ij} is the piezoelectric coefficient. In this case, subscripts i and j are defined as 3. Therefore, the equation can then be expressed as $D_3 = d_{31}\sigma_1$. Considering areas of electrode and cross section, Eq. (1) can then be expressed as

$$\frac{Q}{A_{cross}} = d_{31}\frac{\nu F}{A_{cross}} \tag{2}$$

where Q is charge, A_{cross} are areas of cross-section, and F is an applied force. Then, piezoelectric coefficient can be expressed as

$$d_{31} = \frac{\frac{Q(i)}{A_{elect.}}}{\frac{\nu F}{A_{cross.}}} \tag{3}$$

A_{cross} are 2.62 mm^2 and charges can be attained by numerical integration which is the similar method with Simpson's rule [37] expressed as

$$Q_{(i)} = \ Q_{i-1} + \frac{I_i \ + \ I_{i+1}}{2} \ \times (t_{i+1} - t_i) \tag{4}$$

where I_i is output current at i th and t_i is the time at i and Eq. (5) can be rewritten as

$$d_{33} = \ \frac{Q(i)}{2.62} \tag{5}$$

d_{33} can then be determined at Q_{max} and Q_{min} and each attained d_{33} is divided by 2 to get $\pm \ d_{33}$ as Eq. (6) describes

$$\pm \ d_{33} \ = \ \frac{d_{33}^{max} \ - \ d_{33}^{min}}{2} \tag{6}$$

The calculated result determines the piezoelectric coefficients of films fabricated by 3D printing and solvent-cast processes.

The result of piezoelectric coefficient as shown in table 2 indicates that 3D printed sample shows 233% higher piezoelectric coupling coefficient after thermal poling. The increase means that the 3D printing process has more influence on the piezoelectric property because it provided homogeneous dispersion, reduced porosities and cracks, and alleviated agglomeration of BT nanoparticles.

Table 2.2: Piezoelectric coefficient d_{31} of 3D printed and solvent-cast 9wt.%-BT/PVDF films before and after thermal poling process.

	Before thermal poling	After thermal poling
3D printed film d_{31} (pC/N)	2.9×10^{-3}	21×10^{-3}
Solvent-cast film d_{31} (pC/N)	7.4×10^{-3}	9.0×10^{-3}

2.4 SUMMARY

The piezoelectric property of 3D printed and solvent-casted BT/PVDF films was characterized and compared by using SEM, XRD, FTIR, and fatigue load frame. SEM results of solvent-casted film has higher degree of agglomeration, porosities, and cracks in comparison with 3D printed one. XRD spectra show the significant homogeneous dispersion of BT particles in the 3D printed film compared to solvent-cast one. FTIR demonstrated that more β-phase content was present relatively in solvent-cast film than 3D printed one due to the fact that PVDF dipole alignment was occurred around the surface of BT nanoparticles which act as nucleation agents. Nevertheless, piezoelectric responses show higher current output in 3D printed film than solvent-cast one due to the homogeneous dispersion and alleviation of agglomeration for BT particles as well as removing porosities and cracks resulted from the filament extrusion and 3D printing process. The 3D printing technique not only improves the piezoelectric property, but also provides freedom of design to fabricate different shapes of form of active nanocomposites. The use of 3D printer may open the door to large-scale manufacturing of active nanocomposites-based materials for sensors, actuator, and dielectric devices.

Chapter 3: Development of Integrated 3D Printing with Traditional Poling Process for Pressure Sensor Application

3.1 Integrated 3D Printing and Corona Poling Process of PVDF Piezoelectric Films for Sensor Application

This section presents a novel process to fabricate piezoelectric films from polyvinylidene fluoride (PVDF) polymer using integrated fused deposition modeling (FDM) 3D printing and corona poling technique. Corona poling is one of many effective poling processes that has received attention to activate PVDF to be a piezoelectric responsive material. The corona poling process occurs when a PVDF polymer is exposed to a high electric field created and controlled through an electrically charged needle and a grid electrode under heating environment. FDM 3D printing has seen extensive progress in fabricating thermoplastic materials and structures, including PVDF. However, typically post processing such as poling is needed to align the dipoles in order to gain piezoelectric properties. To further simplify the piezoelectric sensors and structures fabrication process, this paper proposes an integrated 3D printing process with corona poling to fabricate piezoelectric PVDF sensors without post poling process. This proposed process, named 'Integrated 3D Printing and Corona poling (IPC) process', uses the 3D printer's nozzle and heating bed as anode and cathode to create poling electric fields and a controlled heating environment. This nozzle travels along the programmed path with fixed distance between nozzle tip and sample's top surface. Simultaneously, the electric field between the nozzle and bottom heating pad promotes the alignment of dipole moment in PVDF molecular chains. The crystalline phase transformation and output current generated by printed samples under different electric fields in this process were characterized by a Fourier transform infrared spectroscopy (FTIR) and through fatigue load frame. It is demonstrated that piezoelectric PVDF films with enhanced β phase percentage can be fabricated using the IPC process. In addition, mechanical properties of printed PVDF was investigated by tensile testing. It is expected to expand the use of additive manufacturing to

fabricate piezoelectric PVDF-based devices for applications such as sensing and energy harvesting.

3.1.1 Introduction

Poly(vinylidene) fluoride (PVDF) is a widely-studied polymer for its high piezo- and pyro-electric response among polymers [38-40]. PVDF is a semi-crystalline material that has a unique molecular conformation with repeated unit of $(-CF_2-CH_2-)$ that has large dipole moment of 7.58×10^{-28} C·cm [41]. It can be morphed into four different states; α, β, γ, δ, where it is naturally found in the electrically unresponsive, α-phase [42]. Since its discovery, PVDF β-phase has gained a large amount scientific interest due to its unique planar zigzag (TTT) conformation that presents the highest net-dipole among its crystal phases [33]. Along with its high piezo response, PVDF's chemical robustness, mechanical properties, high flexibility, and low-cost make it an ideal material to be used in the sensor and actuator industry.

β-phase transformation has been extensively studied for its transformation feasibility, previous research indicates several methods to obtain β-phase transformation [43-45]. The most common method is by mechanically stretching the sample by a stretch ratio of 3-5 to transform α-phase to β-phase [46]. After being mechanically stretched, β-phase crystals are aligned through a high electric field, this process is known as electric poling. There are several methods of applying electric poling such as contact poling, corona poling, and electro-spinning [47, 48]. Corona poling presents significant advantages as it eliminates the need of positive electrode contact to sample because it uses the air between a highly charged needle and the sample to produce a corona discharge of ions [49]. The ions then land on the sample and create a charge layer on the surface of the sample, generating the an electric field [49]. However, this process requires higher electric voltages on needle electrode up to 280 MV/m and mesh grid electrode about 0.2-5 kV for less than 60 min poling time to increase piezoelectric coefficient compared to other electric poling based methods [12, 49]. Currently, commercially developed PVDF films are manufactured through mechanical drawing while poling the sheet as it is being extruded. This process presents difficulties

because the drawing deforms the quality of the PVDF sheet and the β-phase content varies from sheet to sheet [21]. These inconsistencies have led to the investigation of alternative methods to fabricate piezoelectric PVDF. Previous research has indicated the use of Fused Deposited Modeling (FDM) 3D printers, where PVDF's thermoplastic property is exploited to enable a free-form manufacturing of PVDF β-phase [50]. This developed electric poling assisted additive manufacturing (EPAM) process is only limited to one single layer fabrication and has small electrode area to harvest output energy due to fabrication characteristics. In addition, previous research has not provided convincing quantitative characterization and measurement on printed PVDF with respect to β-phase content and output current.

In this paper, we report a novel technique for PVDF β-phase transformation through FDM 3D printing, where a high electric field is applied through a corona poling process where a high voltage is applied between the nozzle of the 3D printer and conducting plate that serves as the 3D printer's substrate. In this process, we eliminate the use of the corona mesh grid electrode as we control the nozzle to travel evenly above the electrode and provides a uniform distribution of ions around the sample. The nozzle always maintains a fixed distance above the PVDF sample with a constant voltage, and it moves at a sustained speed around the sample. Different samples were fabricated under varying electric voltages. For qualitative material characterization and piezoelectric measurement, all samples were tested via a fatigue load frame to measure the piezoelectric output current generated by mechanical forces. Each sample was characterized via a Fourier Transform Infrared Spectroscopy (FTIR), which is a well-known method used to characterize β-phase content in PVDF. With this process, it was proved that the growth of piezoelectric response due to the increasing presence of β-phase through the use of Integrated 3D Printing and Corona poling (IPC) process that possesses the potential for a free-form modeling of piezoelectric devices such as pressure sensing and energy harvesting areas.

Experimental Details: Integrated 3D Printing and Corona Poling (IPC) Process

The IPC process illustrated in Figure 3.1 combines FDM 3D printing with corona poling process to fabricate free-form devices under the control of dipole alignment of PVDF polymer. FDM 3D printing technique is a process that deposits material in the form of a continuous flow in layer-by-layer fashion to build a 3D structure [51]. The FDM printer consists of a stepper motor to feed filament, two heaters, and two temperature sensors on both the nozzle and the heating bed. A heating element is used to melt solid state PVDF polymer filament into semi-molten state. This semi-molten PVDF polymer hardens immediately after extrusion from the nozzle. This deposited PVDF molecular chains in layers are randomly aligned and predominantly α-phase crystalline structure shown in Figure 3.1(a).

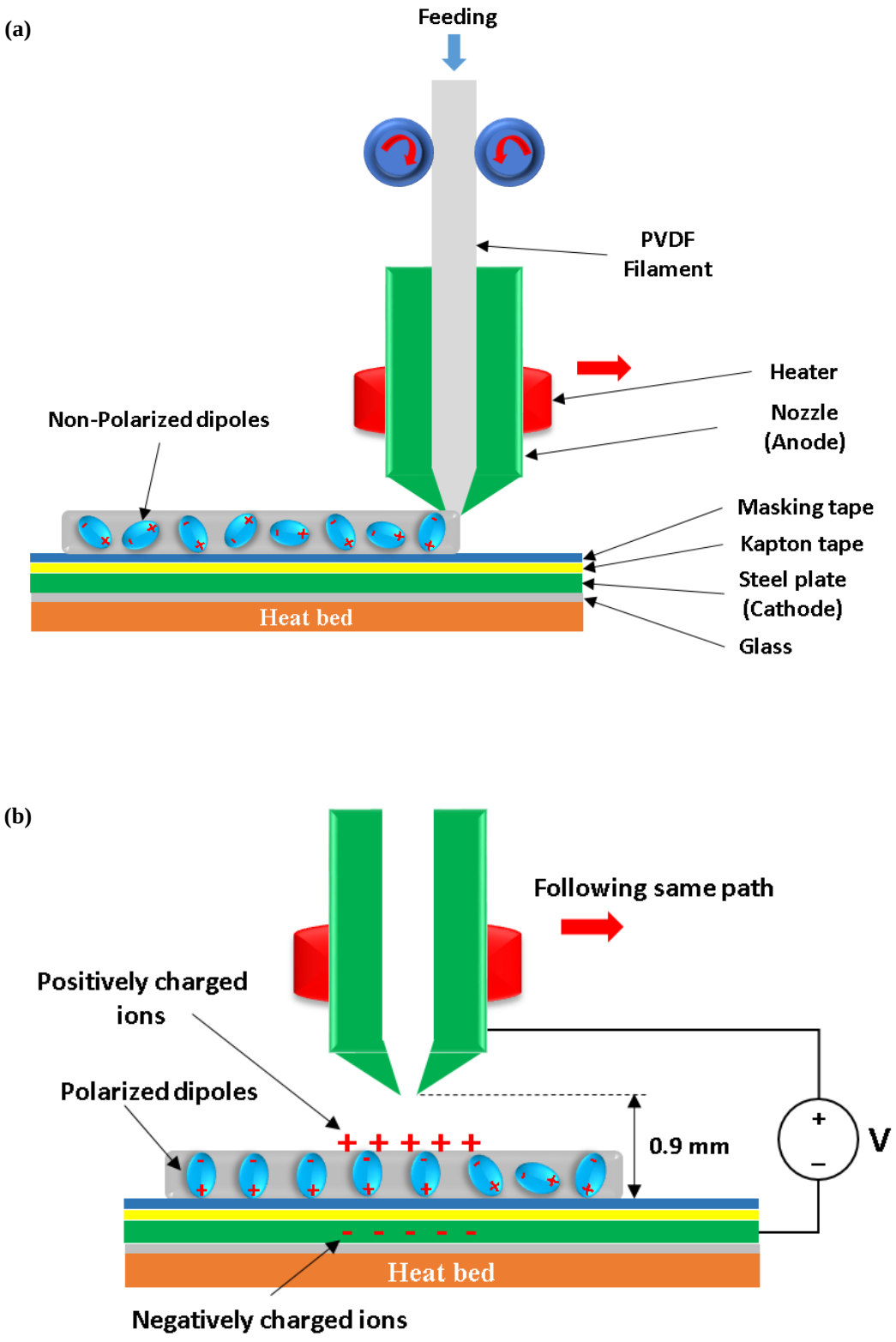

Figure 3.1: Schematic of IPC process setup: (a) 3D printing of PVDF layer, (b) corona poling process.

After printing layers, as shown in Figure 3.1(b), the nozzle, without filament extrusion, follows the same printing path but with a fixed distance between nozzle and heating bed. At the same time, a high electric voltage is applied on the nozzle and heat bed at temperatures of 250 °C and 60 °C, respectively, which can increase the mobility of the PVDF molecular chains. Applied electric voltage ionizes atmospheric air particles and attaches them to a surface of printed PVDF layers [49]. These ionized positive charges create an electric field to the transverse direction of printed PVDF layers between PVDF layer surface and printing heat bed. The high electric field promotes PVDF molecular chain alignment and transforms from α to β-phase crystalline structure. As the nozzle moves around the sample following the original path, PVDF molecular chains are more intensively polarized in local area where the nozzle is moving. Therefore, there is no need to use stainless steel grid for uniform distribution of positive ions. This printed PVDF device is expected to have a strong β-phase conformation which is electroactive and enables it to be used in applications such as energy harvesting and sensor utilization. The proposed technique has great advantages of reducing fabrication cost and time, increasing design flexibility and piezoelectric surface geometry compared with traditional poling processes and recently developed EPAM process [50].

3.1.2 Experimental

PVDF Filament and Film Fabrication

PVDF pellets (M_W ~ 534,000; Sigma-Aldrich) were used to prepare filament extrusion. Pellets were fed to a filament extruder (Filabot) at a temperature of 195 °C. Filament of 2.7 mm diameter was extruded and spooled, special measures were taken to avoid contamination during extrusion.

3D printing process started with print parameter setup using the Slic3r software which is a tool that converts digital 3D models into printing instructions, ".STL" files, and customize printing parameters such as tool path, fill pattern, etc. A concentric fill pattern was selected due to mechanically stable geometry when stressed by fatigue load frame as shown in Figure 3.2.

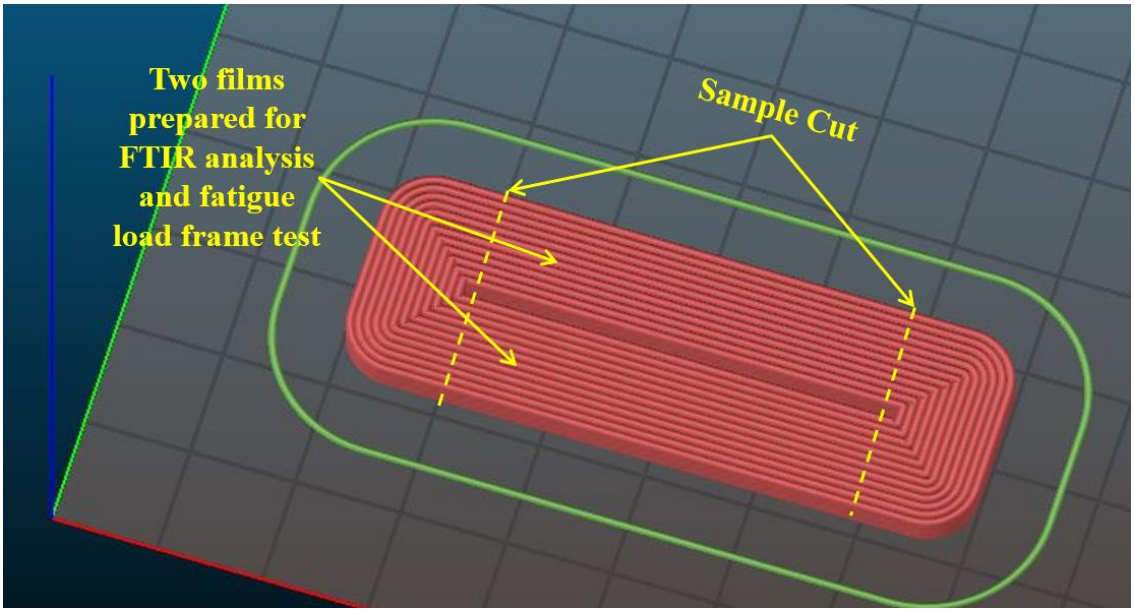

Figure 3.2: A captured image of concentric fill pattern design prepared before generating .STL file in Slic3r software.

Fabricated PVDF filament was then inserted to the 3D printer. FDM printing is used as it provides the potential to be one of the most commercially cheap and simple additive manufacturing techniques that consists of X-Y-Z rectilinear axes. In this study, the FDM 3D printer (Lulzbot Taz 5) was modified to allow the application of high electric voltage as shown in Figure 3. A glass plate was placed on heat bed to prevent electric flow through the whole 3D printer body. A steel plate was then placed on top of the glass plate to work as a cathode. Two layers of tape were attached on top of the steel plate. The first layer is Kapton tape (0.03 mm in thickness) which is an insulation tape to prevent electric breakdown between the nozzle and the steel plate. The other is a masking tape (Scotch, 0.05mm in thickness) that is attached on top of the Kapton tape to improve the adhesiveness of PVDF when deposited from the nozzle. This masking tape helps release the printed film by hands. The fabricated thin film was measured to be 0.33 mm of thickness with dimensions of 10 × 25 mm. Detailed printing parameters are shown in table 3.1.

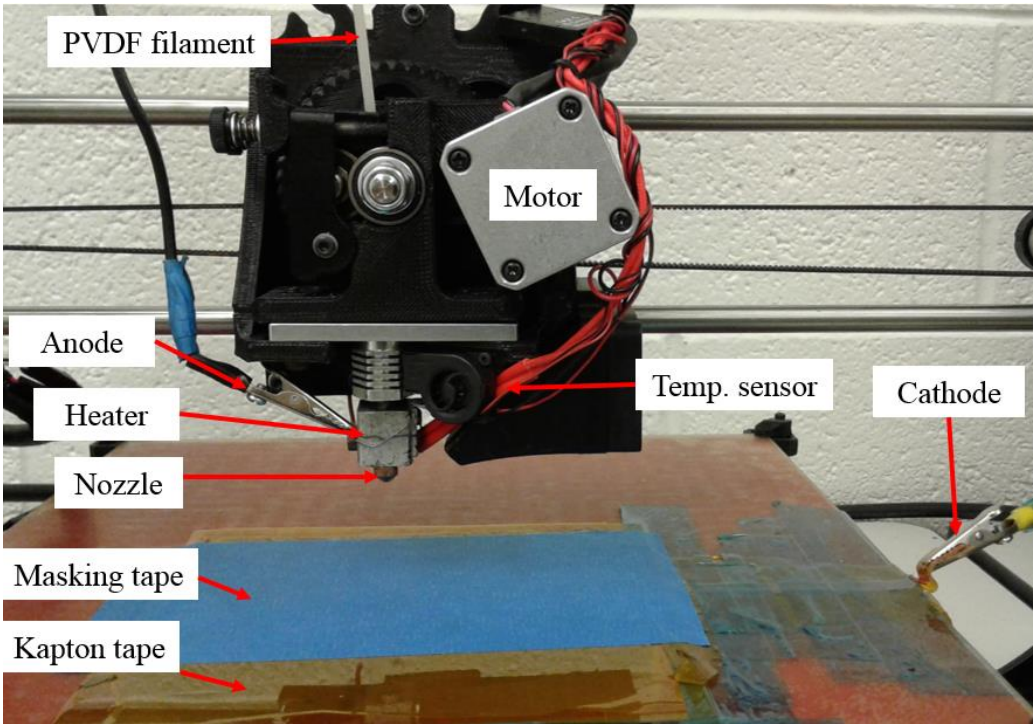

Figure 3.3: Experimental setup of integrated FDM 3D printing technique and corona poling process.

The printing process came to halt after fabricating first layer, the nozzle was then raised up about 0.9 mm because it was about as close as the nozzle could be without risking the nozzle touch the sample and to have enough space to apply a high electric voltage between nozzle and sample surface. Varying voltages were applied up to 12 kV (13.3 MV/m = 12 kV/0.9 mm). 12 kV was the maximum electric voltage in which the process was not disturbed with an electric breakdown. The printing process resumed with increased heating bed temperature and decreased printing speed to promote PVDF molecular chain alignment as shown in table 1 with respect to detail parameters of IPC process. These parameters were selected to print piezoelectric device with high quality and while allowing continuous polarization. For suitable printing parameters, it was found that nozzle temperature and printing speed are appropriate from 230 to 260˚C and lower than 10mm/s, respectively for higher adhesiveness to depositing bed surface. If the temperature is higher or lower than the appropriate temperature range, PVDF is likely to be degraded or hard to stick on bed surface. Distance from nozzle tip to bed surface and nozzle diameter come from 3D printer manual

guide. For suitable poling parameters, nozzle temperature remains the same because PVDF film's surface is likely to be melt when it is higher than 260˚C under 0.9 mm distance between nozzle tip and bed surface. The correlation between various heating bed temperature or applied voltages and piezoelectric properties are studied with respect to β-phase transformation and current output. Slower nozzle speed promotes more PVDF molecular chain alignment in theory. Note that the printing speed of 1mm/s during the IPC process is the slowest possible speed allowed by 3D printer's software and it is also important for user to maintain distance from the 3D printer during the IPC process as part of safety precautions involving high voltage applications.

Table 3.1: Experimental conditions of 3D printing and IPC process.

3D Printing parameters	**Conditions**	**IPC process parameters**	**Conditions**
Nozzle temp. (°C)	250	Nozzle temp. (°C)	250
Bed temp. (°C)	23	Heating bed temp. (°C)	23, 60, 100, 140
Print speed (mm/s)	10	Nozzle speed (mm/s)	1
Nozzle diameter (mm)	0.35	Nozzle diameter (mm)	0.35
Layer height (mm)	0.3	Applied voltages (kV)	3, 6, 9, 12
Distance from nozzle tip to bed surface (mm)	0.3	Distance from nozzle tip to bed surface (mm)	0.9

Structural, Morphological, and Functional Characterizations

Fourier transform infrared spectroscope (FTIR, Agilent Technologies Cary 630 ATR-IR) analysis was performed in the 600-1600 cm^{-1} wavenumber range at room temperature in order to characterize the infrared spectrum of absorption of IPC processed films. Piezoelectric response was characterized by a fatigue load frame (Bose ElectroForce Biodynamic 5160) and current was measured with a picoammeter (Keithley 6485) as shown in Figure 3.4(a). To quantify the piezoelectric property of film fabricated by IPC process, samples were prepared with 8 × 23 mm silver conductive paint electrodes in top and bottom surfaces. The electrodes were then extended with adhesive Cu tape to allow a proper connection to the picoammeter as shown in Figure 3.4(b). Dynamic force was applied on PVDF film to measure periodic output current, the fatigue load

frame generated 50 cyclic loads on the sample under a range from 5 to 45 N at 1 Hz while the picoammeter measured the current output. To prevent noise from fatigue machine during measurement, the two grips handing the sample were covered with insulating tape.

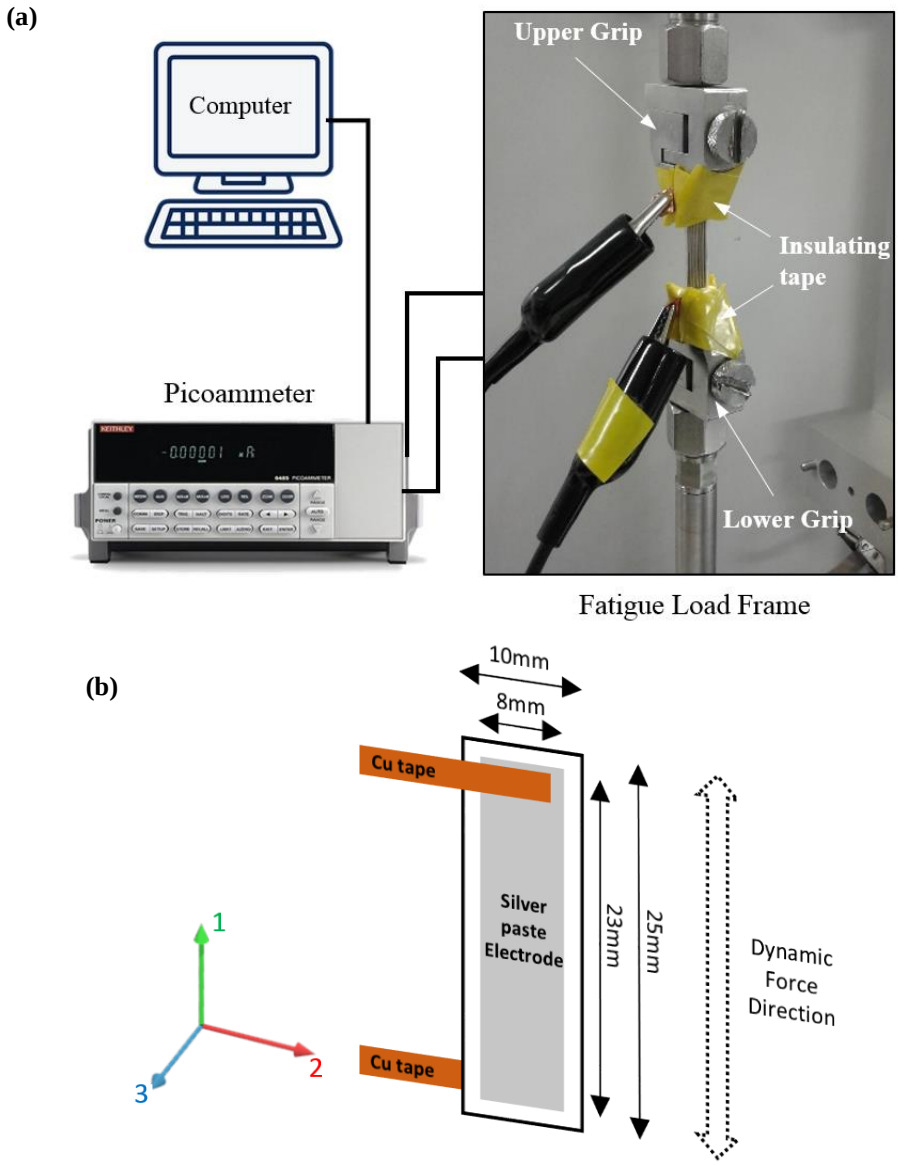

Figure 3.4: Schematic diagram of (a) the experimental setup for piezoelectric output current measurement and (b) sample and electrode design.

Mechanical Property Analysis

Mechanical properties of the IPC PVDF films were analyzed by tensile testing machine (eXpert 5600 series, ADMET MTESTQuattro). It was conducted at the speed of 5 mm/min under room temperature. The sample's dimension was same as the sample for fatigue load frame test as shown in Figure 3.4(b).

3.1.3 Results and discussion

Fourier Transform Infrared Spectroscopy (FTIR) Analysis

PVDF is a semi-crystalline polymer, especially β-phase is one of the highest electroactive properties among four crystalline phases (α, β, γ, δ) [52-54]. The α- and β-phases are most easily detected by FTIR absorption which can be used to calculate the amount of phase transformation and chain orientation. The α-phase present a large number of characteristic bands such as absorption bands at 489, 614, 766, 795, 855, and 976 cm^{-1} [44]. Some other researchers reported α phase absorption band at 764 or 763 [49, 55]. The presence of β phase can be observed through the characteristic bands at 840 and 1279 cm^{-1}. The β-phase contents in each sample were calculated from the absorption bands at 764 and 840 cm^{-1} which are characteristics of α- and β-phases respectively. Assuming that the infrared absorption follows the Lambert-Beer law, A_α and A_β absorbance at 764 and 840 cm^{-1}, respectively, are given by Eq. (1) below [56]:

$$A_{\alpha,\beta} = Log\left(\frac{I^{0}_{\alpha,\beta}}{I_{\alpha,\beta}}\right) = C \cdot K_{\alpha,\beta} \cdot X_{\alpha,\beta} \cdot L \tag{1}$$

where the subscripts α and β are defined as the crystalline phases, I^0 and I are the incident and transmitted intensities of the radiation, respectively. The L is defined as a sample thickness, C is an average monomer concentration, K is the absorption coefficient at the respective wave number, and X is the degree of crystallinity of each phase [56]. For a system containing α- and β-phases, the relative fraction of the β-phase, $F(\beta)$, can be calculated using Eq. (2) [56]:

$$F(\beta) = \frac{X_\beta}{X_\alpha + X_\beta} = \frac{A_\beta}{(K_\beta/K_\alpha)A_\alpha + A_\beta} = \frac{A_\beta}{1.26A_\alpha + A_\beta} \quad (2)$$

where K_α (6.1×10^4 cm^2/mol) and K_β (7.7×10^4 cm^2/mol) are the absorption coefficients at the respective wave number.

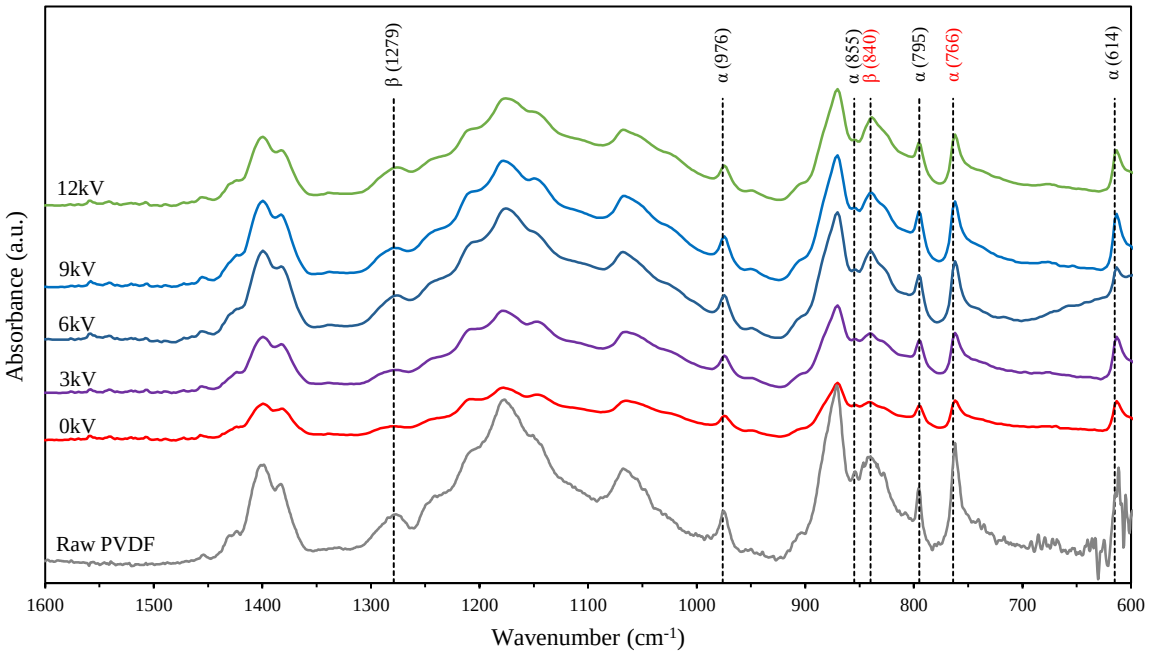

Figure 3.5: FTIR spectra for IPC PVDF films with raw PVDF and different electric voltages applied under room temperature of the heating bed.

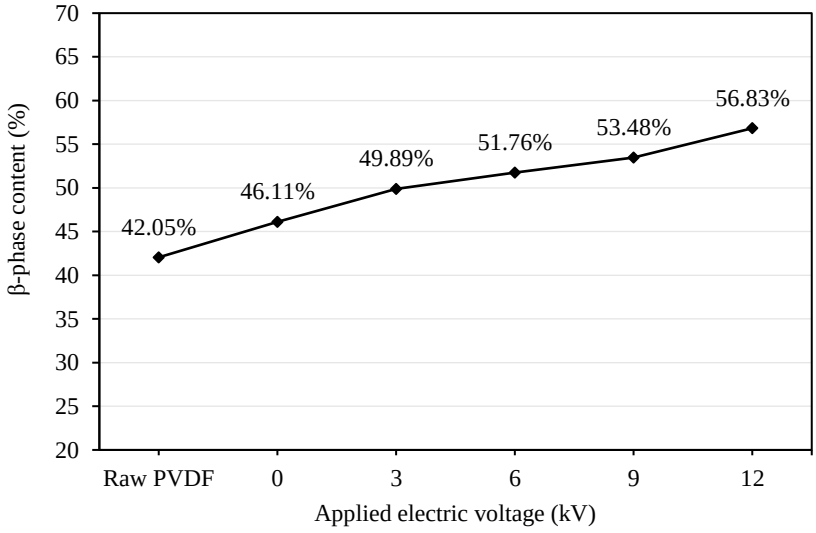

Figure 3.6: β-phase contents for IPC PVDF films with raw PVDF and different electric voltages applied under room temperature of the heating bed.

The comparison of FTIR spectra with respect to different electric voltages applied over the process is shown in Figure 3.5. The β-phase at 840 cm^{-1} band was increased relatively to α-phase at 766 cm^{-1} when increasing the electric voltage. The content of β-phase with respect to the electric voltage was increasing and the highest amount of β-phase ($F(\beta)$ = 56.83 %) was achieved at 12 kV as shown in Figure 3.6.

Optimal heating bed temperature which also mostly affects the molecular chain mobility was determined as well. Figure 3.7 indicates that β-phase under room temperature (23 °C) is the largest relatively to α-phase than increased temperatures and its content was significantly higher than others as shown in Figure 3.8. It is assumed that a heat surrounding sample underneath leads to depolarization.

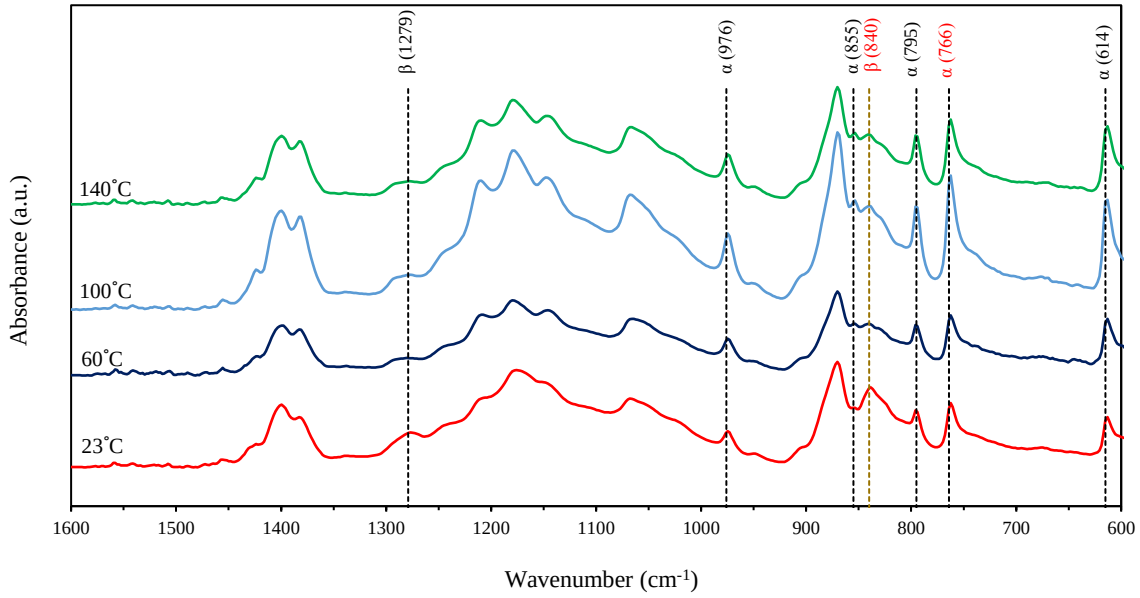

Figure 3.7: FTIR spectra for IPC PVDF films with different heating bed temperatures.

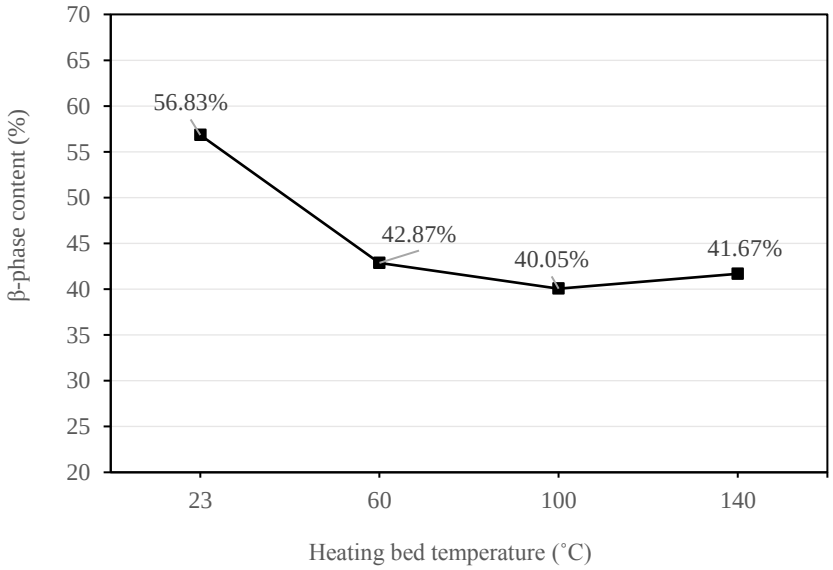

Figure 3.8: β-phase contents for IPC PVDF films with different heating bed temperatures under 12kV electric voltage.

Measurement of piezoelectric property

There are several ways to measure the piezoelectric property of PVDF films fabricated by IPC technique. Typically, high piezoelectric materials such as ceramics are measured through a

d_{33} meter. In this case, PVDF has a much lower piezoelectric constant than ceramics, therefore, it is not convenient use the d_{33} meter. An alternate way to measure the piezoelectricity is by feeding the sample's output to a charge amplifier circuit, the circuit would in turn amplify the output and allow for the characterization of the piezoelectric effect. To further simplify the characterization, we use a picoammeter to measure the output current from the printed samples. The picoammeter allows us to measure current output within the pico-amp range. IPC processed films are then tested in a fatigue load frame that applies 50 cyclic loads of 40 N at 1 Hz from the output as shown in Figure 3.9, a piezoelectric current response can be measured and allow us to calculate the d_{31} coefficient [57].

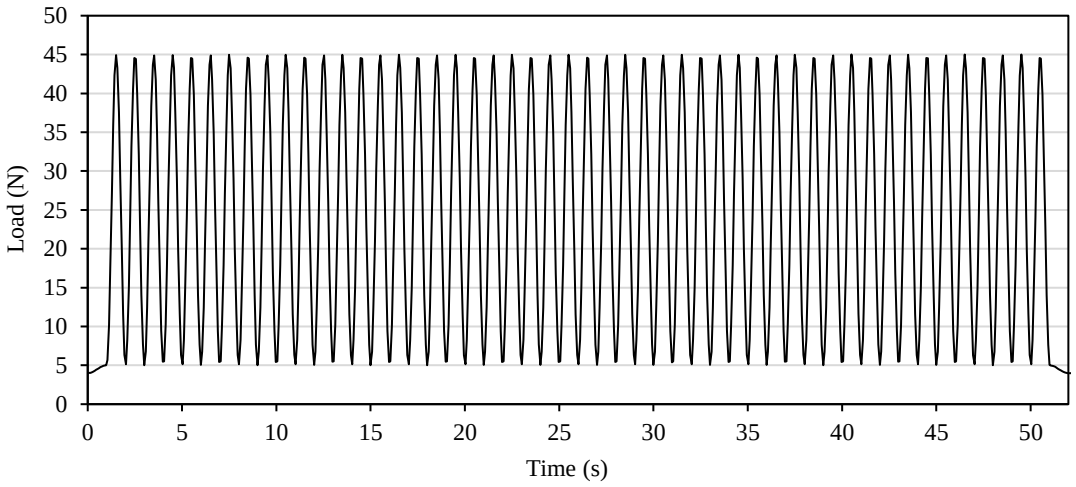

Figure 3.9: Cyclic loads at 1 Hz applied on samples by fatigue machine.

Figure 3.10 presents the current output results produced by IPC films fabricated with different electric voltages; 0, 3, 6, 9, and 12 kV. It was measured that a PVDF film fabricated under 12 kV produced the highest current output at ± 0.106 nA, when the film is subjected to cyclic loading, which indicates a total charge of approximately ± 0.033 nC was generated as shown in Figure 3.11. The output currents under 9, 6, and 3kV produced ± 0.054 nA, ± 0.045 nA, and ± 0.015 nA respectively and were linearly decreasing as decrease of applied electric voltages as well as output charges, ± 0.016 nC, ± 0.010 nC, ± 0.005 nC, respectively. On the other hand, a film

fabricated under 0 kV produced random output current only about ± 0.0008 nA and the output charge about 0.001 nC which are considered as noise. These results demonstrate that the higher electric voltage promotes higher electroactive structure and piezoelectric property during IPC process.

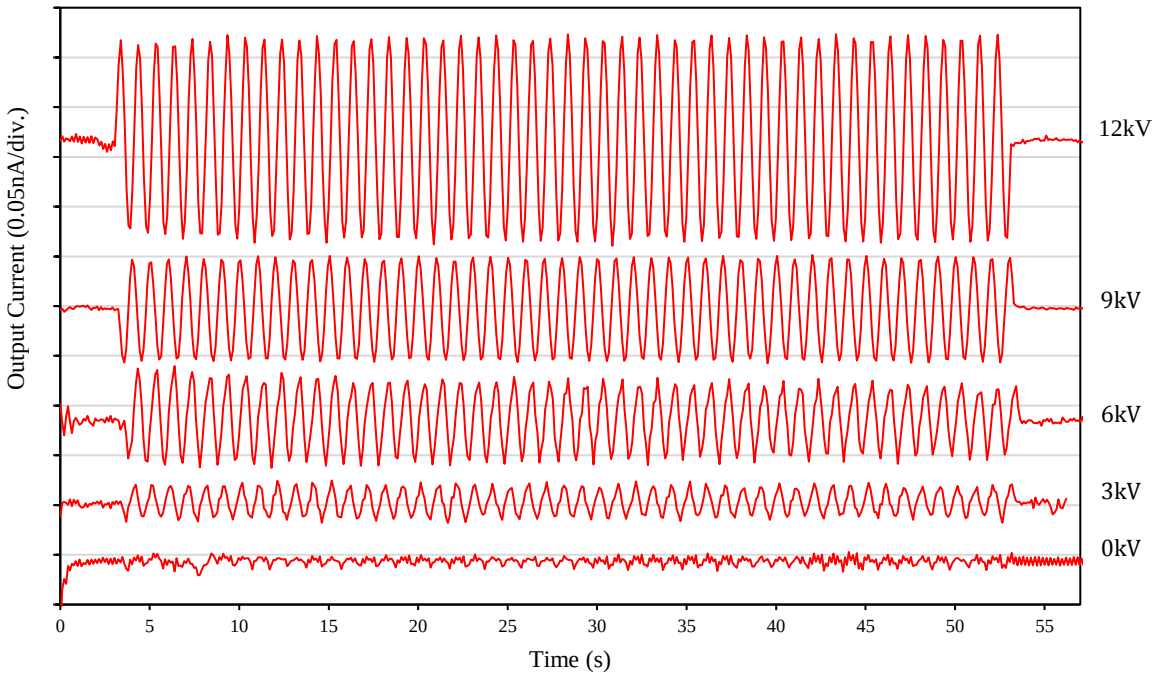

Figure 3.10: Current output of IPC PVDF films fabricated under different electric voltages.

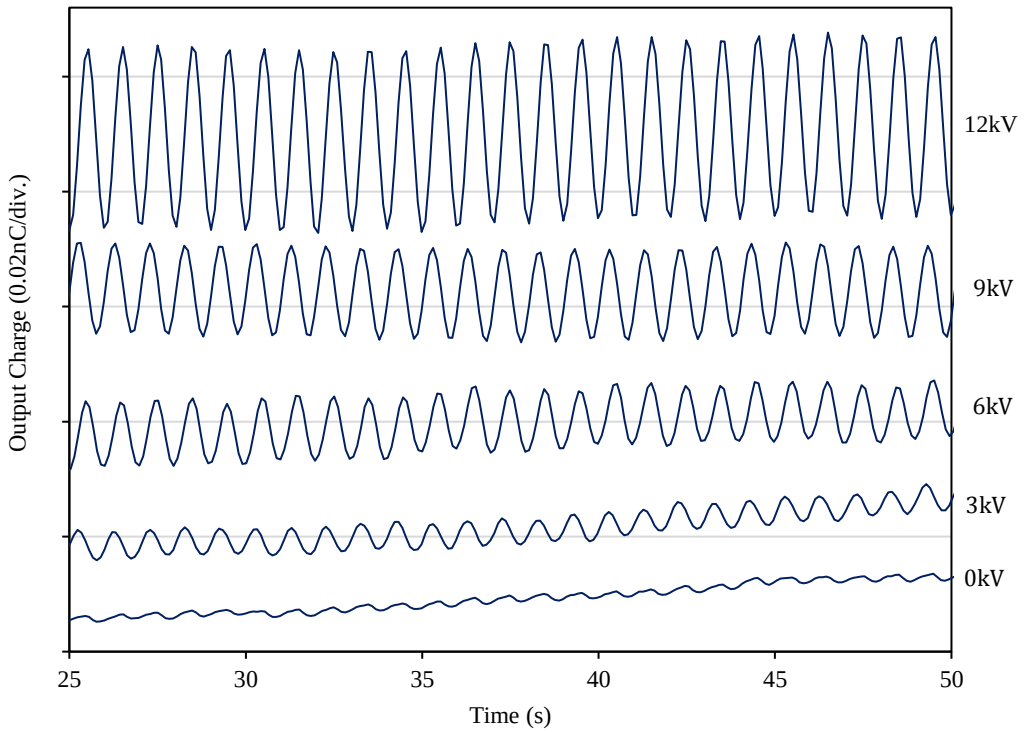

Figure 3.11: Charge output of IPC PVDF films fabricated under different electric voltages.

After the qualitative assessment of IPC fabricated PVDF films, quantitative analysis was carried out to calculate the piezoelectric coefficient (d_{31}) by using the equation below:

$$D_i = d_{ij}\sigma_j \tag{3}$$

where D_i is the electrical displacement, d_{ij} is the piezoelectric coefficient, and σ_j is the applied stress. In this case, subscripts i and j are defined as 3 and 1 respectively as shown in Figure 4(b). Therefore, the equation can then be expressed as $D_3 = d_{31}\sigma_1$. Considering the areas of the electrode and cross-section of the sample, Eq. (3) can then be expressed as

$$\frac{Q(i)}{A_{elect}} = d_{31}\frac{\nu F}{A_{cross}} \tag{4}$$

where $Q(i)$ is charge at i th, A_{elect} and A_{cross} are areas of electrode and cross-section respectively, ν is Poisson's ratio, and F is an applied force. Then, the piezoelectric coefficient can be expressed as

$$d_{31} = \frac{\frac{Q(i)}{A_{elect}}}{\frac{\nu F}{A_{cross}}} \tag{5}$$

A_{elect} and A_{cross} are 198 mm^2 and 2.64 mm^2 respectively and Poisson's ratio is determined as 0.34 [58]. Charges can be attained by numerical integration expressed as

$$Q_{(i)} = Q_{i-1} + \frac{I_i + I_{i+1}}{2} \times (t_{i+1} - t_i) \tag{6}$$

where I_i is output current at i th and t_i is the time at i and Eq. (5) can be rewritten as

$$d_{31} = \frac{\frac{Q(i)}{198}}{\frac{0.34 \times 40N}{2.64}} \tag{7}$$

d_{31} can then be determined at Q_{max} and Q_{min} and each attained d_{31} is divided by 2 for $\pm\ d_{31}$ as Eq. (8) describes.

$$\pm\ d_{31} = \frac{d_{31}^{max} - d_{31}^{min}}{2} \tag{8}$$

The calculated result determines the piezoelectric coefficients of IPC films fabricated with different electric voltages as shown in Figure 3.12. The results of the piezoelectric coefficient as shown in table 2 indicating that the film processed under 12 kV shows that the piezoelectric coefficient has been significantly increased by about 15×10^{-3} pC/N after IPC process compared to 3.3×10^{-4} pC/N generated by the one without electric voltage. Figure 3.12 presents a diagram that d_{31} is linearly increasing with the increase of applied electric voltage. This increase demonstrates

that the IPC process provides for dipole alignment of PVDF polymer and the higher electric voltage is applied the stronger piezoelectric become. It was confirmed that those results showed a good agreement with those of output current results and of FTIR analysis.

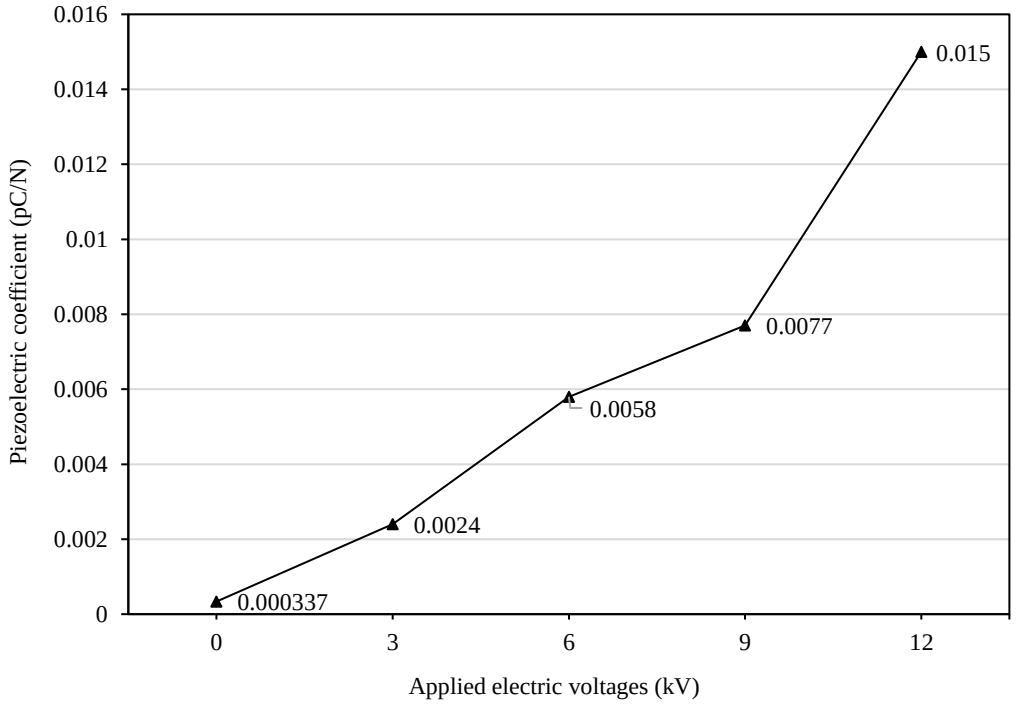

Figure 3.12: Piezoelectric coefficient change of IPC PVDF films processed under different electric voltages.

Mechanical Property Analysis

The influence of the IPC process in mechanical properties of PVDF was explored by analyzing the tensile behaviors of the IPC PVDF film. Morphological changes through IPC process influenced mechanical property of PVDF film [59]. Figure 3.13 shows the stress-strain curves for the IPC PVDF films fabricated under 0 kV and 12 kV. It was found that an ultimate strength of the IPC PVDF film after the IPC process under 12 kV is increased from 17.0 MPa to 19.8 MPa, however strain is decreased from 45.4 % to 38.6 %. This result indicated that the PVDF poled film has somewhat superior mechanical properties than the unpoled film because the PVDF poled film has enhanced orientation in the interphase region between crystalline and non-crystalline phases.

In other word, less oriented molecular structure in the unpoled film will influence inferior mechanical properties [59].

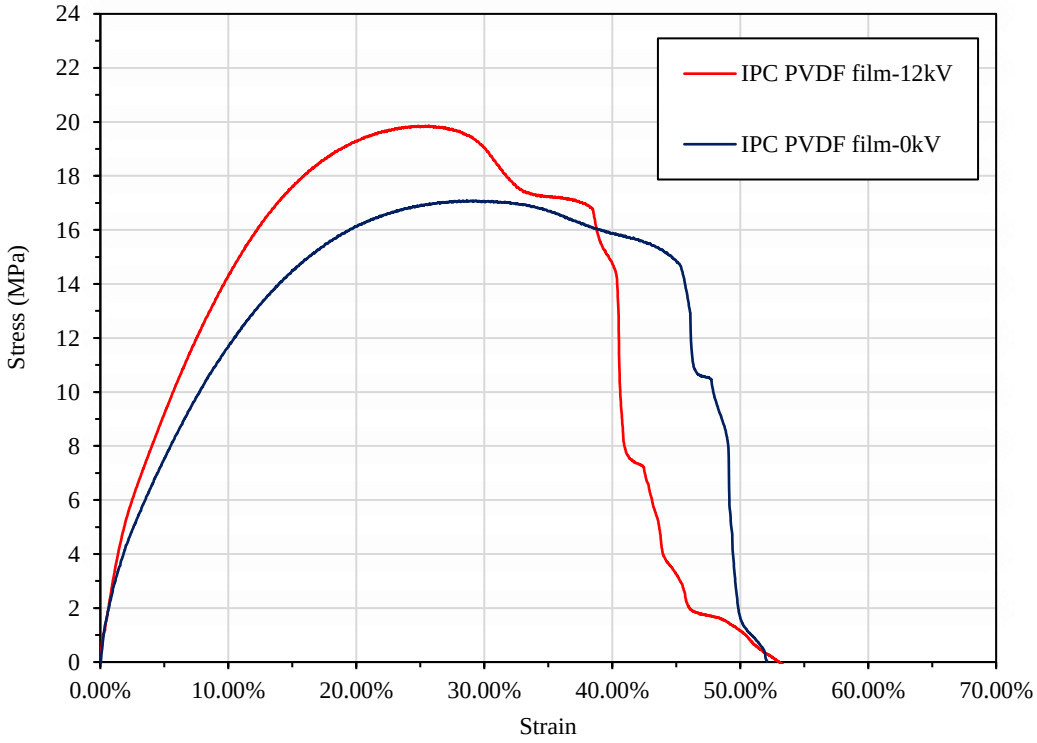

Figure 3.13: Stress-strain curve of IPC PVDF films fabricated under 0kV and 12kV.

3.1.4 Summary

In this study, the integrated 3D printing and corona poling (IPC) process was presented to fabricate PVDF piezoelectric film for sensor application. The piezoelectric property of the IPC PVDF films was characterized by FTIR analysis and fatigue load frame. Stronger electric voltage transforms higher β-phase content resulted from FTIR analysis and produces greater current output and piezoelectric coefficient (d_{31}). The IPC process developed in this research can lead to piezoelectric output current up to ± 0.106 nA while applying 12kV electric voltage during the IPC process. In addition, it was found that increasing the heating bed temperature reduces the piezoelectricity of the PVDF film. From the tensile testing result, it was investigated that the ultimate strength of the IPC PVDF film is enhanced after the IPC process due to the molecular

structure changes. The results indicate that IPC process is able to produce the piezoelectric PVDF film. For further research, longer poling time and higher electric voltage could be applied to enhance its piezoelectricity. In addition, fillers such as piezoelectric ceramics and stress-reinforcing materials can be potentially added to enhance the piezoelectricity. This novel IPC process is expected to broaden the use of additive manufacturing embedded with corona poling process to fabricate piezoelectric PVDF based devices for sensing and energy harvesting application with low cost, simple fabrication, and design flexibility.

3.2 3D PRINTING OF $BaTiO_3$/PVDF COMPOSITES WITH ELECTRIC IN-SITU POLING FOR PRESSURE SENSOR APPLICATIONS

This section presents 3D printing of piezoelectric sensors using $BaTiO_3$ (BT) filler in a poly(vinylidene) fluoride (PVDF) matrix through electric in-situ poling during the 3D printing process. Several conventional methods require complicated and time-consuming procedures. Recently developed electric poling-assisted additive manufacturing (EPAM) process paved the way for printing of piezoelectric filaments by incorporating polarizing processes that include mechanical stretching, heat press, and electric field poling simultaneously. However, this process was limited to fabrication of a single PVDF layer and quantitative material characterizations such as piezoelectric coefficient and β phase percentage were not investigated. In this paper, we propose an enhanced EPAM process that applies a higher electric field during 3D printing. To further increase piezoelectric response, BT ceramic filler was used in the PVDF matrix. It was found that a 55.91% PVDF β-phase content is nucleated at 15wt% of BT. The output current and β-phase content gradually increase as the BT weight percentage increases. SEM analysis demonstrated that larger agglomerates are formulated as the increase of BT filler contents and resulted in increase of toughness and decrease of tensile strength. The highest fatigue strength was observed at 3wt.%-BT and the fatigue strength gradually decreases as the BT filler contents increases.

3.2.1 Introduction

The advancement of 3D printing technology has given rise to a novel field of study which has recently attracted a great deal of attention. This field of study focuses on the fabrication of programmable and functional material and is now commonly known as four dimensional (4D) printing technology [60]. By combining emerging 3D printing technologies with composite materials, industries have the potential to implement novel fabrication processes along with enhanced materials to fabricate programmable devices in a cost-effective way [61, 62]. One of the materials being used for sensors and energy harvesting is poly(vinylidene) fluoride (PVDF) polymer, which converts mechanical energy to electrical energy when subjected to an external force or vice versa [38]. PVDF is a semi-crystalline polymer that consists of long molecular chains

with repeated units of $–[\ CF_2 - CH_2] -$ which has a large dipole moment of 7.58×10^{-28} C·cm [41]. It exhibits a polymorphism based on crystal orientations: α, β, γ, and δ phases. Of these, β-phase has attracted a great deal of attention for having the largest dipole moment among the possible phases. A typical process to transform PVDF from its natural α- to β-phase is by axially stretching the polymer by a factor of 4:1 followed by the application of a high electric field to align the dipole structures [38, 63, 64]. For these properties, PVDF is among the most desirable polymers for sensor applications due to its highest remnant polarization [10, 65]. In addition, this polymer has excellent thermal and mechanical properties, making it an ideal material for 4D printing due to its thermoplastic and programmable piezoelectric behavior.

Electric poling-assisted additive manufacturing (EPAM) is a recently developed 3D printing process that incorporates electric poling to allow simultaneous printing and poling [50]. Recently, said process was reported on with the successful fabrication of single layer, piezoelectric devices printed directly from pure PVDF polymer filament while applying a high electric field between nozzle tip and printing bed. This technique is a continuous fabrication process of PVDF held at high temperature during stretching and electric poling. It was demonstrated that ±1.5 nA output current can be generated from a single layer. However, quantitative material characterization in terms of β-phase content and piezoelectric coupling coefficient d_{31}/d_{33} have not been explored. In addition, qualitative measurement of PVDF output current was conducted by applying an external force through a bare hand, which is more of a qualitative assessment instead of quantitative measurement.

Piezoelectric ceramics such as lead zirconate-titanate (PZT) and barium titanate (BT) have been utilized for their excellent dipole moment, high electromechanical coupling coefficient, and high dielectric constant in PVDF matrix to enhance the piezoelectric property [66-69]. Among these ceramics, BT is preferred as inorganic filler due to its environmentally friendly nature and ease in handling as a lead-free material [12]. However, piezoelectric ceramics require higher temperature for fabrication processing and can sometimes be too brittle to be used.

In this paper, we report the fabrication of BT/PVDF composites, where BT ceramic filler was used in a PVDF matrix to enhance piezoelectric response. Different weight percentages of BT filler ranging from 3%-15% were used and the piezoelectric response as a function of weight percentage of BT was characterized. The EPAM process was modified to increase the maximum capacity of the electric field for better polarization with the number of layers while conducting electric in-situ poling of BT/PVDF composites. In addition, mechanical properties (tensile and fatigue tests) of printed materials were tested to analyze the mechanical effects of BT filler on the PVDF matrix. Potentially, the process will enable the low-cost mass production of composite piezoelectric devices for use in the sensor industry [62, 70].

3.2.2 Experimental

Commercial PVDF powder (M_W~534,000; Sigma-Aldrich) and BT powder (700nm; Inframat®) were used as the main components to prepare the nanocomposite filament. N-Dimethylformamide (DMF, OmniSolv®) was used as the solvent material to dissolve PVDF. The BT and PVDF powder were mixed via the solvent-casting process which is an alternative method of mechanical mixing for uniform distribution of BT Filler. The solution was prepared by dissolving PVDF powder in DMF solvent (1:10 weight ratio). The solution was then placed in a water bath at 80°C and was stirred using a magnetic stir bar at 300rpm for approximately 30 minutes. After PVDF powder fully dissolved, BT powder was introduced to the solution. This attained composite solution was then heated and stirred using the same parameters for approximately 15 minutes. BT build up at the bottom of solution was addressed by ultra-sonication (Branson Sonifier 450) for 20 minutes. The DMF solvent was then evaporated by dispersing the composite solution onto a glass substrate and heated to a temperature of 80°C for 12 hrs. The procedure yields a thin sheet of BT/PVDF composites, which were then sliced down to be easily extruded by a filament extruder machine (Filabot). The diameter of the extruded filament and extruding temperature are 2.89 mm and 195 °C respectively.

EPAM combines FDM 3D printing with an electric poling process to fabricate free-form single structures while maintaining uniform alignment of dipoles in the PVDF polymer [9]. This process includes effective poling factors such as shear force, heat, and electric field for polarization. However, the previous experimental setup was limited by electrical shortage when undergoing the poling process. It was found that applying more than 2MV/m may cause electric breakdown which emits a transient electromagnetic disturbance that could cause the printer to lose communication with the computer. Another limitation found in the previous study was that the EPAM technique used was limited to fabricate only a single layer for a piezoelectric device. Therefore, the EPAM process was modified to enable the application of a higher electric field (40MV/m) and print multiple layers as shown in Figure 3.14. The FDM machine (Lulzbot TAZ 5) was modified and detailed modifications are described as followings:

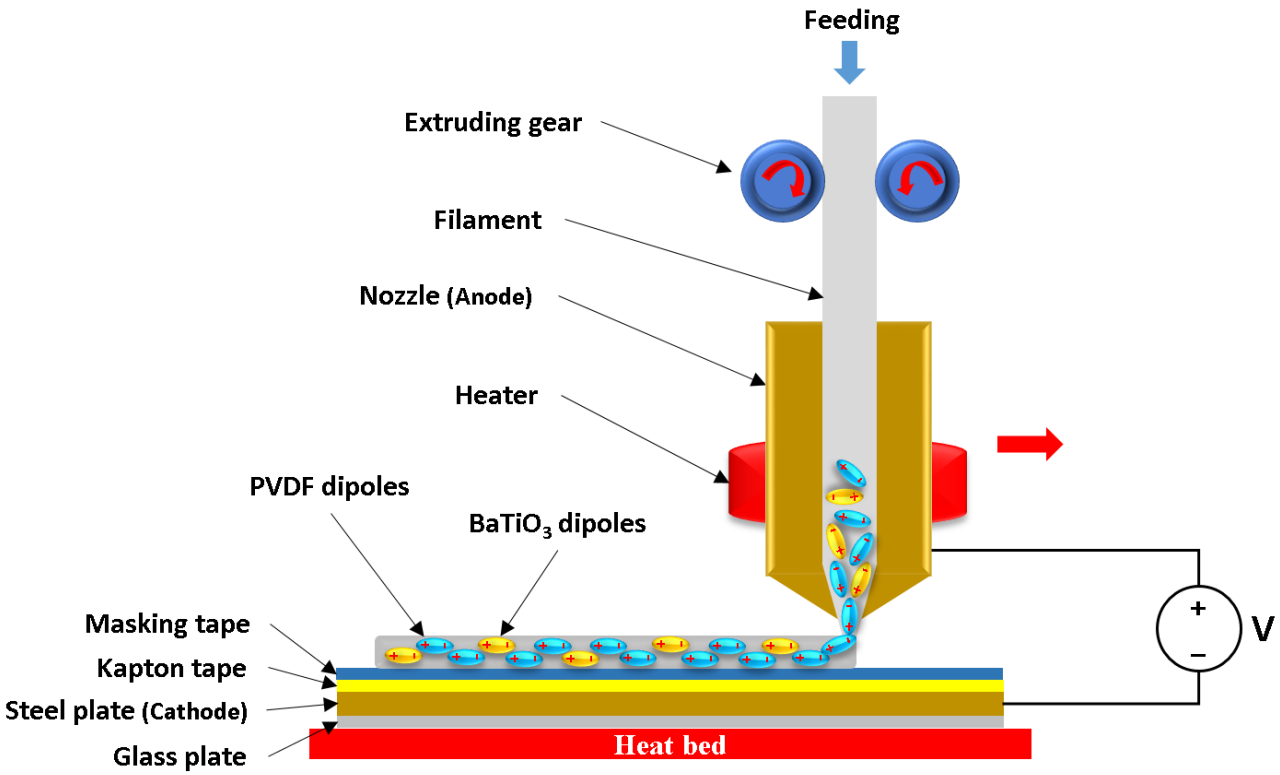

Figure 3.14: Schematic of the in-situ 3D printing and dipole alignment of PVDF and BT filler.

1) **Modification of hardware setup**: Cathode electrode placed at the heating bed was switched by adding a glass and steel plate on top of the heating bed to prevent electric shock on 3D printer as shown in Figure 3.14. The electrical breakdown often occurs because Kapton tape tends to be easily burned when hot nozzle tip is close and molten material is deposited onto Kapton tape. Due to this reason, masking tape is laid over the Kapton tape to prevent electric breakdown and to help deposited material to adhere firmly onto the bed as shown in Figure 3.14. Therefore, high electric field can be applied up to 40 MV/m without electrical breakdown as well as preventing high electrical shock inside 3D printer. 40 MV/m is enough electric field larger than coercive field (0.5-1.6MV/m) of BT nanoparticles [17, 71] and close to coercive field (50MV/m) of PVDF [18].

2) **Design of 3D model for piezoelectric device**: General printing layer pattern such as zigzag will decrease the piezoelectric coupling coefficient since each layer side by side can significantly cancel electric charges of aligned dipoles. Therefore, in order to have all dipoles in each layers be aligned to the same direction, a concentric fill pattern was set up using Slic3r software which is a tool that converts digital 3D models into printing instruction and customize printing parameters such as tool path, fill pattern, etc. as shown in Figure 3.15.

(a)

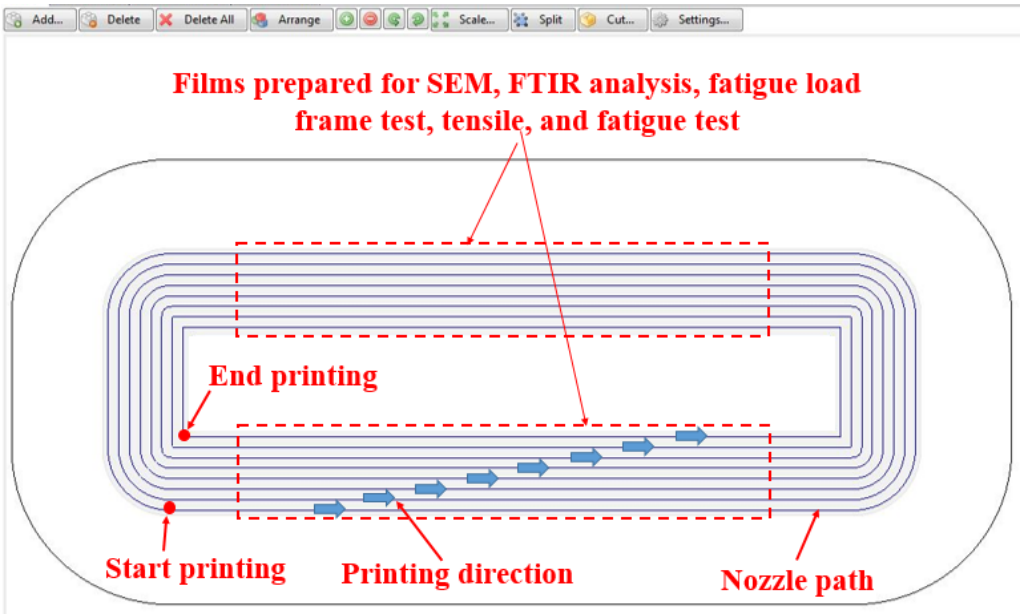

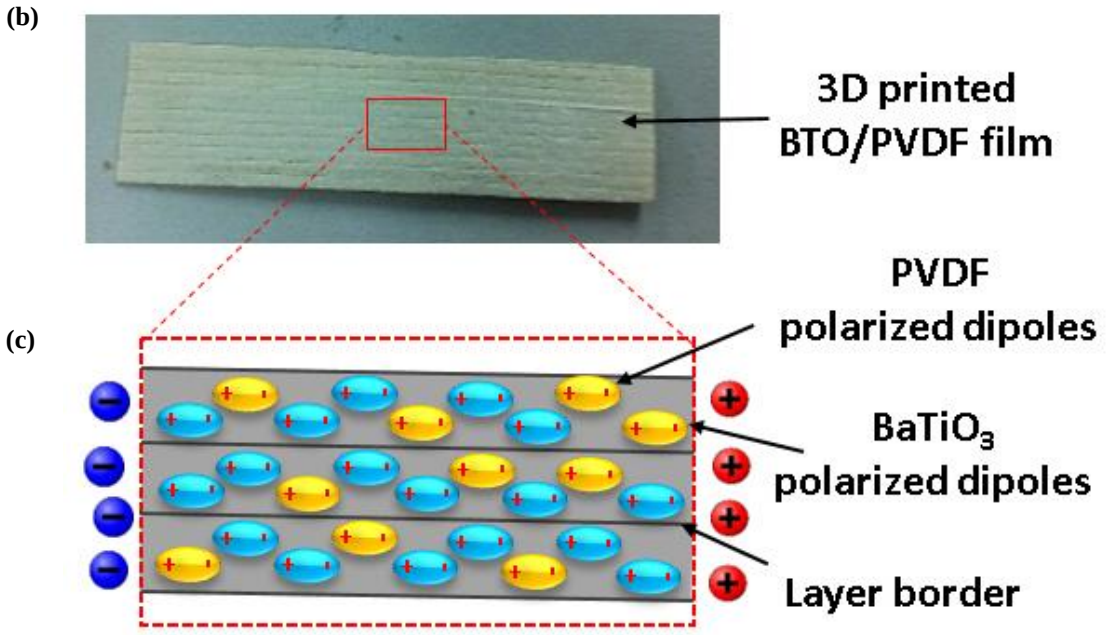

Figure 3.15: (a) A captured image of concentric fill pattern design created in Slic3r software, (b) 3D printed BT/PVDF films and (c) schematic of dipole alignment of PVDF and BT NPs fabricated by modified EPAM process.

Modified EPAM process enables infinite number of layers in X and Y axes meaning that large area of piezoelectric film can be fabricated under higher electric field. For the cyclic load frame test, eight layers were printed under 40 MV/m with varying concentration of BT powders: 0, 3, 6, 9, 12, and 15wt.%. Increasing the weight content above 15%-BT would increase severe clogging within the nozzle which could potentially damage the 3D printer. Other printing process parameters were unchanged with respect to previous research and are described in Table 3.2. Final film was 0.33 mm in thickness with dimensions of 7.5 × 40 mm.

Table 3.2: Experimental conditions of the modified EPAM process

Process parameters	**Conditions**
Nozzle temp. (°C)	230
Heating bed temp. (°C)	100
Extrusion speed (mm/s)	3
Electric field (MV/m)	40
Materials ($BaTiO_3$ wt. %)	0, 3, 6, 9, 12, 15

The morphology of 3D printed nanocomposites films was observed using a scanning electron microscopy (SEM, TM-1000, Hitachi). A Fourier transform infrared spectroscopy (FTIR, Agilent Technologies Cary 630 ATR-IR) analysis was performed in the 600-1600 cm^{-1} wavenumber range at room temperature in order to characterize an infrared spectrum of absorption of 3D printed nanocomposites films. For piezoelectric property analysis, piezoelectric output current was measured by fatigue load frame (Bose ElectroForce-BioDynamic, TA Instruments) and picoammeter (Keithley 6485) as shown in Figure 3.16(a). To quantify the piezoelectric property of 3D printed film, samples were prepared with silver conductive paint electrodes in both cross-sectional surfaces. The electrodes were then extended with Cu tape to allow a proper connection to the picoammeter as shown in Figure 3.16(b). Cyclic force was applied on BT/PVDF film to measure periodic output current, the fatigue load frame generated 50 cyclic loads on the sample under a range from 5 to 45N at 1Hz while the picoammeter measured the current output [57]. To prevent noise from fatigue machine during measurement, two grips handing the sample were covered with electrical insulating tape. Tensile and fatigue testings were performed by eXpert 5600 series (ADMET MTESTQuattro) and Bose ElectroForce-BioDynamic (TA Instruments), respectively. The tensile test was conducted at the speed of 5 mm/min [72]. Fatigue test was conducted in tension-tension cyclic mode at frequency f = 3 Hz which is appropriate for the thermal effect and ratio of the minimum to maximum stress in cycle is 0.1 (R = S_{min}/S_{max},

S_{max}: 95% of its static tensile strength under room temperature) [73]. All samples were subjected to cyclic loading until the final fracture during fatigue life measurement. The sample's dimension was same as the sample for fatigue load frame test as shown in Figure 3.16(b).

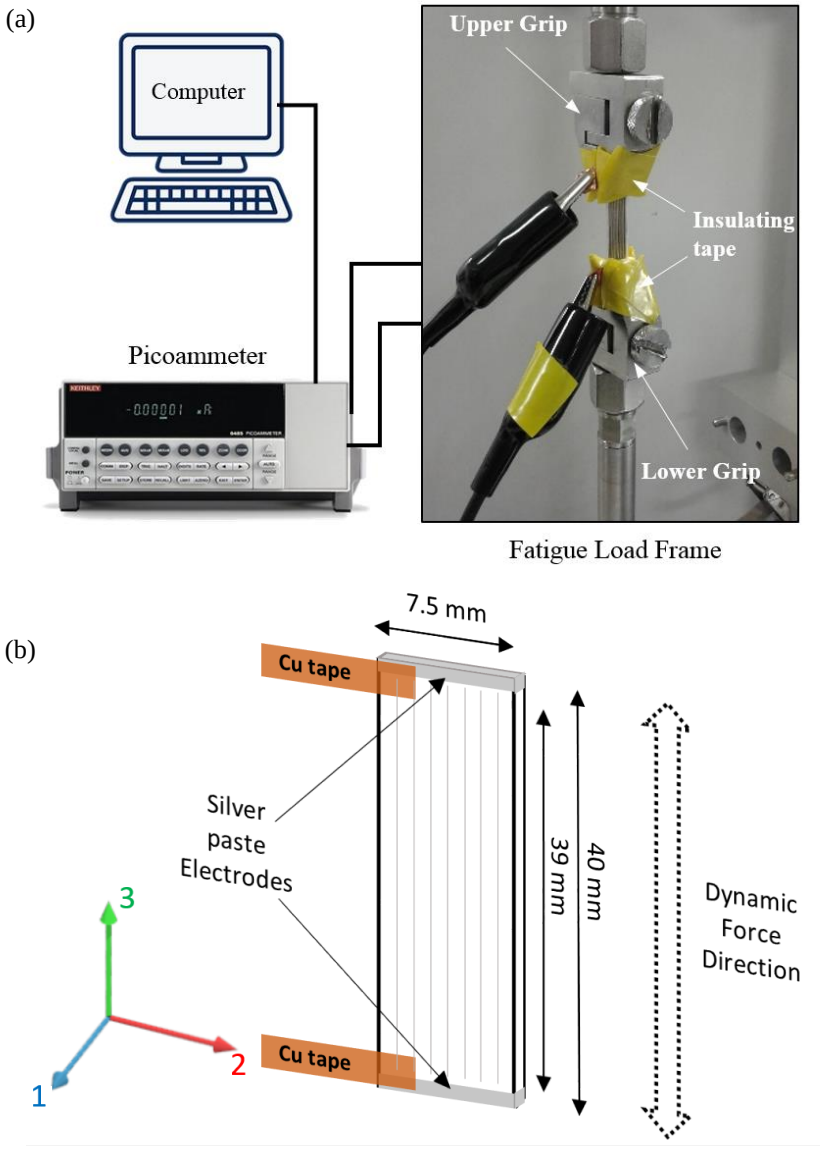

Figure 3.16: Schematic of (a) the experimental setup for piezoelectric output current measurement and (b) sample and electrode design for piezoelectric property, fatigue, and tensile tests.

3.2.3 Results and Discussion

Scanning Electron Microscopy (SEM) Analysis

The surface topography of 3D printed composite films with different BT filler content were comparatively examined by SEM analysis and shown in Figure 3.17. As shown in Figure 3.17, higher amount of BT filler was observed as filler contents increase. As BT filler contents increase, amount of filler agglomerates and their sizes were observed to increase relatively in the PVDF matrix as shown in Figure 3.17(b-f) and it was also observed that voids appeared in the matrix and their relative sizes increased with BT content. In addition, micro-cracks in the matrix started to be seen at 9wt.%-BT in Figure 3.17(d) and relatively larger cracks were observed at 12 and 15wt.%-BT as shown in Figure 3.17(e) and (f).

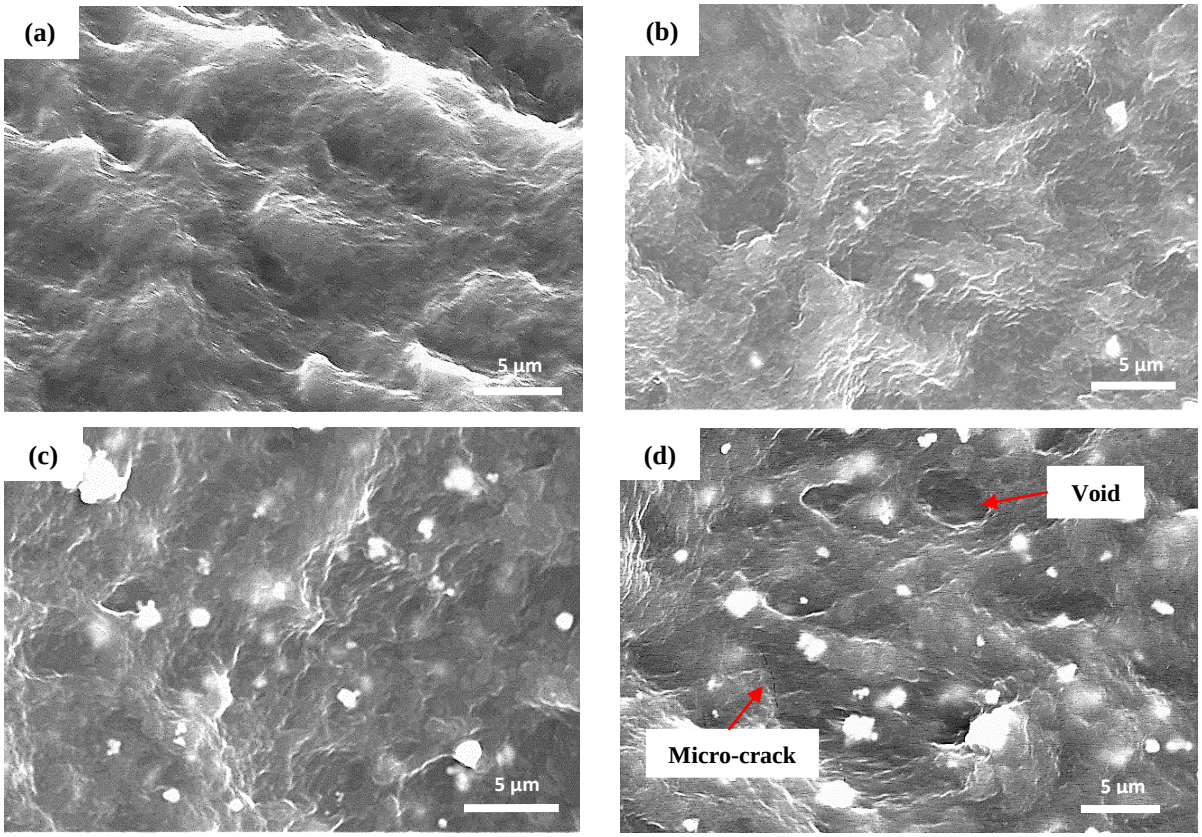

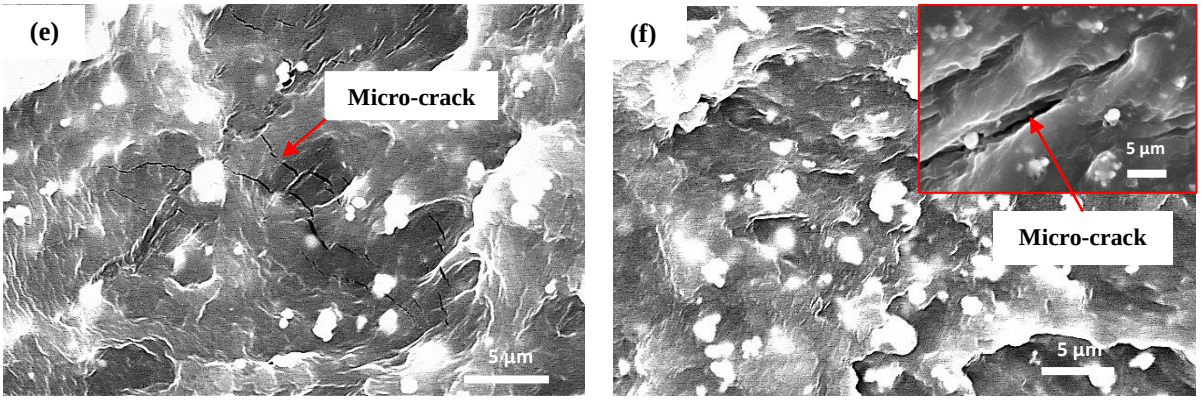

Figure 3.17: SEM images of the surfaces of 3D printed composite films with compositions of (a) PVDF, (b) 3wt.%-BT/PVDF, (c) 6wt.%-BT/PVDF, (d) 9wt.%-BT/PVDF, (e) 12wt.%-BT/PVDF, (f) 15wt.%-BT/PVDF.

Fourier Transform Infrared Spectroscopy (FTIR) Analysis

The most electroactive phase of PVDF is β-phase among other crystalline phases (α, β, γ, δ) [52-54]. This β-phase can be nucleated by the presence of BT particles, which can act as nucleation sites [24]. In order to quantify the β-phase content in the 3D printed BT/PVDF films, Fourier transform infrared spectroscopy (FTIR) analysis was performed following α-phase bands at 614, 766, 795, 855, and 976 cm^{-1} and β-phases absorption bands, at 840, 884, and 1279 cm^{-1} [44, 74]. β- and γ-phases resemble each other structurally and spectroscopically at 510, 840, and 884 cm^{-1} [31, 74], which makes it more difficult to differentiate. In addition, only β-phase (all-trans (TTT) conformation) has a strong piezoelectric response because of its largest spontaneous polarization (7×10^{-30} Cm per unit cell), therefore, only β-phase was considered when analyzing IR absorption bands [26, 30, 31, 74]. The comparison of FTIR spectra with respect to different BT filler content is shown in Figure 3.18. The β-phase at 840 cm^{-1} band was simultaneously increasing relative to α-phase at 766 cm^{-1} band in accordance with a linear increase in BT filler content.

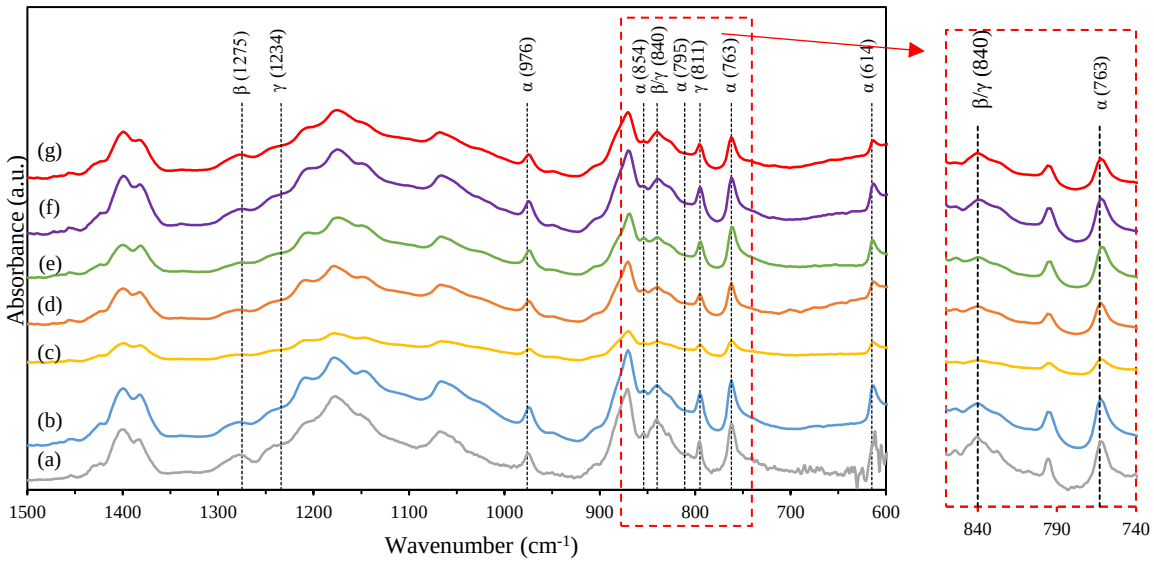

Figure 3.18: FTIR spectra for (a) non-poled 3D printed PVDF and poled 3D printed: (b) PVDF, (c) 3wt.%-BT/PVDF, (d) 6wt.%-BT/PVDF, (e) 9wt.%-BT/PVDF, (f) 12wt.%-BT/PVDF, (g) 15wt.%-BT/PVDF.

To calculate piezoelectric coefficient d_{33} [74],

$$D_i = d_{ij}\sigma_j \qquad (3)$$

where D_i is the electrical displacement, σ_j is the applied stress, and d_{ij} is the piezoelectric coefficient. In this case, subscripts i and j are defined as 3. Therefore, the equation can then be expressed as $D_3 = d_{33}\sigma_3$. Considering areas of electrode and cross section, Equation (3) can then be expressed as

$$\frac{Q}{A_{cross}} = d_{33}\frac{F}{A_{cross}} \qquad (4)$$

where Q is charge, A_{cross} are areas of cross-section, and F is an applied force. Then, piezoelectric coefficient can be expressed as

$$d_{33} = \frac{Q}{F} \qquad (5)$$

Charges can be attained by numerical integration which is the similar method with Simpson's rule [37, 74] expressed as

$$Q_{(i)} = \ Q_{i-1} + \frac{I_i \ + \ I_{i+1}}{2} \ \times (t_{i+1} - t_i) \qquad (6)$$

where I_i is output current at i th and t_i is the time at i and Equation (7) can be rewritten as

$$d_{33} = \ \frac{Q(i)}{40N} \qquad (7)$$

d_{33} can then be determined at Q_{max} and Q_{min} and each attained d_{33} is divided by 2 to get $\pm \ d_{33}$ as Equation (8) describes

$$\pm \ d_{33} \ = \ \frac{d_{33}^{max} \ - \ d_{33}^{min}}{2} \qquad (8)$$

The highest amount of β-phase content ($F(\beta)$ = 55.91 %) was achieved at 15wt.%-BT content among others as shown in Figure 3.19. This is 30.41% increase compared to β-phase content of the non-poled PVDF ($F(\beta)$ = 42.87 %). β-phase content gradually increased with the increase of the BT filler content. It is assumed that β-phase growth was affected mainly by the inclusion of BT filler because the nucleation of the β-phase of the PVDF is proportional to the specific area of the filler during thermal processes such as filament extrusion and 3D printing [24]. The in-situ poling 3D printing process slightly increased the β-phase content from 42.87% to 44.87%, as seen in Figure 3.19. The increase of β-phase after poling process is consistent with literature [50].

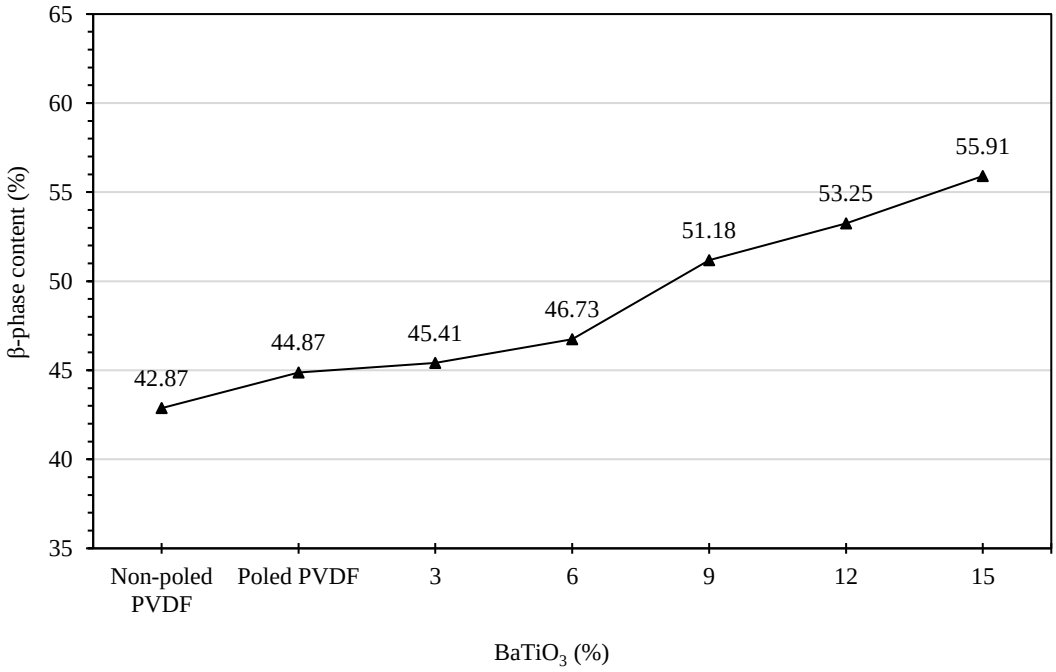

Figure 3.19: β-phase content for non-poled 3D printed PVDF and poled 3D printed PVDF/BT films with different BT contents.

Piezoelectric Property Measurement

Characterization of piezoelectricity was simplified by using a fatigue load frame and picoammeter to measure the output current from 3D printed samples. 3D printed films were tested in a fatigue load frame that applies 50 cyclic controlled tension of 40 N at 1 Hz while the picoammeter measures current output within the pico-amp range (Figure 3.20) [74].

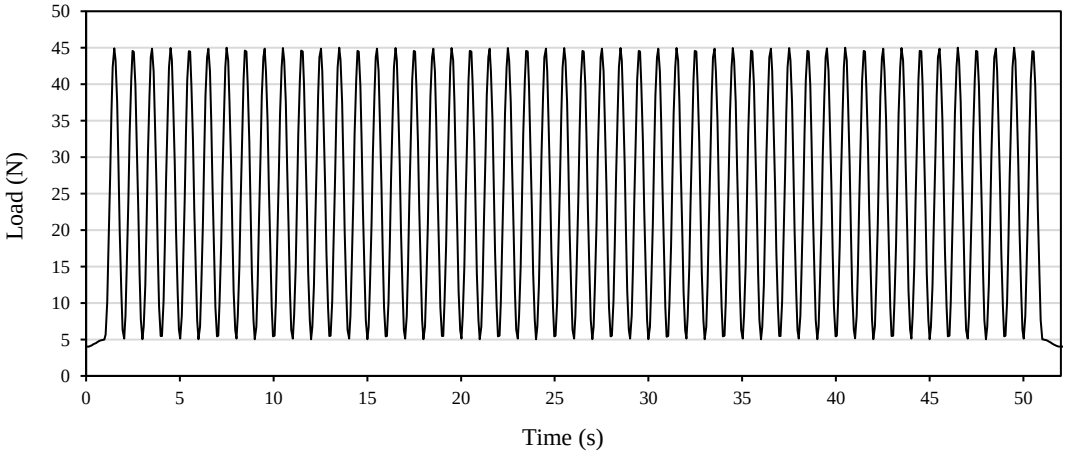

Figure 3.20: Cyclic loads at 1 Hz applied on samples by fatigue machine.

Figure 3.21 presents the current output results produced by 3D printed BT/PVDF films fabricated under the same printing and poling parameters. It was measured that the highest current output is ±0.0442 nA observed at 15wt.%-BT content. This is 1033% increase compared to the output current of no in-situ PVDF. Then the current outputs gradually decreased as BT filler content decreased (±0.0294 nA at 12wt.%, ±0.0168 nA at 9wt.%, ±0.0075 nA at 6wt.%, ±0.0073 nA at 3wt.%, ±0.0065 nA at 0wt.%-BT, ±0.0039 nA at no in-situ PVDF). To confirm the output current is piezoelectric current generated from the composites, Acrylonitrile Butadiene Styrene (ABS) was printed and tested using the same testing setup. It is shown in Figure 3.21 that the current signal is not periodical as applied force, therefore, the current signal is considered as noise. It was confirmed that these piezoelectric electrical current results show a good agreement with those of β-phase content's trend. The output current difference between poled and non-poled PVDF shows a good agreement with FTIR analysis and indicates that electric in-situ poling during the 3D printing process slightly affected β-phase transformation of PVDF polymer.

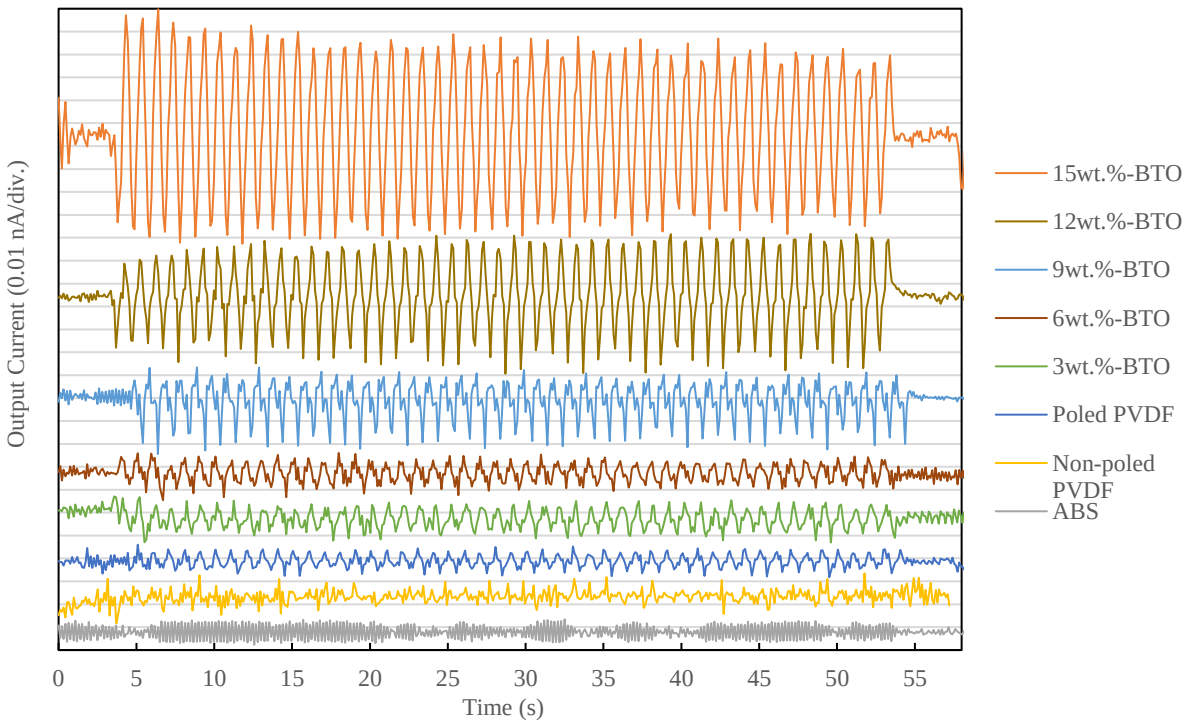

Figure 3.21: Output currents of ABS, non-poled PVDF, poled PVDF, and BT/PVDF films with different BT contents under 40N.

The calculated result determines the piezoelectric coefficients of 3D printed films (see Method S4). Figure 3.22 indicates that the piezoelectric coefficient of the poled PVDF has been slightly increased by 42% compared to the non-poled PVDF. This demonstrates that the in-situ poling process slightly influenced β-phase transformation. However, by adding BT filler the piezoelectric coefficient has significantly increased by 0.101 pC/N compared to non-poled PVDF. This is about 1342% increase and indicates that the BT filler played an important role of enhancing piezoelectric coefficient.

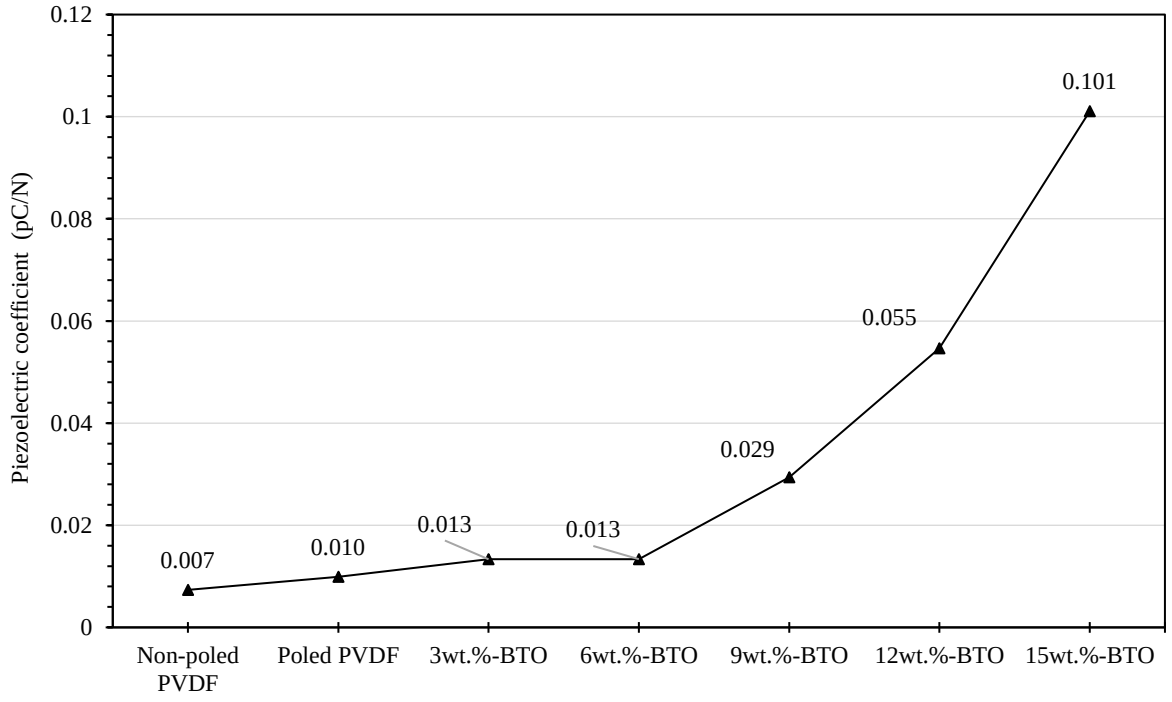

Figure 3.22: Piezoelectric coefficients of non-poled PVDF, poled PVDF, and BT/PVDF films with different BT contents under 40N.

Mechanical Property Analysis

The influence of the presence of BT filler in the mechanical properties of PVDF matrix was explored by analyzing the tensile and fatigue behaviors of 3D printed BT/PVDF composite

films. In general, filler increases tensile strength because mobility of the polymer chains is restricted by the dispersion of filler under low filler content [75]. Figure 3.23 indicates that the ultimate tensile strength of the 3D printed 3wt.%-BT/PVDF film was enhanced about 45.83% compared to PVDF and began to degrade as BT filler content increased and was decreased to 7.63% at 15wt.%-BT. This can be attributed to the following reasons: (1) BT filler are more likely to agglomerate and be heterogeneously distributed in higher loading systems. As shown in Figure 3.23, it is demonstrated that BT agglomerates increased in higher filler content [76]; and (2) voids and micro-cracks were created during the fabrication process and increased with higher filler content [77, 78]. This means that the total amount of cross linking of PVDF molecular chains was decreased. Therefore, these agglomerates and defects led to the degradation of the tensile strength after 3wt.%-BT. However, strain was increased linearly as BT filler content increased and the sample were elongated up to 500%. It is assumed that increased filler helped prevent crack propagation, therefore higher BT filler increased the toughness property.

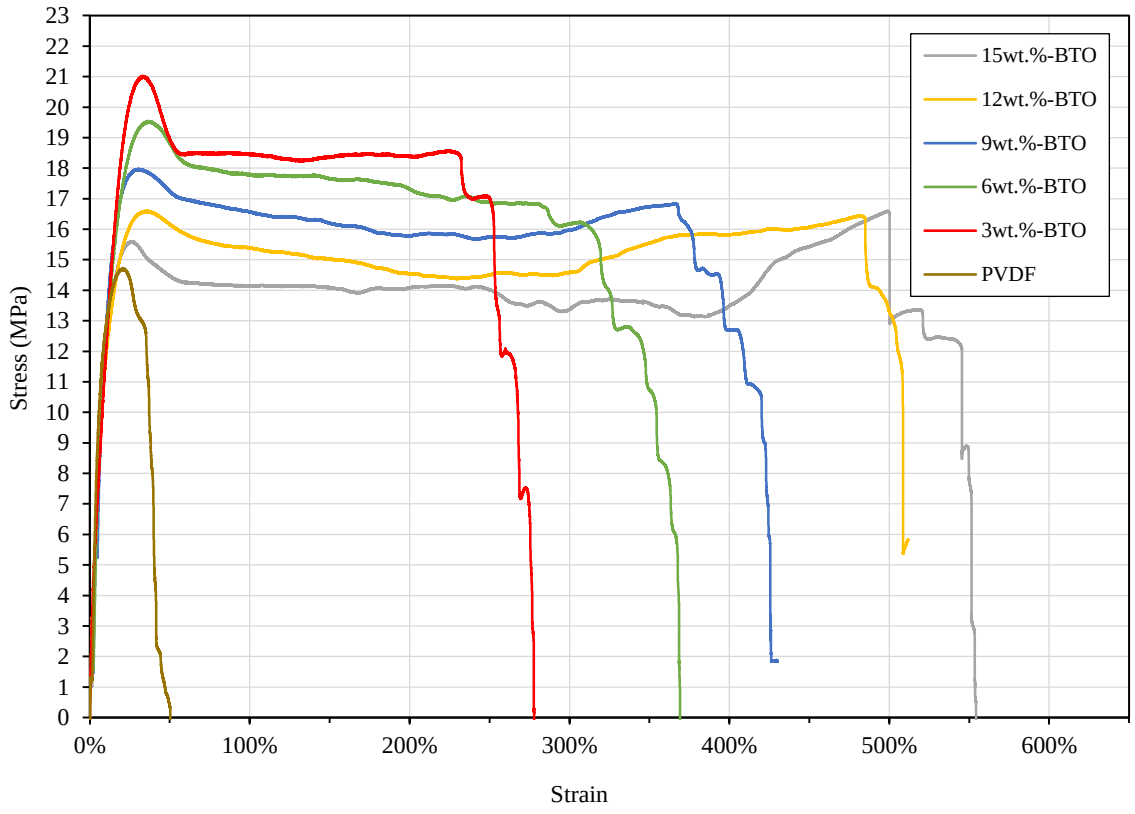

Figure 3.23: Stress-strain curve at the strain rate of 5mm/min for 3D printed PVDF/BT films with different BT contents.

To determine the dynamic loading fatigue strength of the composites, fatigue-life testing was performed and shown in Figure 3.24. It indicates that fatigue strength at 3wt.%-BT shows the best enhancement compared with pure PVDF. When the amount of BT filler content increased, there is a decrease trend in the fatigue strength. This decrease in the fatigue strength with higher BT filler can be explained with the following reasons: (1) during the fatigue cycle, filler agglomerates act as steric obstacles which prohibits PVDF polymer from flowing into the BT agglomerates and eventually creating defects such as holes and voids between BT and PVDF matrix [75]; and (2) aggregated filler causes poor load transmission, stress accumulation, and subsequent origin of new cracks [72, 75, 79]. Therefore, these agglomerates and aggregated filler led to the degradation of the fatigue strength after 3wt.%-BT.

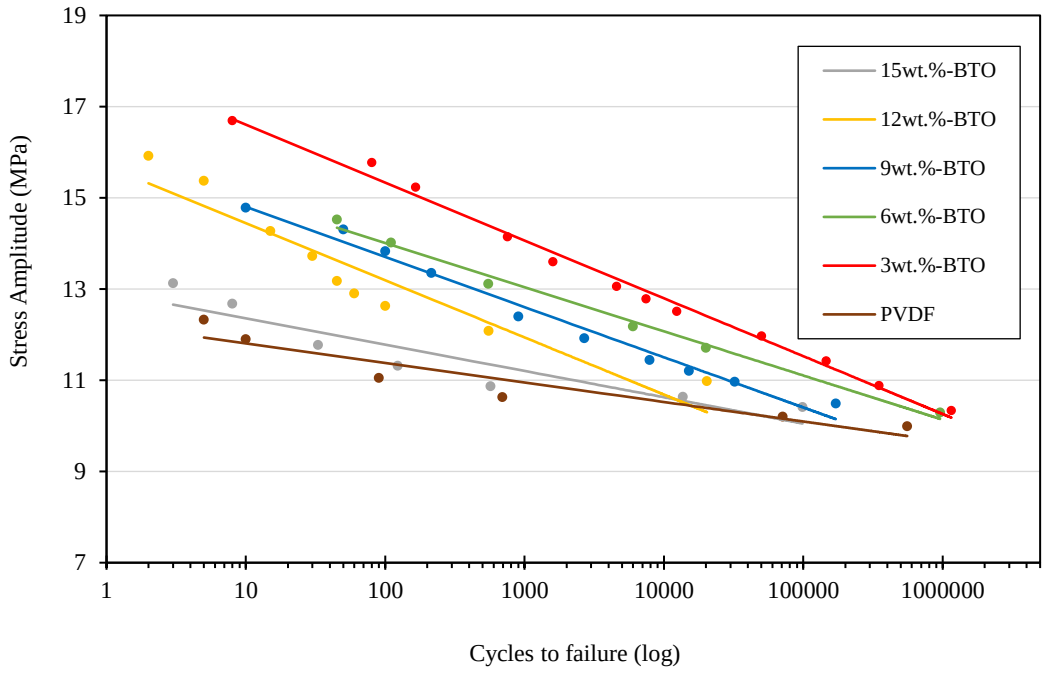

Figure 3.24: Generalized S-N curve for 3D printed PVDF/BT films with different BT contents.

3.2.4 Summary

In this study, BT/PVDF composites were fabricated using an integrated 3D printing and in-situ poling process for sensor applications. It was investigated that the fabrication process slightly affected PVDF β-phase transformation, however BT fillers played a more important role in the piezoelectric effect regarding transformation from α- to β-phase of PVDF due to nucleation on filler surfaces during fabrication process based on the results of FTIR and output current. Therefore, the PVDF β-phase and output current at 15wt.%-BT increased by 30.41% and 1033%, respectively when compared to non-poled PVDF. In SEM images, larger agglomerates and defects (i.e. voids and cracks) were formulated with the increase of BT and resulted in degradation of tensile strength but significantly higher toughness. In addition, the inclusion of BT also increased the fatigue strength of PVDF. The highest tensile and fatigue strengths were seen at 3wt.%-BT and gradually decreased as the filler content increased because of defect creation, poor load

transmission, stress accumulation from agglomerates and aggregated filler during tensile and fatigue life measurement.

Chapter 4: Design of Nanocomposites for Multifunctional Devices

4.1 Increased Piezoelectric Response in Functional Nanocomposites through MWCNT Interface and Fused-Deposition Modeling 3D Printing

MWCNTs are utilized to resolve low coupling coefficient issue by dispersing MWCNTs in PVDF matrix to create stress reinforcing network, dispersant, and electron conducting functions for BT nanoparticles. Various BT and MWCNTs percentages of nanocomposite film are fabricated by FDM 3D printing which can simplify the fabrication process as well as lower cost and design flexibility. Increasing MWCNTs and BT particles gradually increase piezoelectric coefficient (d_{31}) by 0.13 pC/N with 0.4wt.%-MWCNTs/18wt.%-BT. These results provide not only a technique to print piezoelectric nanocomposites but also unique materials combination for sensor application.

4.1.1 Introduction

Piezoelectric materials have long been investigated due to their unique characteristic of converting mechanical stress to electric charges and vice versa [9, 80]. Of the piezoelectric polymers and ceramics, poly(vinylidene fluoride) (PVDF) and barium titanate (BT) have seen wide applications in electronics, sensing/energy harvesting, and bioengineering [10, 81, 82]. The combination of these two materials yields both excellent mechanical and piezoelectric properties so that BT/PVDF nanocomposites are attractive for energy harvesting and sensor applications due to their simple and convenient fabrication process, low cost, and excellent properties [12, 83]. However, it has an intrinsic low direct piezoelectric coupling coefficient which is a drawback with regard to the piezoelectric effect and sensor applications [83-85]. Therefore, graphitic carbon such as graphene oxide or multiwall carbon nanotubes (MWCNTs) have been utilized to enhance both electric and stress transfer to the ceramic particles and uniform dispersion [71, 86, 87]. In order to better enhance stress reinforcing, it is studied that a 3-trimethoxysilylpropyl methacrylate (TMSPM) linker molecular is covalently grafted on the BT particle surface. This surface modification of covalent bonding showed higher piezoelectricity than a graphitic carbon network [71]. In addition, there are several traditional methods for preparing BT/PVDF nanocomposites such as spin-coating, and hot-embossing. Nonetheless, these methods entail complicated and time-

consuming processes, quality issues, etc. [74]. Recently, additive manufacturing technology has been introduced to printing piezoelectric 3D structures [50, 74, 83]. It is reported that the fused deposition modeling (FDM) 3D printing process significantly improves homogeneous dispersion of BT nanoparticles in the PVDF matrix, enhancing piezoelectric properties [74]. In addition, the FDM 3D printing technique is integrated with corona poling, which is one of the traditional poling processes, to simplify fabrication of piezoelectric PVDF films through sequential processes [74]. Kim et. al invented a 3D printing technique to optically fabricate photosensitive polymer based-BT nanocomposites with surface modification [71]. A photoliable polymer was induced to encapsulate piezoelectric nanoparticles during photo-polymerization. This technique can produce 3D structure of piezoelectric nanocomposites but is limited to combination with photosensitive polymers.

Herein, we report FDM 3D printing of MWCNTs/BT/PVDF nanocomposite films, where BT ceramic nanoparticle fillers and a PVDF polymer matrix are used as piezoelectric constituents and MWCNTs as electrical and mechanical transfer network in the system for stress reinforcing, dispersant, and conducting function for nanoparticles. Various BT (0 – 18wt.%) and MWCNTs (0 – 0.4wt.%) weight percentages are tested by SEM, XRD, FTIR, fatigue load frame, and human hands to analyze piezoelectric properties for use in pressure sensor.

4.1.2 Experimental

To fabricate continuous nanocomposites filament for printing, commercial PVDF powder (MW~534,000; Sigma-Aldrich, USA), BT powder (700nm; Inframat®, USA), and MWCNTs powder (Diameter: 8-15 nm, length: 10-50 μm, Cheaptubes®, USA) are mixed with N-Dimethylformamide solvent (DMF, OmniSolv®) via the solvent-casting method. As schematic illustration of the synthesis process is shown in Figure 4.1(a).

The BT and CNTs powder were introduced to DMF solvent and this solution was then placed in a bath sonication for 30 min in order for uniform distribution of nanoparticles. The solution is prepared by dissolving PVDF powder (1:10 weight ratio in PVDF:DMF solvent). The

solution is then placed in a water bath at 80°C and is stirred using a magnetic stir bar at 300rpm for approximately 30 minutes. After the PVDF powder fully dissolves for approximately 15 minutes, BT and CNTs built up at the bottom of solution is addressed by ultra-sonication (Branson Sonifier 450) for 20 minutes. DMF solvent is then evaporated by dispersing nanocomposites solution onto a glass substrate and heated to a temperature of 90°C for 12 hrs. The procedure yields a thin sheet of BT/PVDF nanocomposite, and these casted nanocomposites are sliced down to be easily extruded by filament extruder machine (Filabot). The diameter of the extruded filament and extruding temperature are 2.9 mm and 195 °C respectively. These resultant thin sheets of nanocomposites are sliced down to be easily extruded by a filament extruder machine (Filabot®) and the nanocomposite filament (see Figure 4.1(b)-i) is used to 3D print a thick film by a fused deposition modeling 3D printer (Lulzbot® Taz 5) for a pressure sensor application as shown in Figure 4.1(b)-ii and (b)-iii. These filament extrusion and 3D printing processes are proved in literature to provide better dispersion of nanoparticles in the matrix than solvent-casting, therefore enhancing piezoelectric and mechanical properties [74].

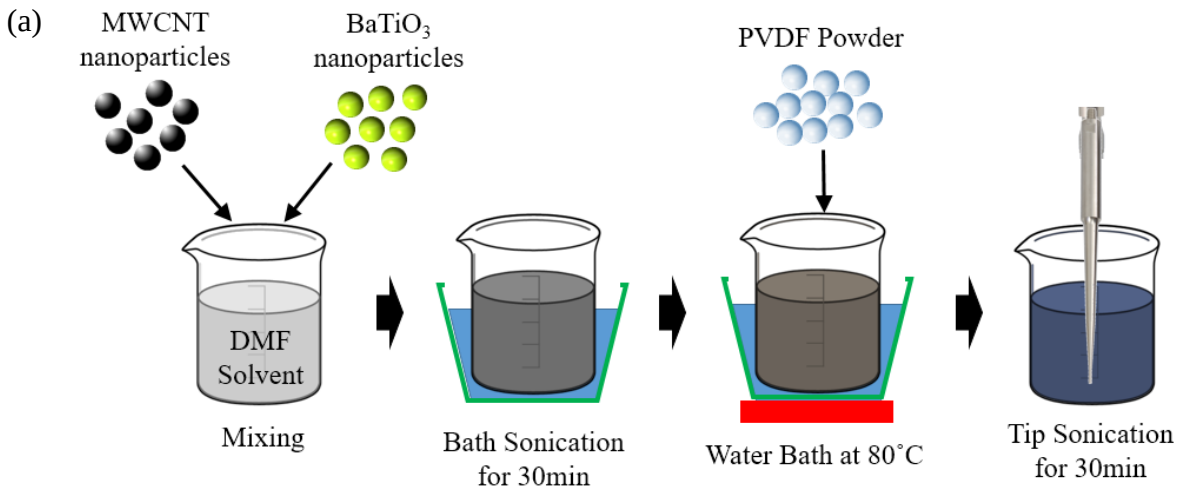

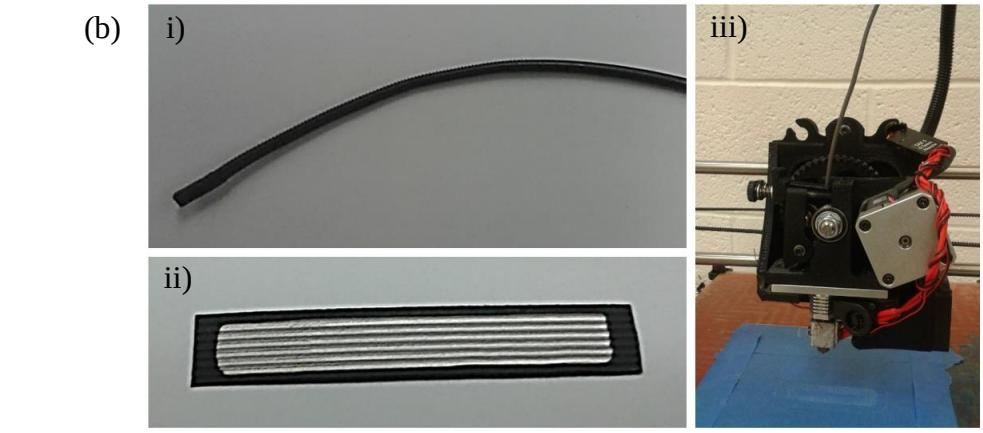
(b)
i)
ii)
iii)

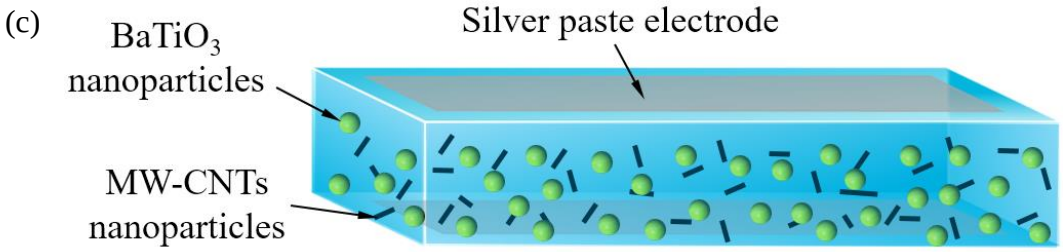
(c)
BaTiO3 nanoparticles
MW-CNTs nanoparticles
Silver paste electrode

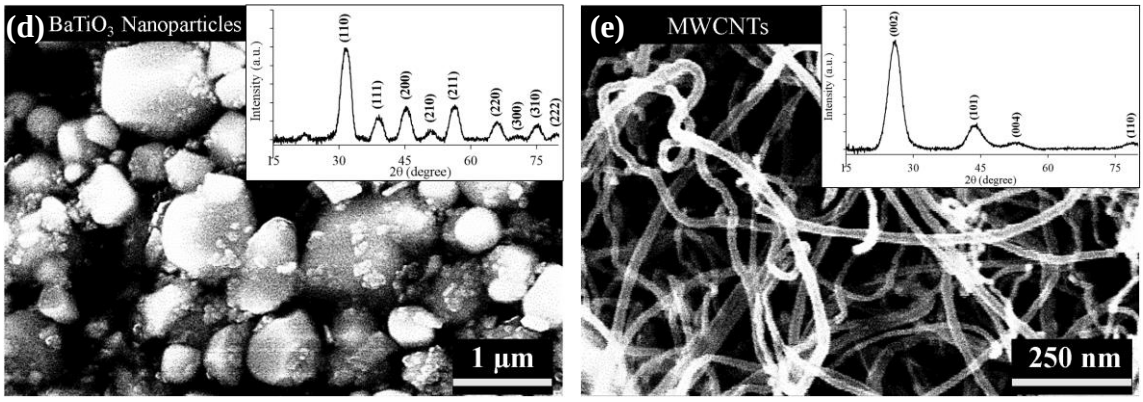
(d) BaTiO3 Nanoparticles
Intensity (a.u.)
2θ (degree)
(110)
(111)
(200)
(210)
(211)
(220)
(300)
(310)
(222)
1 µm
(e) MWCNTs
(002)
(101)
(004)
(110)
250 nm

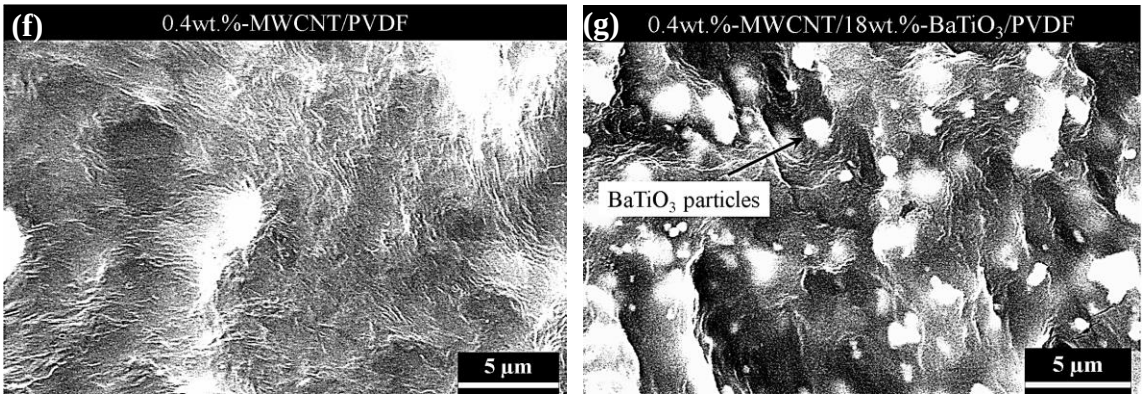
(f) 0.4wt.%-MWCNT/PVDF
5 µm
(g) 0.4wt.%-MWCNT/18wt.%-BaTiO3/PVDF
BaTiO3 particles
5 µm

Figure 4.1: (a) schematic illustration of the synthesis process for MWCNT/BT/PVDF nanocomposites, (b) i) extruded nanocomposite filament, ii) 3D printed nanocomposite film device covered with silver paste, and iii) FDM 3D printer, (c) schematic illustration of the printed nanocomposite sensor device, and SEM images of (d) BT nanoparticles (the inset shows XRD analysis for BT nanoparticles), (e) MWCNT (the inset shows XRD analysis on MWCNT), (f) 0.4wt.%-MWCNT/PVDF, and (g) 0.4wt.%-MWCNT/18wt.%BT/PVDF.

For the cyclic load frame test, eight layers are printed with varying concentration of BT powders: 0, 6, 12, and 15 weight percentages and MWCNTs: 0, 0.1, 0.4 weight percentages. Increasing the weight content above 18%-BT would increase severe clogging within the nozzle which could potentially damage the 3D printer. In addition, increasing the weight content above 0.4%-MWCNTs would increase the electrical break down during the electric poling process. For the printing parameter, the film is printed at 230°C of nozzle temperature, 23°C of heating bed temperature, and 10mm/s of extrusion speed. The printing pattern is described in Figure 4.2. Final film was 0.55 mm in thickness with dimensions of 6 × 35 mm.

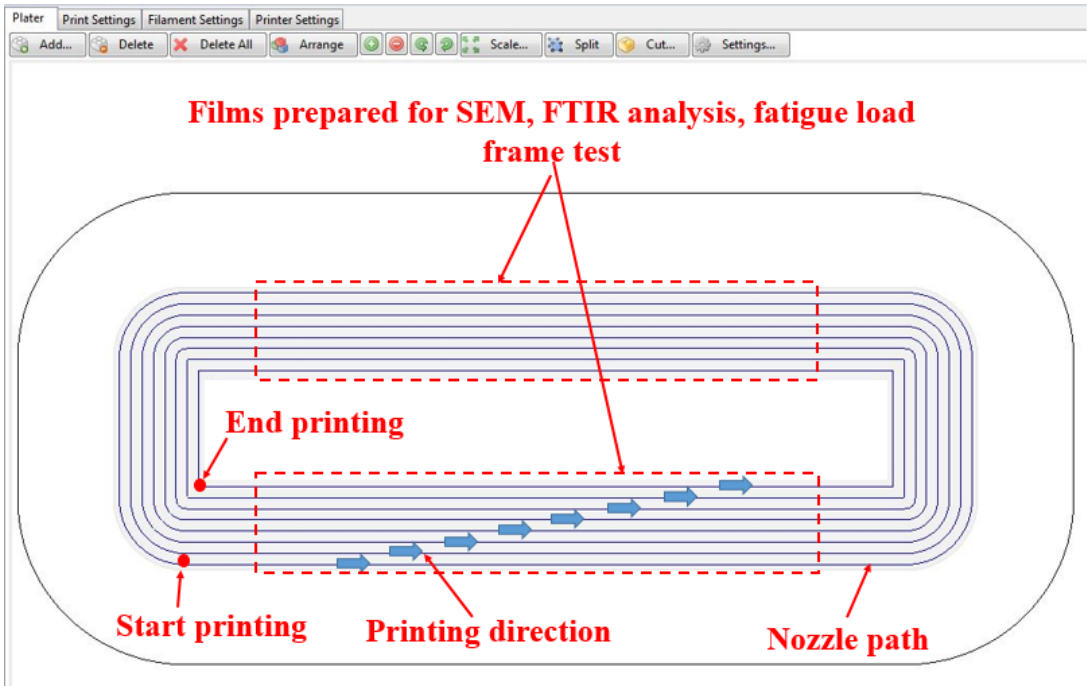

Figure 4.2: A captured image of concentric fill pattern design created in Slic3r software used for SEM, FTIR, and fatigue load frame test.

4.1.3 Results and discussion

The printed nanocomposites film is depicted in Figure 4.1Figure (c). BT particles and PVDF polymer are not compatible with each other because of their respective hydrophobic and hydrophilic characteristics, so the combinations of these two offers a low stress transfer efficiency between the ceramic nanoparticles and the polymer matrix [75, 84]. MWCNTs are dispersed in this nanocomposites for stress reinforcing and conducting functional agents between BT particles and the PVDF polymer [87, 88]. Although MWCNTs are still hydrophobic, active mechanical stress reinforcing between BT and PVDF will be significantly caused when applying external stress [71, 87]. These agents can efficiently load external stress onto BT particles through the PVDF matrix and the piezoelectric charges generated by BT particles are conducted through MWCNTs [86].

Scanning Electron Microscopy (SEM) Analysis

The morphology and crystalline structure of the materials are analyzed by scanning electron microscopy (SEM, TM-1000, Hitachi) and X-ray diffraction (XRD, D8 Discover diffractometer, Bruker). SEM images and spectra in Figure 4.1(d) and (e) demonstrate commercially purchased pure BT nanoparticles and MWCNTs. Figure 4.1(f) and (g) indicate the well distributed MWCNTs and agglomeration of BT nanoparticles are observed to increase as its percentage increases in the PVDF matrix as shown in details in Figure 4.3.

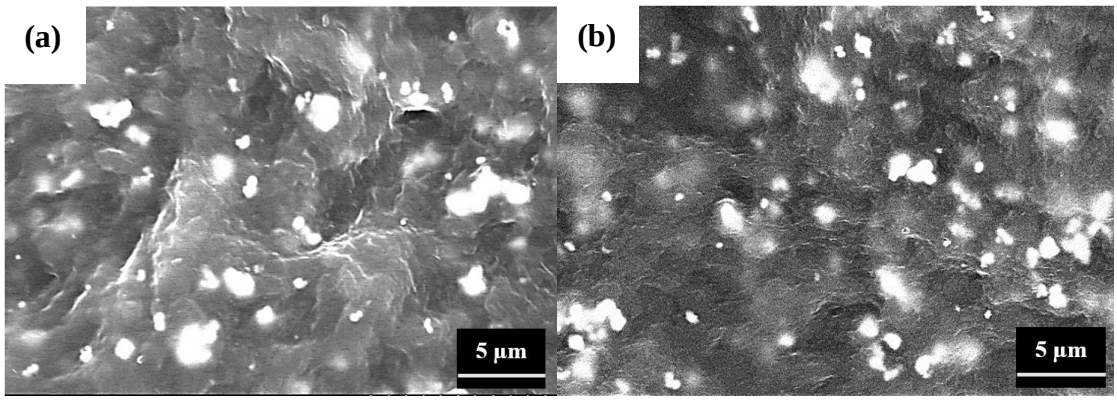

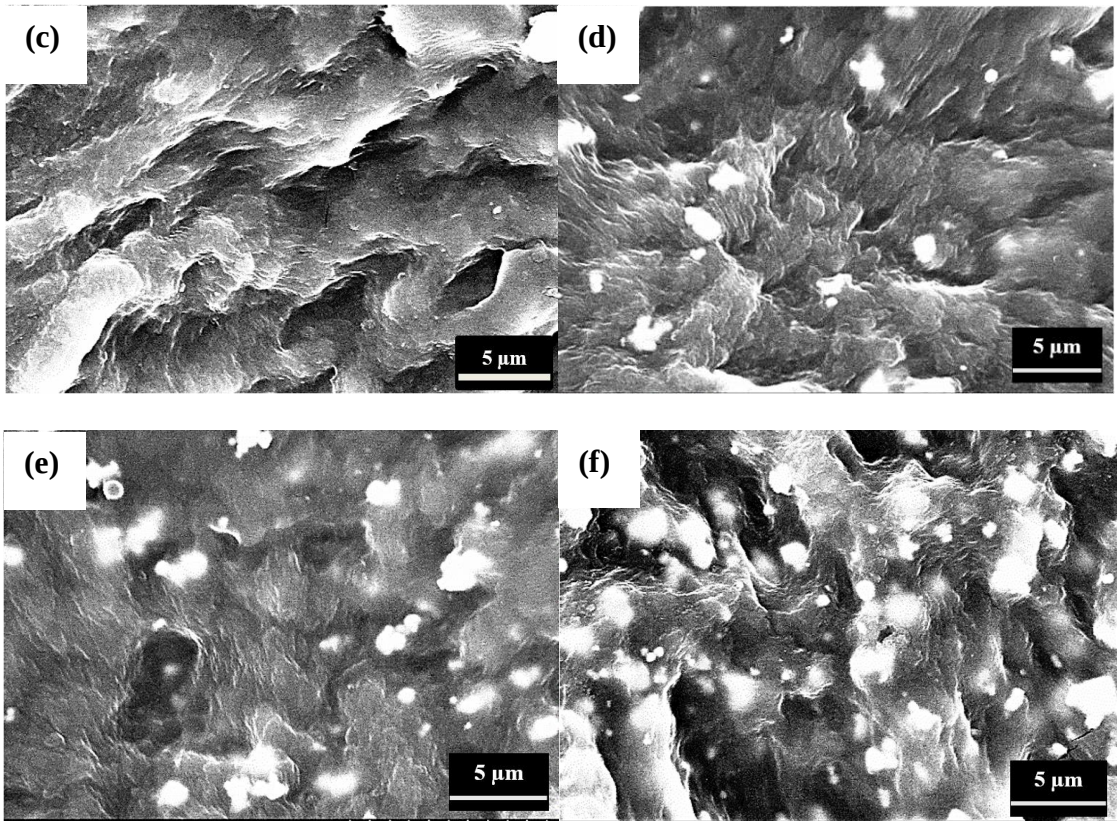

Figure 4.3: SEM images of (a) 12wt.%-BT/PVDF, (b) 0.1wt.%-MWCNTs/12wt.%-BT/PVDF, (c) 0.4wt.%-MWCNT/PVDF, (d) 0.4wt.%-MWCNT/6wt.%-BT/PVDF, (e) 0.4wt.%-MWCNT/12wt.%-BT/PVDF, (f) 0.4wt.%-MWCNT/18wt.%-BT/PVDF.

Piezoelectric Property Analysis

For piezoelectric property analysis, piezoelectric output voltage and current in a fatigue load frame (Bose ElectroForce-BioDynamic, TA Instruments), are measured by Voltmeter (InstruNet i-400), and Pico ammeter (Keithley 6485) as shown in Figure 4.4(a)-ii [62, 74]. Sample can be fabricated with large area, but due to the geometry of the fatigue grip, nanocomposites samples were printed with dimensions of 6×35×0.55mm as shown in Figure 4.4(a)-i. To quantify the piezoelectric property of the printed film, samples are prepared with silver conductive paint electrodes on both surfaces. The electrodes are then attached with copper (Cu) tape to allow a proper connection to the Pico ammeter as shown in Figure 4.4(a)-ii. Cyclic force is applied on the printed nanocomposites to measure periodic output current and voltage; the fatigue load frame generated 30 cyclic loads on the sample at 0.5 - 4Hz while the Pico ammeter measured the current

output [74]. To prevent noise and artifacts from the fatigue machine during measurement, the two grips handling the film are covered with electrical insulating tape.

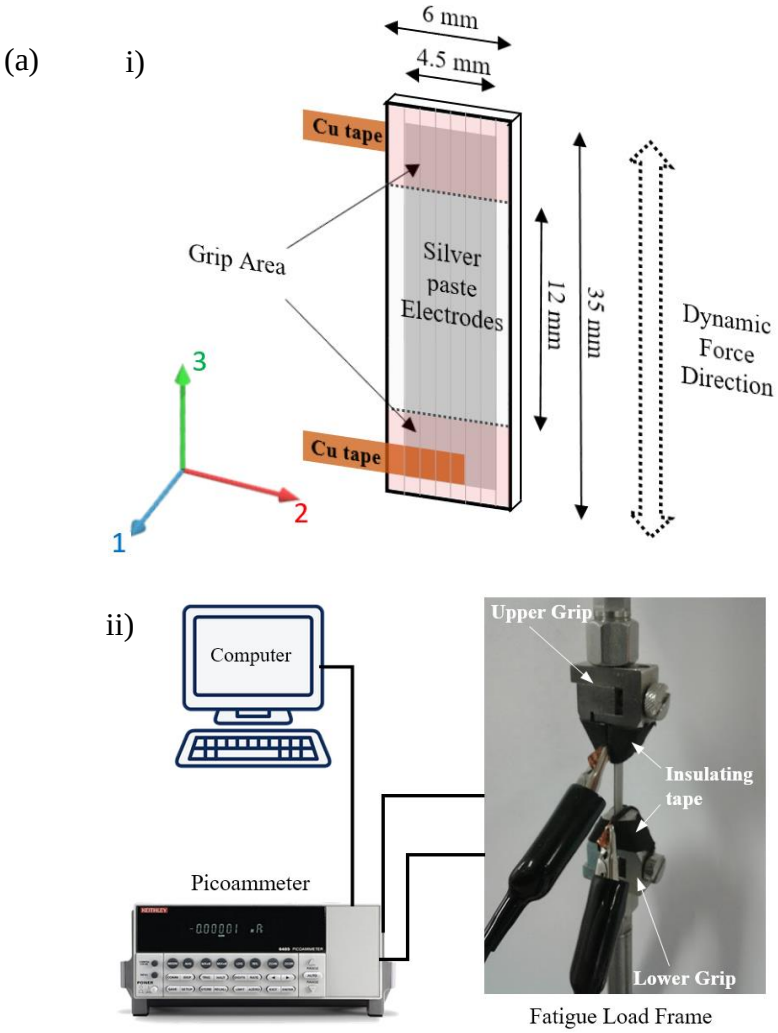

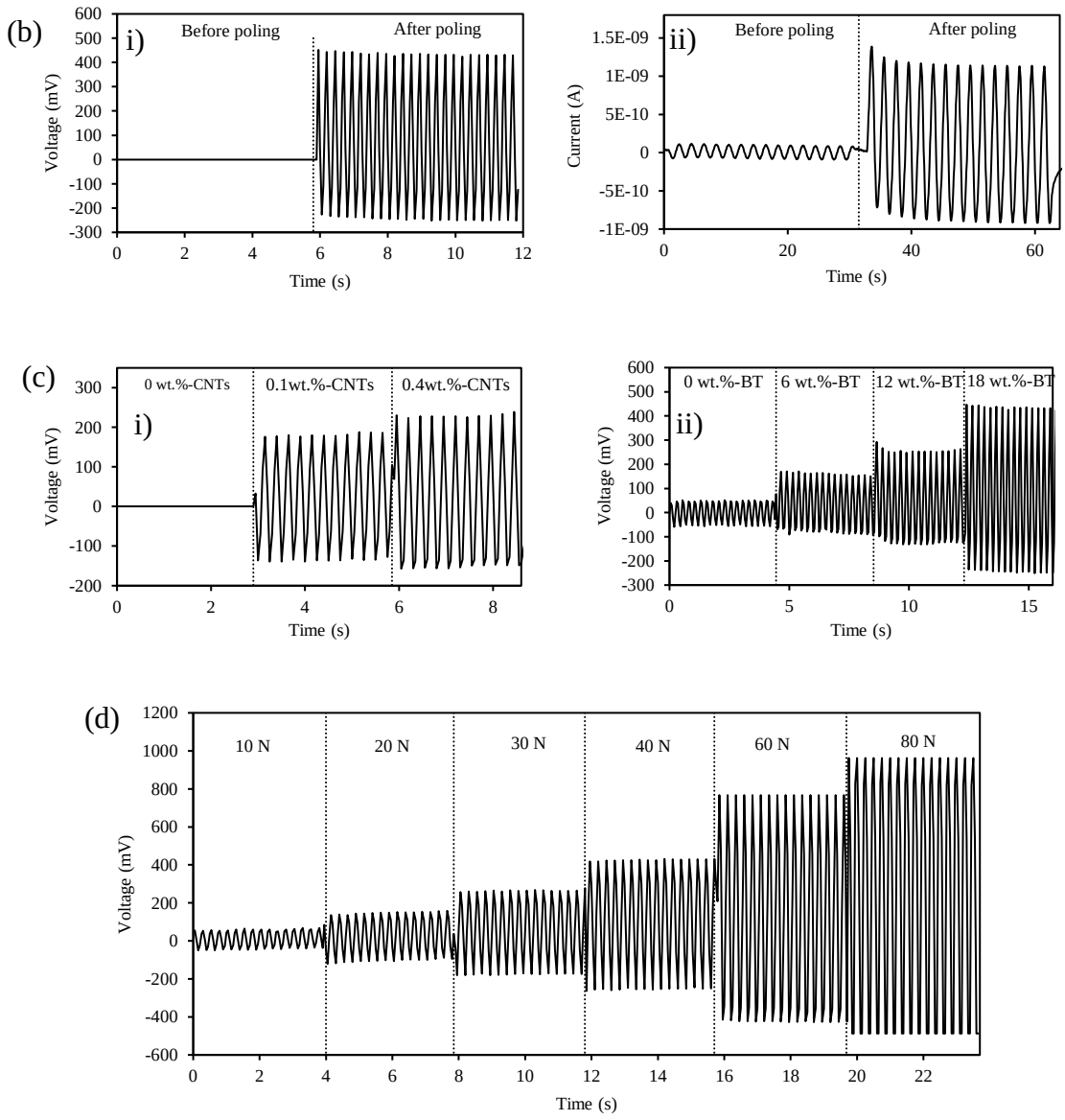

Figure 4.4: (a) schematic illustration of i) sample design and ii) experimental setup for piezoelectric output measurement, (b) the measured i) voltage and ii) current output results generated by 0.4wt.%-MWCNT/18wt.%-BT/PVDF under 40 N before and after electric poling, (c) voltage output results generated by i) various MWCNTs content of 12wt.%-BT/PVDF and ii) various BT particle contents of 0.4wt.%-MWCNT/PVDF under 40 N, and (d) voltage output results generated by 0.4wt.%-MWCNT/18wt.%-BT/PVDF under various forces (10, 20, 30, 40, 60, and 80 N).

Electric poling is applied under 3MV/m for 15 hours to the printed nanocomposite films after 3D printing fabrication. Note that three samples for each nanocomposite are tested for FTIR

analysis and output electricity. Figure 4.4(b)-i and ii show output voltage and current produced by the printed nanocomposites film before and after the electric poling process. Amplitude of voltage outputs generated from the nanocomposite films before and after poling treatment increases from ±0 mV to ±340 mV and current outputs from ±0.084 nA to ±0.94 nA. BT nanoparticles dispersed in matrix should be polarized through post-poling process. This result indicates that electric poling has activated piezoelectricity of the BT particles and that the BT particles and MWCNTs are mechanically and electrically interacting with each other. Charges generated from BT particles and PVDF due to the MWCNTs interaction can be efficiently transferred to external electrodes through conductive channel of MWCNTS. Figure 4.4(c)-i and c-ii indicate results of voltage outputs produced by various MWCNTs and BT nanoparticles percentages. In Figure 4.4(c)-i, 12wt.%-BT/PVDF nanocomposites film is characterized without MWCNTs to study the role of MWCNTs within the printed nanocomposites. No reliable output signal is observed. However, with an increase in MWCNT content the output voltages increased by ±192 mV under 0.4wt.%-MWCNTs which is the maximum percentage over which electrical breakdown occurs during electrical poling. For electrical poling process, the least amount of coercive electric field for BT particles about 0.5 – 1.6 MV/m is required [17, 84]. However, the breakdown strength lowers down as MWCNTs increase and 0.4wt.%-MWCNTs content is limitation before experiencing breakdown. This increase of the voltage amplitude indicates that MWCNTs play a significant role as a stress reinforcing agent within the nanocomposites. In Figure 4.4(c)-ii, when there is 0.4wt.%-MWCNTs in the PVDF matrix and no BT nanoparticle content, the piezoelectric output voltage generated is ±49 mV. This is because PVDF β-phase was formed on high specific surface areas of MWCNTs [86]. As BT particle content increases, the voltage output increases up to ±340 mV at 18wt.%-BT which is the maximum percentage of BT content that can be extruded in the FDM 3D printer nozzle. With 0.4wt.%-MWCNTs/18wt.%-BT/PVDF film (which showed the highest generated output voltage), output voltages were measured under various external forces applied by fatigue load frame. Figure 4.4(d) shows that a higher amplitude of output voltages was produced at higher external forces, increased by ±725 mV under 80 N.

Fourier transform infrared spectroscopy (FTIR, Agilent Technologies Cary 630 ATR-IR) analyses are performed in the 600-1600 cm^{-1} wavenumber range at room temperature to characterize the degree of crystallinity of α- and β-phases of the PVDF before and after the electric poling process [22, 26, 32]. IR absorption bands at 766 and 840 cm^{-1} which are respectively characteristic of α- and β-phases are observed for analysis of the phase transformation. Based on the results of IR absorption bands (see Figure S3), the β-phase contents of each printed nanocomposite film are calculated as described as following:

(1) FTIR spectra before electric poling process

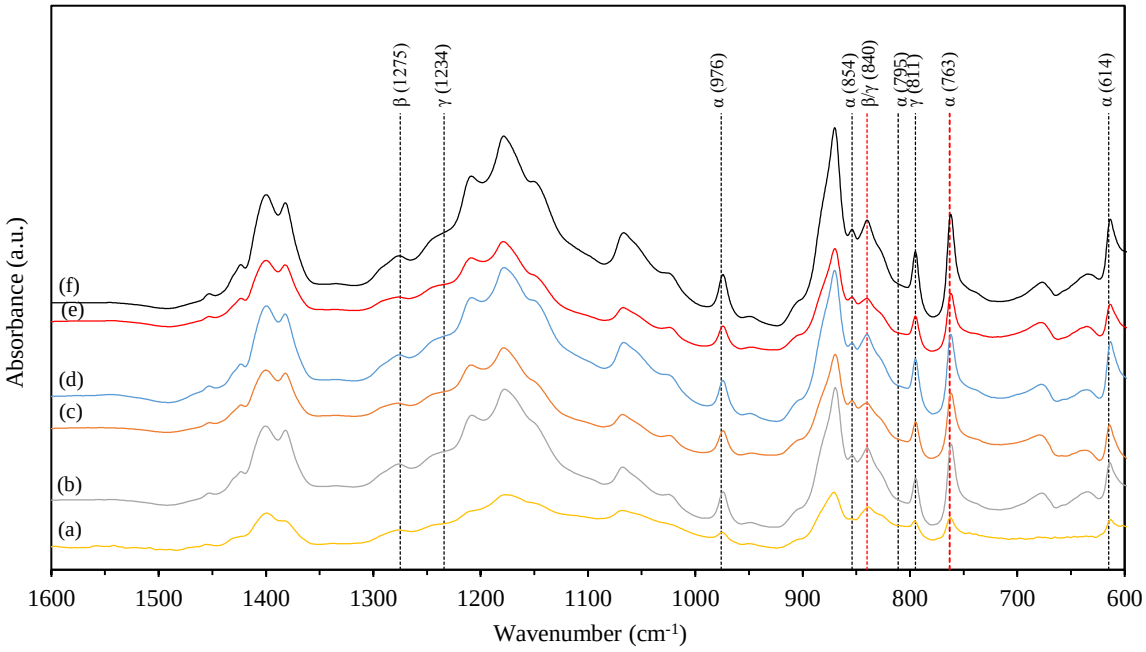

(2) FTIR spectra after electric poling process

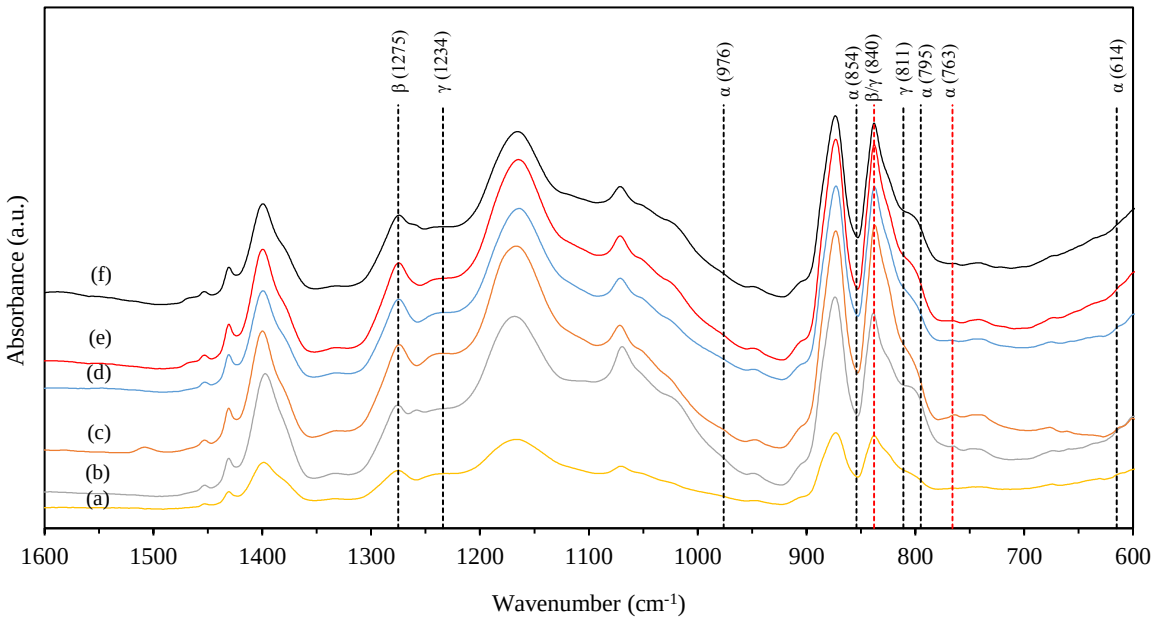

Figure 4.5: FTIR spectra of the printed nanocomposites (1) before and (2) after electric poling: (a) 12wt.%-BT/PVDF, (b) 0.1wt.%-MWCNT/12wt.%-BT/PVDF, (c) 0.4wt.%-MWCNT /PVDF, (d) 0.4wt.%-MWCNT/6wt.%-BT/PVDF, (e) 0.4wt.%-MWCNT/12wt.%-BT/PVDF, (f) 0.4wt.%-MWCNT/18wt.%-BT/PVDF.

The β-phase contents of each sample are calculated, specifically, at the absorption bands of 764 and 840 cm^{-1} which are characteristics of α- and β-phases respectively. Assuming that the infrared absorption follows the Lambert-Beer law, A_α and A_β absorbance at 764 and 840 cm^{-1}, respectively, are given by equation (1) below [56]:

$$A_{\alpha,\beta} = Log\left(\frac{I^{0}_{\alpha,\beta}}{I_{\alpha,\beta}}\right) = C \cdot K_{\alpha,\beta} \cdot X_{\alpha,\beta} \cdot L \qquad (1)$$

where the subscripts α and β are defined as the crystalline phases, I^0 and I are the incident and transmitted intensities of the radiation, respectively. The L is defined as a sample thickness, C is an average monomer concentration, K is the absorption coefficient at the respective wave number, and X is the degree of crystallinity of each phase [56]. For a system

containing α- and β-phases, the relative fraction of the β-phase, $F(\beta)$, can be calculated using equation (2) [56]:

$$F(\beta) = \frac{X_\beta}{X_\alpha + X_\beta} = \frac{A_\beta}{(K_\beta/K_\alpha)A_\alpha + A_\beta} = \frac{A_\beta}{1.26A_\alpha + A_\beta} \quad (2)$$

where K_α (6.1×10^4 cm^2/mol) and K_β (7.7×10^4 cm^2/mol) are the absorption coefficients at the respective wave number.

In Figure 4.6(a), β-phase contents significantly increased after electric poling and as MWCNTs increased by 70.3% of β-phase at 0.4wt.%-MWCNTs/12wt.%-BT/PVDF. It is certain that MWCNTs led to a high degree of conversion from α-phase to β-phase. Under the same amount of MWCNTs (0.4wt.%), the analysis of β-phase contents showed an increasing trend as BT particles were increased.

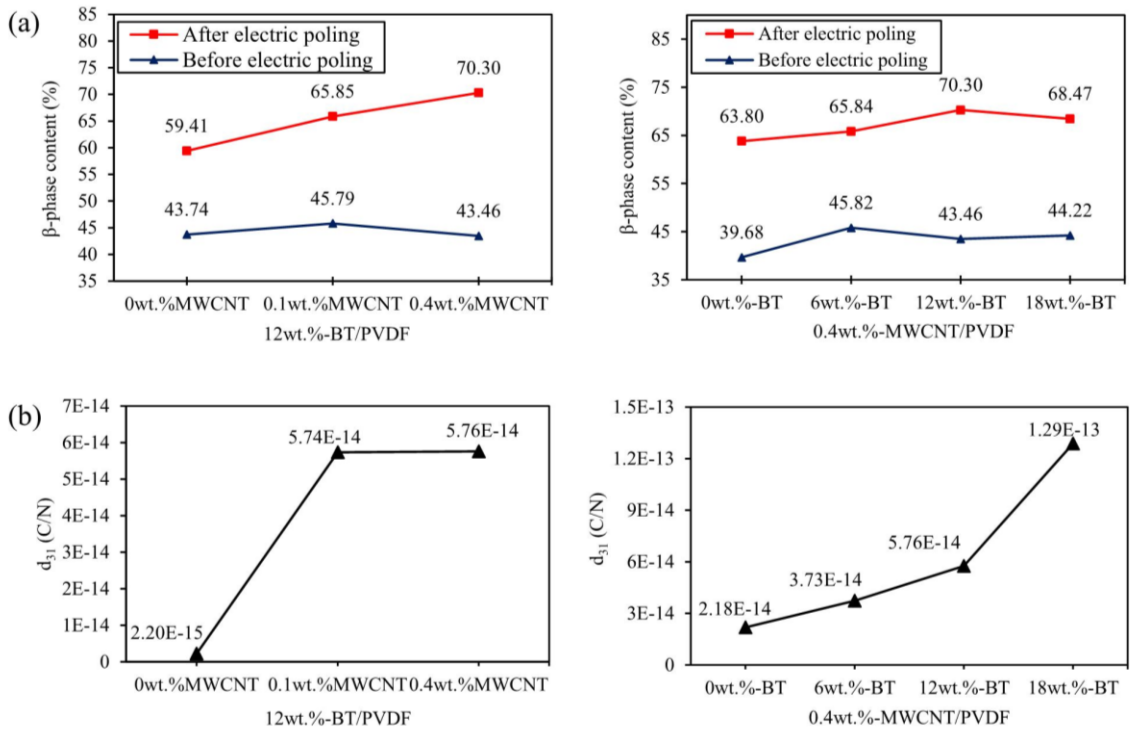

Figure 4.6: (a) β-phase contents of the printed nanocomposites with various MWCNTs and BT particle contents before and after electric poling process and (b) piezoelectric coefficients (d_{31}) of the printed nanocomposites with various MWCNTs and BT particles contents.

Based on the voltage output results of Figure 4.4(c)-i and (c)-ii, piezoelectric coefficients (d_{31}) of each printed nanocomposite film are calculated with various compositions using measured relative permittivity as shown in Table 4.1.

Table 4.1: Dielectric Properties of the Printed MWCNT/BT/PVDF Nanocomposites Films

Composition	Relative Permittivity (ε_r) at 1 kHz
12wt.%-BT/PVDF	16.9
0.1wt.%-MWCNT/12wt.%-BT/PVDF	31.2
0.4wt.%-MWCNT/PVDF	30.5
0.4wt.%-MWCNT/6wt.%-BT/PVDF	31.7
0.4wt.%-MWCNT/12wt.%-BT/PVDF	25.0
0.4wt.%-MWCNT/18wt.%-BT/PVDF	36.5

To calculate the piezoelectric coefficient (d_{31}) by using the equation (3) below:

$$D_i = d_{ij}\sigma_j \tag{3}$$

where D_i is the electrical displacement, d_{ij} is the piezoelectric coefficient, and σ_j is the applied stress. In this case, subscripts i and j are defined as 3 (applying force direction) and 1 (poling direction) respectively as shown in Figure 4.4(a)-i. Therefore, the equation can then be expressed as $D_3 = d_{31}\sigma_1$. Considering the areas of the electrode and cross-section of the sample, equation (4) can then be expressed as,

$$\frac{Q}{A_{elect}} = d_{31}\frac{\nu F}{A_{cross}} \tag{4}$$

where Q is charge, A_{elect} and A_{cross} are areas of electrode and cross-section respectively, ν is Poisson's ratio which is 0.34 [58], and F is an applied force. The Q is equal to CV which are capacitance and voltage, respectively. C can be expressed to $\varepsilon_r\varepsilon_0 A_{elect}/d$. Then, the piezoelectric coefficient can be expressed as,

$$d_{31} = \frac{\varepsilon_r\varepsilon_0 A_{cross} V}{vdF} \tag{5}$$

where ε_r is relative permittivity of the printed nanocomposites film, ε_0 is 8.854×10^{-12} C/Vm, and d is its thickness. A_{cross} are 2.47 mm^2. Then d_{31}^{max} and d_{31}^{min} are determined at maximum and minimum of voltages and forces as equation (6) describes.

$$d_{31}^{max} = \frac{\varepsilon_r\varepsilon_0 A_{cross} V_{max}}{vdF_{max}}, \qquad d_{31}^{min} = \frac{\varepsilon_r\varepsilon_0 A_{cross} V_{min}}{vdF_{min}} \tag{6}$$

F_{max} and F_{min} are 5 N and 45 N, respectively. Each attained d_{31} is divided by 2 for $\pm\ d_{31}$ as shown in following equation (7)

$$\pm\ d_{31} = \frac{d_{31}^{max} - d_{31}^{min}}{2} \tag{7}$$

In Figure 4.6(b), d_{31} has significantly increased from 0.002 to 0.058 pC/N when MWCNTs' content increases under 12wt.%-BT. This indicates that the addition of MWCNTs enhances performance of stress reinforcing between BT particles and the matrix. Under the same amount of MWCNTs (0.4wt.%), d_{31} is tested with various percentage of BT particles. The result indicates that the d_{31} increases from 0.022 (0wt.%-BT) to 0.13 pC/N (18wt.%-BT) as BT particles increase, a 492% increase. The measured d_{31} of the nanocomposites is comparable with pure BT ceramics or composites (79 ~ 185 pC/N) [89, 90], thus overcomes the low direct piezoelectric coupling associated with piezoelectric polymer composites.

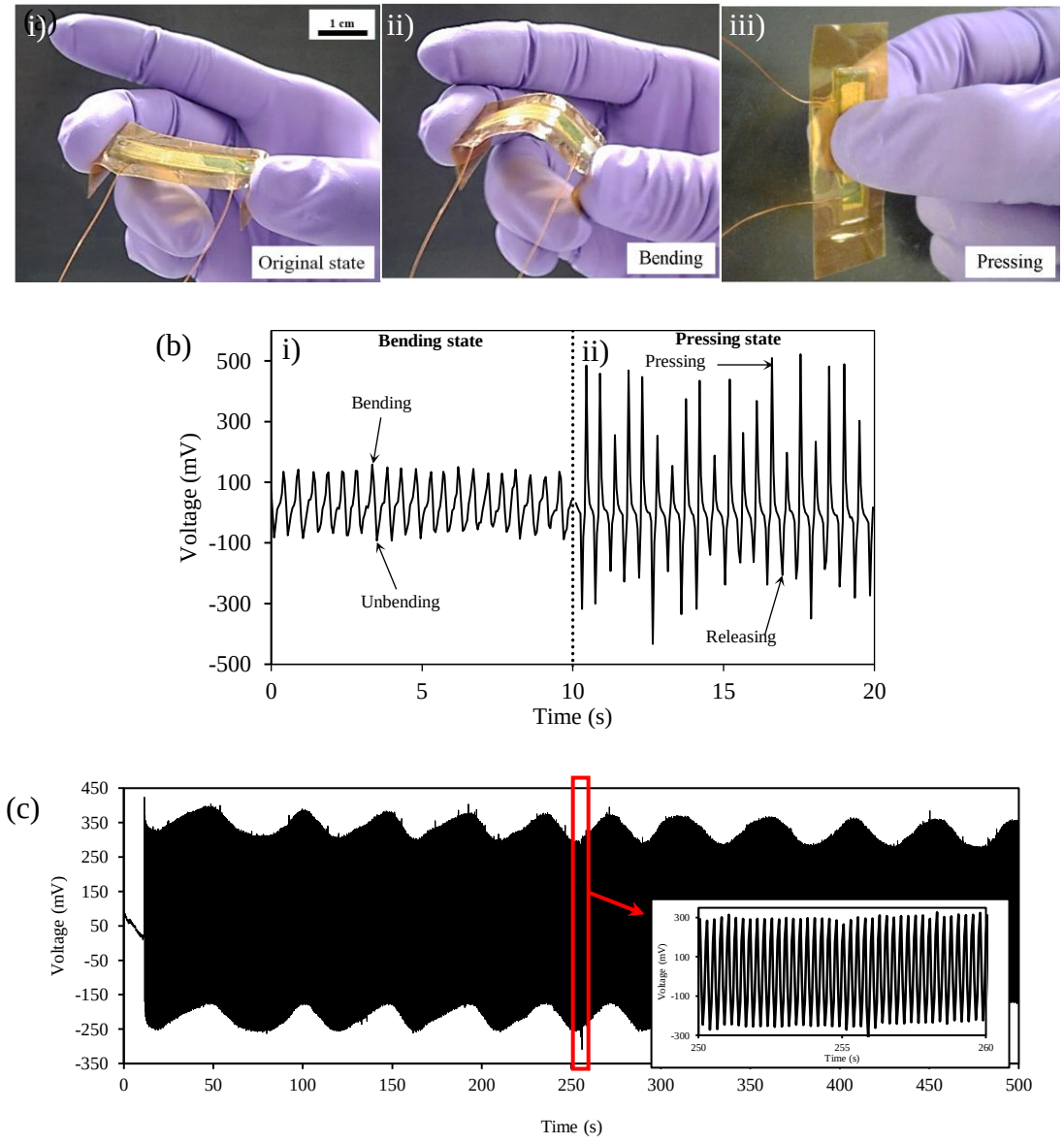

Figure 4.7: (a) Optical images of the printed nanocomposite sensor device in i) original, ii) bending, and iii) pressing states, (b) the measured voltage output signals of 0.4wt.%-MWCNT/18wt.%-BT/PVDF film generated by i) bending and ii) pressing motions by human fingers, (c) the durability test result of 0.4wt.%-MWCNT/18wt.%-BT/PVDF film under 2,000 periodic cycles (4 Hz) using fatigue load frame.

To further demonstrate the piezoelectric sensor application, the feasibility of use printed piezoelectric nanocomposites for pressure sensor application was demonstrated. The output

voltage signal is measured when bending (90˚) and pressing (40-50 N) by human fingers shown in Figure 4.7. Figure 4.7(a)-i shows the printed nanocomposites film and hands covered respectively by Kapton film and gloves, to exclude external electrostatic charges. Two Cu wires attached on both silver electrodes are extended to connect to the data acquisition machine. In Figure 4.7(a)-ii, upon bending the sample, the output voltage was measured to be ±120 mV. Upon pressing in the middle of the sample, the amplitude of the output voltage increased to ±435 mV at most. In Figure 4.7(c), durability test is implemented at 4 Hz frequency for 2000 cycles to confirm the mechanical stability of the printed nanocomposite film. The amplitude of voltage output remains constant after 2000 cycles. The printed film also shows the same piezoelectric stability after 3 days. The bottom inset of Figure 4.7(c) shows the magnified voltage signal from 250 to 260 sec.

4.1.4 Summary

MWCNT/BT/PVDF nanocomposite film is printed by FDM 3D printing technique for use in sensor applications. The FDM 3D printing technique can simplify fabrication process of piezoelectric film with lower cost and greater design flexibility compared to traditional fabrication processes. Various BT and MWCNTs percent nanocomposite films were printed, characterized, and tested by SEM, XRD, FTIR, fatigue load frame, and human finger to ensure the piezoelectric performance. It is demonstrated that MWCNTs plays important roles of transforming PVDF α- to β-phase and enhancing the efficiency of mechanical to electrical conversion between BT and PVDF interfaces. The increasing MWCNTs' percent in the system results in an increase in electrical output which, indicates that the increased surface areas of MWCNTs interacts well with BT nanoparticles, therefore providing a stress reinforcing effect between the BT and PVDF. In addition, increasing the BT particles' percent in the system showed an increase in electrical output by ±340 mV under 40 N and ±725 mV under 80 N at 18wt.%. Piezoelectric coefficient (d_{31}) is calculated and the results show good agreement with electrical output generated by the printed nanocomposite films. The highest d_{31} is 0.13 pC/N at 0.4wt.%-MWCNTs/18wt.%-BT/PVDF, comparable to pure BT ceramic. By bending and pressing with fingers, the printed film generates

about ±120 mV and ±435 mV, respectively. The mechanical stability of the printed nanocomposite film is proved by durability test for 2000 cycles without any amplitude changes. These results demonstrate feasibility in its commercial application. These compounds and the FDM 3D printing technique are expected to broaden the use of additive manufacturing to print piezoelectric nanocomposite device for sensor applications.

4.2 Enhanced Dielectric Properties of Three Phase Dielectric MWCNTs/$BaTiO_3$/PVDF Nanocomposites for Energy Storage using Fused Deposition Modeling 3D Printing

This section studied the effect of fused deposition modeling (FDM) 3D printing on three phase dielectric nanocomposites using poly(vinylidene) fluoride (PVDF), $BaTiO_3$ (BT), and multiwall carbon nanotubes (CNTs). PVDF polymer and BT ceramics are piezo-, pyro- and di-electric materials extensively used for sensor and energy storage/harvesting applications due to their unique characteristic of dipole polarization. To increase dielectric property, CNTs have been recently utilized for uniform dispersion of BT nanoparticles, ultrahigh polarization density, and local micro-capacitor among matrix. It was proved that 3D printing process provides homogeneous dispersion of nanoparticles, alleviating agglomeration of nanoparticles and reducing micro-crack/voids in matrix which can potentially enhance their dielectric property than traditional methods. In this research, these three-phase nanocomposites are fabricated through FDM 3D printing process and characterized for dielectric property. Increasing both BT and CNT nanoparticles improves dielectric properties, while CNTs have a percolation threshold near 1.7wt.%. The most desirable combination of dielectric constant and loss properties (118 and 0.11 at 1 kHz) is achieved with nanocomposites containing 1.7wt.%-CNT/45wt.%-BT/PVDF. These results provide not only a technique to 3D print dielectric nanocomposites with improved dielectric property but also large-scale electronic device manufacturing possibility with freedom of design, low cost, and faster process.

4.2.1 Introduction

The fabrication of materials with a high dielectric energy density is highly desirable in the energy storage applications such as capacitors, field effect transistors (FETs), and other embedded electronics [80-82, 91-93]. For dielectric capacitors, a material with a high dielectric energy density allows for increased energy storage, which is desirable in fields as disparate as computer electronics and signal processing to developing military technologies [91] such as railguns. Dielectric materials are electrical insulators that become polarized to store energy when exposed to an external electric field, and some of this energy can then be recovered when the external field relaxes. Furthermore, 3D printability is another highly desirable property as it improves both ease

and flexibility of manufacturing and allows for improved cost-effectiveness and scaling of production [94].

Polymers are a good candidate for their general ease of manufacture, physical flexibility, and compatibility with fused deposition modeling (FDM) 3D printing [74, 95-97]. Polyvinylidene fluoride (PVDF) has a notably higher dielectric constant of near 10 [98] compared to the typical 2-5 of other polymers [99, 100], making it a common choice for study in dielectric and piezoelectric materials [91, 101, 102]. Another advantage of polymers is the capability to tune their electrical or mechanical properties through the introduction of fillers into the polymer matrix [91]. Ferroelectric ceramics are one popular choice for modifying the electrical properties of polymers, among them, barium titanate (BT) has a particularly high dielectric strength of 1200-5000 [91, 103]. The surface area of filler particles can have an impact in determining the effective permittivity: nano-scale particles with a large surface area to volume ratio, can improve the dielectric strength of the resulting nanocomposite [91]. However, at high volume fractions, ceramic agglomerates in the polymer matrix thus reduces the effective surface area to volume fraction ratio. Agglomeration lowers the overall dielectric strength [104] and leads to voids and micro-cracks in its structure that can reduce the strength and flexibility of the resulting material. To alleviate the issue, fillers can act as surface modifying agents for ceramic particles to reduce the size and impact of these voids and micro-cracks thus improve the dielectric strength [104]. Furthermore, electrically conductive fillers can improve the dielectric strength up to percolation threshold [104, 105]. According to percolation theory, when a conductive filler is added to an insulative dielectric material, the dielectric permittivity follows the formula [91, 105]:

$$\varepsilon_{\text{eff}} \propto \varepsilon_{\text{base}} \left| f_{\text{p}} - f_{\text{cond}} \right|^{-s}, \text{where } f_{\text{cond}} < f_{\text{p}} \quad (1)$$

where ε_{eff} is the resulting dielectric constant, $\varepsilon_{\text{base}}$ is the dielectric constant of the base composite, f_{p} is the percolation threshold volume fraction of the composite, f_{cond} is the volume fraction of the conductive filler, and s is the critical exponent of the composite, with a value in the range of 0.8-1.0. However, as this threshold is approached, the smaller insulative spaces between conductive filler particles can lead to an overall lower electric breakdown strength.

Multi-walled carbon nanotubes (CNTs) are conductive and previous work has been found it can act as a surface-modifying agent to BT in a polymer matrix [104], allowing it to simultaneously take advantage of the effects of percolation theory and surface modification. However, CNTs also tend to agglomerate themselves due to their chemical structure, small scale, and large aspect ratio [104, 105], so some care must be taken during fabrication to optimize dispersion.

In this article, we explore the impact adding BT and CNT fillers on the dielectric properties of FDM 3D printed PVDF nanocomposites. The dielectric permittivity of polymer composites depends on the volume fraction of the BT ceramic filler and CNT conductive filler up to the percolation threshold, as well as the quality of uniform dispersion of the fillers throughout the PVDF polymer matrix.

4.2.2 Experimental

Materials, Filament Fabrication, and 3D Printing

To fabricate continuous CNT/BT/PVDF nanocomposite filaments for 3D printing, commercial PVDF powder (MW~534,000; Sigma-Aldrich), BT powder (700 nm; Inframat®), multi-wall carbon nanotubes (CNTs) powder (Diameter: 8-15 nm, length: 10-50 μm, Cheaptubes®), and N-Dimethylformamide solvent (DMF, OmniSolv®) were used. The 700 nm BT nanoparticles were selected because of its highest dielectric constant at 1 kHz in higher loading system compared to other BT nanoparticle sizes [106]. The BT and CNTs were mixed in DMF solvent (1:10 weight ratio of PVDF powder) and sonicated for 30 min for uniform dispersion. PVDF powder was added to the prepared solution which was then placed in a water bath at 80°C until the PVDF powder fully dissolves. BT build up at the bottom of solution was addressed by ultra-sonication (Branson Sonifier 450) for 15 min. DMF solvent was then evaporated by dispersing the nanocomposite solution onto a glass substrate and heated to a temperature of 80 °C for 12 hrs. The schematic diagram of solvent casting procedure is shown in Figure 4.8(a). The procedure yields a thin sheet of nanocomposite and this casted nanocomposite sheet was sliced down to be easily extruded by a filament extruder machine (Filabot®). The diameter of the extruded filament and extruding temperature were about 2.9±0.05 mm and 205 °C respectively. The nanocomposite filament as

shown in Figure 4.8(b-i) was used to 3D print a thick film by a fused deposition modeling 3D printer (Lulzbot® Taz 5, see Figure 4.8(b-ii)) also known as extrusion-based process, which deposits materials in a continuous flowing layer by layer process to build a 3D structure [4] for dielectric energy storage application. These filament extrusion and 3D printing processes have been demonstrated to improve uniform dispersion of nanoparticles in the matrix, therefore improving dielectric properties [74].

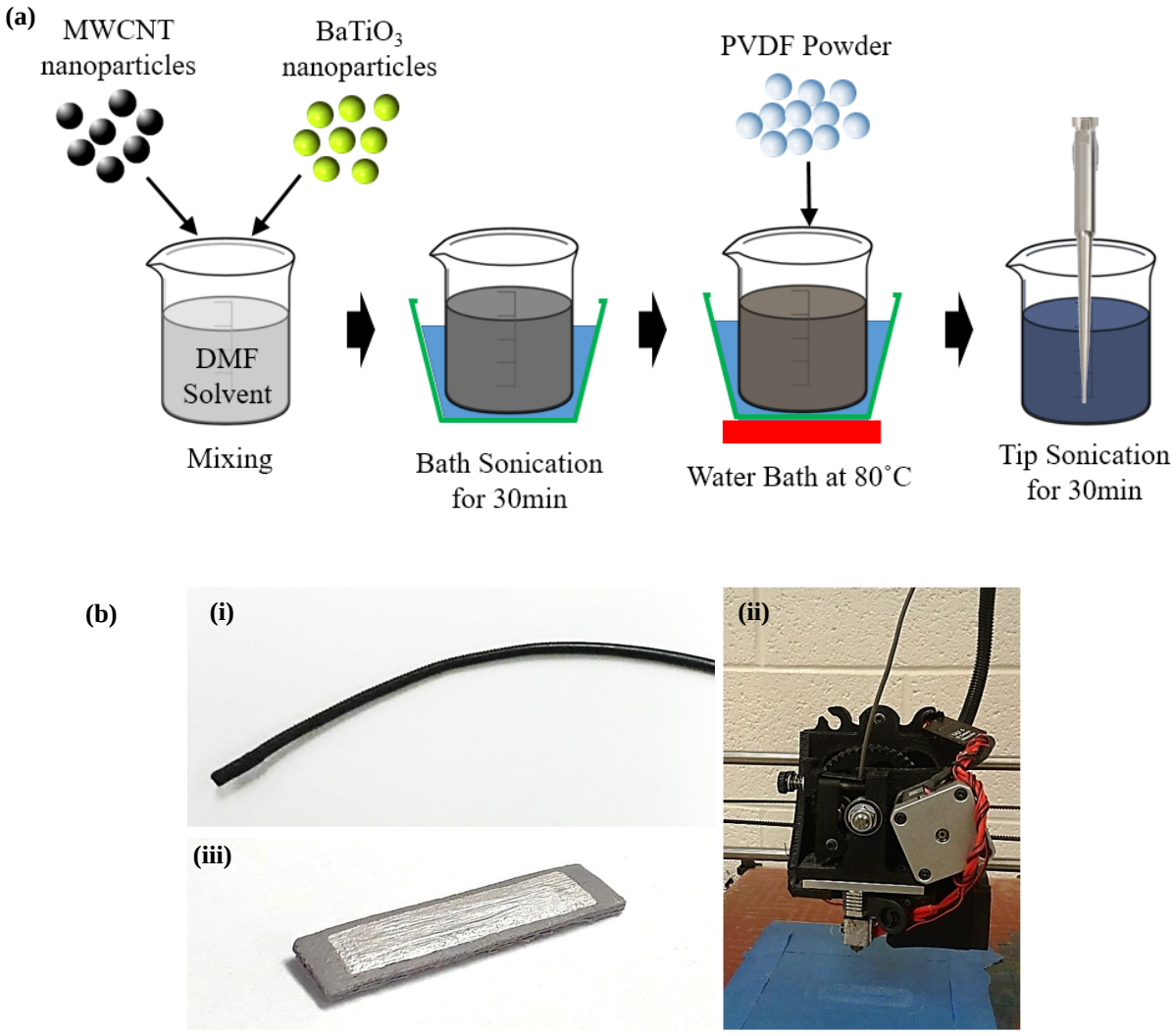

Figure 4.8: (a) Schematic illustration for solvent casting procedure and (b) fabricated CNT/BT/PVDF nanocomposite filament (i), FDM 3D printer single extrusion tool head (ii), and one-way extruded film with silver paint electrodes for dielectric and breakdown analyses (iii) *[97]*.

Fabricated nanocomposite filament was then inserted into an FDM 3D printer. The FDM 3D printer was used to fabricate thick films of 1.7±0.05 mm in thickness (5 layers) with dimensions of 30×11 mm at a nozzle temperature of 220 ˚C, printing speed was set at 5 mm/s, and heating bed temperature at 120 ˚C. It is important to note that nanocomposites may burn and clog the nozzle when printing at such high temperatures. The issue is addressed by limiting the amount of time the filament remains within the heated nozzle. The nanocomposite films were printed using a one-way extrusion pattern rather than the conventional perimeter then zigzag pattern to achieve a more consistent film surface quality at only a single layer [107].

Characterizations

The morphology of the 3D printed nanocomposites samples was observed using a scanning electron microscopy (SEM, TM-1000 Hitachi) [108]. For dielectric characterization, silver paint electrodes were applied to the top and bottom surfaces of the one-way extruded nanocomposite films and dried in room temperature for 2 hours as shown in Figure 4.8(b-iii). The dielectric constant and dielectric loss for each of the 3D printed nanocomposites were analyzed using an LCR meter (1920 Precision, IED lab). Breakdown strength testing was performed in a bath filled with silicon oil (Sigma-Aldrich): the films with silver electrodes were connected to a high voltage power supply and tested by raising the voltage at approximately 100 V/s while submerged in the bath [109].

4.2.3 Results and discussion

Dielectric Properties of 3D Printed Nanocomposites

The dielectric constant and dielectric loss of the 3D printed nanocomposites with respect to varying BT content and varying CNT content are investigated and shown in Figure 4.10. All of the dielectric permittivity results show gradual decrease with increase of frequency because of dipole mobility reduction where the dipoles are not sufficiently mobile to displace as the frequency of the applied electric field exceeds the relaxation frequency [110]. Most of dielectric loss value starts from high at relatively low frequency (interfacial polarization), decrease at increasing

frequency but increase at high frequency (dipolar polarization) due to the energy conversion from electromagnetic to thermal energy. Figure 4.10(a) and (b) indicate that as BT content increases in the PVDF matrix the dielectric constant at 1 kHz gradually increases to 30.2 at 45wt.%-BT from 15.2 at solvent casted PVDF and sharply increase to 38.5 at 60wt.%-BT because more charges are accumulated by higher dielectric constant ceramic particles [104], then decreases slightly to 37.2 at 75wt.%-BT also as shown in Figure 4.10(a). Note that the dielectric constant (ε_r) is calculated from the following equation:

$$\varepsilon_r = Ct/\varepsilon_0 A \tag{1}$$

where *C* is capacitance, *t* is the distance between the two electrodes, ε_0 is the permittivity of free space (8.85×10^{-12} F/m), and *A* is the area of the electrodes. In addition, in Figure 4.12(a) it is observed the drastic reduction of the electrical conductivity at the same content. Note that the AC conductivity $(\sigma_{ac}, S/m)$ is calculated from the following equation [111]:

$$\sigma_{ac} = \varepsilon_r \varepsilon_0 \omega \ tan \ \delta \tag{2}$$

where ω is the angular frequency (i.e. $\omega = 2\pi f$), and $tan \ \delta$ is the loss tangent. These drastic changes of the dielectric constant/AC conductivity are referred to the percolation threshold in terms of BT nanoparticles. Beyond this point, leakage of charges caused by the direct connection between BT nanoparticles leads to a drop of the dielectric constant and a rise of AC conductivity. 3D printed PVDF film obtains higher dielectric constant (16.6) than the solvent casted PVDF (15.0) because extrusion processes of filament and 3D printing provide molecular alignment (i.e. β and δ-phases) and removal of micro-cracks and voids [74]. Figure 4.9 indicates voids and micro-cracks created in solvent casted PVDF and BT/PVDF nanocomposites films are removed after extrusion processes. Due to this reason, the dielectric constant achieved through 3D printing shows higher or comparable values compared with the reported results [112, 113].

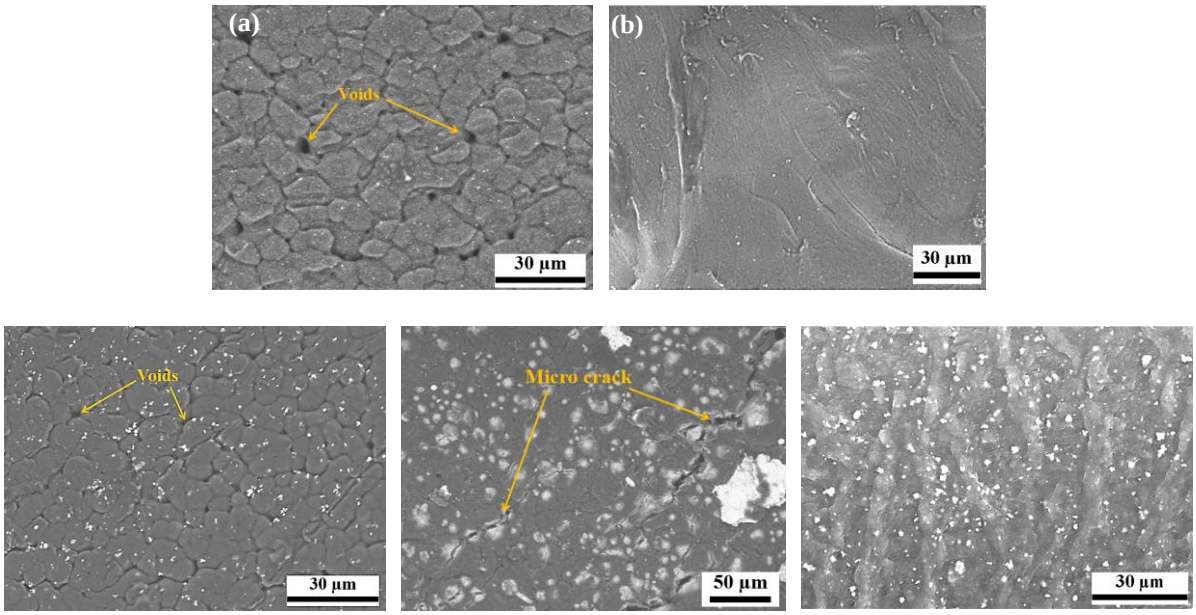

Figure 4.9: SEM image of (a) solvent casted and (b) 3D printed PVDF film respectively, (c) top and (d) bottom surfaces of solvent casted 12wt.%-BT/PVDF films respectively where voids and micro-cracks are observed in matrix, and (e) 3D printed 12wt.%-BT/PVDF films where void and micro-crack are removed through extrusion processes.

Dielectric loss increases as BT contents increase and shows high dielectric loss up to 0.27 at 1 kHz shown in Figure 4.10(b). This can be explained that high percentage of hard and brittle fillers tends to create micro-cracks internally or externally and responsible for large leakage current. In addition, the increase in dielectric loss may attribute to increasing conduction loss caused by their higher conductivity than the polymer matrix [101, 112, 114]. However, as dielectric loss exhibits decrease when it is closer to the percolation threshold [104], 60wt.%-BT shows relatively lower dielectric loss (0.07) and AC conductivity than other nanocomposites because more charges are accumulated in interfaces due to enhanced relative dielectric constant in the mixture matrix without any leakage current [104].

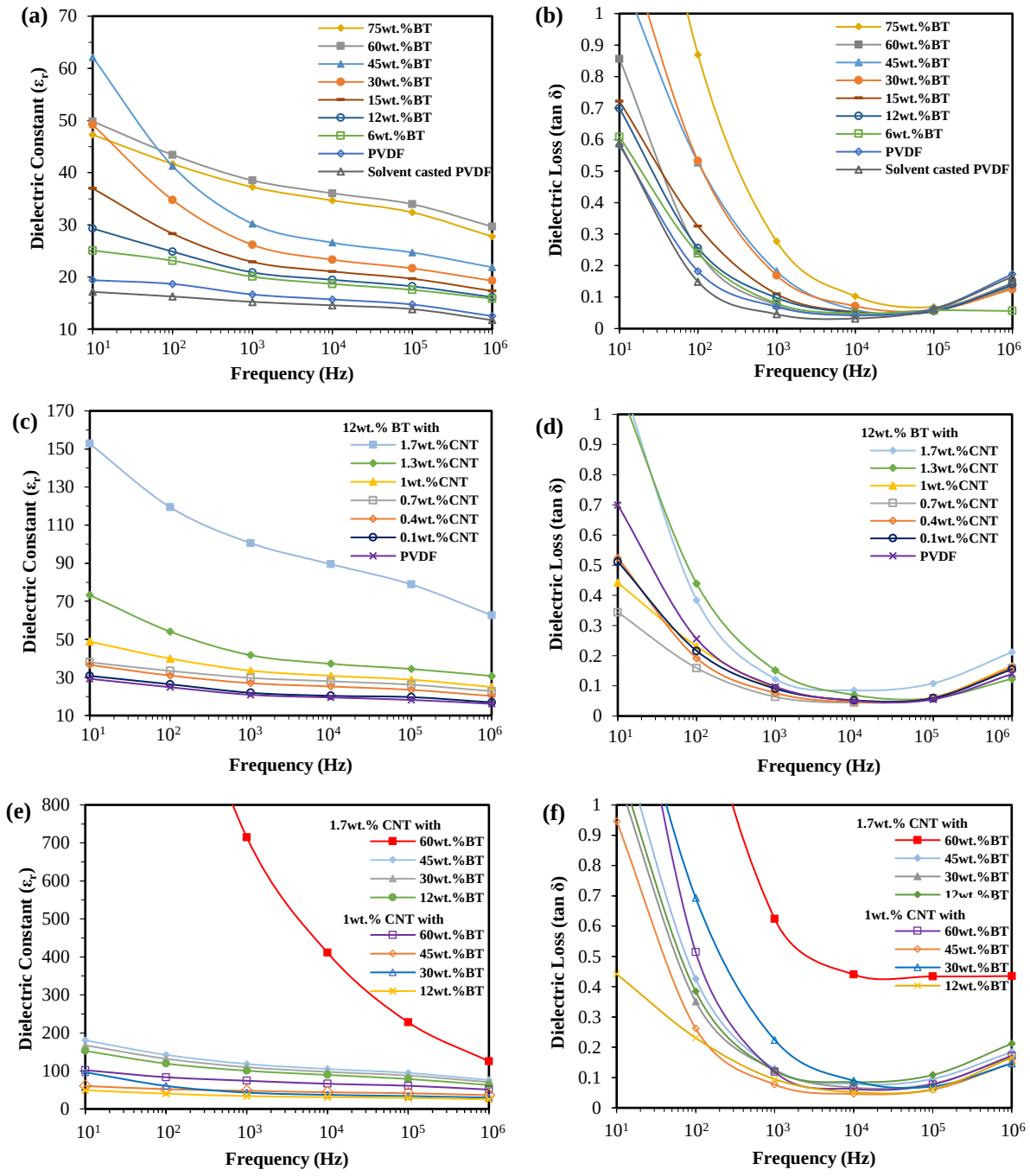

Figure 4.10: Dielectric constant (ε_r) and dielectric loss (tan δ) respectively as a function of frequency from 10^1 to 10^6 Hz of (a) and (b) PVDF with varying BT content, (c) and (d) 12wt.%-BT with varying CNT content, (e) and (f) 1wt.% and 1.7wt.%-CNT with varying BT contents.

Figure 4.10(c) and (d) indicate that the dielectric constant increases as the CNT content increases at 12wt.%-BT. After a gradual increase, there is a sudden increase of dielectric constant

from 41.7 at 1.3wt.%-CNT to 100.5 at 1.7wt.%-CNT (at 1 kHz) as also shown in Figure 4.11(b). This jump of dielectric constant is referred as the percolation threshold in terms of the CNT in this nanocomposite system. The theoretic percolation threshold easily calculated according to percolation theory equation (1) is found at $f_p \approx$ 0.865 vol.% which is around 1.7wt.%-CNT. Table 4.2 provides volume fraction for all 3D printed nanocomposites.

Table 4.2: Weight percent vs. volume percent of the 3D printed CNT/BT/PVDF nanocomposites

Weight percent	**Volume percent**
6 wt.%-BT/PVDF	1.852 vol.%-BT
12 wt.%-BT/PVDF	3.875 vol.%-BT
15 wt.%-BT/PVDF	4.959 vol.%-BT
30 wt.%-BT/PVDF	11.24 vol.%-BT
45 wt.%-BT/PVDF	19.47 vol.%-BT
60 wt.%-BT/PVDF	30.72 vol.%-BT
75 wt.%-BT/PVDF	47.00 vol.%-BT
0.1 wt.%-CNT/12 wt.%-BT	0.032 vol.%-CNT/3.877 vol.%-BT
0.4 wt.%-CNT/12 wt.%-BT	0.129 vol.%-CNT/3.881 vol.%-BT
0.7 wt.%-CNT/12 wt.%-BT	0.226 vol.%-CNT/3.885 vol.%-BT
1 wt.%-CNT/12 wt.%-BT	0.324 vol.%-CNT/3.889 vol.%-BT
1.3 wt.%-CNT/12 wt.%-BT	0.421 vol.%-CNT/3.893 vol.%-BT
1.7 wt.%-CNT/12 wt.%-BT	0.552 vol.%-CNT/3.898 vol.%-BT
1 wt.%-CNT/30 wt.%-BT	0.376 vol.%-CNT/11.29 vol.%-BT
1 wt.%-CNT/45 wt.%-BT	0.434 vol.%-CNT/19.56 vol.%-BT
1 wt.%-CNT/60 wt.%-BT	0.514 vol.%-CNT/30.89 vol.%-BT
1.7 wt.%-CNT/30 wt.%-BT	0.641 vol.%-CNT/11.32 vol.%-BT
1.7 wt.%-CNT/45 wt.%-BT	0.741 vol.%-CNT/19.63 vol.%-BT
1.7 wt.%-CNT/60 wt.%-BT	0.878 vol.%-CNT/31.01 vol.%-BT

Figure 4.12 also demonstrates the percolation threshold with a similar trend of sudden increase in AC conductivity at the same range of CNT content. It is noted that 2wt.%-CNT is

observed to be electrically conductive. It is found that the dielectric constant in 3D printed three phase nanocomposites is more than two times higher than in two phase nanocomposites due to the following reasons: 1) According to the micro-capacitor model, each two adjacent CNT nanoparticles can locally serve as the two electrodes among ceramic nanoparticles and polymer matrix [104], 2) CNT nanoparticles have ultrahigh surface area that can induce an ultrahigh polarization density, resulting in an increased dielectric constant [115], 3) since when alone both CNT and BT strongly tend to entangle together into agglomerates, together the CNT and BT nanoparticles interact, reducing agglomeration of the CNT networks in the polymer matrix so that this mixture leads to an increased dielectric property [101]. As a result, the relative dielectric constant of the 3D printed nanocomposites can be enhanced by increasing CNT content, meaning that the distance between CNT nanoparticles can be reduced and ultrahigh surface area can be increased, and by increasing BT content, meaning that the relative dielectric constant of the matrix region (i.e. BT, PVDF) between CNT nanoparticles can be increased and more uniform dispersion of the conductive material can be achieved. Dielectric loss values of the 3D printed nanocomposites are distributed in range from 0.07 to 0.15 which is obvious that all contained CNT samples at 12wt.%-BT are highly insulating as the AC conductivity and shows frequency dependent capacitive behavior. Similarly, at 45wt.% and 60wt.%-BT, as CNT content increases the percolation thresholds are more obvious near 1.7wt.%-CNT at which the drastic change of the dielectric constant occurs.

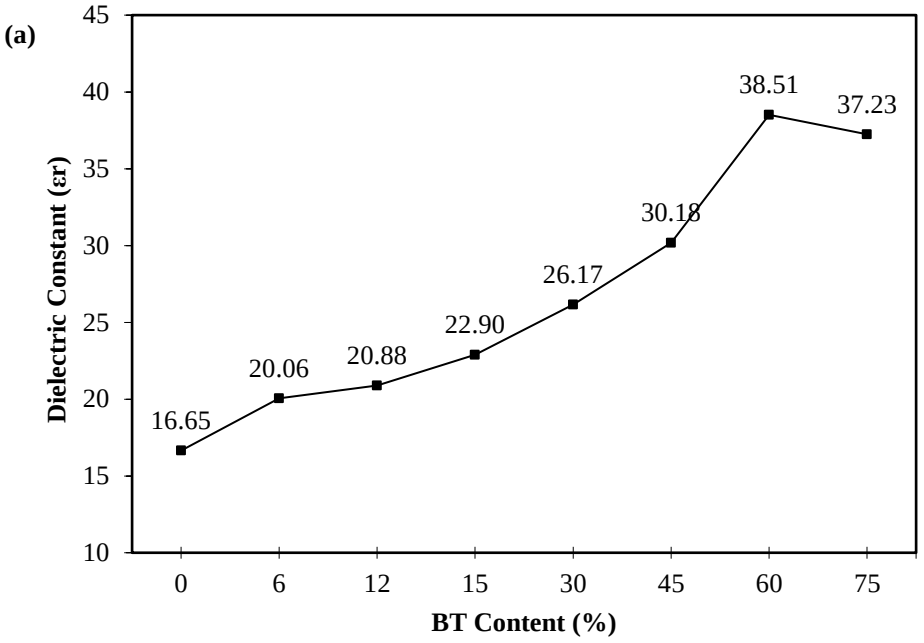
(a)
Dielectric Constant (εr)
45
40
35
30
25
20
15
10
38.51
37.23
30.18
26.17
22.90
20.88
20.06
16.65
0
6
12
15
30
45
60
75
BT Content (%)

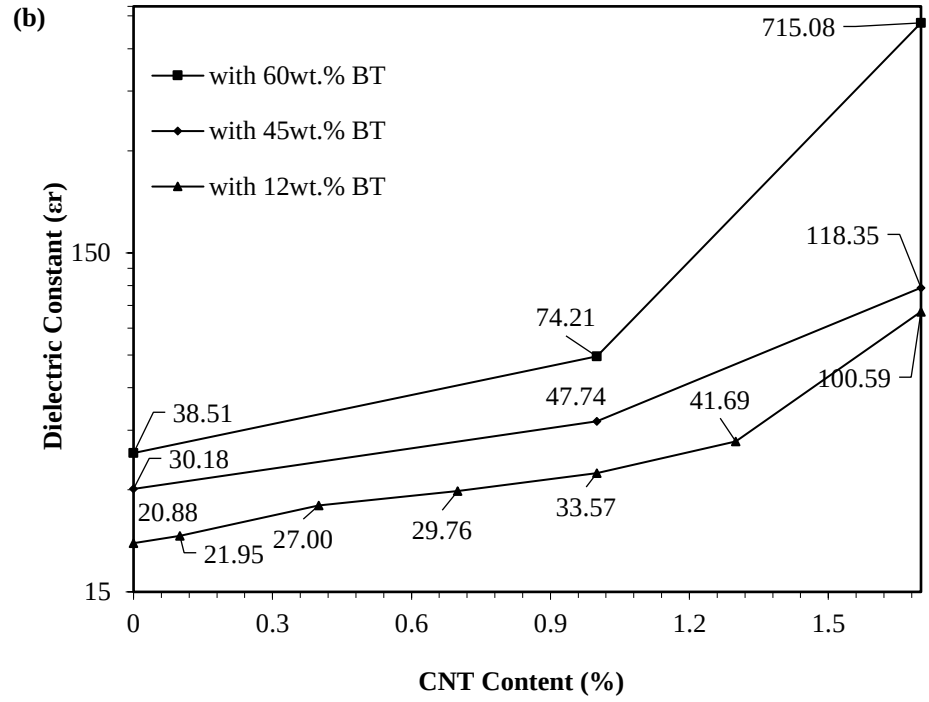
(b)
Dielectric Constant (εr)
150
15
with 60wt.% BT
with 45wt.% BT
with 12wt.% BT
715.08
118.35
74.21
47.74
41.69
100.59
38.51
30.18
20.88
21.95
27.00
29.76
33.57
0
0.3
0.6
0.9
1.2
1.5
CNT Content (%)

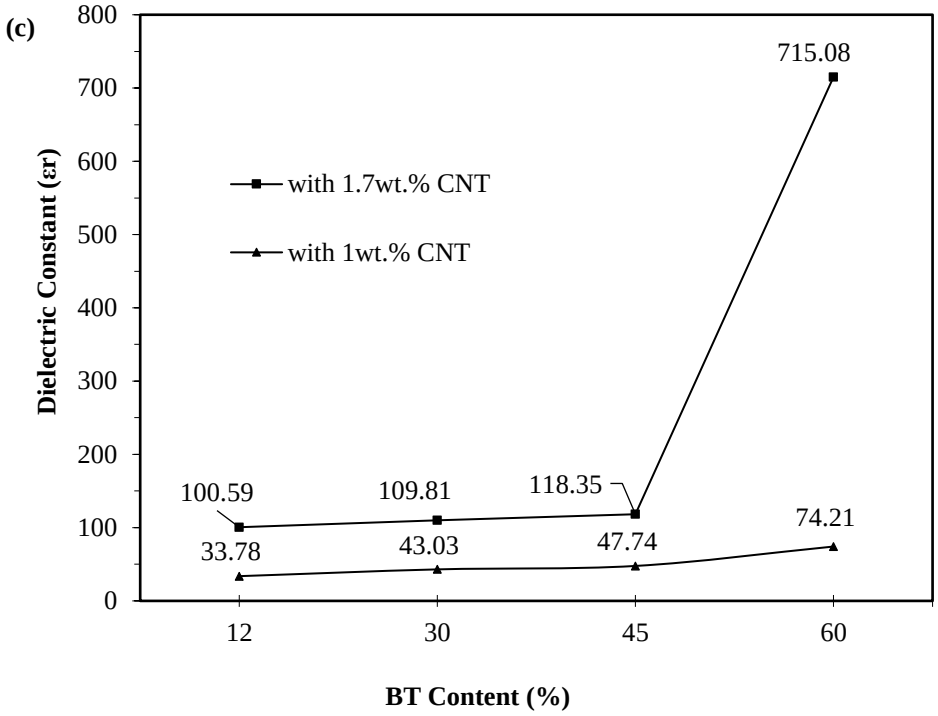

Figure 4.11: Dielectric constant (ε') as a function of (a) varying BT content with no CNT, (b) carrying CNT content at 12wt.%-BT, and (c) varying BT content at 1wt.% and 1.7wt.%-CNT measured at room temperature and 10^3 Hz.

Figure 4.10(e) and (f) indicate the dielectric constant and dielectric loss with respect to 1wt.% and 1.7wt.%-CNT with varying BT contents. As increasing BT contents either at 1 or 1.7wt.%-CNT, dielectric constants increase gradually but suddenly at 1.7wt.%-CNT/60wt.%-BT because the dielectric constant is sharply enhanced near the percolation threshold of CNT nanoparticles also as shown in Figure 4.10(c). This is a good agreement with the calculated theoretic percolation threshold value (0.865 vol.%). Therefore, it shows a high dielectric constant of 715 but with a high dielectric loss raised up to 0.62 as well as a higher AC conductivity as shown in Figure 4.12(c) compared with other 3D printed nanocomposites. For dielectric device application, this high dielectric loss is undesired because of the high energy loss due to heating [113]. In Figure 4.10(c), it is observed that 1.7wt.%-CNT has dielectric constant one order of magnitude higher than 1wt.%-CNT which shows that CNT played a significant role in enhancing

dielectric properties. The dielectric loss values are distributed around 0.1 except for 1wt.%-CNT/30wt.%-BT and 1.7wt.%-CNT/60wt.%-BT.

Polymer-based nanocomposites with conductive particles for dielectric applications usually have very narrow adjustment windows of the dielectric constant on changing filler contents [115]. The adjustment windows for the 3D printed CNT/BT/PVDF nanocomposites in this research is approximately within 1.7wt.%-CNT and 45wt.%-BT in the dielectric loss of 0.11. Results discussed herein show a higher dielectric constant and comparable dielectric loss at similar BT and CNT content previously reported in the literature [101, 104, 113] which used surface modification, miscible-immiscible coagulation, etc. Better methods such as the uniform dispersion [102, 116] or surface modification [113, 114, 117-119] method for nanoparticles can be integrated with FDM 3D printing process to further enhance the dielectric property.

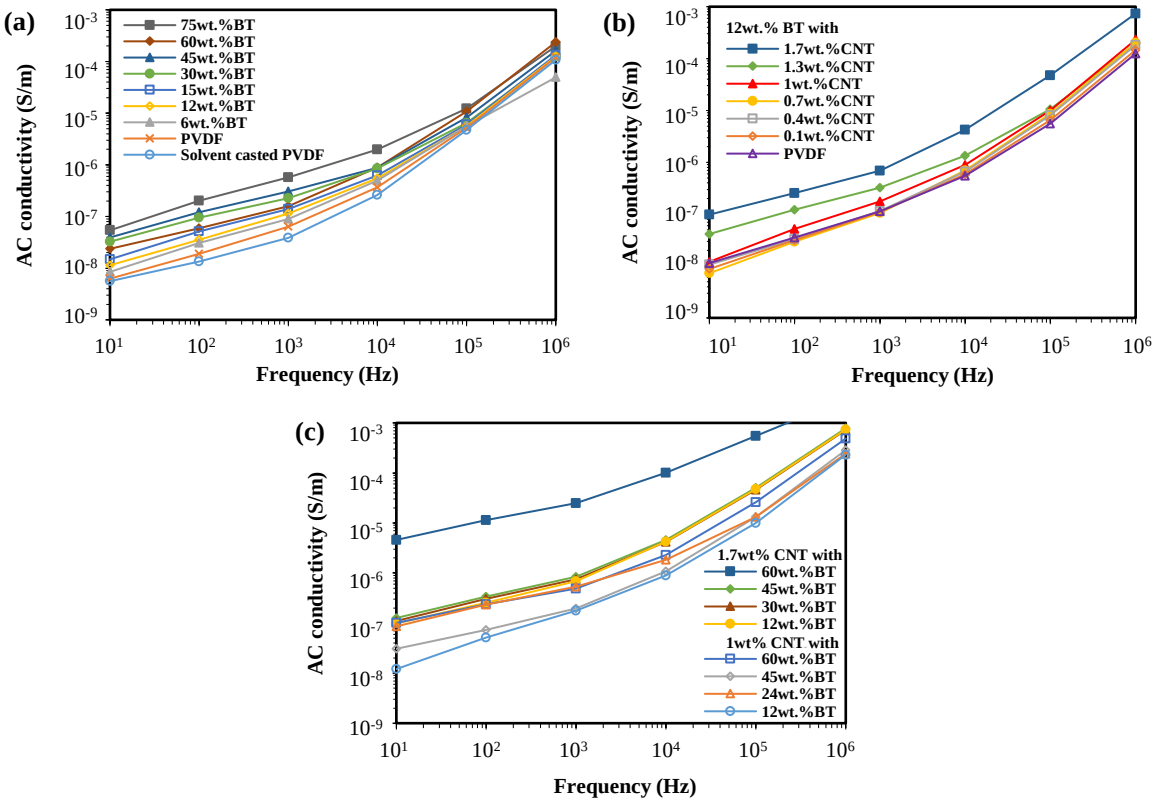

Figure 4.12: AC conductivity as a function of frequency from 10^1 to 10^6 Hz of (a) PVDF with varying BT content, (b) 12wt.%-BT with varying CNT content, (c) varying BT content at 1wt.% and 1.7wt.%-CNT.

Breakdown Strength and Energy Storage Performance of 3D Printed Nanocomposites

To determine the energy storage characteristic of the nanocomposites, breakdown strength for the 3D printed nanocomposites is also investigated with varying BT and CNT contents. Figure 4.13(a) shows that breakdown strength diminishes with increasing BT content until 30wt.%-BT because defects such as micro-cracks and voids increase with increasing BT nanoparticle amounts [74, 96] thus more interfacial polarizations (local electric field) are occurred at defect sites which affect breakdown strength [104, 119]. Then the breakdown strength rebounds at 30wt.%-BT due to the following reasons: 1) the field fluctuation may be reduced beyond 30wt.%-BT [120], 2) it may be attributed to interaction between fillers and matrix. More polymer chains interact with increasing specific surface of BT nanoparticles, tightly bonding together. This suppressed mobility of the polymer chains dominantly reduces the charge carrier transfer than increasing defects therefore it gives a rise to higher breakdown strength [119], and 3) the increasing micro-voids may be filled with dominated BT nanoparticles thus the defect sites can be reduced. However, Similarly, the breakdown strengths at both 1wt.% and 1.7wt.%-CNT are reduced at 30wt.%-BT in Figure 4.13(c). Figure 4.13(b) indicates that more CNTs leads to the linear decrease of breakdown strength due to the creation of conductive networks in the polymer matrix.

(a)

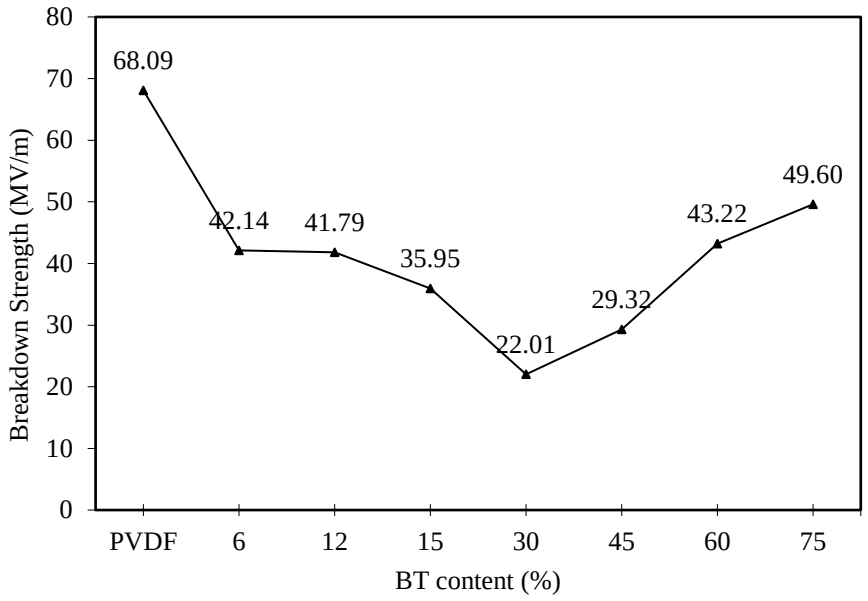
Breakdown Strength (MV/m)
80
70
60
50
40
30
20
10
0
68.09
42.14
41.79
35.95
22.01
29.32
43.22
49.60
PVDF
6
12
15
30
45
60
75
BT content (%)

(b)

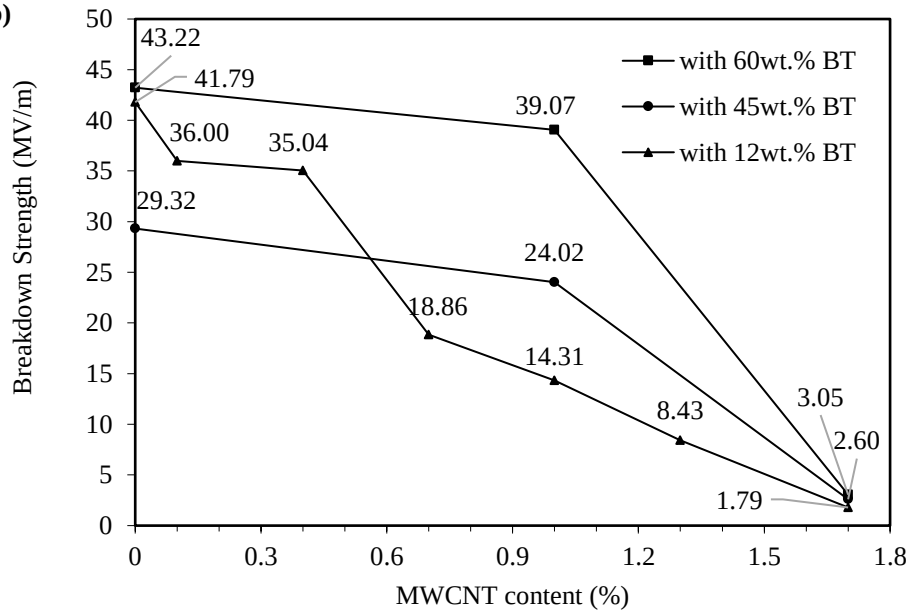
Breakdown Strength (MV/m)
50
45
40
35
30
25
20
15
10
5
0
43.22
41.79
39.07
36.00
35.04
29.32
24.02
18.86
14.31
8.43
3.05
2.60
1.79
with 60wt.% BT
with 45wt.% BT
with 12wt.% BT
0
0.3
0.6
0.9
1.2
1.5
1.8
MWCNT content (%)

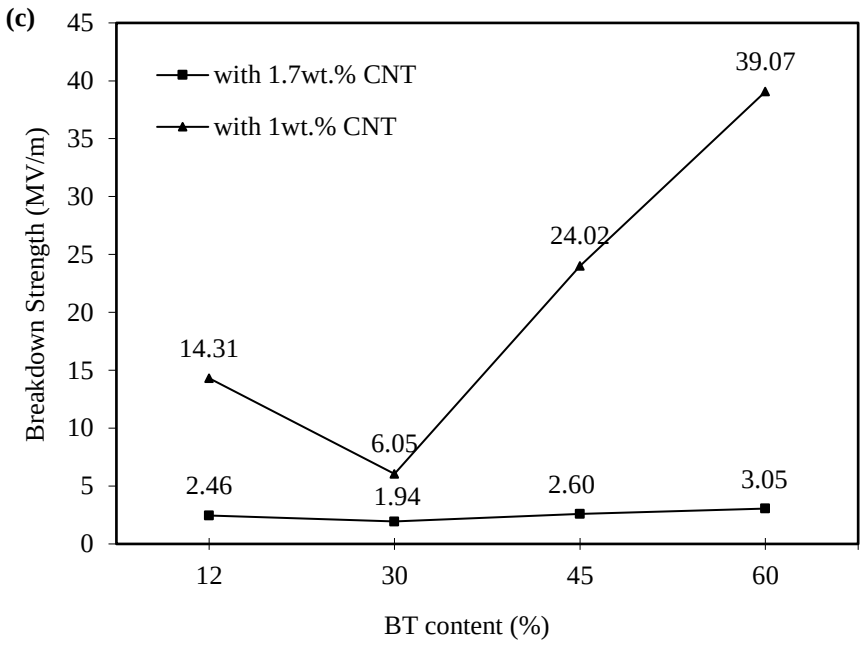

Figure 4.13: Breakdown strength as a function of (a) PVDF with varying BT content, (b) varying CNT content at 12wt.%-BT, and (c) varying BT content at 1wt.% and 1.7wt.%-CNT.

Energy density (*U*) of the 3D printed nanocomposites is calculated based on the measured dielectric constant and breakdown strength using the following equation:

$$U = \varepsilon_r \varepsilon_0 E^2/2 \tag{3}$$

where *E* is the applied electric field between the two electrodes. Figure 4.14(a), (c), and (e) show the energy density as a function of the electric field at each breakdown point with varying CNT and BT contents. The highest obtained energy density among the 3D printed nanocomposites without CNT is 0.38 J cm^{-1} with an applied 50 MVm^{-1} at 75wt.%-BT/PVDF as shown in Figure 4.14(a). Figure 4.14(c) shows that the highest energy density among nanocomposite containing 12wt.%-BT with varying CNT content is 0.15 J cm^{-1} under 42 MVm^{-1} without CNT in the nanocomposite, and maximum energy density decreases as CNT content increases. Figure 4.14(e) shows the highest energy density of 3D printed nanocomposites containing 1wt.% and 1.7wt.%-CNT with varying BT content is 0.45 J cm^{-1} under 39 MVm^{-1} at 1wt.%-CNT/60wt.%-BT. Nanocomposites with 1.7wt.%-CNT all have maximum energy densities less than 0.01 J cm^{-1}.

Figure 4.14(b), (d), and (f) indicate the energy density as a function of the electric field strange ranging from 1 to 5 MV/m accordingly.

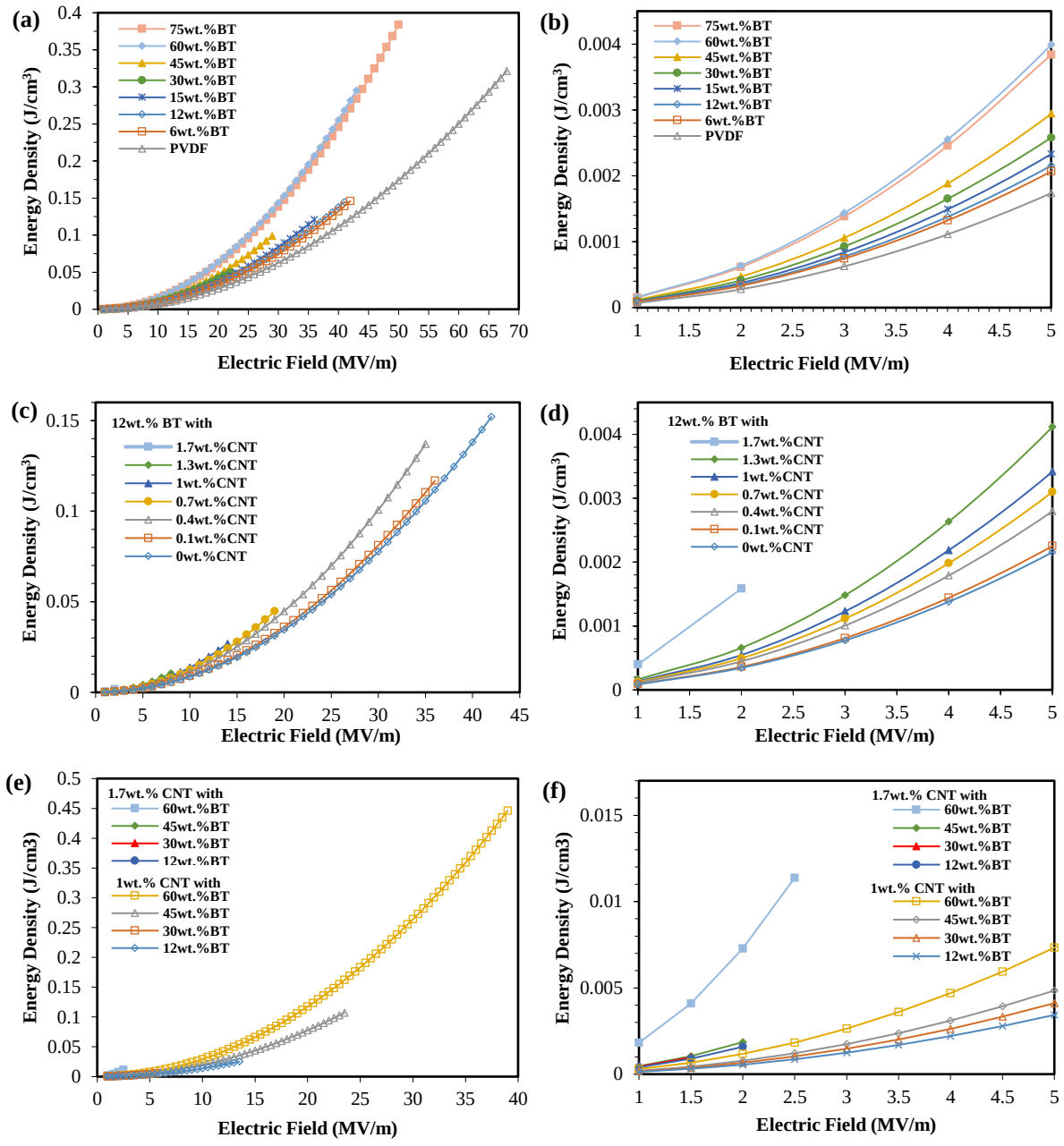

Figure 4.14: Calculated energy density as a function of electric field strength (MV/m) of (a-b) PVDF with varying BT content, (c-d) varying CNT content at 12wt.%-BT, and (e-f) varying BT content with 1wt.% and 1.7wt.%-CNT.

4.2.4 Summary

In this study, an FDM 3D printing process was utilized to fabricate and characterize three phase MWCNT/BT/PVDF nanocomposites for use in a dielectric application. Effective dispersion of nanoparticles and alleviation of agglomerates/micro-cracks/voids by the 3D printing process can be achieved to enhance dielectric property. 3D printed PVDF films show higher dielectric property than solvent casted PVDF because defects are reduced and the dipoles of polymer molecules are partially aligned during the 3D printing process. The addition of CNT and BT nanoparticles into a PVDF matrix improve dielectric property but the thresholds of each CNT and BT in PVDF matrix are found near 1.7wt.% and 60wt.% respectively and the highest dielectric constant is obtained 118 at 1.7wt.%-CNT/45wt.%-BT within dielectric loss of 0.11 at 1 kHz. In addition, the energy density of 0.45 J cm^{-1} at 39 MVm^{-1} was achieved in the 3D printed nanocomposites containing 1wt.%-CNT/60wt.%-BT. The presented study still requires continuous efforts to reduce the dielectric loss by incorporating surface modification or uniform dispersion methods for the nanoparticles. This study opens the future to integrate 3D printing technologies, which contributes the advantage of design flexibility and simple fabrication at low cost, empowering the production of dielectric devices in flexible, embedded electronics, and in energy storage.

4.3 MULTIFUNCTIONAL SENSING USING 3D PRINTED MWCNTS/$BaTiO_3$/PVDF NANOCOMPOSITES

This section studied multifunctional sensing capabilities on nanocomposites composed of poly(vinylidene) fluoride (PVDF), $BaTiO_3$ (BT), and multiwall carbon nanotubes (CNTs) fabricated by fused-deposition modeling 3D printing. To improve the dielectric property within BT/PVDF composites, CNTs have been utilized to promote ultrahigh polarization density and local micro-capacitor among BT and polymer matrix. The 3D printing process provides homogeneous dispersion of nanoparticles, alleviating agglomeration of nanoparticles, and reducing micro-crack/voids in matrix which can enhance their dielectric property. In this research, we demonstrated that by utilizing unique advantages of this material combination and a 3D printing technique, sensing capabilities for temperature and strain can be engineered with different content variations of included BT and CNTs. It is observed that the sensing capability for temperature change with respect to a 25 to 150 °C range can be improved as both BT and CNTs inclusions increase and is maximal with 1.7wt.%-CNTs/60wt.%-BT/PVDF nanocomposites; while sensing capability for strain change in a 0 to 10 mm range is maximal with 1wt.%-CNTs/12wt.%-BT/PVDF nanocomposites. In addition, it is found that the best combination for mechanical toughness is 1wt.%-CNTs/12wt.%-BT/PVDF with 24.2 MPa and 579 % in ultimate stress and strain respectively. These results demonstrated the technique to 3D print multifunctional nanocomposites with temperature and strain sensing capabilities as well as increased mechanical property. Furthermore, this research demonstrated the feasibility for large-scale multifunctional sensor device manufacturing with freedom of design, low-cost, and an accelerated process.

4.3.1 Introduction

Polyvinylidene fluoride (PVDF) and $BaTiO_3$ (BT) are well known smart materials used as piezo-/di-electric devices for sensor and energy storage due to its unique characteristics [9, 10, 80]. In order to improve the piezo-/di-electric performance as well as tensile strength, the introduction of organic fillers such as carbon fiber, carbon nanotubes (CNTs), and carbon black have been extensively investigated by incorporating them in polymer composites [81, 82, 87, 101, 104].

Researchers investigated other areas of CNTs based strain sensors using their piezo-capacitive and resistive effects on highly stretchable elastomer substrate or in a polymer matrix for robotics, structural health monitoring, human skin, interactive electronics, smart clothing, and strain gauge [121-126]. Strain sensing of polymer CNTs nanocomposites is based on the electrical property changes induced by external stresses, concepts of the destruction of the CNTs' conductive networks, and alternation of resistance changes due to variation of the distance between CNTs [123]. These CNTs were used to act as stretchable electrodes or to mix with polymer materials tested within limited lower strain parameters. The latter studies are using the structural material itself as the intrinsic sensor which is also referred to as self-sensing and has advantages of multi-functionality, low-cost, high durability, a large sensing volume, and the absence of mechanical property degradation [123, 127].

Recently, it is proved that processes of filament extrusion and fused-deposition modeling (FDM) 3D printing provide homogeneous dispersion of BT and possibly other additives in PVDF as well as alleviating agglomerates and removing voids and cracks [74]. The 3D printed piezo-/di-electric nanocomposites using FDM 3D printing technique was studied to improve both their electrical and mechanical performances by integrating polymer with piezo-/di-electric ceramics. This printing technique can provide great improvements for piezoelectric coupling coefficient, relative dielectric permittivity (118), ultimate stress (21 MPa), and ultimate strain (500 %) respectively [74, 95, 96, 128]. With the outstanding toughness of the 3D printed multifunctional nanocomposites, it can be potentially used as an intrinsic self-powered pressure sensor and energy storage out of a 3D structure [74, 128]. By utilizing the particular characteristics of CNTs and BT nanoparticles in a PVDF matrix and unique property of FDM 3D printing technique [128], other sensing capabilities can be explored in strain and temperature changes based on capacitance change in the distance variation of CNTs' networks under strain change and in phase transformation of BT ceramics with local micro-capacitor of CNT electrodes under temperature change. In this study, we explore the impact of filler content of BT and CNTs below percolation threshold on electrical property changes of FDM 3D printed CNTs/BT/PVDF nanocomposites for

multifunctional temperature and strain sensing applications. In addition, tensile testing is performed to characterize tensile stress and strain on each sample for their mechanical property.

4.3.2 Experimental

For the fabrication of filaments that harness a continuous CNTs/BT/PVDF nanocomposite needed for 3D printing, the following materials were used: PVDF powder (MW~534,000; Sigma-Aldrich), BT powder (700 nm; Inframat®), multi-wall carbon nanotubes (CNTs) powder (Diameter: 8-15 nm, length: 10-50 μm, Cheaptubes®), and N-Dimethylformamide solvent (DMF, OmniSolv®). With respect to varying BT nanoparticle sizes, BT powder with 700 nm nanoparticle size withholds its maximum capacitance at 1 kHz in greater loading systems [129]. The solvent casting method is found in Figure 4.15**Error! Reference source not found.**(a) and was used to m ix CNTs/BT/PVDF uniformly. For this uniformly dispersed mixture of BT and CNTs in DMF solvent, the materials were sonicated for 30 min and had a 1:10 weight ratio of PVDF powder. The addition of PVDF powder was inputted after the sonication and the total mixture was placed in a water bath for 10-15 min, or until the PVDF powder visibly dissolved at 80 °C. Ultra-sonication (Branson Sonifier 450) was applied to the solution for 15 min that allowed BT and CNTs clusters to be alleviated. Lastly, the nanocomposite solution was treated by evaporating DMF solvent once poured out into a glass substrate and placed to be heated on a hot plate for 12 hrs at 80 °C.

The hardened sheet produced by solvent casting was cut and fed into the filament extruder. The extruded filament diameter and temperature were roughly 2.9 ±0.05 mm and 205 °C, respectfully, as shown in Figure 4.15(b). This filament extrusion was repeated three times for BT nanoparticles's unform dispersion and DMF solvent's evaporation. Specifically, the 3D printer utilized to print films was a fused-deposition modeling (FDM) 3D printer (Lulzbot® Taz 5) as seen in Figure 4.15(d). This printing method was chosen for the purpose of having continuity in the layer by layer material deposit process on the heating bed [4]. The methods provided for the filament extrusion and printing procedures are deemed to improve the matrix of the structures with nanoparticles being dispersed uniformly which refine the dielectric properties [74]. The FDM 3D

printer with a nozzle temperature of 230 ˚C, printing speed of 5 mm/s, nozzle diameter of 0.5 mm, and heating bed temperature at 60 ˚C, produced 0.5 ±0.05 mm thick films (1 layer). Ideally, this process should produce films with consistent ease. However, it is valuable to consider that the nanocomposites used may create blockage in the nozzle head since they are being subjected to high temperatures and high shear strains. The blockage can be avoided by limiting the amount of time the filament spends in the heated nozzle or by correctly addressing the diameter of the filament used since the variance from each may greatly deviate depending on the extrusion. The nanocomposite films were printed using a one-way extrusion pattern rather than the conventional perimeter then zigzag pattern to achieve a more consistent film surface quality at only a single layer for sensing and tensile testing [107].

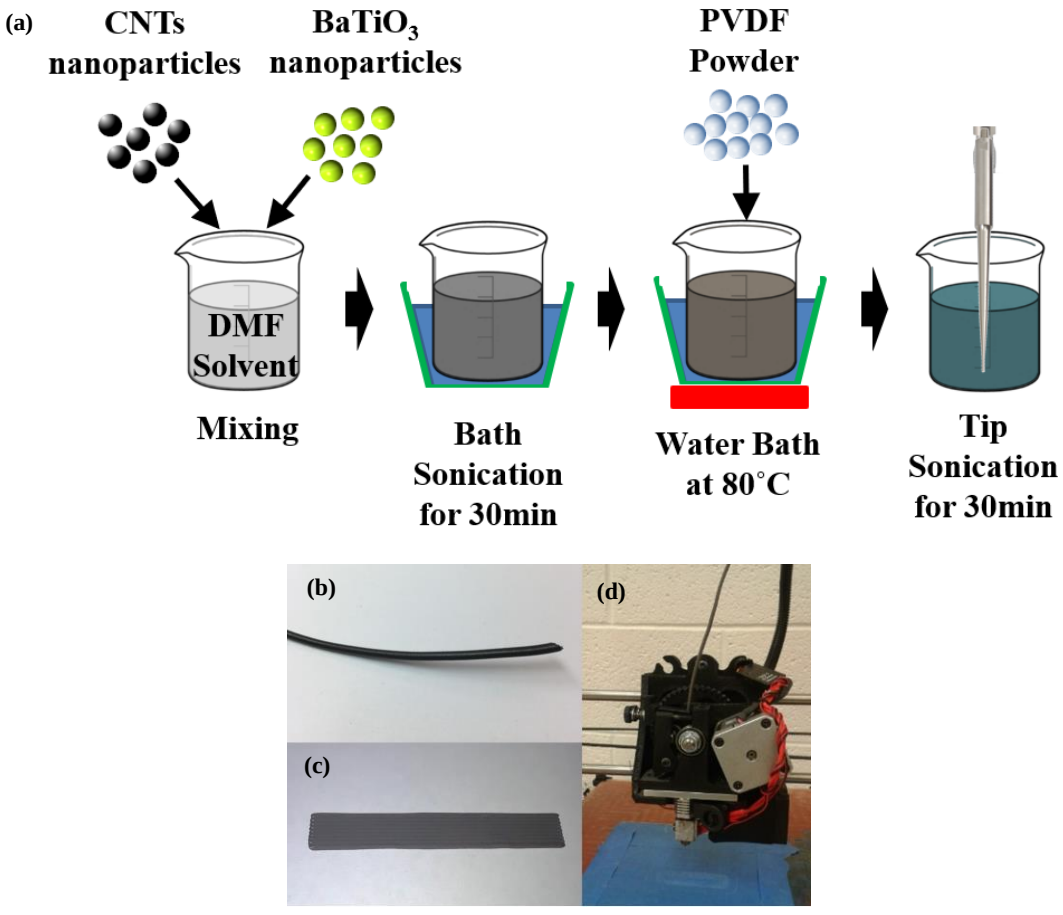

Figure 4.15: (a) Schematic illustration procedure of solvent casting procedure for CNTs/BT/PVDF nanocomposites, (b) fabricated nanocomposites filament, (c) one-way extruded nanocomposite film, and (d) fused-deposition modeling 3D printer single extrusion tool head.

Dried solvent casted nanocomposites were heated up at 205 and 230˚C for filament extrusion and 3D printing process, respectively. The filament extrusion at 205˚C was repeated three times for uniform dispersion. Several times of thease heating processes promoted to evaporate DMF enough.

The morphology of the 3D printed nanocomposite samples was observed using a scanning electron microscopy (SEM, TM-1000 Hitachi) while X-ray diffraction (XRD) was performed to characterize crystallinity using CuKα radiation on a D8 Discover diffractometer (Bruker, USA). For the nanocomposite films extruded, dielectric property was characterized using electrodes in the form of conductive silver paint (High Purity Silver Paint, SPI supplies, USA) on opposing surfaces. An LCR meter (1920 Precision, IED lab) was utilized to connect the electrodes of each individual 3D printed nanocomposites for considering the capacitance of each sample. Temperature testing was carried out by submerging the sample in a silicon oil (Sigma-Aldrich) and connecting the silver electrodes. Using a hot plate, each film was cut into a 5×5×0.5 mm dimension and tested from 25 to 150 ˚C with incrementing temperatures of 25 ˚C for a total six data point range as shown in Figure 4.16(a)(c). Each sample was then tested for capacitance value. Strain sensing capabilities were proved from painting 5×7 mm electrodes on corresponding sides of the films shown in Figure 4.16(b)(d) and deeming a displacement rate of 3 mm/min using a tensile testing machine (ADMET MTESTQuattro eXpert 5600 series). Recordings of the capacitance were taken at each 1 mm displacement with a frequency of 1 kHz. Similarly, tensile testing was gathered by the same principle with a displacement rate of 3 mm/min [130]. These testing setups for characterization can be further understood in Figure 4.16.

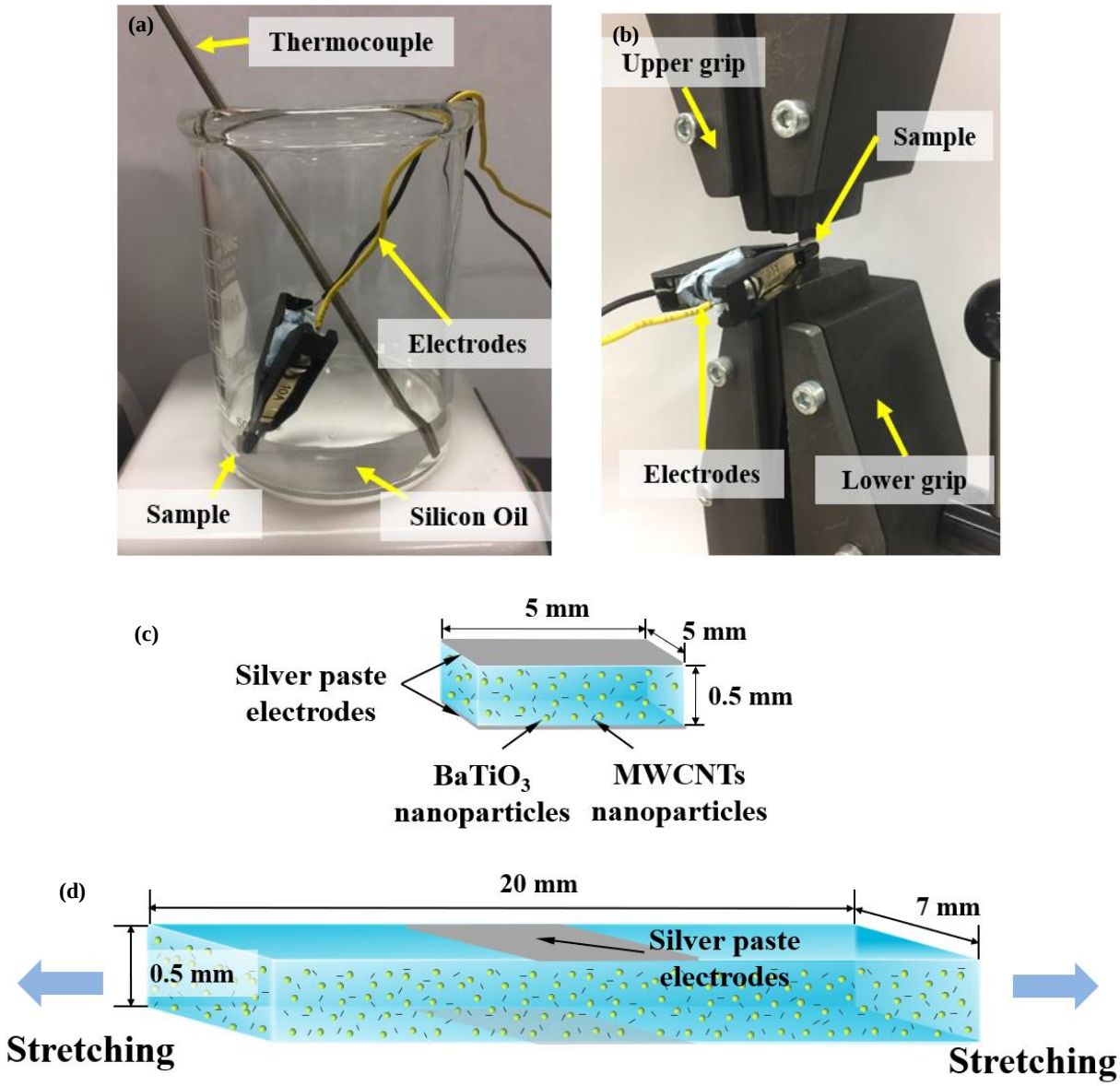

Figure 4.16: Testing set-up for (a) temperature sensing test, (b) strain sensing test, and schematic sample preparation for (c) temperature sensing and (d) strain sensing.

4.3.3 Results and Discussion

Scanning Electron Microscopy (SEM) Analysis

The surface topography of the 3D printed nanocomposite films with varying BT and CNTs content was comparatively examined by SEM as shown in Figure 4.17. Higher amounts of BT agglomerates are seen as BT contents increase. The size of BT agglomerates is relatively increasing as BT contents increase as well. Voids are relatively observed more in 60wt.%-BT

compared to 12 and 40wt.%. However, micro-cracks are not observed throughout SEM images of all nanocomposites. In Figure 4.17(c), as CNTs content increases, CNTs clusters are more obvious in PVDF matrix, agglomerated, and surround the BT agglomerates.

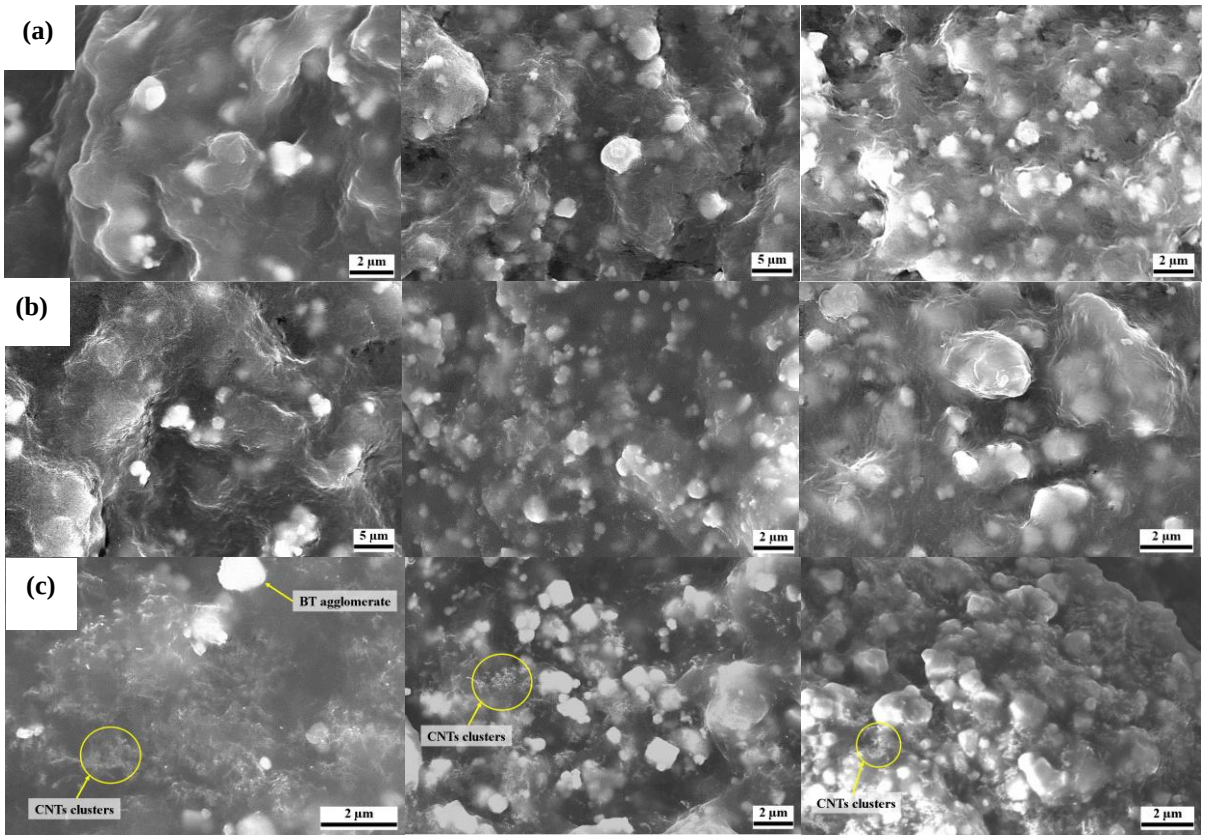

Figure 4.17: SEM images of the surfaces of 3D printed nanocomposites with compositions of (a) 12, 40, 60wt.%-BT with no CNTs (left to right), (b) 12, 40, 60wt.%-BT with 1wt.%-CNTs (left to right), (c) 12, 40, 60wt.%-BT with 1.7wt.%-CNTs (left to right).

X-Ray Diffraction (XRD) Analysis

To confirm the elemental makeup of the 3D printed nanocomposites, the XRD patterns of pure PVDF, BT, CNTs, BT/PVDF, and CNTs/BT/PVDF nanocomposites were characterized as shown in Figure 4.18. The peaks corresponding to BT and PVDF remain in the XRD pattern of the 3D printed nanocomposites, while the peak of CNTs disappeared due to the low filler content [131].

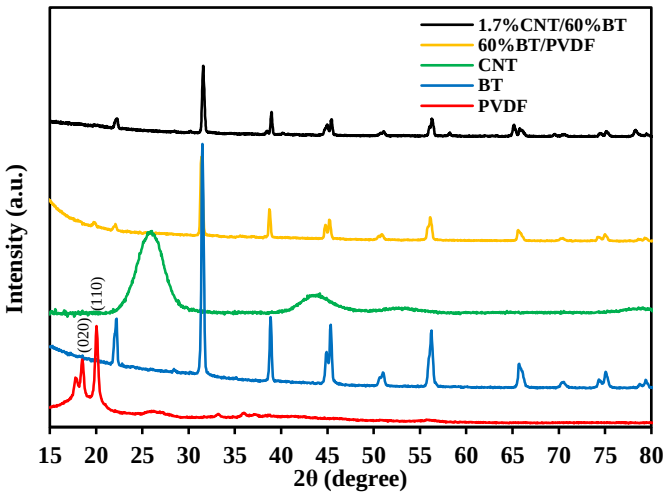

Figure 4.18: XRD patterns of pure PVDF, BT, CNT and the 60wt.%-BT/PVDF, and 1.7wt.%-CNT/60wt.%-BT/PVDF nanocomposites.

Temperature Sensing Capability

To characterize a temperature sensibility of the 3D printed nanocomposites, 3D printed films with varying BT and CNTs contents in PVDF matrix were tested at elevated temperature in the silicon oil environment. As shown in Figure 4.19, all nanocomposites films show an increasing trend of the capacitance at 1 kHz as temperature elevates from 25 to 150 °C. All films started deforming and melting at temperatures above 150 °C. In Figure 4.19 (a), pure PVDF film (T_m: 177 °C) shows a slightly changing rate in the capacitance than films with BT particles since molecular mobility of pure PVDF is significantly promoted with increasing temperature. At low temperature, PVDF molecules have difficulty in responding to applied electrical field due to poor molecular mobility. At high temperature, the mobility is significantly improved but still restricted by hydrogen bonding [132]. In theory, BT has a Curie temperature around 125 °C where the capacitance suddenly drops [133]. However, the Curie peak for BT particles is absent in the PVDF matrix when temperature increases. It is found that there are some possibilities for causing the disappearance of BT's Curie peak as following reasons: 1) the extent of tetragonal deformation of BT particles is progressively reduced as BT particle size decreases below 5 µm. Below 5 µm of BT particle size, there is an increasingly important surface charge effect which the polarization

that results from the tetragonal structure is locked. This size effect (> 1μm) of ultra-fine BT particles results in a locked tetragonal structure by the surface charge effect so that capacitance increases without reduction at Curie temperature [134-137], 2) large number of defects are caused by O^{2-} deficiency in perovskite structure. Therefore there is probability that F^- from PVDF may substitute some of the O^{2-} vacancy or loosely coupled with Ti ion in BT so that these bonding may rock the BT phase transformation [137, 138], and 3) diffuse phase transition in BT [139, 140]. At high temperatures, BT particles retain better polarization, therefore, the changing rate in capacitance arises as increasing BT particles in PVDF. As seen in Figure 4.19(b)-(d), addition of CNTs fillers lead to a much higher capacitance at room temperature due to the following reasons: 1) according to the micro-capacitor model, each two adjacent CNTs can locally serve as two electrodes among ceramic nanoparticles and polymer matrix [104], 2) CNTs nanoparticles have ultrahigh surface area that can induce an ultrahigh polarization density, resulting in an increased capacitance [115], 3) both CNTs and BT strongly tend to entangle into agglomerates, however, when used together the CNTs and BT nanoparticles interact and reduce agglomeration of the CNTs networks in the polymer matrix so that this mixture leads to an increased capacitance property [101]. Under elevating temperatures up to 150 ˚C, the changing rate in the capacitance arises as more CNTs are introduced in the BT/PVDF system. This is because the increased polarization of BT nanoparticles is exponentially amplified between locally distributed two adjacent CNTs electrodes. In Figure 4.19(e), among the varying BT and CNTs content, 1.7wt.%CNT/60wt.%BT shows the highest changing rate in the capacitance which means the highest temperature sensibility. Figure 4.19(f) shows the repeatability test of the 3D printed 1.7wt.%-CNT/60wt.%-BT/PVDF nanocomposites which is the best performing sample in terms of changing rate in capacitance. The changing rate in capacitance during 1^{st}, 2^{nd}, 3^{rd} heating and cooling are almost consistent and maintain capacitance value within the range of 0.0039 nF throughout the temperature.

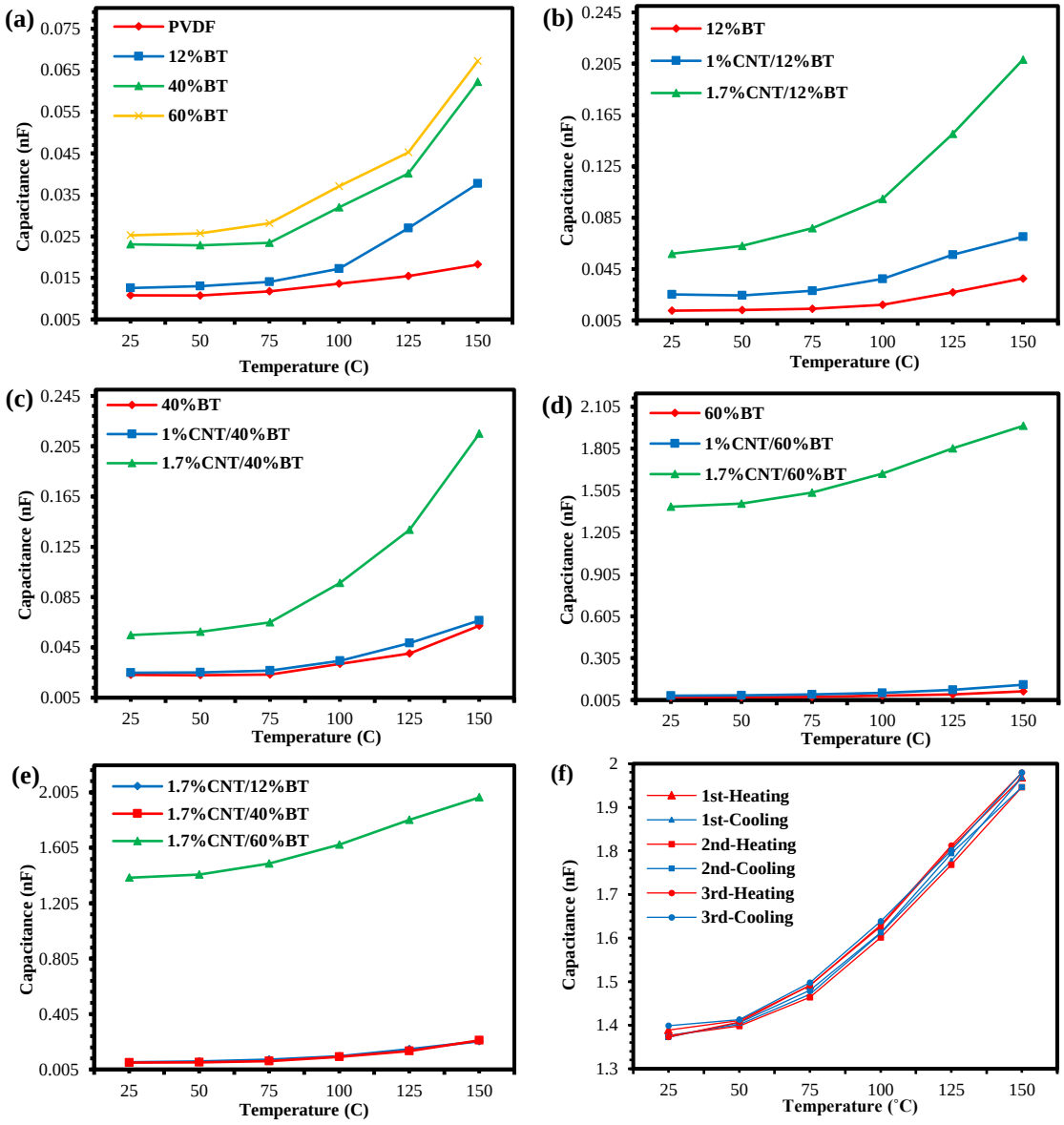

Figure 4.19: Capacitance (F) as a function of temperature from 25 °C to 150 °C of (a) pure PVDF with varying BT content, (b) fixed 12wt.%-BT with varying CNTs content, (c) fixed 40wt.%-BT with varying CNTs content, (d) fixed 60wt.%-BT with varying CNTs content, (e) fixed 1.7wt.%-CNTs with varying BT content, and (f) 1.7wt.%-CNT/60wt.%-BT/PVDF nanocomposites with repeated heating and cooling for repeatability analysis.

Strain Sensing Capability

To characterize the strain sensibility of 3D printed nanocomposites, the capacitance of 3D printed films with varying BT and CNTs contents in PVDF matrix were measured at 1 mm increments until reaching a 10 mm displacement using a tensile machine. The maximum noted

displacement was derived because silver pastes electrodes experience micro-cracks and lose electrical conductivity after 10 mm. Stretchable electrodes such as conducting polymer (printed CNTs, carbon composites, graphene, and Ag nanowires) or inorganic solutions (PEDOT:PSS) were not used in this study [141-149]. However simple silver paint method [150, 151] was chosen to find the composition which has highest changing rate in capacitance and measure its relative change in capacitance under cyclic load within maximum displacement of 1.5 mm. In Figure 4.20, all the 3D printed nanocomposites samples have shown increasing capacitance as displacement increases due to the decrease of capacitance thickness. In Figure 4.20(a), the changing rate in the capacitance among BT/PVDF system is maximal at 12wt.%-BT/PVDF as the strain is induced and decreased over 40 and 60wt.%-BT. This is because Poisson's ratio of the 3D printed nanocomposites at high ceramic loading is relatively lower than one at low ceramic loading so that the distance change rate between two electrodes is not significant.

In Figure 4.20(b), the addition of CNTs inclusion at 12wt.%-BT shows the changing rate in the capacitance is maximal at 1wt.%-CNTs due to the following reasons: 1) CNTs chains are stretched and rearranged along the direction of tensile strain, thus better local micro-capacitance within BT and PVDF can be formed [152], and 2) two adjacent CNT local electrodes get closer which leads to a higher changing rate in the capacitance. Moreover, the capacitance is decreased at 1.7wt.%-CNT. This decrease in the changing rate in the capacitance is due to the microstructure change of the nanocomposites [129] as following: Theoretically, clusters of CNTs can be formed in BT/PVDF systems because the CNTs tend to entangle together although BT nanoparticles help improve uniform dispersion of CNTs with suitable mixture process [115]. Note that BT nanoparticles form inter-particle barriers within CNTs network, therefore they prevent CNTs from direct mutual connection and destroyed conductive paths. This cluster is effective to create high capacitance but can be destroyed by stretching which causes capacitance to decrease. At low CNTs loadings, the concentration of CNTs cluster is low so that capacitance change is not significant. However, at high CNTs loadings around 2wt.%, the concentration of CNTs cluster is high and CNTs network is easily destroyed in the nanocomposites when strain is induced; then the

capacitance change becomes significant [129]. Under 40 and 60wt.%-BT, the changing rate shows a similar trend as shown in Figure 4.20(c)-(d), however this changing rate is reduced when BT content increases because the Poisson's ratio decreases as adding more inclusions. Therefore, the changes of distance between electrodes and CNTs rearrangement would be slight.

Figure 4.20(e) shows that the highest changing rate in the capacitance is observed at 1wt.%-CNT/12wt.%-BT/PVDF among the other compositions. The dynamic strain test is performed to characterize repeatability of the 3D printed nanocomposites under strain change. The best performing sample at 1wt.%-CNT/12wt.%-BT/PVDF is tested in ranges from 5 to 50, 100, and 130 N (displacement ranges from 0.3 to 0.55, 1, and 1.5 mm), applying 10 cyclic loads at 1 Hz. Note that the sample was ruptured above 130 N. As shown in Figure 4.20(f), relative changes in capacitance are 20, 600, and 670 % under 45, 95, 125 N (0.52, 0.7, 1.2 mm in displacement). The changing rate from 20 to 600 % is not matched with the changing rate in applied stress from 45 to 95 N because when considering true strain, cross-sectional area of the sample at 95 N was much smaller than one at 45 N.

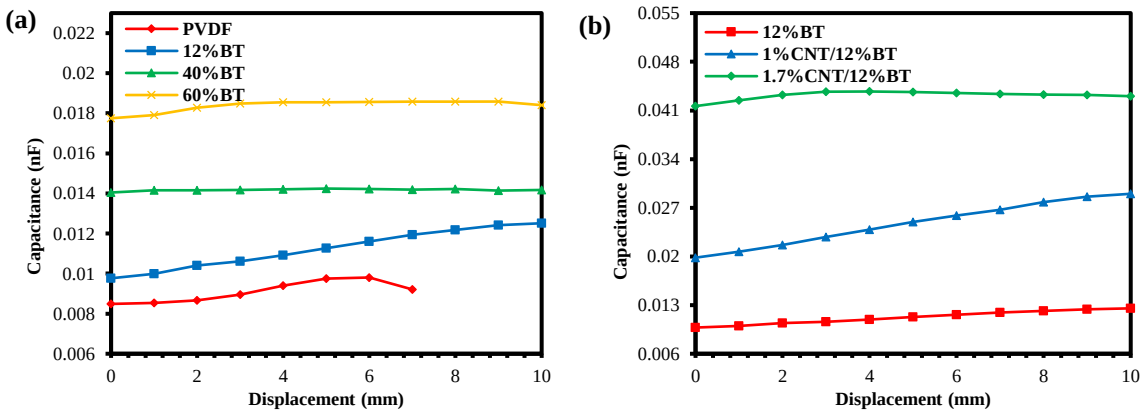

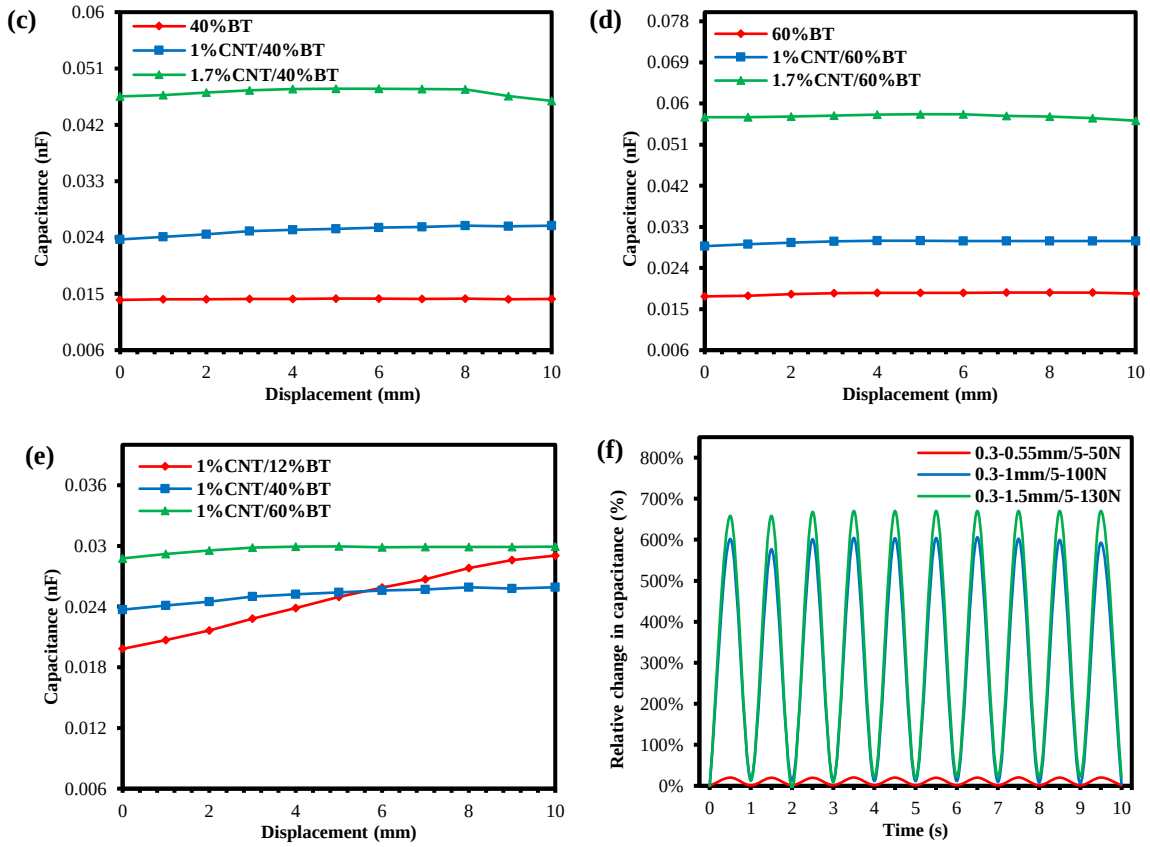

Figure 4.20: Capacitance (F) as a function of displacement from 0 to 10 mm by 1 mm increment: (a) pure PVDF with varying BT content, (b) fixed 12wt.%-BT with varying CNTs content, (c) fixed 40wt.%-BT with varying CNTs content, (d) fixed 60wt.%-BT with varying CNTs content, (e) fixed 1wt.%-CNTs with varying BT content, and (f) dynamic strain test with relative change in capacitance as a function of 10 cyclic loads in ranges from 5 - 50, 100, 130 N under frequency of 1 Hz for 3D printed 1wt.%-CNT/12wt.%-BT/PVDF nanocomposites film.

Mechanical Property Analysis

The influence of the presence of BT and CNTs nanoparticles in the mechanical properties of PVDF matrix was examined by analyzing the tensile behavior of the 3D printed CNTs/BT/PVDF nanocomposites films. Figure 4.21(a) shows a stress-strain curve for each sample with varying weight percentages of CNTs and BT tested at the strain rate of 3 mm/min. In general, low inclusion content means that inclusion increases tensile strength because amorphous segment motions of the polymer chains is restricted by the dispersion of inclusion [75, 153]. However, at a high loading system the tensile strength decreases as inclusion content increases as shown in

Figure 4.21(b). Exceptionally, there is an increase in the ultimate stress for BT/PVDF nanocomposites without CNTs at 40wt.%-BT. Although it is observed that 12wt.%-BT shows higher ultimate stress than 40wt.%-BT around 50% strain, the 40wt.%-BT breaks at a higher stress due to the following reason: tensile stress right before rupture leads the polymer chains to be oriented and aligned along the tensile load direction which increases the strength and stiffness of the polymer in stretching direction, also known as strain hardening [154]. During the rupture moment, BT agglomerates can contribute as reinforcement in the polymer matrix and eventually it transpires to second ultimate stress also shown in other peaks. The more BT content that is in the polymer matrix, the higher ultimate stress can occur before the rupture. As introducing more CNTs content in BT/PVDF nanocomposites, significant improvement in ultimate stress is observed at 1wt.%-CNTs (24.2 MPa) and then it diminishes at 1.7wt.%-CNTs (18.4 MPa). Similarly, ultimate stress decreases as BT content increases. This relationship can be attributed by the following reasons: 1) inclusions of BT and CNTs are more likely to agglomerate and be heterogeneously distributed in higher loading systems also shown in Figure 4.17, demonstrating that BT agglomerates and CNTs clusters increase in higher inclusion content [76, 96] and 2) voids and micro-cracks can be created during the fabrication process and increased with higher filler content [77, 78, 96]. This means that the total amount of bonding of PVDF molecular chains was decreased [96]. Therefore, these agglomerates and defects led to the degradation of the tensile strength after 12wt.%-BT and 1wt.%-CNTs.

Higher ultimate strains are observed around 550 % at 12 and 40wt.%-BT with no CNTs or 1wt.%-CNTs. It is assumed that increased inclusion helped prevent crack propagation. However, at content loading of 60wt.%-BT and 1.7wt.%-CNTs, the ultimate strains are abruptly diminished because the 3D printed nanocomposites became brittle due to reasons mentioned above. Among the 3D printed nanocomposites, it is observed that 1wt.%-CNTs/12wt.%-BT/PVDF shows the highest mechanical toughness (24.2 MPa and 579 %). Figure 4.22 shows the ruptured 3D printed tensile samples in each. Note that all of samples were contracted in the direction of the tensile loading.

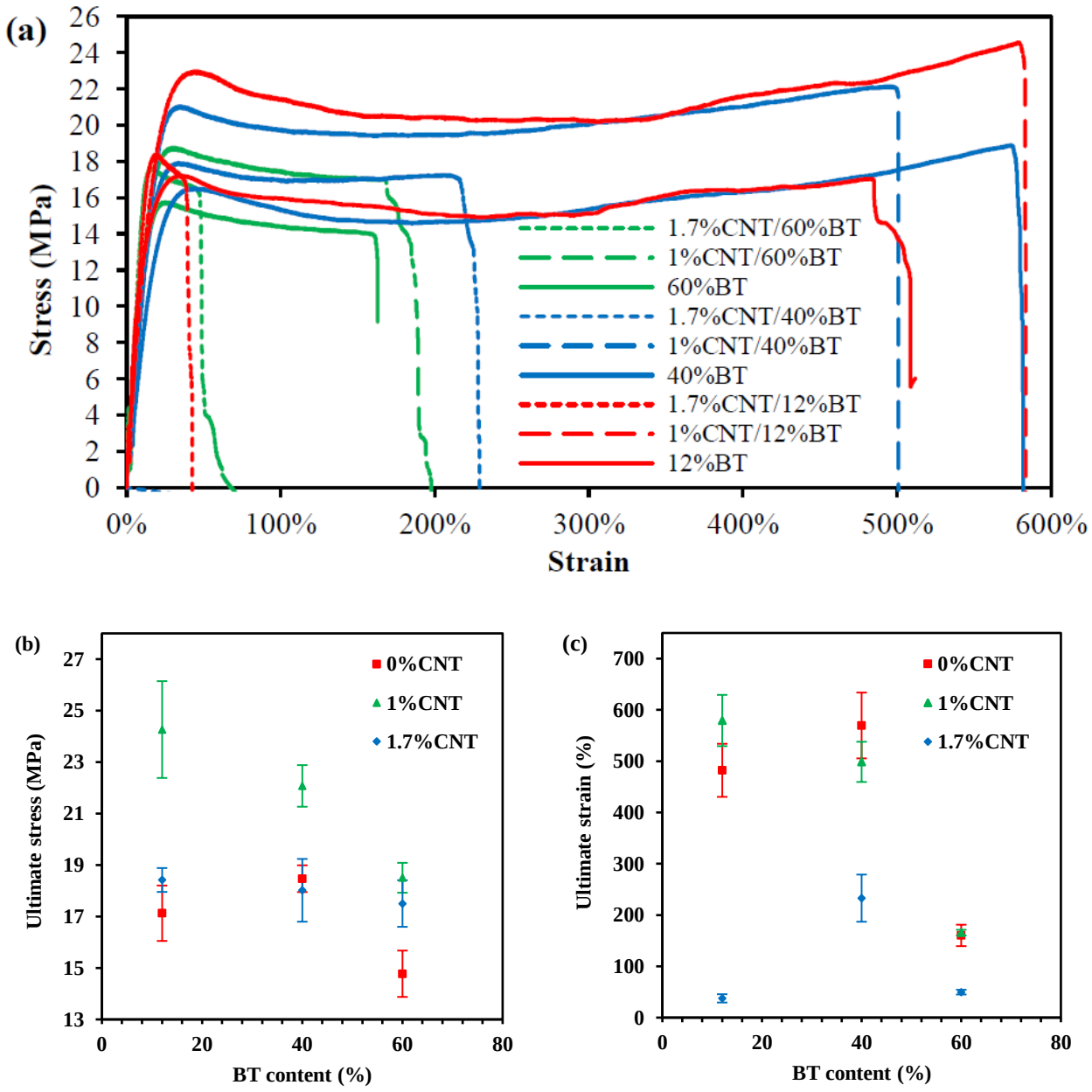

Figure 4.21: (a) stress-strain curve at the strain rate of 3 mm/min for 3D printed CNT/BT/PVDF samples, (b) ultimate stress as a function of varying BT and CNTs, (c) ultimate strain as a function of varying BT and CNTs.

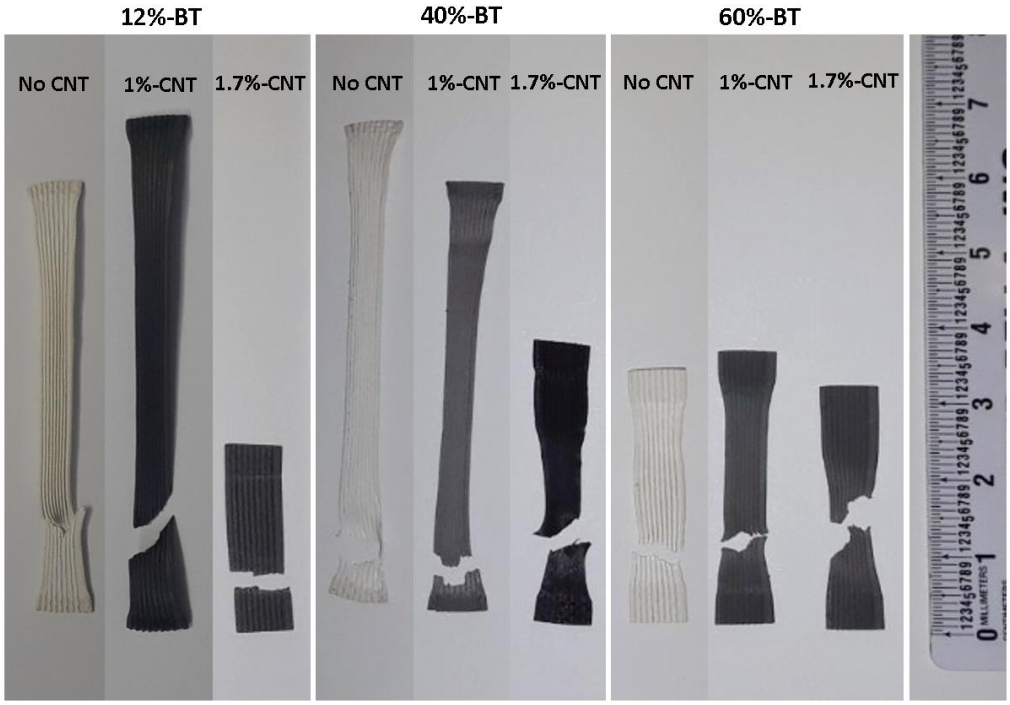

Figure 4.22: Ruptured samples after tensile testing.

4.3.4 Summary

In this study, CNTs/BT/PVDF nanocomposites were fabricated using FDM 3D printing process for temperature and strain sensing applications. It is found that the capacitance property of the 3D printed nanocomposites can be utilized in sensing the changes of temperature and strain. The highest sensibility for temperature is observed in nanocomposites containing 1.7wt.%-CNTs/60wt.%-BT/PVDF which are the maximum loading for BT and CNTs percolation threshold. The highest sensibility for strain is observed in nanocomposites containing 1wt.%-CNTs/12wt.%-BT/PVDF. The nanocomposites above 1wt.%-CNTs resulted in the degradation of the changing rate in the capacitance. This degradation was because the CNTs cluster effectively destructs capacitance as the strain is induced. It is observed that the addition of more than 12wt.% of BT particles degrades the changing rate in the capacitance because Poisson's rate is not significant at a higher loading system. The combination between CNTs and BT inclusions contributes to a high changing rate in the capacitance when it comes to the temperature and strain changes. The superior mechanical performance is observed in nanocomposites containing 1wt.%-CNTs/12wt.%-

BT/PVDF showing 24.2 MPa and 579 % for mechanical stress and strain, respectively. These improved mechanical properties stem from CNTs and BT reinforcements. However, ultimate stress starts decreasing after 1wt.%-CNTs and 12wt.%-BT and ultimate strain after 1wt.%-CNTs and 40wt.%-BT. This study opens the door to integrate the FDM 3D printing technique, which contributes the advantages of design flexibility and simple fabrication at low cost, to empower the fabrication of temperature and strain sensor devices with enhanced mechanical robustness.

Chapter 5: Fabrication and Characterization of PVDF/Photopolymer Resin Composites for Piezoelectric Pressure Sensing Application using Stereolithography (SL) 3D printing

A simple and facile stereolithography (SL) 3D printing technique was utilized to fabricate piezoelectric photopolymer based polyvinylidene fluoride (PVDF) composites. Different process variables, such as solvent (N,N-Dimethylformamide, DMF) to PVDF ratio and PVDF solution to photopolymer resin ratio, were engineered to optimize the dispersion of the PVDF into the photopolymer resin so as to achieve the maximum piezoelectric coupling coefficient. Our results demonstrate that a ratio of 1:10 (PVDF:DMF) and 2wt.%-PVDF/photopolymer resin was optimal for the best dissolution of the PVDF, 3D printability, and piezoelectric properties. Under these conditions, the composite generated ± 0.121 nA under 80 N dynamic loading excitation. We believe that the findings of this work would promote many further studies on the low-cost mass production of flexible piezoelectric polymer composites with higher quality surface finish and design flexibility.

5.1 INTRODUCTION

Polyvinylidene fluoride (PVDF) is a widely studied polymer for its high ferroelectric response among polymers [38-40]. PVDF is a semi-crystalline material that has a unique molecular conformation with repeated unit of ($-CF_2-CH_2-$) that has large dipole moment of 7.58×10^{-28} C·cm [41]. It can be morphed into four different states; α, β, γ, and δ, where it is naturally found in the electrically unresponsive, α-phase [42]. Since its discovery, PVDF β-phase has gained a large amount scientific interest due to its unique planar zigzag (TTT) conformation that presents the highest net-dipole among its crystal phases [33]. Along with its high piezoelectric response, PVDF's chemical robustness, mechanical properties, high flexibility, and low-cost make it an ideal material to be used in the areas of tactile and strain sensors, transducer, and energy storage, etc.

Recently, additive manufacturing technology has been introduced to print piezoelectric 3D structures [71, 97, 155, 156]. It is reported that the fused deposition modeling (FDM) 3D printing process significantly improves homogeneous dispersion of piezoelectric ceramics nanoparticles in

the Poly(vinylidene) fluoride (PVDF) matrix. This enhances piezoelectric properties by alleviating agglomeration and removing voids and cracks [155, 156]. In addition, the FDM 3D printing technique is integrated with corona poling, which is one of the traditional poling processes, to simplify the fabrication of piezoelectric PVDF films through sequential processes [83]. Fabrication of FDM 3D printing based piezoelectric nanocomposites has improved in recent years contributing to the advances in design flexibility and simple fabrication of low-cost flexible sensor and energy storage devices. However, this FDM technique has some disadvantages, for example: weak tensile strength perpendicular to the build axis, poor surface finish, delamination from temperature fluctuation, and long building time compared to other additive manufacturing techniques [4]. In contrast, stereolithography (SL) technique has an ability to resolve these issues [157]. SL was the first additive manufacturing process introduced in the mid-1980s [158]. It builds a 3D structure based on photopolymerization of liquid resin comprised of monomer, photoinitiator, and other additives, which induce desired mechanical properties. For these reasons, using digital light processing (DLP) 3D printing, which are under the category of SL 3D printing, researchers designed piezoelectric composites to optically fabricate photosensitive polymer based $BaTiO_3$ (BT) nanocomposites with surface modification [71]. This photosensitive polymer was induced to encapsulate piezoelectric nanoparticles during photo-polymerization. This technique can produce 3D structure of piezoelectric composites with high piezoelectric coefficient (~39 pC/N) after thermal poling post-process [71]. More recently, a research has been carried out to study 3D printing of shape memory polymer (SMP) using the SL technique with a heated resin tank modification to enable SMP to be photopolymer printable [159].

Application of the SL 3D printing technique along with the utilization of the inherent piezoelectric properties of the PVDF to fabricate photopolymer based PVDF composites could be an attractive way for the fabrication of 3D structures. Moreover, SL 3D printing technique provides better surface finish, design flexibility, and low cost, compared to FDM 3D printing and other traditional methods such as solvent-casting, spin-coating, and hot-embossing [11]. However, the PVDF and photopolymer resin (PR) are not miscible with one another. Hence, mixing PVDF

directly with the PR produces sediments and agglomerates of PVDF and eventually produces poor piezoelectric response. This happens because of the agglomeration of a high amount of solid PVDF powder in the PR and thereby the interface between PVDF agglomerates and the PR are not strongly connected to each other. As a result, the external forces are unable to properly applied onto PVDF polymer molecular chains. Therefore, it is necessary to disperse each individual PVDF molecular chain into the PR, removing any agglomeration of PVDF and further enhancing the piezoelectric response. Typically, strong polar solvents, such as N,N-Dimethylformamide (DMF), N-Methyl-2-pyrrolidone (NMP), have been reported to be used to uniformly disperse PVDF molecular chains for piezoelectric sensor and Li-ion battery applications [160-163].

In this chapter, we investigated the fabrication of piezoelectric photopolymer based PVDF composites by exploiting the bottom-up projection based SL 3D printing technique. The performance of the 3D printed piezoelectric composites were evaluated in terms of β-phase transformation and piezoelectric coefficient. The β-phase transformation was investigated by the FTIR spectroscopy whereas the piezoelectric coefficient was measured by the dynamic load frame. The DMF was utilized as a solvent to uniformly disperse the PVDF molecular chains into the PR. In this regard, optimal ratios between PVDF and DMF, and between PVDF and the PR in terms of 3D printability, precipitation, and piezoelectric properties were also studied. Potentially, this work will enable low-cost mass production of flexible piezoelectric polymer composites with higher quality finished surface and design flexibility.

5.2 EXPERIMENTAL

5.2.1 Materials

Commercial photopolymer resin (clear resin, formlabs®) was used as the main component for photopolymer based PVDF composites. It is composed of mixtures of methacrylate monomer, methacrylate oligomer, and photoinitiator. PVDF powder (MW~534,000; Sigma-Aldrich) was used as piezoelectric polymer additives. N,N-Dimethylformamide (DMF, OmniSolv®) was used as the solvent material to disperse PVDF into the PR.

5.2.2 Synthesis and Fabrication

PVDF powder was dissolved in DMF at a temperature of 75 ˚C in a water bath for 15 min. The photopolymer resin was added to PVDF solution under maintained temperature. Then a total of 100g of final mixture was stirred by hand using a glass rod for 10 minutes to achieve uniform dispersion. Schematic synthesis process is illustrated in Figure 5.1(a). The commercial SL 3D printer (Form 1+) purchased from formlabs® was used to 3D print sample films in dimension of 30×5×1 mm as shown in Figure 5.1(b) and (c). A layer thickness of 100 microns was used for all the samples as the printing resolution. After 3D printing, the samples were cleansed with ethanol and then dried for 15 hours to remove the DMF. Electrical poling was conducted under 3 MV/m for 15 hours in order to test them in the dynamic load frame for piezoelectric response.

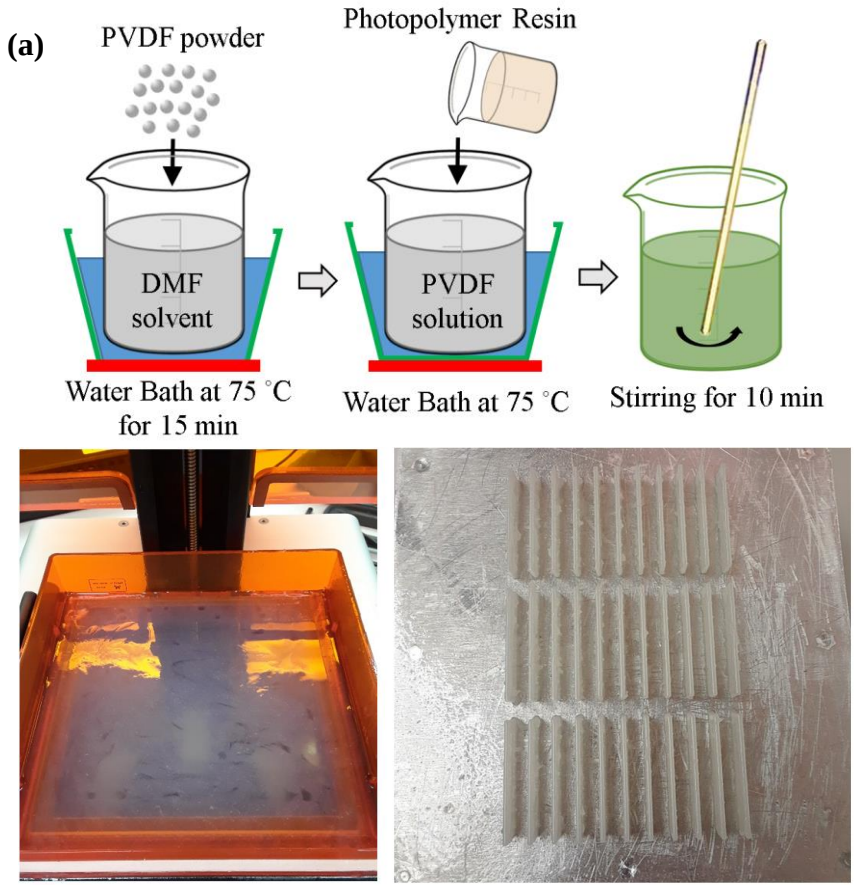

(c)

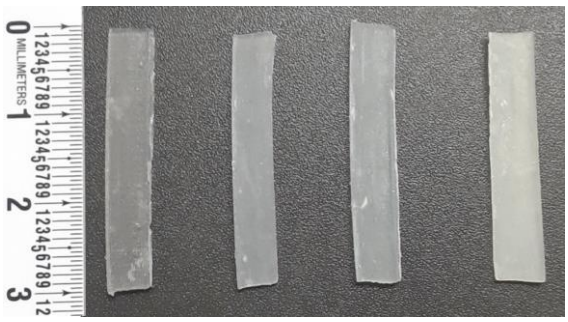

Figure 5.1: (a) Schematic illustration of the synthesis process for PVDF/Resin composites, (b) composites resin placed in resin tank of the bottom-up projection-based SL 3D printer and 3D printed composites samples on the bottom-up building platform, and (c) prepared samples for analyses (from left, pure PR, 1, 2.5, and 5wt.%-PVDF/PR).

5.2.3 Structural, Morphological, and Functional Characterizations

The morphology of the nanocomposites was observed in a scanning electron microscopy (SEM, TM-1000, Hitachi). X-ray diffraction was performed on each sample in order to characterize crystallinity using CuKα radiation on a D8 Discover diffractometer (Bruker, USA). Fourier transform infrared spectroscope (FTIR, Agilent Technologies Cary 630 ATR-IR) analysis was performed in the 600-1600 cm^{-1} wavenumber range at room temperature in order to characterize the infrared spectrum of absorption of 3D printed samples. Piezoelectric output current and voltage were measured by fatigue load frame (Bose ElectroForce) and Pico-ammeter (Keithley 6485).

5.2.4 Experimental Setup

To quantify the piezoelectric property of PVDF/Resin composites, 3D printed samples were prepared with 3×10 mm silver paint electrodes in top and bottom surfaces. The electrodes were then extended with Cu tape to allow a proper connection with the Pico-ammeter for current measurement as shown in Figure 5.2(a). Dynamic force was applied on the 3D printed samples to measure periodic output current. Fatigue load frame generated 30 cyclic loads on the sample under different ranges from 0 to 20, 40, 60, and 80 N at 1 Hz while the Pico-ammeter was used to measure current output. To prevent noise from the fatigue machine during the measurement, two grips holding the sample were covered with insulating tape as shown in Figure 5.2(b).

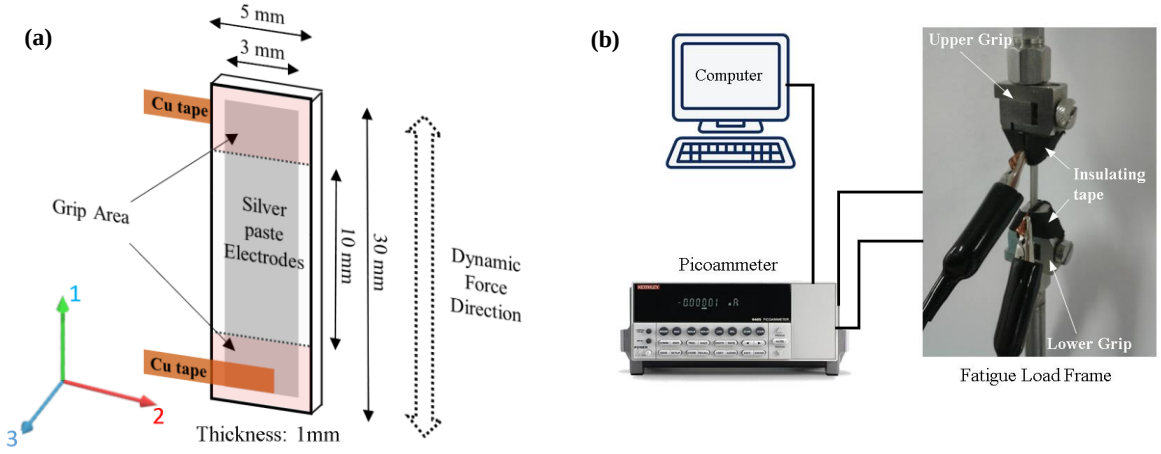

Figure 5.2: Schematic illustration of (a) sample and electrode design and (b) the experimental setup for piezoelectric output measurement.

5.3 Results and Discussion

5.3.1 Polymerization Mechanism

Figure 5.3 schematically illustrates the photopolymerization of the methacrylate monomer and oligomer along with the PVDF that is previously dispersed in the PR resin. When the mixture is exposed to UV light, the photoinitiator absorbs the light energy and dissociates into free radicals, which are highly reactive and initiates the radical catalyzed polymerization of the oligomer and the monomer. This step where free radicals are generated called as the initiation step of the photopolymerization. After the radical is generated, it triggers the polymerization of the monomer and the oligomers increasing the chain length and cross-linking of the polymer, which is also called as the propagation. In detail, each free photogenerated radical has an unpaired electron and are highly unstable so that this free radical attacks and breaks the C=C of the methacrylate monomer and the oligomer into repeating units of $[\text{-C-C-}]_n$ to combine and create myriads of more radicals [164]. These newly generated radical attacks more of the C=C of the methacrylate and combine with them to form the long polymer chain with due cross-linking. This process continues until every single monomer and oligomer is consumed to form the polymer [157]. At this stage of the polymerization the propagation step stops and it leads to the termination step. In termination step,

two radicals combine together to make a sigma bond and this step consumes all the radicals and terminates the polymerization process. However, during the propagation step, the PVDF molecules become trapped within the 3-dimensional cross-linked structure of the polymer.

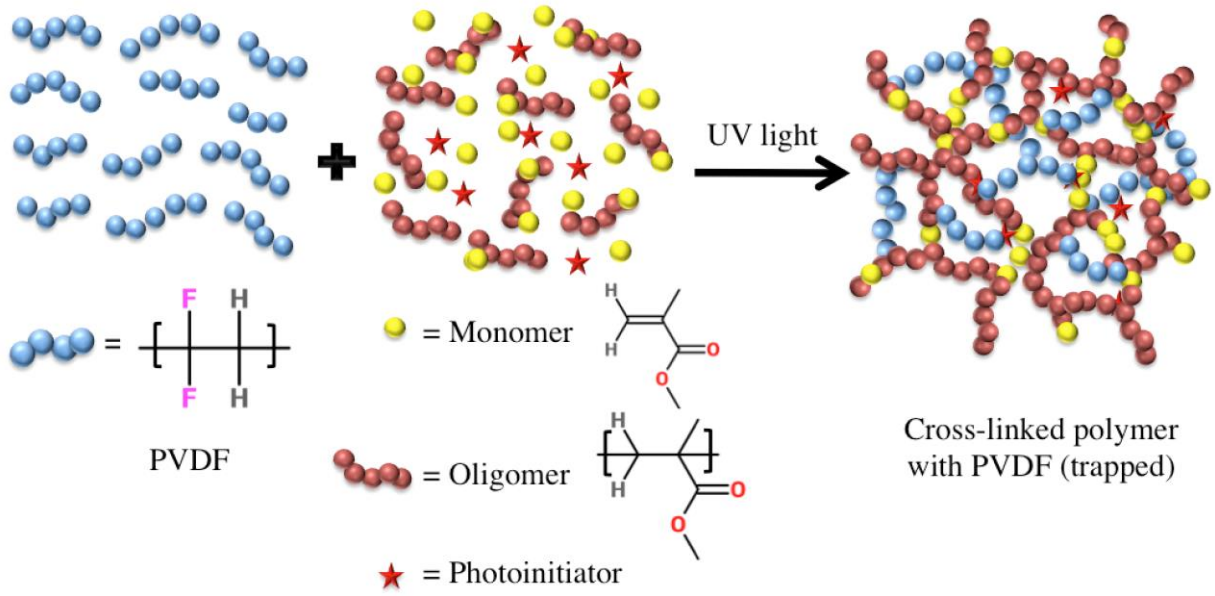

Figure 5.3: Schematic representation for the photopolymerization of the methacrylate monomer and oligomers along with the PVDF solution in DMF.

5.3.2 Optimization of Piezoelectricity and Manufacturability

Firstly, it is necessary to determine whether or not the dissolution process of PVDF is required in order to attain maximal piezoelectricity. Therefore, 5 and 15wt.%-PVDF powders were directly dispersed into the PR at 75 ˚C and sonicated for 15 min for uniform dispersion. Afterward, all the processes were performed as described in Experimental section. Characterization of piezoelectricity was simplified by using a fatigue load frame and the Pico-ammeter to measure the output current from the SL 3D printed composites. Figure 5.4(a) shows that current output of SL 3D printed composites slightly increases to ± 0.015 nA, as the PVDF amount increases from 0 to 15wt.%. This insignificant enhancement of piezoelectricity observed can be explained by the PVDF agglomerates present in the resin. In addition, the low piezoelectric coupling efficiency between PVDF agglomerates and the PR have led to low piezoelectric output current. In order to

avoid the agglomeration of the PVDF and enhance the coupling efficiency, strong solvent is necessary to dissolve the PVDF powder homogeneously in the PR. In this study, PVDF powder is dissolved in DMF as a strong polar solvent, however, it was observed that the PVDF precipitated in the PR because it is assumed that the PR is much weaker (i.e. poorer) solvent for PVDF than DMF. It was found that there is a saturation point where the PR can accommodate PVDF solution. Similar phenomena were reported by other studies as well [165-167]. However, this study demonstrates various process variables and conditions to optimize the dispersion in the PR without the agglomeration of the PVDF, which is eventually compatible with SL 3D printing technique. By experimental iteration changing ratio of PVDF:DMF in the PR, the optimal ratio of PVDF and DMF for the PR can be obtained. As shown in Figure 5.4(b), the precipitation percentage diminishes from 11.6 to 5wt.% as increasing the DMF amount. This means that more DMF solvent reduces precipitation of PVDF molecules and helps it disperse within the PR. Figure 5.4(c) shows piezoelectric current output results on samples made of 2wt.%-PVDF/PR with different DMF solvent ratios. It was found that 1:10 ratio performs the best compared to other ratios. It generated an output current of ± 0.055 nA which is 3.5 times higher than the one from 15wt.%-PVDF/PR without dissolution process. 1:15 ratio shows lower current output because it is assumed that higher amount of DMF solvent, which is almost close to amount of the PR, dilutes PVDF content as well as the PR. In addition, since 1:15 ratio contains higher DMF solvents, the final product becomes softer as ratio increases. Additionally, the photopolymer resin becomes non-printable at more than 1:15 ratio due to overwhelmed amount of DMF solvent.

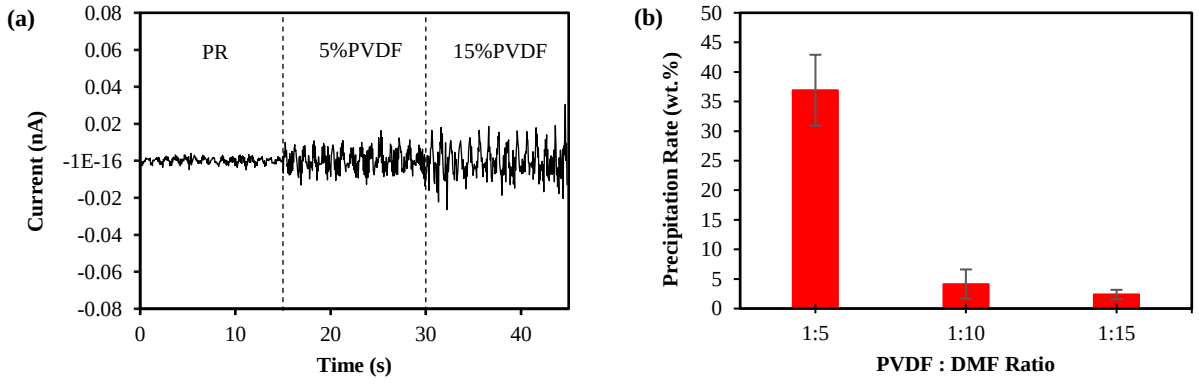

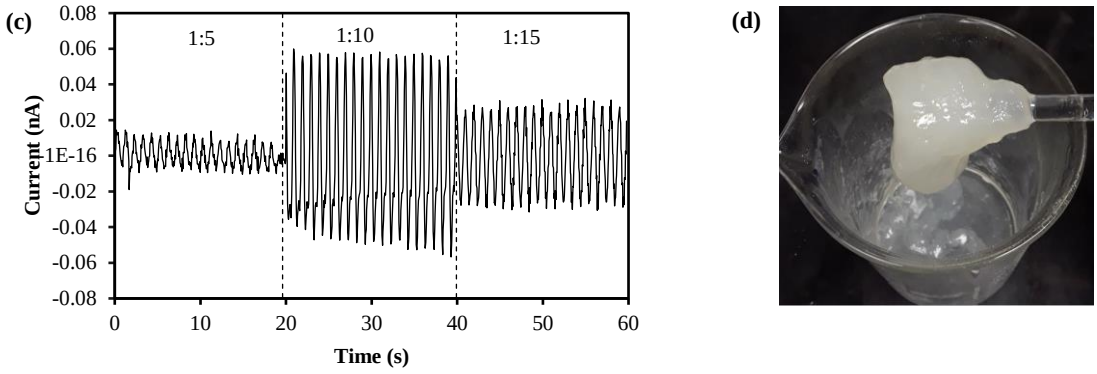

Figure 5.4: (a) Piezoelectric output current of pure PR, 5 and 15wt.%-PVDF/PR composites under dynamic force of 60 N at 1 Hz before dissolution treatment, (b) precipitation rate (wt.%) at PVDF:DMF ratio of 1:5, 1:10, and 1:15, and (c) piezoelectric output current of 2wt.%-PVDF/PR at PVDF:DMF ratio of 1:5, 1:10, and 1:15, and (d) bulk precipitation polymerization observed when PVDF was mixed with PR in a 1:5 ratio.

5.3.3 Characterizations by SEM, XRD, FTIR Analyses

Based on attained optimal ratio (1:10) for PVDF:DMF, increasing contents (1, 2, 4, 5wt.%) of PVDF within the PR and pure PR are 3D printed and characterized to analyze surface morphology and phase of PVDF of each sample using SEM, XRD, and FTIR. In Figure 5.5(a-b), surface images of 5wt.%-PVDF/PR without DMF dissolution treatment indicate that a higher amount of PVDF particles was agglomerated on the PR matrix, indicating that PVDF particles are not soluble in the PR. Figure 5.5(c) shows surface image of pure PR which has smooth surface. It is noted that white particles shown on the surface are debris or contaminates. On the contrary of pure PR, surface of the sample becomes coarser as increasing PVDF as shown in Figure 5.5(d-e). It is inferred that precipitation polymerization in the micro-scale has occurred within the PR.

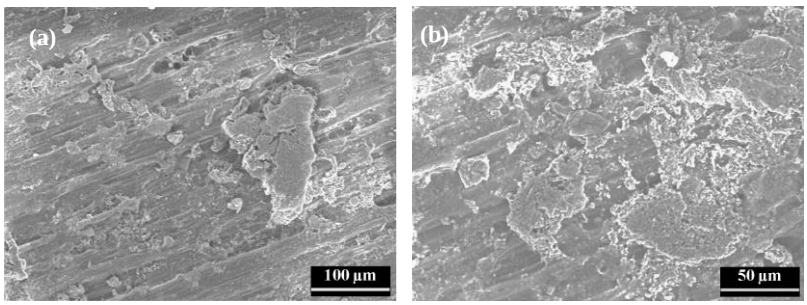

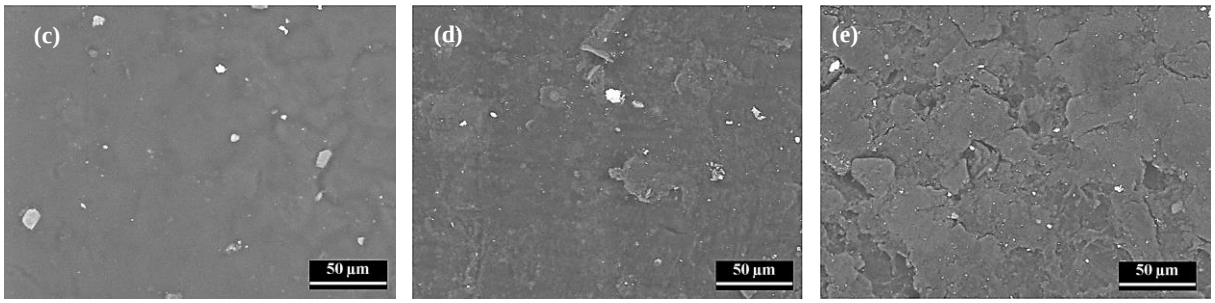

Figure 5.5: SEM images for surfaces of 3D printed (a-b) 5wt.%-PVDF/PR composites without DMF dissolution treatment, (c) pure PR, (d) 2wt.%-PVDF/ PR, and (e) 5wt.%-PVDF/PR composites with DMF dissolution treatment.

The XRD patterns of each sample are characterized as shown in Figure 5.6(a). Reflections at 20.0° (110) and 18.4° (020) correspond to α-phase of PVDF are observed at all the samples that contains PVDF [155]. Since PVDF content in 3D printed composites is small, quantitative analysis for β- and γ-phases transformation using the XRD would be difficult to be determined. Therefore, the FTIR analysis was conducted for quantitative analysis of phase transformation on PVDF after electric poling process and determine the presence of different functional groups in the PVDF/PR composites.

The FTIR spectra for α-, β-, and γ-phases were analyzed at IR absorption bands of 762, 808, and 835 cm^{-1}, respectively as shown in Figure 5.6(b) [22, 26, 30, 155]. Due to transparency of the 1 and 2wt.%-PVDF/PR samples and limited sensitivity of FTIR instrument on small PVDF concentration, it is assumed that peaks correspond to α- and β-phases were not detected except for 4 and 5wt.%-PVDF/PR samples. A peak correspond to γ-phase was slightly shifted to the right and grew sharply as PVDF content increases, meaning that electric poling process has induced some of PVDF dipoles to be aligned for active materials. The FTIR spectra of the pure PR shows the presence of hydroxyl (O-H), aliphatic (C-H), and carbonyl (C=O) functional groups by their characteristic stretching vibrations at 3331, 2920, and 1700 cm^{-1}, respectively as shown in Figure 5.7(a) [128, 168, 169]. The ester (C-O-CH_3) functional group could also be identified at 1240 and 1104 cm^{-1} [170]. The alkyl CH bending of CH_3 and CH_2 could be located at 1452 and 1530 cm^{-1} [170]. All these functional groups indicate the presence of methacrylate functional group in the

polymer with the presence of some water or alcohol as the impurities. It is believed the water or alcohol came from the photopolymer resin solution, where they were used as the solvent of the photopolymer resin. On the other hand, as shown in Figure 5.7(b), the FTIR spectra of the 5wt.%-PVDF/PR shows some additional peaks, which are characteristic to the functional group of the PVDF. For example, the C-F stretching vibrations of the α, β, and γ-crystalline phases of the PVDF could be observed at 762, 808, and 835 cm^{-1}, respectively [171]. The presence of some DMF could also be observed in the composites, which came from the solvent that was used for the dissolution of the PVDF.

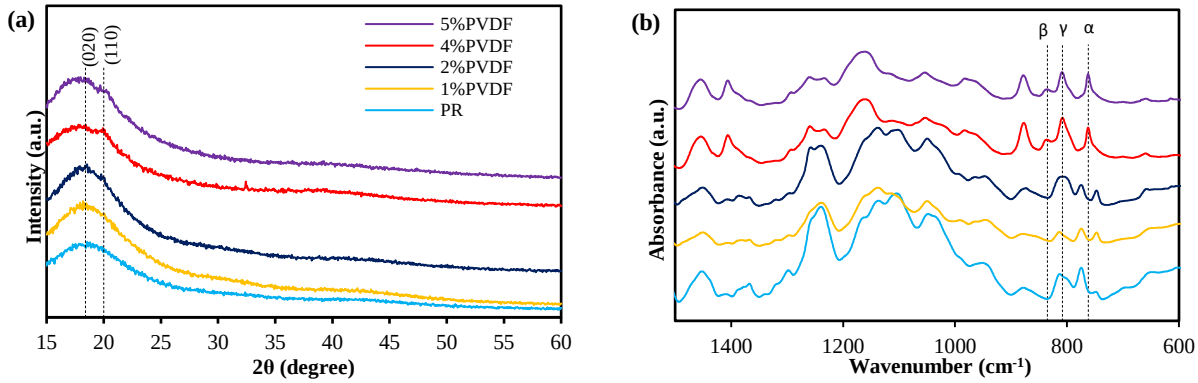

Figure 5.6: (a) XRD patterns and (b) FTIR spectra for pure resin, 1, 2, 4, and 5wt.%-PVDF/PR composites before and after electrical poling, respectively.

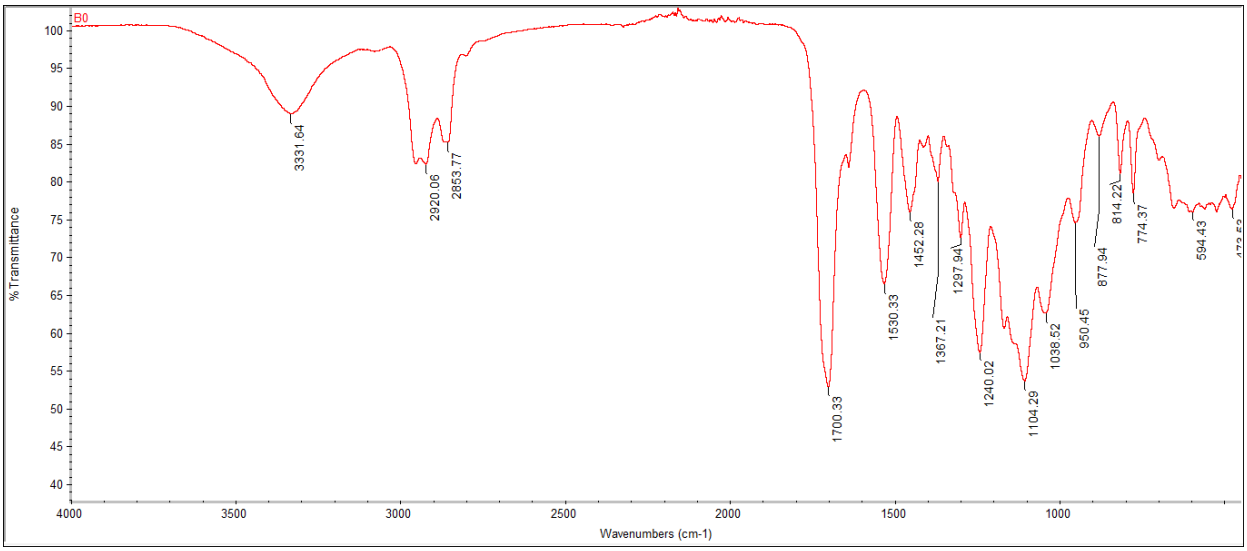

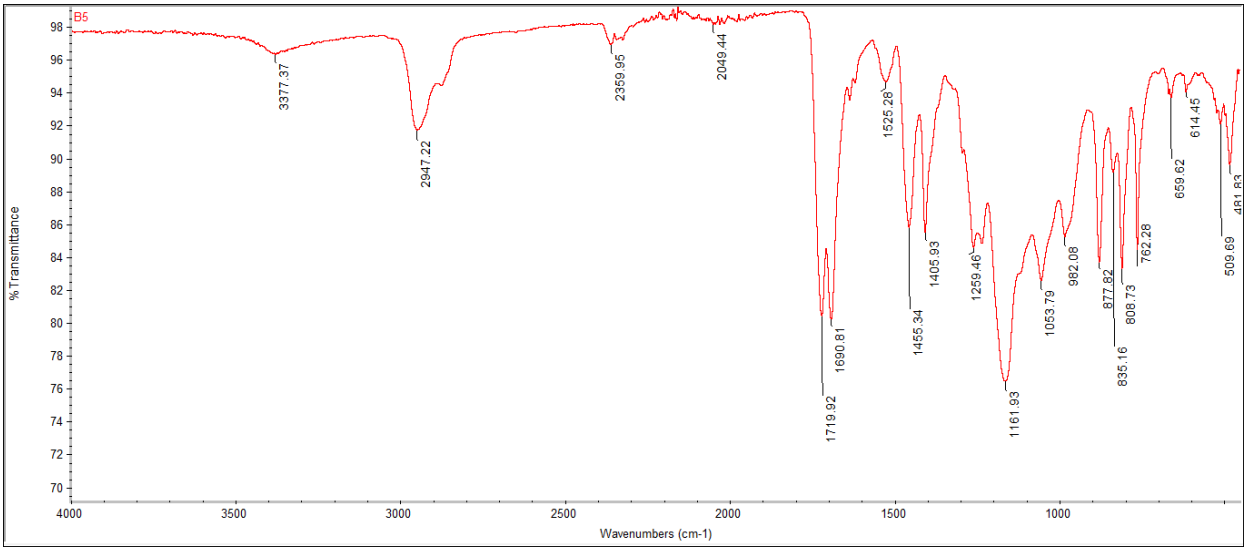

Figure 5.7: FTIR spectra of a) pure photopolymer resin and b) 5wt.%-PVDF/PR.

5.3.4 Piezoelectric properties

SL 3D printed composites sample with increasing PVDF contents in the PR and pure PR were tested in a fatigue load frame to measure piezoelectric responses and piezoelectric coefficient (d_{31}). Figure 5.8 shows the results for current output and piezoelectric coefficients of pure PR, 1, 2, 2.5, 4, 5wt.%-PVDF/PR. In Figure 5.8, as increasing PVDF contents in the PR, generated current outputs drastically increase by ± 0.053 nA at 2wt.%-PVDF and gradually decrease. This can be explained based on the fixed PVDF:DMF ratio to 1:10, DMF amount becomes larger as increasing PVDF content, thus the total mixture of composites resin is too diluted with DMF solvent. Even though PVDF has a greater percentage in terms of resin, it is lower overall due to the DMF used to dissolve it. This will lower the piezoelectric response. Based on the current output, d_{31} of each sample can be calculated by following [172]:

$$D_i = d_{ij}\sigma_j \tag{1}$$

where D_i is the electrical displacement, σ_j is the applied stress, and d_{ij} is the piezoelectric coefficient. In this case, subscripts i and j are defined as 3 and 1, respectively as

shown in Figure 5.2Figure (a). Therefore, the equation can then be expressed as $D_3 = d_{31}\sigma_3$. Considering areas of electrode and cross section, Eq. (1) can then be expressed as

$$\frac{Q}{A_{elect}} = d_{31}\frac{\nu F}{A_{cross}} \tag{2}$$

where Q is charge, A_{elect} and A_{cross} are areas of electrode and cross-section, respectively, ν is Poisson's ratio, and F is an applied force. Then, piezoelectric coefficient can be expressed as

$$d_{31} = \frac{(Q_{max}-Q_{min})A_{cross}}{A_{elect}\ \nu F} \tag{3}$$

where Poisson's ratio is determined as 0.333 [58] and Q_{max} and Q_{min} are maximum and minimum charges, respectively where measured for each cycle. These charges can be attained with numerical integration expressed as

$$Q_{(i)} = Q_{i-1}\frac{I_i + I_{i+1}}{2} \times (t_{i+1} - t_i) \tag{4}$$

where I_i is output current at ith and t_i is the time at ith. And after each 30 peak is calculated through the Eq. (3), taking the average on d_{31} of each 30 peaks turned to the piezoelectric coefficient as shown in Figure 5.8. The result of d_{31} as shown in Figure 5.8 indicates that SL 3D printed 2wt.%-PVDF/PR has the highest d_{31} with 0.014 pC/N which is 46 % higher than the one from the pure PR. Additionally, d_{31} shows the same trend compared with the piezoelectric current output.

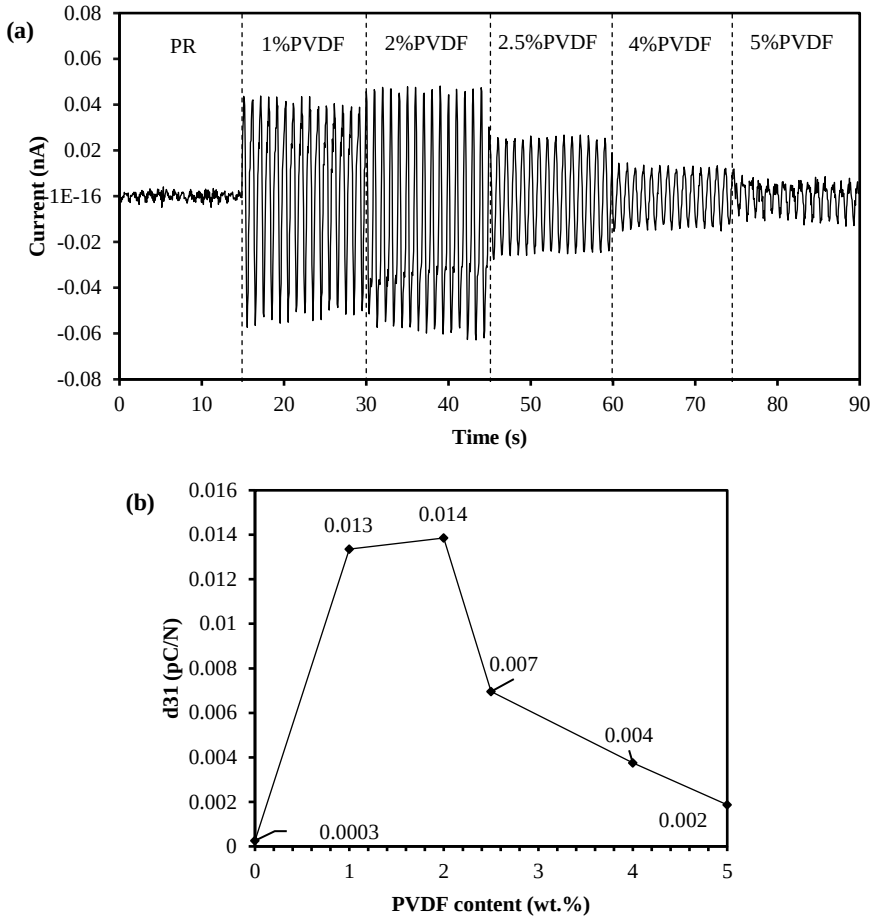

Figure 5.8: Measurement of piezoelectric properties: (a) current output and (b) piezoelectric coefficients of pure PR, 1, 2, 2.5, 4, and 5wt.%-PVDF/PR under applied force of 60 N and 1 Hz.

Different dynamic forces from 20 to 80 N were applied on the 2wt.%-PVDF/PR composites as shown in Figure 5.9. As increasing the force applied on the sample, the current output gradually increases and reaches ± 0.121 nA under 80 N. Additionally, the sample ruptured when 90 N were applied.

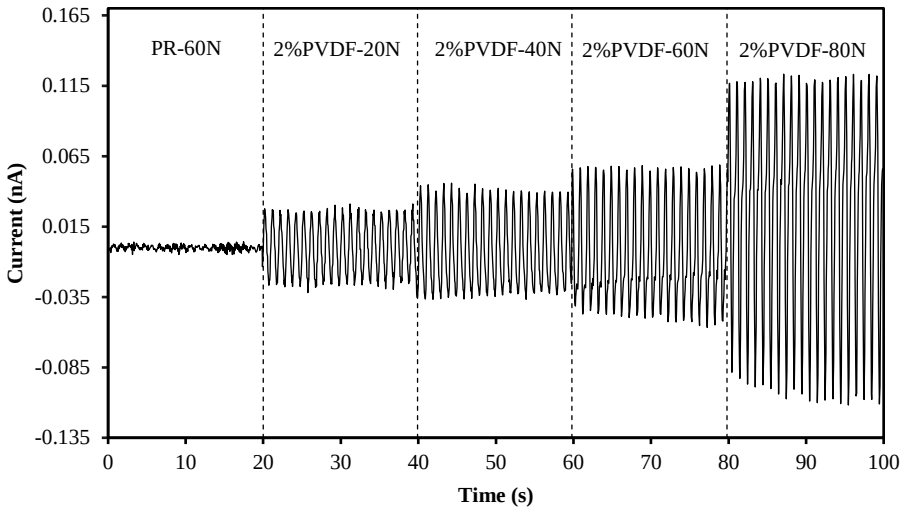

Figure 5.9: Piezoelectric current output generated from 2wt.%-PVDF/PR at increasing applied forces from 20 to 80 N.

5.4 SUMMARY

Piezoelectric photopolymer resin based PVDF composites were fabricated using the SL 3D printing technique. The composites were characterized using XRD, SEM, and dynamic testing. Dynamic testing and pico-ammeter where used to measure the piezoelectric properties of the composite and its potential use in pressure sensing applications. Due to the insolubility between PVDF and the PR causing PVDF sediments and agglomerates, DMF solvent was used to disperse PVDF molecular chains uniformly into the PR. Optimal ratio between PVDF and DMF was experimentally investigated 1:10 with high performing piezoelectric properties and manufacturability. At fixed 1:10 ratio, increasing amount of PVDF content within the PR was studied and it was found that 2wt.%-PVFD/PR composites show the highest piezoelectric properties with ± 0.053 nA and 0.014 pC/N. At increased dynamic forces, it was observed that the composites generate ± 0.180 nA under 80 N. These results demonstrate the feasibility in its commercial application for pressure sensors. These compounds and the SL 3D printing technique are expected to broaden the use of additive manufacturing to print piezoelectric nanocomposite devices for sensor applications. For further research, other solvent can be studied to solubilize PVDF amount in the PR in order to enhance the piezoelectricity.

Chapter 6: Conclusions

6.1 Brief Summary of Dissertation and Results

In this dissertation, feasibility of 3D printing piezoelectric devices has been studied with integration of traditional poling process and nanomaterials for multi-functional nanocomposites. Firstly, the piezoelectric property of FDM 3D printed and solvent-casted BT/PVDF films was characterized and compared in terms of morphological and phase transformation analyses and piezoelectric performance. It was found that traditional fabrication process yields higher degree of agglomeration, porosities, and cracks in comparison with 3D printed one. However, XRD spectra show the significant homogeneous dispersion of BT particles in the 3D printed film compared to solvent-cast one. Piezoelectric responses show higher current output in 3D printed film than solvent-cast one due to the homogeneous dispersion and alleviation of agglomeration for BT particles as well as removing porosities and cracks resulted from the filament extrusion and 3D printing process.

Using this found advantages of FDM 3D printing process, it was integrated with corona poling process to fabricate PVDF piezoelectric film for sensor application. Stronger electric voltage transforms higher β-phase content resulted from FTIR analysis and produces greater current output and piezoelectric coefficient (d_{31}). The IPC process can lead to piezoelectric output current up to ± 0.106 nA while applying 12kV electric voltage during the IPC process. The results indicate that IPC process is able to produce the piezoelectric PVDF device that can be commercialized for mass production. Moreover, BT/PVDF composites were fabricated using an integrated 3D printing and electrical in-situ poling process for sensor applications. It was investigated that the output current at 15wt.%-BT increased by 30.41% and 1033%, respectively when compared to non-poled PVDF due to BT inclusion. In SEM images, larger agglomerates and defects (i.e. voids and cracks) were formulated with the increase of BT and resulted in degradation of tensile strength but significantly higher toughness. In addition, the inclusion of BT also increased the fatigue strength of PVDF. The highest tensile and fatigue strengths were seen at 3wt.%-BT and gradually decreased as the filler content increased because of defect creation, poor

load transmission, stress accumulation from agglomerates and aggregated filler during tensile and fatigue life measurement.

Following that 3D printing of BT and PVDF nanocomposites, MWCNTs was dispersed in BT/PVDF for improving mechanical coupling coefficient between PVDF and BT nanoparticles. It is demonstrated that MWCNTs plays important roles of transforming PVDF α- to β-phase and enhancing the efficiency of mechanical to electrical conversion between BT and PVDF interfaces. The increasing MWCNTs' percent in the system results in an increase in electrical output which, indicates that the increased surface areas of MWCNTs interacts well with BT nanoparticles, therefore providing a stress reinforcing effect between the BT and PVDF. The highest d_{31} is 0.13 pC/N at 0.4wt.%-MWCNTs/18wt.%-BT/PVDF, comparable to pure BT ceramic. Bending and pressing with fingers generates about ±120 mV and ±435 mV, respectively, which demonstrate well feasibility in its commercial application. Using the same 3D printed nanocomposites, dielectric properties were studied for capacitor application by utilizing effect of FDM 3D printing process which is effective dispersion of nanoparticles and alleviation of agglomerates/micro-cracks/voids by the 3D printing process can be achieved to enhance dielectric property. The addition of CNT and BT nanoparticles into a PVDF matrix improve dielectric property but the thresholds of each CNT and BT in PVDF matrix are found near 1.7wt.% and 60wt.% respectively and the highest dielectric constant is obtained 118 at 1.7wt.%-CNT/45wt.%-BT within dielectric loss of 0.11 at 1 kHz. In addition, the energy density of 0.45 J cm^{-1} at 39 MVm^{-1} was achieved in the 3D printed nanocomposites containing 1wt.%-CNT/60wt.%-BT, which are relatively higher values achieved than other past research works. In addition, the capacitance property of the 3D printed nanocomposites can be utilized in sensing the changes of temperature and strain. The highest sensibility for temperature is observed in nanocomposites containing 1.7wt.%-CNTs/60wt.%-BT/PVDF which are the maximum loading for BT and CNTs percolation threshold. The highest sensibility for strain is observed in nanocomposites containing 1wt.%-CNTs/12wt.%-BT/PVDF. The nanocomposites above 1wt.%-CNTs resulted in the degradation of the changing rate in the capacitance. This degradation was because the CNTs cluster effectively destructs

capacitance as the strain is induced. It is observed that the addition of more than 12wt.% of BT particles degrades the changing rate in the capacitance because Poisson's rate is not significant at a higher loading system. The combination between CNTs and BT inclusions contributes to a high changing rate in the capacitance when it comes to the temperature and strain changes. The superior mechanical performance is observed in nanocomposites containing 1wt.%-CNTs/12wt.%-BT/PVDF showing 24.2 MPa and 579 % for mechanical stress and strain, respectively. These improved mechanical properties stem from CNTs and BT reinforcements. However, ultimate stress starts decreasing after 1wt.%-CNTs and 12wt.%-BT and ultimate strain after 1wt.%-CNTs and 40wt.%-BT.

Lastly, Stereolithography 3D printing technique was utilized to fabricate the piezoelectric photopolymer resin based PVDF composites. Due to the insolubility between PVDF and the PR causing PVDF sediments and agglomerates, DMF solvent was used to disperse PVDF molecular chains uniformly into the PR. Optimal ratio between PVDF and DMF was experimentally investigated 1:10 with high performing piezoelectric properties and manufacturability. At fixed 1:10 ratio, increasing amount of PVDF content within the PR was studied and it was found that 2wt.%-PVFD/PR composites show the highest piezoelectric properties with ± 0.053 nA and 0.014 pC/N. At increased dynamic forces, it was observed that the composites generate ± 0.180 nA under 80 N. These results demonstrate the feasibility in its commercial application for pressure sensors. These compounds and the SL 3D printing technique are expected to broaden the use of additive manufacturing to print piezoelectric nanocomposite devices for sensor applications.

6.2 Recommendations for Future Work

This dissertation has performed fundamental research and applications for pressure sensor and energy storage. The studied CNT/BT/PVDF nanocomposites have lots of potentials to be explored more in other areas. This 3D printed nanocomposites can be investigated for energy harvesting application if there can be developed rectifying circuit that can harvest current output in range of pico-scale. Additionally, since BT and PVDF are under ferroelectric category therefore, pyroelectric effect can be investigated with or without inclusion of CNT nanoparticles which may affect pyroelectric respond due to high thermal conductivity.

SL 3D printing of PVDF within photopolymer resin was studied in this dissertation. SL 3D printing, as opposed to FDM technique, provide higher surface resolution and finish for 3D structure. This technique doesn't require much post process and treatment as much as FDM one. This research can be continuously carried over by including BT and CNT nanoparticles in photopolymer resin-based PVDF in order to improve piezoelectric and mechanical performances.

Lastly, both FDM and SL 3D printing techniques must incorporate with base materials such as thermoplastic and photopolymer resin to build up 3D structure due to their unique 3D printing setup. Therefore, it is impossible to 3D print high volume percent of piezoelectric ceramics. Paste extrusion (PE) technique can be an alternative method to print high volume piezoelectric ceramics with small amount of resin as a sacrificial material during sintering process. This PE 3D printing of high volume piezoelectric ceramics would overcome current limitation of piezoelectric ceramics fabrication.

References

[1] S. Zhang, H. J. Lee, and T. R. Shrout, "NBT based lead-free piezoelectric materials for high power applications," ed: Google Patents, 2013.

[2] D. Fu and M. Itoh, "Role of Ca off-centering in tuning the ferroelectric phase transitions in Ba (Zr, Ti) O3 system," *arXiv preprint arXiv:1503.00406,* 2015.

[3] B. Jaffe, *Piezoelectric ceramics* vol. 3: Elsevier, 2012.

[4] M. Vaezi, S. Chianrabutra, B. Mellor, and S. Yang, "Multiple material additive manufacturing–Part 1: a review: this review paper covers a decade of research on multiple material additive manufacturing technologies which can produce complex geometry parts with different materials," *Virtual and Physical Prototyping,* vol. 8, pp. 19-50, 2013.

[5] R. Gauvin, Y.-C. Chen, J. W. Lee, P. Soman, P. Zorlutuna, J. W. Nichol, *et al.*, "Microfabrication of complex porous tissue engineering scaffolds using 3D projection stereolithography," *Biomaterials,* vol. 33, pp. 3824-3834, 2012.

[6] A. Cohen, A. Laviv, P. Berman, R. Nashef, and J. Abu-Tair, "Mandibular reconstruction using stereolithographic 3-dimensional printing modeling technology," *Oral Surgery, Oral Medicine, Oral Pathology, Oral Radiology, and Endodontology,* vol. 108, pp. 661-666, 2009.

[7] F. P. Melchels, J. Feijen, and D. W. Grijpma, "A review on stereolithography and its applications in biomedical engineering," *Biomaterials,* vol. 31, pp. 6121-6130, 2010.

[8] Y. Rao, S. Ogitani, P. Kohl, and C. Wong, "Novel polymer–ceramic nanocomposite based on high dielectric constant epoxy formula for embedded capacitor application," *Journal of Applied Polymer Science,* vol. 83, pp. 1084-1090, 2002.

[9] M. T. Sebastian and H. Jantunen, "Polymer–ceramic composites of 0–3 connectivity for circuits in electronics: a review," *International Journal of Applied Ceramic Technology,* vol. 7, pp. 415-434, 2010.

[10] A. Salimi and A. Yousefi, "Conformational changes and phase transformation mechanisms in PVDF solution- cast films," *Journal of Polymer Science Part B: Polymer Physics,* vol. 42, pp. 3487-3495, 2004.

[11] A. Chiolerio, M. Lombardi, A. Guerriero, G. Canavese, S. Stassi, R. Gazia, *et al.*, "Effect of the fabrication method on the functional properties of BaTiO3: PVDF nanocomposites," *Journal of Materials Science,* vol. 48, pp. 6943-6951, 2013.

[12] Y. Jiang, Y. Ye, J. Yu, Z. Wu, W. Li, J. Xu, *et al.*, "Study of thermally poled and corona charged poly (vinylidene fluoride) films," *Polymer Engineering & Science,* vol. 47, pp. 1344-1350, 2007.

[13] E. Wong, S. Koh, K. Lee, and R. Rajoo, "Advanced moisture diffusion modeling and characterisation for electronic packaging," in *Electronic Components and Technology Conference, 2002. Proceedings. 52nd*, 2002, pp. 1297-1303.

[14] M. Rong, M. Zhang, and W. Ruan, "Surface modification of nanoscale fillers for improving properties of polymer nanocomposites: a review," *Materials science and technology,* vol. 22, pp. 787-796, 2006.

[15] P. Martins, C. Caparros, R. Gonçalves, P. Martins, M. Benelmekki, G. Botelho, *et al.*, "Role of nanoparticle surface charge on the nucleation of the electroactive β-poly (vinylidene fluoride) nanocomposites for sensor and actuator applications," *The Journal of Physical Chemistry C,* vol. 116, pp. 15790-15794, 2012.

[16] F. Ning, W. Cong, J. Qiu, J. Wei, and S. Wang, "Additive manufacturing of carbon fiber reinforced thermoplastic composites using fused deposition modeling," *Composites Part B: Engineering,* vol. 80, pp. 369-378, 2015.

[17] K. Nagata and T. Kiyota, "Piezoelectric Properties of Low Coercive-Field BaTiO3 Ceramics and Its Application," *Japanese journal of applied physics,* vol. 28, p. 98, 1989.

[18] B. Dickens, E. Balizer, A. DeReggi, and S. Roth, "Hysteresis measurements of remanent polarization and coercive field in polymers," *Journal of applied physics,* vol. 72, pp. 4258-4264, 1992.

[19] B. Vazquez, H. Vasquez, and K. Lozano, "Preparation and characterization of polyvinylidene fluoride nanofibrous membranes by forcespinning™," *Polymer Engineering & Science,* vol. 52, pp. 2260-2265, 2012.

[20] C. Muralidhar and P. Pillai, "XRD studies on barium titanate (BaTiO3)/polyvinylidene fluoride (PVDF) composites," *Journal of materials science,* vol. 23, pp. 410-414, 1988.

[21] D. M. Esterly and B. J. Love, "Phase transformation to β- poly (vinylidene fluoride) by milling," *Journal of Polymer Science Part B: Polymer Physics,* vol. 42, pp. 91-97, 2004.

[22] X. Cai, T. Lei, D. Sun, and L. Lin, "A critical analysis of the α, β and γ phases in poly (vinylidene fluoride) using FTIR," *RSC Advances,* vol. 7, pp. 15382-15389, 2017.

[23] R. Gregorio and E. Ueno, "Effect of crystalline phase, orientation and temperature on the dielectric properties of poly (vinylidene fluoride)(PVDF)," *Journal of Materials Science,* vol. 34, pp. 4489-4500, 1999.

[24] S. F. Mendes, C. M. Costa, C. Caparrós, V. Sencadas, and S. Lanceros-Méndez, "Effect of filler size and concentration on the structure and properties of poly (vinylidene fluoride)/BaTiO3 nanocomposites," *Journal of Materials Science,* vol. 47, pp. 1378-1388, 2012.

[25] S. K. Ghosh, M. M. Alam, and D. Mandal, "The in situ formation of platinum nanoparticles and their catalytic role in electroactive phase formation in poly (vinylidene fluoride): a simple preparation of multifunctional poly (vinylidene fluoride) films doped with platinum nanoparticles," *RSC Advances,* vol. 4, pp. 41886-41894, 2014.

[26] D. Mandal, K. Henkel, and D. Schmeißer, "The electroactive β-phase formation in Poly (vinylidene fluoride) by gold nanoparticles doping," *Materials Letters,* vol. 73, pp. 123-125, 2012.

[27] M. M. Alam, S. K. Ghosh, D. Sarkar, S. Sen, and D. Mandal, "Improved dielectric constant and breakdown strength of γ-phase dominant super toughened polyvinylidene fluoride/TiO2 nanocomposite film: an excellent material for energy storage applications and piezoelectric throughput," *Nanotechnology,* vol. 28, p. 015503, 2016.

[28] T. K. Sinha, S. K. Ghosh, R. Maiti, S. Jana, B. Adhikari, D. Mandal, *et al.*, "Graphene-Silver-Induced Self-Polarized PVDF-Based Flexible Plasmonic Nanogenerator Toward the Realization for New Class of Self Powered Optical Sensor," *ACS applied materials & interfaces,* vol. 8, pp. 14986-14993, 2016.

[29] A. Tamang, S. K. Ghosh, S. Garain, M. M. Alam, J. r. Haeberle, K. Henkel, *et al.*, "DNA-Assisted β-phase Nucleation and Alignment of Molecular Dipoles in PVDF Film: A Realization of Self-Poled Bioinspired Flexible Polymer Nanogenerator for Portable Electronic Devices," *ACS applied materials & interfaces,* vol. 7, pp. 16143-16147, 2015.

[30] B. S. Ince-Gunduz, R. Alpern, D. Amare, J. Crawford, B. Dolan, S. Jones, *et al.*, "Impact of nanosilicates on poly (vinylidene fluoride) crystal polymorphism: Part 1. Melt-crystallization at high supercooling," *Polymer,* vol. 51, pp. 1485-1493, 2010.

[31] M. Benz and W. B. Euler, "Determination of the crystalline phases of poly (vinylidene fluoride) under different preparation conditions using differential scanning calorimetry and infrared spectroscopy," *Journal of applied polymer science,* vol. 89, pp. 1093-1100, 2003.

[32] K. Matsushige, K. Nagata, S. Imada, and T. Takemura, "The II-I crystal transformation of poly (vinylidene fluoride) under tensile and compressional stresses," *Polymer,* vol. 21, pp. 1391-1397, 1980.

[33] A. Salimi and A. Yousefi, "Analysis method: FTIR studies of β-phase crystal formation in stretched PVDF films," *Polymer Testing,* vol. 22, pp. 699-704, 2003.

[34] S. K. Ghosh and D. Mandal, "Efficient natural piezoelectric nanogenerator: Electricity generation from fish swim bladder," *Nano Energy,* vol. 28, pp. 356-365, 2016.

[35] S. K. Ghosh, T. K. Sinha, B. Mahanty, and D. Mandal, "Self- poled Efficient Flexible "Ferroelectretic" Nanogenerator: A New Class of Piezoelectric Energy Harvester," *Energy Technology,* vol. 3, pp. 1190-1197, 2015.

[36] S. K. Ghosh and D. Mandal, "High-performance bio-piezoelectric nanogenerator made with fish scale," *Applied Physics Letters,* vol. 109, p. 103701, 2016.

[37] E. Süli and D. F. Mayers, *An introduction to numerical analysis*: Cambridge university press, 2003.

[38] H. Kawai, "The piezoelectricity of poly (vinylidene fluoride)," *Japanese Journal of Applied Physics,* vol. 8, p. 975, 1969.

[39] A. J. Lovinger, "Poly (vinylidene fluoride)," in *Developments in crystalline polymers—1*, ed: Springer, 1982, pp. 195-273.

[40] E. Fukada, "History and recent progress in piezoelectric polymers," *IEEE Transactions on ultrasonics, ferroelectrics, and frequency control,* vol. 47, pp. 1277-1290, 2000.

[41] Y. Ye, Y. Jiang, Z. Wu, and H. Zeng, "Phase transitions of poly (vinylidene fluoride) under electric fields," *Integrated Ferroelectrics,* vol. 80, pp. 245-251, 2006.

[42] P. Sajkiewicz, A. Wasiak, and Z. Gocłowski, "Phase transitions during stretching of poly (vinylidene fluoride)," *European polymer journal,* vol. 35, pp. 423-429, 1999.

[43] L. Li, M. Zhang, M. Rong, and W. Ruan, "Studies on the transformation process of PVDF from α to β phase by stretching," *RSC Advances,* vol. 4, pp. 3938-3943, 2014.

[44] P. Martins, A. Lopes, and S. Lanceros-Mendez, "Electroactive phases of poly (vinylidene fluoride): determination, processing and applications," *Progress in polymer science,* vol. 39, pp. 683-706, 2014.

[45] V. RP, D. V. Khakhar, and A. Misra, "Studies on α to β phase transformations in mechanically deformed PVDF films," *Journal of applied polymer science,* vol. 117, pp. 3491-3497, 2010.

[46] V. Sencadas, R. Gregorio Jr, and S. Lanceros-Méndez, "α to β phase transformation and microestructural changes of PVDF films induced by uniaxial stretch," *Journal of Macromolecular Science®,* vol. 48, pp. 514-525, 2009.

[47] D. Sun, C. Chang, S. Li, and L. Lin, "Near-field electrospinning," *Nano letters,* vol. 6, pp. 839-842, 2006.

[48] T. Kaura, R. Nath, and M. Perlman, "Simultaneous stretching and corona poling of PVDF films," *Journal of Physics D: Applied Physics,* vol. 24, p. 1848, 1991.

[49] S. K. Mahadeva, J. Berring, K. Walus, and B. Stoeber, "Effect of poling time and grid voltage on phase transition and piezoelectricity of poly (vinyledene fluoride) thin films using corona poling," *Journal of Physics D: Applied Physics*, vol. 46, p. 285305, 2013.

[50] C. Lee and J. A. Tarbutton, "Electric poling-assisted additive manufacturing process for PVDF polymer-based piezoelectric device applications," *Smart Materials and Structures*, vol. 23, p. 095044, 2014.

[51] K. V. Wong and A. Hernandez, "A review of additive manufacturing," *ISRN Mechanical Engineering*, vol. 2012, 2012.

[52] R. Gregorio Jr and M. Cestari, "Effect of crystallization temperature on the crystalline phase content and morphology of poly (vinylidene fluoride)," *Journal of Polymer Science Part B: Polymer Physics*, vol. 32, pp. 859-870, 1994.

[53] V. Sencadas, R. Gregorio Filho, and S. Lanceros-Mendez, "Processing and characterization of a novel nonporous poly (vinilidene fluoride) films in the β phase," *Journal of Non-Crystalline Solids*, vol. 352, pp. 2226-2229, 2006.

[54] H. S. Nalwa, "Recent developments in ferroelectric polymers," *Journal of Macromolecular Science, Part C: Polymer Reviews*, vol. 31, pp. 341-432, 1991.

[55] J. Liu, X. Lu, and C. Wu, "Effect of Preparation Methods on Crystallization Behavior and Tensile Strength of Poly (vinylidene fluoride) Membranes," *Membranes*, vol. 3, pp. 389-405, 2013.

[56] V. Sencadas, M. V. Moreira, S. Lanceros-Méndez, A. S. Pouzada, and R. Gregório Filho, "α-to β Transformation on PVDF films obtained by uniaxial stretch," in *Materials science forum*, 2006, pp. 872-876.

[57] J. Granstrom, J. Feenstra, H. A. Sodano, and K. Farinholt, "Energy harvesting from a backpack instrumented with piezoelectric shoulder straps," *Smart Materials and Structures*, vol. 16, p. 1810, 2007.

[58] A. Vinogradov and F. Holloway, "Electro-mechanical properties of the piezoelectric polymer PVDF," *Ferroelectrics*, vol. 226, pp. 169-181, 1999.

[59] R. L. Hadimani, D. V. Bayramol, N. Sion, T. Shah, L. Qian, S. Shi, *et al.*, "Continuous production of piezoelectric PVDF fibre for e-textile applications," *Smart Materials and Structures,* vol. 22, p. 075017, 2013.

[60] Q. Ge, C. K. Dunn, H. J. Qi, and M. L. Dunn, "Active origami by 4D printing," *Smart Materials and Structures,* vol. 23, p. 094007, 2014.

[61] Q. Ge, A. H. Sakhaei, H. Lee, C. K. Dunn, N. X. Fang, and M. L. Dunn, "Multimaterial 4D printing with tailorable shape memory polymers," *Scientific Reports,* vol. 6, 2016.

[62] K. Hoejin, T. Fernando, W. Yanyu, V. Dino, L. Yirong, and T. Tzu-Liang, "Integrated 3D printing and corona poling process of PVDF piezoelectric films for pressure sensor application," *Smart Materials and Structures,* 2017.

[63] V. Bharti, T. Kaura, and R. Nath, "Ferroelectric hysteresis in simultaneously stretched and corona-poled PVDF films," *IEEE transactions on dielectrics and electrical insulation,* vol. 4, pp. 738-741, 1997.

[64] S. Lanceros-Mendez, J. Mano, A. Costa, and V. Schmidt, "FTIR and DSC studies of mechanically deformed β-PVDF films," *Journal of Macromolecular Science, Part B,* vol. 40, pp. 517-527, 2001.

[65] L. Seminara, M. Capurro, P. Cirillo, G. Cannata, and M. Valle, "Electromechanical characterization of piezoelectric PVDF polymer films for tactile sensors in robotics applications," *Sensors and Actuators A: Physical,* vol. 169, pp. 49-58, 2011.

[66] V. Corral-Flores and D. Bueno-Baqués, *Flexible Ferroelectric BaTiO3-PVDF Nanocomposites*: INTECH Open Access Publisher, 2011.

[67] T. R. Shrout and S. J. Zhang, "Lead-free piezoelectric ceramics: Alternatives for PZT?," *Journal of Electroceramics,* vol. 19, pp. 113-126, 2007.

[68] T. Takenaka, K.-i. Maruyama, and K. Sakata, "(Bi1/2Na1/2) TiO3-BaTiO3 system for lead-free piezoelectric ceramics," *Japanese Journal of Applied Physics,* vol. 30, p. 2236, 1991.

[69] V. K. Thakur and R. K. Gupta, "Recent progress on ferroelectric polymer-based nanocomposites for high energy density capacitors: synthesis, dielectric properties, and future aspects," *Chemical reviews,* vol. 116, pp. 4260-4317, 2016.

[70] J. P. Szabo, J. A. Hiltz, C. G. Cameron, R. S. Underhill, J. Massey, B. White, *et al.*, "Elastomeric composites with high dielectric constant for use in Maxwell stress actuators," in *Smart Structures and Materials*, 2003, pp. 180-190.

[71] K. Kim, W. Zhu, X. Qu, C. Aaronson, W. R. McCall, S. Chen, *et al.*, "3D optical printing of piezoelectric nanoparticle–polymer composite materials," *ACS nano,* vol. 8, pp. 9799-9806, 2014.

[72] F. A. Sanchez and J. González- Benito, "PVDFBaTiO3/carbon nanotubes ternary nanocomposites: Effect of nanofillers and processing," *Polymer Composites,* 2015.

[73] V. A. Kagan, I. Palley, and N. Jia, "Plastics part design: Low cycle fatigue strength of glass-fiber-reinforced polyethylene terephthalate (PET)," *Journal of reinforced plastics and composites,* vol. 23, pp. 1607-1614, 2004.

[74] H. Kim, T. Fernando, M. Li, Y. Lin, and T.-L. B. Tseng, "Fabrication and characterization of 3D printed BaTiO3/PVDF nanocomposites," *Journal of Composite Materials,* p. 0021998317704709, 2017.

[75] M.-Y. Shen, T.-Y. Chang, T.-H. Hsieh, Y.-L. Li, C.-L. Chiang, H. Yang, *et al.*, "Mechanical properties and tensile fatigue of graphene nanoplatelets reinforced polymer nanocomposites," *Journal of Nanomaterials,* vol. 2013, p. 1, 2013.

[76] Y. Zhou, F. Pervin, L. Lewis, and S. Jeelani, "Experimental study on the thermal and mechanical properties of multi-walled carbon nanotube-reinforced epoxy," *Materials Science and Engineering: A,* vol. 452, pp. 657-664, 2007.

[77] Y. Zhou, F. Pervin, L. Lewis, and S. Jeelani, "Fabrication and characterization of carbon/epoxy composites mixed with multi-walled carbon nanotubes," *Materials Science and Engineering: A,* vol. 475, pp. 157-165, 2008.

[78] Y.-K. Choi, K.-i. Sugimoto, S.-M. Song, Y. Gotoh, Y. Ohkoshi, and M. Endo, "Mechanical and physical properties of epoxy composites reinforced by vapor grown carbon nanofibers," *Carbon,* vol. 43, pp. 2199-2208, 2005.

[79] S.-Y. Yang, W.-N. Lin, Y.-L. Huang, H.-W. Tien, J.-Y. Wang, C.-C. M. Ma, *et al.*, "Synergetic effects of graphene platelets and carbon nanotubes on the mechanical and thermal properties of epoxy composites," *Carbon,* vol. 49, pp. 793-803, 2011.

[80] W. Xu, H. Yang, W. Zeng, T. Houghton, X. Wang, R. Murthy, *et al.*, "Food-Based Edible and Nutritive Electronics," *Advanced Materials Technologies,* p. 1700181, 2017.

[81] H. Kim, M. A. I. Shuvo, H. Karim, J. C. Noveron, T.-l. Tseng, and Y. Lin, "Synthesis and characterization of CeO2 nanoparticles on porous carbon for Li-ion battery," *MRS Advances,* pp. 1-9, 2017.

[82] H. Kim, M. A. I. Shuvo, H. Karim, M. I. Nandasiri, A. M. Schwarz, M. Vijayakumar, *et al.*, "Porous Carbon/CeO2 Nanoparticles Hybrid Material for High-Capacity Super-Capacitors," *MRS Advances,* pp. 1-10, 2017.

[83] H. Kim, F. Torres, Y. Wu, D. Villagran, Y. Lin, and T.-L. B. Tseng, "Integrated 3D printing and corona poling process of PVDF piezoelectric films for pressure sensor application," *Smart Materials and Structures,* vol. 26, p. 085027, 2017.

[84] H. Kim, F. Torres, D. Villagran, C. Stewart, Y. Lin, and T. L. B. Tseng, "3D Printing of BaTiO3/PVDF Composites with Electric In Situ Poling for Pressure Sensor Applications," *Macromolecular Materials and Engineering,* 2017.

[85] H. Kim, T. Fernando, M. Li, Y. Lin, and T.-L. B. Tseng, "Fabrication and characterization of 3D printed BaTiO3/PVDF nanocomposites," *Journal of Composite Materials,* p. 002199831770470, 2017.

[86] Y. Ahn, J. Y. Lim, S. M. Hong, J. Lee, J. Ha, H. J. Choi, *et al.*, "Enhanced piezoelectric properties of electrospun poly (vinylidene fluoride)/multiwalled carbon nanotube composites due to high β-phase formation in poly (vinylidene fluoride)," *The Journal of Physical Chemistry C,* vol. 117, pp. 11791-11799, 2013.

[87] K. I. Park, M. Lee, Y. Liu, S. Moon, G. T. Hwang, G. Zhu, *et al.*, "Flexible nanocomposite generator made of BaTiO3 nanoparticles and graphitic carbons," *Advanced Materials,* vol. 24, pp. 2999-3004, 2012.

[88] A. Mandal and A. K. Nandi, "Ionic liquid integrated multiwalled carbon nanotube in a poly (vinylidene fluoride) matrix: formation of a piezoelectric β-polymorph with significant reinforcement and conductivity improvement," *ACS applied materials & interfaces,* vol. 5, pp. 747-760, 2013.

[89] T. Karaki, K. Yan, T. Miyamoto, and M. Adachi, "Lead-free piezoelectric ceramics with large dielectric and piezoelectric constants manufactured from BaTiO3 nano-powder," *Japanese Journal of Applied Physics,* vol. 46, p. L97, 2007.

[90] L. Dong, D. S. Stone, and R. S. Lakes, "Enhanced dielectric and piezoelectric properties of x BaZrO3-(1− x) BaTiO3 ceramics," *Journal of Applied Physics,* vol. 111, p. 084107, 2012.

[91] Z.-M. Dang, J.-K. Yuan, J.-W. Zha, T. Zhou, S.-T. Li, and G.-H. Hu, "Fundamentals, processes and applications of high-permittivity polymer–matrix composites," *Progress in Materials Science,* vol. 57, pp. 660-723, 2012.

[92] T.-L. B. Tseng, C. A. Garcia Rosales, and Y. J. Kwon, "OPTIMIZATION OF WIND TURBINE PLACEMENT LAYOUT ON NON-FLAT TERRAINS," *International Journal of Industrial Engineering,* vol. 21, 2014.

[93] C. A. G. Rosales, C.-C. Huang, and Y. Lin, "Characterization and Quality Assessment of Shape Memory Polymer Parts Fabricated Using Fused Deposition Modelling," in *IIE Annual Conference. Proceedings*, 2017, pp. 1270-1275.

[94] H. Kim, Y. Lin, and T.-L. B. Tseng, "A review on quality control in additive manufacturing," *Rapid Prototyping Journal,* vol. 24, 2017.

[95] H. Kim, F. Torres, Y. Wu, D. Villagran, Y. Lin, and T.-L. Tseng, "Integrated 3D printing and corona poling process of PVDF piezoelectric films for pressure sensor application," *Smart Materials and Structures,* vol. 26, p. 085027, 2017.

[96] H. Kim, F. Torres, D. Villagran, C. Stewart, Y. Lin, and T.-L. B. Tseng, "3D Printing of BaTiO3/PVDF Composites with Electric In Situ Poling for Pressure Sensor Applications," *Macromolecular Materials and Engineering*, p. 1700229, 2017.

[97] H. Kim, F. Torres, M. T. Islam, M. D. Islam, L. A. Chavez, C. A. Garcia Rosales, *et al.*, "Increased piezoelectric response in functional nanocomposites through multiwall carbon nanotube interface and fused-deposition modeling three-dimensional printing," *MRS Communications*, pp. 1-7, 2017.

[98] A. J. Lovinger, "Ferroelectric polymers," *Science*, vol. 220, pp. 1115-1121, 1983.

[99] J. Brandrup, E. H. Immergut, and W. McDowell, *Polymer handbook*: Wiley, 1975.

[100] G. Maier, "Low dielectric constant polymers for microelectronics," *Progress in polymer science*, vol. 26, pp. 3-65, 2001.

[101] Z.-M. Dang, S.-H. Yao, J.-K. Yuan, and J. Bai, "Tailored dielectric properties based on microstructure change in BaTiO3-carbon nanotube/polyvinylidene fluoride three-phase nanocomposites," *The Journal of Physical Chemistry C*, vol. 114, pp. 13204-13209, 2010.

[102] B. Luo, X. Wang, Y. Wang, and L. Li, "Fabrication, characterization, properties and theoretical analysis of ceramic/PVDF composite flexible films with high dielectric constant and low dielectric loss," *Journal of Materials Chemistry A*, vol. 2, pp. 510-519, 2014.

[103] M. Rajib, M. A. I. Shuvo, H. Karim, D. Delfin, S. Afrin, and Y. Lin, "Temperature influence on dielectric energy storage of nanocomposites," *Ceramics International*, vol. 41, pp. 1807-1813, 2015.

[104] Y. Jin, N. Xia, and R. A. Gerhardt, "Enhanced dielectric properties of polymer matrix composites with BaTiO 3 and MWCNT hybrid fillers using simple phase separation," *Nano Energy*, vol. 30, pp. 407-416, 2016.

[105] D. H. McQueen, K.-M. Jäger, and M. Pelíšková, "Multiple threshold percolation in polymer/filler composites," *Journal of Physics D: Applied Physics*, vol. 37, p. 2160, 2004.

[106] Z.-M. Dang, H.-Y. Wang, B. Peng, and C.-W. Nan, "Effect of BaTiO3 size on dielectric property of BaTiO3/PVDF composites," *Journal of Electroceramics*, vol. 21, pp. 381-384, 2008.

[107] D. A. Porter, T. V. Hoang, and T. A. Berfield, "Effects of in-situ poling and process parameters on fused filament fabrication printed PVDF sheet mechanical and electrical properties," *Additive Manufacturing*, vol. 13, pp. 81-92, 2017.

[108] M. T. Islam, N. Dominguez, M. A. Ahsan, H. Dominguez-Cisneros, P. Zuniga, P. J. Alvarez, *et al.*, "Sodium rhodizonate induced formation of gold nanoparticles supported on cellulose fibers for catalytic reduction of 4-nitrophenol and organic dyes," *Journal of Environmental Chemical Engineering*, vol. 5, pp. 4185-4193, 2017.

[109] C. Czech Standard, "EN 60243-1 (IEC 60243-1: 1998)," *Czech Institute for Standardization*, 1999.

[110] H. Tang, Z. Zhou, C. C. Bowland, and H. A. Sodano, "Synthesis of calcium copper titanate (CaCu 3 Ti 4 O 12) nanowires with insulating SiO 2 barrier for low loss high dielectric constant nanocomposites," *Nano Energy*, vol. 17, pp. 302-307, 2015.

[111] S. Mandal, S. Singh, P. Dey, J. Roy, P. Mandal, and T. Nath, "Frequency and temperature dependence of dielectric and electrical properties of TFe 2 O 4 (T= Ni, Zn, Zn 0.5 Ni 0.5) ferrite nanocrystals," *Journal of Alloys and Compounds*, vol. 656, pp. 887-896, 2016.

[112] C. Chanmal and J. Jog, "Dielectric relaxations in PVDF/BaTiO3 nanocomposites," *Express Polymer Letters*, vol. 2, pp. 294-301, 2008.

[113] J. Fu, Y. Hou, M. Zheng, Q. Wei, M. Zhu, and H. Yan, "Improving dielectric properties of PVDF composites by employing surface modified strong polarized BaTiO3 particles derived by molten salt method," *ACS applied materials & interfaces*, vol. 7, pp. 24480-24491, 2015.

[114] K. Yu, Y. Niu, F. Xiang, Y. Zhou, Y. Bai, and H. Wang, "Enhanced electric breakdown strength and high energy density of barium titanate filled polymer nanocomposites," *Journal of Applied Physics*, vol. 114, p. 174107, 2013.

[115] Z. M. Dang, M. S. Zheng, and J. W. Zha, "1D/2D Carbon Nanomaterial- Polymer Dielectric Composites with High Permittivity for Power Energy Storage Applications," *Small*, vol. 12, pp. 1688-1701, 2016.

[116] Y. Xing, "Synthesis and electrochemical characterization of uniformly-dispersed high loading Pt nanoparticles on sonochemically-treated carbon nanotubes," *The Journal of Physical Chemistry B*, vol. 108, pp. 19255-19259, 2004.

[117] V. KumaráThakur, E. JináTan, and P. SeeáLee, "Surface functionalization of BaTiO 3 nanoparticles and improved electrical properties of BaTiO 3/polyvinylidene fluoride composite," *RSC Advances*, vol. 1, pp. 576-578, 2011.

[118] J. Li, J. Claude, L. E. Norena-Franco, S. I. Seok, and Q. Wang, "Electrical energy storage in ferroelectric polymer nanocomposites containing surface-functionalized BaTiO3 nanoparticles," *Chemistry of Materials*, vol. 20, pp. 6304-6306, 2008.

[119] Y. Song, Y. Shen, H. Liu, Y. Lin, M. Li, and C.-W. Nan, "Improving the dielectric constants and breakdown strength of polymer composites: effects of the shape of the BaTiO 3 nanoinclusions, surface modification and polymer matrix," *Journal of Materials Chemistry*, vol. 22, pp. 16491-16498, 2012.

[120] J. Li, L. Zhang, and S. Ducharme, "Electric energy density of dielectric nanocomposites," *Applied physics letters*, vol. 90, p. 132901, 2007.

[121] L. Cai, L. Song, P. Luan, Q. Zhang, N. Zhang, Q. Gao, *et al.*, "Super-stretchable, transparent carbon nanotube-based capacitive strain sensors for human motion detection," *Scientific reports*, vol. 3, p. 3048, 2013.

[122] D. J. Cohen, D. Mitra, K. Peterson, and M. M. Maharbiz, "A highly elastic, capacitive strain gauge based on percolating nanotube networks," *Nano letters*, vol. 12, pp. 1821-1825, 2012.

[123] G. Georgousis, C. Pandis, A. Kalamiotis, P. Georgiopoulos, A. Kyritsis, E. Kontou, *et al.*, "Strain sensing in polymer/carbon nanotube composites by electrical resistance measurement," *Composites Part B: Engineering*, vol. 68, pp. 162-169, 2015.

[124] P. Dharap, Z. Li, S. Nagarajaiah, and E. Barrera, "Nanotube film based on single-wall carbon nanotubes for strain sensing," *Nanotechnology,* vol. 15, p. 379, 2004.

[125] T. Yamada, Y. Hayamizu, Y. Yamamoto, Y. Yomogida, A. Izadi-Najafabadi, D. N. Futaba, *et al.*, "A stretchable carbon nanotube strain sensor for human-motion detection," *Nature nanotechnology,* vol. 6, pp. 296-301, 2011.

[126] I. Kang, M. J. Schulz, J. H. Kim, V. Shanov, and D. Shi, "A carbon nanotube strain sensor for structural health monitoring," *Smart materials and structures,* vol. 15, p. 737, 2006.

[127] D. D. Chung, "Self-monitoring structural materials," *Materials Science and Engineering: R: Reports,* vol. 22, pp. 57-78, 1998.

[128] H. Kim, F. Torres, M. T. Islam, M. D. Islam, L. A. Chavez, C. A. Garcia Rosales, *et al.*, "Increased piezoelectric response in functional nanocomposites through multiwall carbon nanotube interface and fused-deposition modeling three-dimensional printing," *MRS Communications,* 2017.

[129] Z.-M. Dang, S.-H. Yao, and H.-P. Xu, "Effect of tensile strain on morphology and dielectric property in nanotube/polymer nanocomposites," *Applied Physics Letters,* vol. 90, p. 012907, 2007.

[130] F. A. Sanchez and J. González- Benito, "PVDFBaTiO3/carbon nanotubes ternary nanocomposites: Effect of nanofillers and processing," *Polymer Composites,* vol. 38, pp. 227-235, 2017.

[131] X.-M. Meng, X.-J. Zhang, C. Lu, Y.-F. Pan, and G.-S. Wang, "Enhanced absorbing properties of three-phase composites based on a thermoplastic-ceramic matrix (BaTiO 3+ PVDF) and carbon black nanoparticles," *Journal of Materials Chemistry A,* vol. 2, pp. 18725-18730, 2014.

[132] T. Zhou, J.-W. Zha, R.-Y. Cui, B.-H. Fan, J.-K. Yuan, and Z.-M. Dang, "Improving dielectric properties of BaTiO3/ferroelectric polymer composites by employing surface hydroxylated BaTiO3 nanoparticles," *ACS applied materials & interfaces,* vol. 3, pp. 2184-2188, 2011.

[133] V. Petrovsky, T. Petrovsky, S. Kamlapurkar, and F. Dogan, "Dielectric constant of barium titanate powders near Curie temperature," *Journal of the American Ceramic Society,* vol. 91, pp. 3590-3592, 2008.

[134] Z. M. Dang, Y. Q. Lin, H. P. Xu, C. Y. Shi, S. T. Li, and J. Bai, "Fabrication and dielectric characterization of advanced BaTiO3/polyimide nanocomposite films with high thermal stability," *Advanced Functional Materials,* vol. 18, pp. 1509-1517, 2008.

[135] J. W. Liou and B. S. Chiou, "Dielectric tunability of barium strontium titanate/silicone-rubber composite," *Journal of Physics: Condensed Matter,* vol. 10, p. 2773, 1998.

[136] B. W. Lee and K. H. Auh, "Effect of grain size and mechanical processing on the dielectric properties of BaTiO3," *Journal of Materials Research,* vol. 10, pp. 1418-1423, 2011.

[137] C. M. Dhar and P. K. C. Pillai, "Thermocompensated capacitor with barium titanate (BaTiO3)/polyvinylidene fluoride (PVDF) composite," *Journal of Materials Science Letters,* vol. 6, pp. 33-34, 1987/01/01 1987.

[138] C. Muralidhar and P. Pillai, "Dielectric behaviour of barium titanate (BaTiO3)/polyvinylidene fluoride (PVDF) composite," *Journal of materials science letters,* vol. 6, pp. 346-348, 1987.

[139] T. Tsurumi, K. Soejima, T. Kamiya, and M. Daimon, "Mechanism of diffuse phase transition in relaxor ferroelectrics," *Japanese journal of applied physics,* vol. 33, p. 1959, 1994.

[140] B. Lee and K. Auh, "Effect of grain size and mechanical processing on the dielectric properties of BaTiO 3," *Journal of materials research,* vol. 10, pp. 1418-1423, 1995.

[141] K. S. Kim, Y. Zhao, H. Jang, S. Y. Lee, J. M. Kim, K. S. Kim, *et al.*, "Large-scale pattern growth of graphene films for stretchable transparent electrodes," *nature,* vol. 457, p. 706, 2009.

[142] M. Song, D. S. You, K. Lim, S. Park, S. Jung, C. S. Kim, *et al.*, "Highly efficient and bendable organic solar cells with solution- processed silver nanowire electrodes," *Advanced Functional Materials,* vol. 23, pp. 4177-4184, 2013.

[143] W. Gaynor, G. F. Burkhard, M. D. McGehee, and P. Peumans, "Smooth nanowire/polymer composite transparent electrodes," *Advanced Materials,* vol. 23, pp. 2905-2910, 2011.

[144] J. Lee, P. Lee, H. B. Lee, S. Hong, I. Lee, J. Yeo, *et al.*, "Room- temperature nanosoldering of a very long metal nanowire network by conducting- polymer- assisted joining for a flexible touch- panel application," *Advanced Functional Materials,* vol. 23, pp. 4171-4176, 2013.

[145] X. Y. Zeng, Q. K. Zhang, R. M. Yu, and C. Z. Lu, "A new transparent conductor: silver nanowire film buried at the surface of a transparent polymer," *Advanced materials,* vol. 22, pp. 4484-4488, 2010.

[146] H. Lee, I. Kim, M. Kim, and H. Lee, "Moving beyond flexible to stretchable conductive electrodes using metal nanowires and graphenes," *Nanoscale,* vol. 8, pp. 1789-1822, 2016.

[147] M.-S. Lee, K. Lee, S.-Y. Kim, H. Lee, J. Park, K.-H. Choi, *et al.*, "High-performance, transparent, and stretchable electrodes using graphene–metal nanowire hybrid structures," *Nano letters,* vol. 13, pp. 2814-2821, 2013.

[148] C. Yan, W. Kang, J. Wang, M. Cui, X. Wang, C. Y. Foo, *et al.*, "Stretchable and wearable electrochromic devices," *ACS nano,* vol. 8, pp. 316-322, 2013.

[149] M. Amjadi, A. Pichitpajongkit, S. Lee, S. Ryu, and I. Park, "Highly stretchable and sensitive strain sensor based on silver nanowire–elastomer nanocomposite," *ACS nano,* vol. 8, pp. 5154-5163, 2014.

[150] L. Böger, M. H. G. Wichmann, L. O. Meyer, and K. Schulte, "Load and health monitoring in glass fibre reinforced composites with an electrically conductive nanocomposite epoxy matrix," *Composites Science and Technology,* vol. 68, pp. 1886-1894, 2008/06/01/ 2008.

[151] M. D. Rein, O. Breuer, and H. D. Wagner, "Sensors and sensitivity: Carbon nanotube buckypaper films as strain sensing devices," *Composites Science and Technology,* vol. 71, pp. 373-381, 2011/02/07/ 2011.

[152] S.-H. Yao, J.-K. Yuan, T. Zhou, Z.-M. Dang, and J. Bai, "Stretch-modulated carbon nanotube alignment in ferroelectric polymer composites: characterization of the orientation

state and its influence on the dielectric properties," *The Journal of Physical Chemistry C,* vol. 115, pp. 20011-20017, 2011.

[153] D. Bikiaris, "Microstructure and properties of polypropylene/carbon nanotube nanocomposites," *Materials,* vol. 3, pp. 2884-2946, 2010.

[154] C. Miehe, S. Göktepe, and J. M. Diez, "Finite viscoplasticity of amorphous glassy polymers in the logarithmic strain space," *International Journal of Solids and Structures,* vol. 46, pp. 181-202, 2009.

[155] H. Kim, T. Fernando, M. Li, Y. Lin, and T.-L. B. Tseng, "Fabrication and characterization of 3D printed BaTiO3/PVDF nanocomposites," *Journal of Composite Materials,* vol. 52, pp. 197-206, 2018.

[156] H. Kim, F. Torres, D. Villagran, C. Stewart, Y. Lin, and T.-L. B. Tseng, "3D Printing of BaTiO3/PVDF Composites with Electric In Situ Poling for Pressure Sensor Applications," *Macromolecular Materials and Engineering,* vol. 302, p. 1700229, 2017.

[157] X. Song, "SLURRY BASED STEREOLITHOGRAPHY: A SOLID FREEFORM FABRICATION METHOD OF CERAMICS AND COMPOSITES," UNIVERSITY OF SOUTHERN CALIFORNIA, 2016.

[158] C. W. Hull, "Apparatus for production of three-dimensional objects by stereolithography," ed: Google Patents, 1986.

[159] M. Zarek, M. Layani, I. Cooperstein, E. Sachyani, D. Cohn, and S. Magdassi, "3D printing of shape memory polymers for flexible electronic devices," *Advanced Materials,* vol. 28, pp. 4449-4454, 2016.

[160] F. Liu, N. A. Hashim, Y. Liu, M. M. Abed, and K. Li, "Progress in the production and modification of PVDF membranes," *Journal of membrane science,* vol. 375, pp. 1-27, 2011.

[161] H. Kim, M. A. I. Shuvo, H. Karim, J. C. Noveron, T.-l. Tseng, and Y. Lin, "Synthesis and characterization of CeO2 nanoparticles on porous carbon for Li-ion battery," *MRS Advances,* vol. 2, pp. 3299-3307, 2017.

[162] H. Kim, M. A. I. Shuvo, H. Karim, M. I. Nandasiri, A. M. Schwarz, M. Vijayakumar, *et al.*, "Porous Carbon/CeO2 Nanoparticles Hybrid Material for High-Capacity Super-Capacitors," *MRS Advances,* vol. 2, pp. 2471-2480, 2017.

[163] E. Žagar and M. Žigon, "Solution properties of carboxylated polyurethanes and related ionomers in polar solvents (DMF and LiBr/DMF)," *Polymer,* vol. 41, pp. 3513-3521, 2000.

[164] Y. Cai and J. L. Jessop, "Photopolymerization, Free Radical," *Encyclopedia of Polymer Science and Technology*, 2004.

[165] S. Inceoglu, S. C. Olugebefola, M. H. Acar, and A. M. Mayes, "Atom transfer radical polymerization using poly (vinylidene fluoride) as macroinitiator," *Designed Monomers and Polymers,* vol. 7, pp. 181-189, 2004.

[166] D. Zhang and X. Yang, "Precipitation Polymerization," in *Encyclopedia of Polymeric Nanomaterials*, S. Kobayashi and K. Müllen, Eds., ed Berlin, Heidelberg: Springer Berlin Heidelberg, 2021, pp. 1-10.

[167] D. Wang, K. Li, and W. Teo, "Porous PVDF asymmetric hollow fiber membranes prepared with the use of small molecular additives," *Journal of Membrane Science,* vol. 178, pp. 13-23, 2000.

[168] M. A. Ishtiaque Shuvo, G. Rodriguez, M. T. Islam, H. Karim, N. Ramabadran, J. C. Noveron, *et al.*, "Microwave exfoliated graphene oxide/TiO2 nanowire hybrid for high performance lithium ion battery," *Journal of Applied Physics,* vol. 118, p. 125102, 2015.

[169] S. Pal, M. T. Islam, J. T. Moore, J. Reyes, A. Pardo, A. Varela-Ramirez, *et al.*, "Self-assembly of a novel Cu (ii) coordination complex forms metallo-vesicles that are able to transfect mammalian cells," *New Journal of Chemistry,* vol. 41, pp. 11230-11237, 2017.

[170] M. Biswas, J. A. Libera, S. B. Darling, and J. W. Elam, "Kinetics for the Sequential Infiltration Synthesis of Alumina in Poly (methyl methacrylate): An Infrared Spectroscopic Study," *The Journal of Physical Chemistry C,* vol. 119, pp. 14585-14592, 2015.

[171] H. Bai, X. Wang, Y. Zhou, and L. Zhang, "Preparation and characterization of poly (vinylidene fluoride) composite membranes blended with nano-crystalline cellulose," *Progress in Natural Science: Materials International*, vol. 22, pp. 250-257, 2012.

[172] H. Kim, T. Fernando, M. Li, Y. Lin, and T.-L. B. Tseng, "Fabrication and characterization of 3D printed BaTiO3/PVDF nanocomposites," *Journal of Composite Materials*, vol. 0, p. 002199831770470, 2017.

Vita

Dr. Hoejin Kim earned his Bachelor of Science degree in Materials Engineering from Korea University of Technology and Education in 2008. After his Bachelor degree, he graduated from Korea Naval Academy and served in Republic of Korea Navy as Naval Office, a chief of engineer, by 2011. In 2014, he received his Master of Science degree in Manufacturing Engineering Technology from Oregon Institute of Technology. In 2015, he joined the doctoral program in Mechanical Engineering at The University of Texas at El Paso.

Dr. Hoejin worked as a Research Associate for the Department of Industrial, Manufacturing, and Systems Engineering. In addition, he was a Research Associate member of Functional Energy Material Systems Laboratory (FEMS) and Center for Quality, Production, Systems Innovation (CQPSI). While pursuing three and a half years of his Ph.D. degree, Dr. Hoejin Kim published or submitted 20 peer-reviewed journal papers, 5 conference proceeding papers, and filed 1 patent. His researches were presented at Materials Research Society conference in Phoenix as well as at symposium in IMSE day.

Dr. Hoejin's dissertation entitled, "Additive Manufacturing of Multi-Functional Nanocomposites for Sensor and Energy Storage Devices" was supervised by Drs. Tzu-Liang Bill Tseng and Yirong Lin. He will join Intel Corporation at Oregon following by his graduation.

Contact Information: kimhoejin@gmail.com

This dissertation was typed by Hoejin Kim